INVESTIGATION OF STRUCTURAL DAMAGE IN POOL-TYPE FAST REACTOR COMPONENTS DURING THERMAL TRANSIENTS

By

ROSY SARKAR

(ENGG02201604006)

Indira Gandhi Centre for Atomic Research, Kalpakkam

A thesis submitted to the

Board of Studies in Engineering Sciences

In partial fulfillment of requirements

for the Degree of

DOCTOR OF PHILOSOPHY

of

HOMI BHABHA NATIONAL INSTITUTE

December, 2020

Homi Bhabha National Institute[1]

Recommendations of the Viva Voce Committee

As members of the Viva Voce Committee, we certify that we have read the dissertation prepared by Rosy Sarkar entitled "Investigation of Structural Damage in Pool-type Fast Reactor Components during Thermal Transients" and recommend that it may be accepted as fulfilling the thesis requirement for the award of Degree of Doctor of Philosophy.

Chairman – Dr. Shaju K. Albert	
Guide / Convener – Dr. Anil Kumar Sharma	
Examiner - Dr. Ashutosh Mishra	
Member 1- Dr. A.Nagesha	
Member 2- Dr. P. Mangarjuna Rao	P. Mangarjuna Rao
Member 3- Dr. M. Vasudevan	
Technology Advisor- Shri. S. Jalaldeen	

Final approval and acceptance of this thesis is contingent upon the candidate's submission of the final copies of the thesis to HBNI.

I/We hereby certify that I/we have read this thesis prepared under my/our direction and recommend that it may be accepted as fulfilling the thesis requirement.

Date: 20/07/2021

Place: Kalpakkam

Signature
Guide

[1] This page is to be included only for final submission after successful completion of viva voce.

STATEMENT BY AUTHOR

This dissertation has been submitted in partial fulfillment of requirements for an advanced degree at Homi Bhabha National Institute (HBNI) and is deposited in the library to be made available to borrowers under rules of the HBNI.

Brief quotations from this dissertation are allowable without special permission, provided that accurate acknowledgement of source is made. Requests for permission for extended quotation from or reproduction of this manuscript in whole or in part may be granted by the Competent Authority of HBNI when in his or her judgment the proposed use of the material is in the interests of scholarship. In all other instances, however, permission must be obtained from the author.

Name & Signature of the student

(ROSY SARKAR)

DECLARATION

I, hereby declare that the investigation presented in the thesis has been carried out by me. The work is original and has not been submitted earlier as a whole or in part for a degree / diploma at this or any other Institution / University.

(ROSY SARKAR)

List of publications arising from the thesis

Journal

Published/Accepted

1. **Rosy Sarkar**, Suresh Kumar R, Jalaldeen S, Anil Kumar Sharma and Velusamy K, *Ballooning in fuel clad: The first of its kind approach for its investigation in fast reactors*, International Journal of Pressure Vessels and Piping, 160 (2018)24–33.

2. **Rosy Sarkar**, Suresh Kumar R, Jalaldeen S, Anil Kumar Sharma and Velusamy K, *Thermo-mechanical behaviour of primary system components of future FBR during crash Cooling: A numerical simulation*, Nuclear Engineering and Design, 326 (2018) 162–174.

3. **Rosy Sarkar**, Vijayanand V. D, Avinash Kumar Acharya, Anil Kumar Sharma, Suresh Kumar, and Prasad Reddy G, *Experimental Investigation of the Evolution of Fuel Clad Ballooning using Real-Time X-ray Imaging and its Microstructural Studies,* Transactions of Indian Institute of Metals 74, pages1933–1942 (2021).

Under Preparation

1. **Rosy Sarkar**, Anil Kumar Sharma, Suresh Kumar R and Jalaldeen S, *On the Effect of Primary Sodium Heating Rate during Power Raising in Pool-type Fast Reactors*.

Conference/Symposium

[1] **Rosy Sarkar**, Jalaldeen S, Velusamy K, Anil Kumar Sharma, *On The Effect of Primary Sodium Heating Rate during Power Raising based on Inner Vessel Life*, 2nd International Conference on Fatigue, Durability and Fracture Mechanics and Symposium on Condition Assessment/Residual Life Assessment, Bangalore, September 28-30, (2016).

[2] **Rosy Sarkar**, Suresh Kumar R, Jalaldeen S, Velusamy K, Anil Kumar Sharma, *Dependence of Intermediate Heat Exchanger Life on Primary Sodium Heating Rate during Power Raising*, International Conference on Fast Reactors and Related Fuel Cycles: Next Generation Nuclear Systems for Sustainable Development (FR17), Yekaterinburg, Russian Federation, 26–29 June (2017).

[3] **Rosy Sarkar**, Suresh Kumar R, Jalaldeen S, Velusamy K, Anil Kumar Sharma, *Optimization of Primary Sodium Heating Rate to Reduce Power Raising Duration based*

on *Control Plug Life*, SMiRT-24, August 20-25, (2017), BEXCO/Centum Hotel, Busan, Korea.

[4] **Rosy Sarkar**, Suresh Kumar R, Jalaldeen S, Anil Kumar Sharma and Velusamy K, *Effect of Crash Cooling for Submerged Hot Pool Components in Sodium*, National Conference on Thermophysical Properties NCTP, November 6-8, (2017), IGCAR, Kalpakkam.

[5] **Rosy Sarkar**, Vijayanand D, Avinash Kumar Acharya, Suresh Kumar R, Jalaldeen S, Anil Kumar Sharma and Shaju K. Albert, *Structural Integrity Assessment of Fuel Clad Tubes at High Temperature and High Pressure*, ICONS 2018, Second International Conference on Structural Integrity, Dec 14-17, (2018), Chennai.

Dedicated to my beloved Parents…

Acknowledgements

I express my deepest gratitude to Dr. Anil Kumar Sharma, for mentoring, guiding and motivating me to accomplish this research work. His constant pursual for scientific excellence has helped me to shape up this thesis. His focus on building up professional relationships by collaborating with colleagues inspired me to take up higher challenges.

I thank Dr. Shaju K. Albert (Chairman) and Dr. G. Sasikala (Ex-Chairman) for critically reviewing the progress of this study. I thank my DC Members, Dr. A. Nagesha, Dr. P. Mangarjuna Rao, and Dr. M. Vasudevan for their encouragement and insightful comments. It is my privilege to acknowledge Shri. S. Jalaldeen (Technology Advisor and Head SMD) for valuable scientific suggestions during the course of this research work.

I thank Dr. A. K. Bhaduri, (Director, IGCAR), Shri. S. Raghupathy (Director RDTG) and Dr. Anish Kumar (Dean, Engineering Sciences) for granting me permission to pursue the PhD degree at the Homi Bhabha National Institute.

This work would not have been accomplished without the knowledge shared by Dr. K. Velusamy (former AD, NSAG), Dr. R. Suresh Kumar (Head, HTAS), Shri. Kulbir Singh (HTAS) and all my RDTG colleagues. I thank Dr. K. Natesan, Shri. U. Parthasarathy and Shri. Juby Abraham of RDTG for providing the temperature inputs.

I thank Dr. David Vijayanand and Dr. G. Prasad Reddy (MMG), for helping me to carry out the metallurgical investigations. I am delighted to record my acknowledgements to Dr. P. Chellapandi (former Director, RDG) and Prof. Anurag Gupta (IIT Kanpur) for introducing me to the fascinating field of ballooning in tubes. I thank Shri. Avinash Kumar Acharya, Smt. Lydia Gnanadhas and Shri. D. Ponraju (RDTG) for facilitating the digital flat panel detector at the SFEF. I acknowledge the help rendered by Shri. N. Raghu, Shri. Narayan Rao and Shri. Krishna Chaitanya (QAD) for carrying out X-ray imaging. I thank Smt. N. Sreevidya (MMG) for carrying out the fractography tests.

The experimental assistance received from all my lab (SML/HTAS) colleagues, Shri. R. Manu, Shri. G. Venkataiah, Shri. S. Ramesh, Shri. K. Mohan, Shri. B. E. Bhaskar and Shri. M. Aravind is highly acknowledged.

It's my privilege to thank Shri. Tanmay Vasal and Shri. L. Satish Kumar (SWCS) and Shri. Bidyut Maity (BHEL) for providing insight on the steam water system, and Smt. T. Sathiyasheela (SAS), for sharing knowledge on reactor physics aspects.

I would like to express my special thanks to Shri. P. Jegadeesan and Dr. P. Anees (MSG) for sharing the thesis template with me, which simplified my thesis writing.

I am highly indebted to my teachers for inculcating the interest in me for pursuing research as a career. I would like to extend my sincere gratitude to all my friends, especially, Dr. Niruben Amin for giving me mental rejuvenation at times when it was most needed. I could not have completed my PhD without the support of my helper at home, Smt. Latha.

I can never forget the sacrifices and blessings of my father Shri Goutam Sarkar and my mother Smt. Kaberi Sarkar, without whom I could never be what I am now. I am grateful to my parents-in-law, Shri Bishnupada Maity and Smt. Arati Maity, who have provided me with all care and moral support during difficult times. I thank my sister Smt. Manjira Sarkar who has always been my inspiration, and my brother-in-law Shri. Mahesh Babu for helping me at all times. I would like to acknowledge my husband Shri. Bidyut Maity for the sacrifices made, and for his unconditional love. I thank my son Ayan Maity for adjusting with my work schedule, and for energizing me throughout the progress of this work.

(ROSY SARKAR)

Table of contents

List of figures

List of tables

List of abbreviations and symbols

A) List of Abbreviations

Abbreviations	*Definitions*
BDBE	Beyond Design Basis Event
CCOC	Creep Cross Over Curve
CCP	Core Cover Plate
CDF	Cumulative Damage Fraction
CP	Control Plug
CRDM	Control Rod Drive Mechanisms
CSR	Control Safety Rods
DBE	Design Basis Event
DFC	Design Fatigue Curve
DFPD	Digital Flat Panel Detector
DSL	Design Safety Limits
DSR	Diverse Safety Rods
ESP	Equivalent Solid Plate
FBR	Fast Breeder Reactor
FBTR	Fast Breeder Test Reactor
FE	Finite Element
FEM	Finite Element Method
FIV	Flow Induced Vibration
FL	Free Level
GDP	Gross Domestic Product
GFR	Gas-cooled fast reactor
HCF	High Cycle Fatigue
HTCTTF	High Temperature Clad Tube Test Facility
IHX	Intermediate Heat eXchanger
LCF	Low Cycle Fatigue
LFR	Lead-cooled Fast Reactor
LMFBR	Liquid Metal Fast Breeder Reactors
LOCA	Loss of Coolant Accident
LOFA	Loss of Flow Accident
LSP	Lower Stay Plate
LFR	Lead-cooled Fast Reactor
MSR	Molten Salt Reactor
NSSS	Nuclear Steam Supply System
OD	Outer Diameter
OGDHRS	Operation Graded Decay Heat Removal System
PFBR	Prototype Fast Breeder Reactor

PID controller	Proportional Integral Derivative controller
PSP	Primary Sodium Pump
PWR	Pressurized Water Reactor
RABITS	Rupture and Ballooning In TubeS
RCB	Reactor Containment Building
SA	Sub Assembly
SCRAM	Safety Control Rod Accelerated Motion
SEM	Scanning Electron Microscope
SFR	Sodium cooled Fast Reactor
SG	Steam Generator
SGDHRS	Safety Graded Decay Heat Removal System
SRP	Small Rotatable Plug
SS	Stainless Steel
SSP	Secondary Sodium Pump
SWCR	Supercritical Water-Cooled Reactor
TS	Tube Sheets
USP	Upper Stay Plate

B) List of Symbols

Symbol	***Meaning***
ΔL	Level Change
A	Surface area of the component
C_p	Specific heat of solid
E	Youngs Modulus
F	Peak stress
G	Shear modulus
h	Heat transfer coefficient of the convective medium
i	Element number
I	Area moment of inertia
J	Torsion constant (second moment of area)
J.G	Torsional rigidity
K	Thermal conductivity of the body
l	Length of the object the torque is being applied
L	Sodium Level
L_m	Additional local membrane stress
z	Thickness of the body
lbi	Inner surface bottom length
lbo	Outer surface bottom length
Lc	Characteristic length
li.i	Inner discretization regime
lo.i	Outer discretization regime

lti	Inner surface top length
lto	Outer surface top length
M	Bending moment
P	Perimeter of the surface
P_m	Primary membrane stress
P_b	Primary bending stress
P_L	Local primary membrane stress
Q	Secondary stress
r	Distance from axis
R	Radius of curvature of the beam
t	Time
T	Applied torque or moment of torsion
T_{Ar}	Argon cover gas temperature
T_{Na}	Sodium temperature
T_{∞}	Ambient (argon gas) temperature
x	Depth from surface
y	Distance from neutral axis
V	Volume of the body

C) List of Greek letters

Symbol	***Meaning***
α	Thermal diffusivity
θ	Angle of twist in radians
ρ	Density of solid
$\sigma_1, \sigma_2, \sigma_3$	Principal stresses
σ_y	Yield strength
τ	Stress at the outer surface
ΔQ	Cyclic secondary stress

Chapter 1

Introduction

1.1. Background

This chapter includes the introduction to nuclear reactors technology and their significant features, difference between loop-type and pool-type fast reactors, various reactor transients and the details of fast reactor components. Also, the objective and scope of the thesis is highlighted. The organization of the thesis is also illustrated in this chapter.

1.1.1. Nuclear reactors

The socio-economic development of a country like literacy, longevity, GDP and human development are directly dependent upon its per capita energy consumption. Thus the world needs adequate and secure energy supply at affordable costs [1]. The energy resources are broadly categorized into two: renewable and non-renewable. Renewable energy is the energy from a source that is not depleted when used. Ex. Solar, wind, water (hydro), biomass, geothermal etc. Non-renewable energy resources are available in limited supplies, due to the longer time it takes to replenish. Ex: coal, nuclear, oil and natural gas. The non-renewable natural resources are a major source of power but the downside is its negative environmental impact. When compared to oil and coal, nuclear energy is efficient and economical due to the lower quantity of fuel required, producing the same amount of power.

Nuclear energy is efficient and clean source of energy, sustainable, environment friendly and safe. The nuclear reactors are classified into thermal and fast reactors based on the energy of neutrons that cause fission. Thermal reactors are operated at relatively low temperatures, with low neutron energy and flux. Fast reactors are operated at high temperatures with high neutron energy and flux.

1.1.2. Fast reactors

In a fast reactor, the fission chain reaction is sustained by fast neutrons (energy > 0.5 MeV). The nuclear fission reaction as shown in Figure.1.1 is a nuclear reaction in which the nucleus of an atom splits into lighter nuclei when triggered by a neutron.

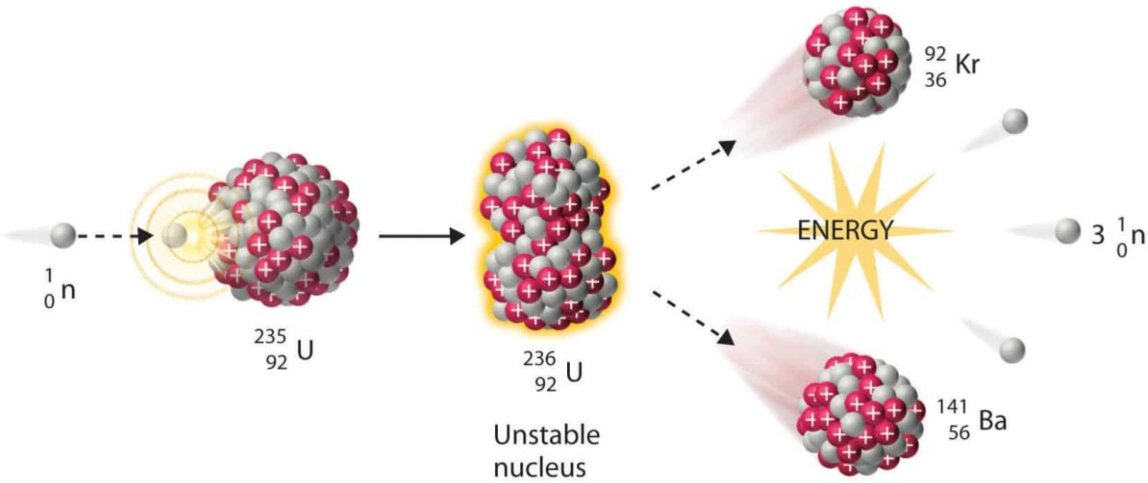

Figure 1.1 Nuclear fission reaction [1 web ref]

Natural Uranuium consists of 0.7 percent of fissile Uranium (U235) and the rest of it is fertile (U238 and traces of U234). In thermal reactors, U235 is normally enriched between 3 and 8 percent by weight and is used as fuel, and the neutrons emitted by nuclear fission are slowed down to 0.01 to 1 eV range by the moderator. The slowed neutrons cause fission in other nuclei and maintain the chain reaction. In fast reactors, the neutrons are not slowed down, and most of the fast neutrons are captured by fertile U238 to form fissile U239, after two beta decays. The plutonium isotope is reprocessed and used as fuel in fast reactors. Thus fast reactors are called fast breeder reactors as they have the potential to produce more fuel than they consume. Fast reactors are preferred due to the effective usage of natural nuclear resources, i.e. Uranium and Thorium. The advantages of fast reactors include its ability to consume existing nuclear waste and higher yield of energy [2].

The various types of fast reactors are

- Sodium-cooled fast reactor

- Lead-cooled fast reactor
- Molten salt reactor and
- Gas-cooled fast reactor

Some of the details of the reactors are given in Table 1.1.

Table 1.1 Comparison of various types of fast reactors [2]

Reactor	**Coolant**	**Temperature (°C)**	**Pros**	**Cons**
SFR	Sodium	550	• High thermal inertia • Temperature margin to boiling is good • Unpressurized reactor vessel • Long R&D experience	• Positive void coefficient • Criticality issues during core meltdown • Violent sodium water and sodium air reactions • Reaction of liquid sodium with MOX fuel
LFR	Lead or Pb-Bi	480-800	• High thermal inertia • High boiling point • Unpressurized reactor vessel and good passive safety • Compatible with water and air	• High melting temperature • Problematic cleaning and decontamination • Corrosive and toxic • Activation of coolant
MSR	Flouride salts	700-800	• No risk of core melting • Reactor control fuel flow • Online removal of fission products • Thorium usage • Limited waste production • Simplified reprocessing	• Fuel in primary circuit, complicated neutronics • Irradiation of heat exchanger • Salts are corrosive • High salt melting temperature • Complicated reactor start-up • No experience

GFR	Helium	850	• Thermal negative feedback • Resistant fuel barrier (ceramic fuel) • Inert coolant	• Low thermal inertia • High-pressure system • Complicated fuel and cladding • High coolant flow • No operating experience • DHR complications

Due to the long R&D experience in SFRs, the Indian fast reactors are chosen to be SFRs. The details of SFRs are explained in the next section.

1.1.3. Sodium-cooled fast reactors

An SFR is a fast reactor that has sodium as a coolant [3]. Liquid sodium is a weak neutron moderator and doesn't moderate the fast neutrons. SFRs have the advantage of high thermal inertia, good temperature margin to boiling, and unpressurized reactor vessel.

The major systems in SFRs are the reactor core and nuclear steam supply system (NSSS). The reactor core consists of the fuel pins and fuel subassemblies (SA). Fuel pins are slender cylindrical tubes filled with fuel pellets. The fuel pins are spaced apart using spacer wires. The spacing is provided for the coolant flow and to accommodate swelling of the clad tubes that is envisaged at target burn up. The SAs facilitate the coolant flow through the fuel pins, provides structural support to the pin bundle, and provides a barrier to limit the propagation of a rupture of a few pins to the rest of the core.

NSSS is the system of components that facilitates the heat generated in the reactor core to be transported to the SG to produce steam. A typical NSSS showing the heat transfer path of PFBR is shown in Figure 1.2 [5]. NSSS consists of primary sodium circuit and secondary sodium circuit. The main components in the primary sodium circuit are PSPs, and the reactor assembly. The major components in the secondary sodium circuit are IHX, SSP, SGs and tanks.

The SFRs have two types of design approaches – pool-type reactors and loop-type reactors as elaborated in the next section.

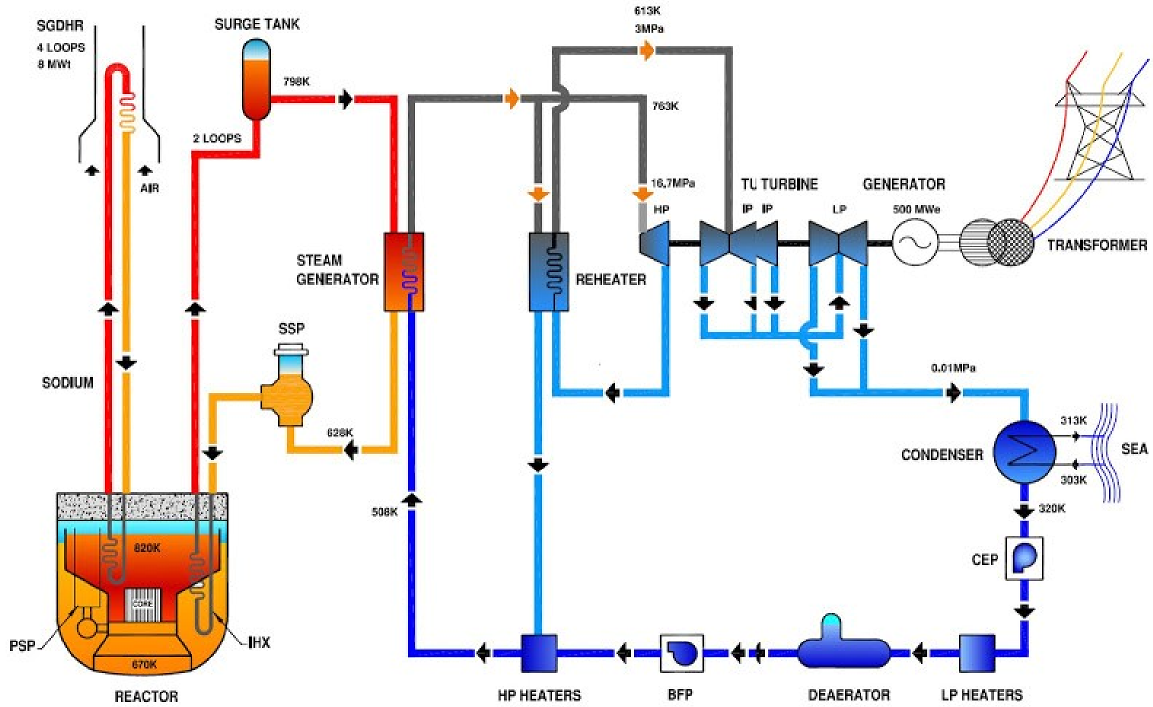

Figure 1.2 Nuclear steam supply system of PFBR [5].

1.1.4. Pool-type and loop-type fast reactors

The SFRs are classified into pool-type reactors and loop-type reactors based on the location of IHX. In pool-type, the IHXs and the PSPs are inside the reactor tank (main vessel), whereas in loop-type, the IHX is outside the reactor, but within the biological shield [5]. The advantages of pool-type reactors are that the loss of primary sodium is extremely unlikely and there are no penetrations in the reactor vessel that leads to its high structural integrity. However, as all the components and sodium are located inside the large vessel it makes the primary system large, which makes its maintenance difficult. On the other hand, loop-type reactors are compact and the maintenance is easier. However, the possibility of sodium leakage is higher in loop-type reactors. Figure 1.2 shows the pool-type concept adopted in PFBR and Figure 1.3 shows the loop-type concept adopted in FBTR.

FBTR is a 40 MWt, sodium cooled, loop-type Indian fast reactor. The heat generated in the reactor is removed by two primary sodium loops. The hot primary sodium is cooled by secondary sodium in the IHX. The heat absorbed by the secondary sodium in IHX is transferred to the corresponding secondary sodium loops, which consists of steam generators. Steam from the steam generators is fed to the steam water circuit comprising turbine-generator and condenser, and electricity is produced.

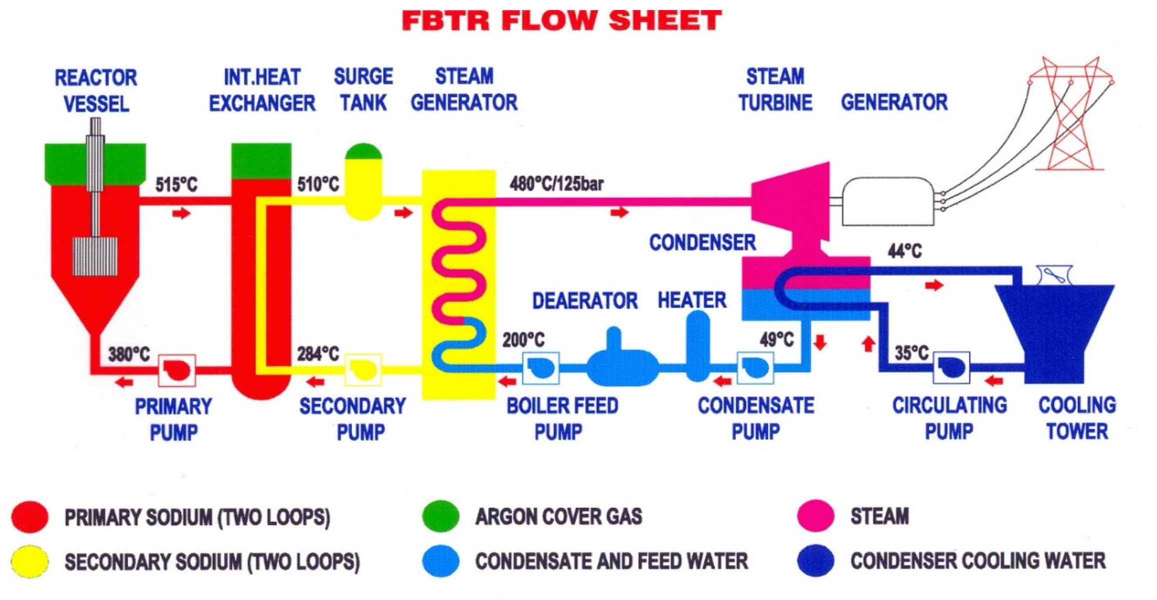

Figure 1.3 Loop-type: Fast Breeder Test Reactor (FBTR) [6]

1.1.5. Geometry and material details of fast reactor

In pool-type reactors, the reactor assembly consists of main vessel along with its internals and the top shield along with the components supported on it. The main vessel supports the core support structure, over which there is a grid plate. The reactor core is on the grid plate. The main vessel is filled with primary sodium and there is argon cover gas above primary sodium. The cover gas accommodates the sodium volume changes at various operating conditions by compressing itself when the sodium volume increases at full power and vice versa. The inner vessel which is fixed at the grid plate separates the hot pool sodium and the cold pool sodium, and provides passages (standpipes) for the PSPs and IHXs. The PSPs pump the cold pool primary sodium to the individual SAs through the grid plate, absorbs the nuclear heat and hot pool sodium cools in the IHX as shown in Figure 1.4.

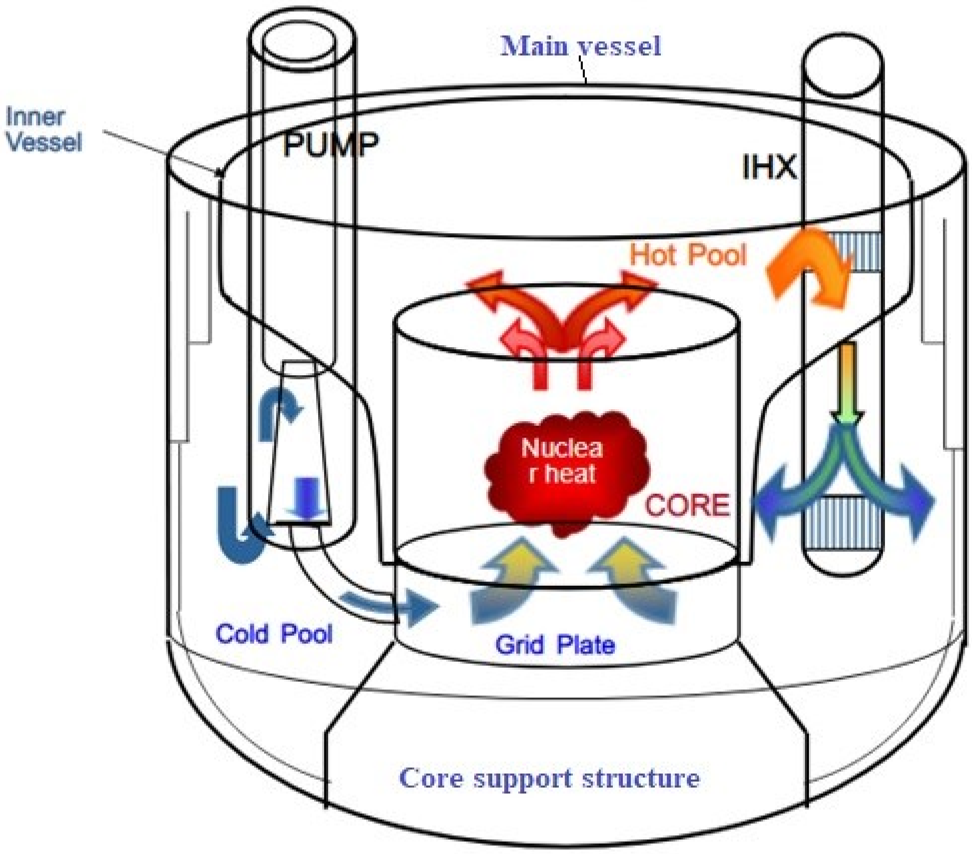

Figure 1.4 PFBR primary circuit [7]

The components that are in contact with primary sodium are CP, inner vessel, PSP standpipe, and IHX (details of each component are given in section 1.1.7). The components of the reactor assembly along with the perspective critical locations are shown in Figure 1.5. The perspective critical locations during thermal transients are categorized into free level interface of sodium and submerged locations. Figure 1.5 shows the free level interface locations as F1, F2, F3 and F4, and the submerged locations as B1, B2 and B3. The submerged locations are the junctions and curvatures of the reactor components in sodium.

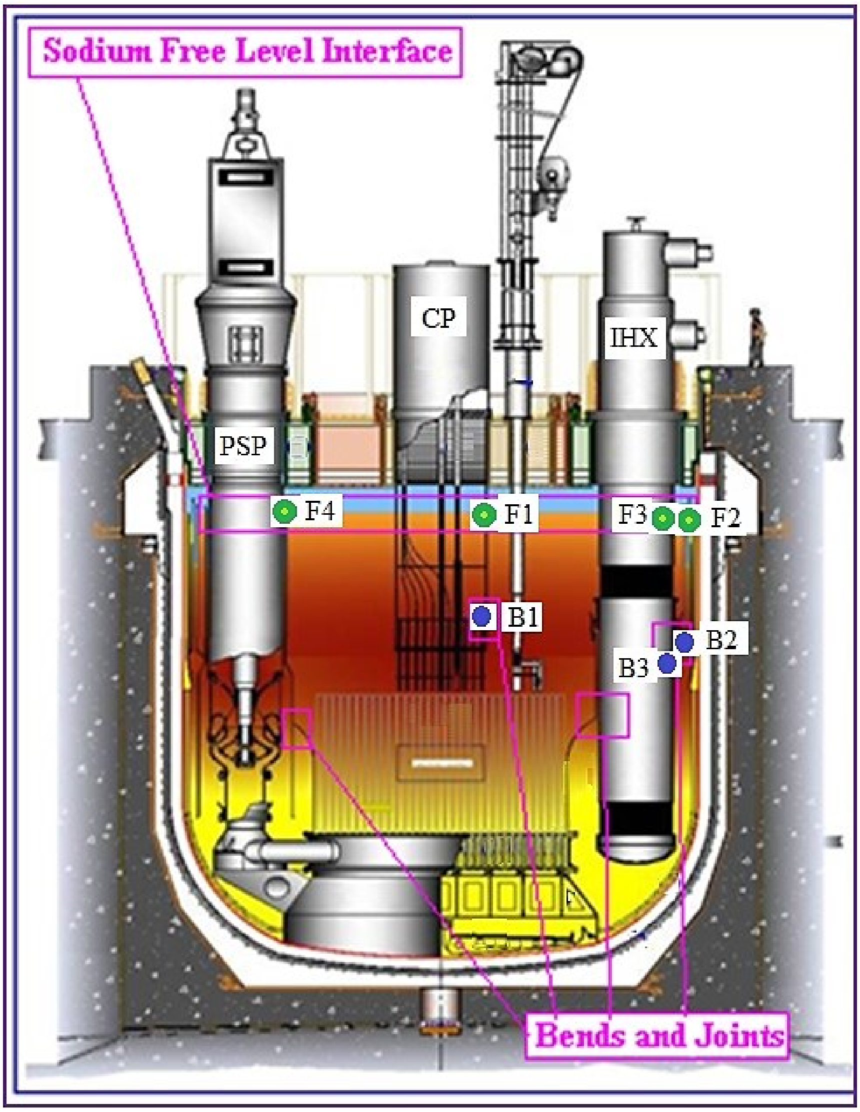

Figure 1.5 Reactor assembly components and the perspective critical locations in view of thermal loadings [4]

SS 316 LN is the material for the construction of the primary system components. All the material properties have been taken at the corresponding temperature. Some of the material properties used in the analysis are given in Table 1.2. All the material properties have been shown at 523 K (average temperature). These material properties are taken from RCC-MR Appendix A3 (2012) [8].

Table 1.2 Material properties

Property	Symbol	Value
Density	ρ	7837 kg/m^3
Young's Modulus	E	1.8 E5 MPa
Poisson's Ratio	ν	0.3
Expansion coefficient	A	16.9 E-6 /K
Conductivity	K	17.74 W/mK
Specific Heat	C	540 J/kgK

1.1.6. Reactor transients

A reactor transient is said to occur when there is a change in the reactor coolant temperature, pressure or both and affects the reactor's power output. The transients can take place by adding or removing neutron poison; accident conditions or increase/decrease of electrical load on the turbine generator [2 web ref]. In the PFBR, the various events that take place in a reactor are broadly classified as DBE and BDBE. The DBE have the frequency of occurrence more than 10^{-6} per reactor year, whereas the BDBE have the frequency of occurrence less than 10^{-6}/ry. The DBE are classified into four categories according to the frequency of their occurrences as given in Table 1.3. Examples of the events for each category have also been included in the table [9].

The start-up and shutdown of the reactor also involve reactor coolant temperature change and are the examples of thermal transients.

Table 1.3 Design Basis Events and Beyond Design Basis Events [9]

Category (name)		**Frequency of occurrence**	**Examples**
DBE	1 (normal)	Planned operation	● Normal operation
	2 (upset)	$> 10^{-2}$/ry	● One PSP trip ● Partial blockage in a fuel SA ● One SSP trip
	3 (emergency)	$< 10^{-2}$/ry but $> 10^{-4}$/ry	● One PSP seizure ● Operation base earthquake ● One SSP seizure
	4 (faulted)	$\leq 10^{-4}$/ry but $> 10^{-6}$/ry	● One primary pipe rupture ● Main vessel leak ● Safe shutdown earthquake
BDBE		$\leq 10^{-6}$/ry	● Leakage from both main vessel and safety vessel ● Airplane crash on site ● Failure of core support structure

1.1.7. Reactor assembly components in PFBR

During certain thermal transients (start-up and shutdown), the primary sodium temperature increases or decreases, and thereby sodium expands or contracts accordingly, resulting in change in the primary sodium level. Hence the primary system components, namely, CP, inner vessel, IHX and PSP standpipes, which are in contact with sodium are the critical components. The free level interface of sodium and the junctions that are submerged in sodium are the critical locations during thermal transients. The details of these critical components along with the critical locations are given in this section.

1.1.7.1. Control plug

The CP supports 12 CRDMs, 210 thermo well tubings in six groups, 3 failed fuel localization modules, a CCP, one central canal plug, lattice plate and other associated supports. Except for the 12 CRDMs and central canal plug, all other components mentioned above form an integral part of CP. CP is in turn supported on SRP [10]. The CP bottom portion (which is the critical region) consists of CCP, USP, LSP and outer shell. The schematic sketch of CP is shown in Figure 1.6.

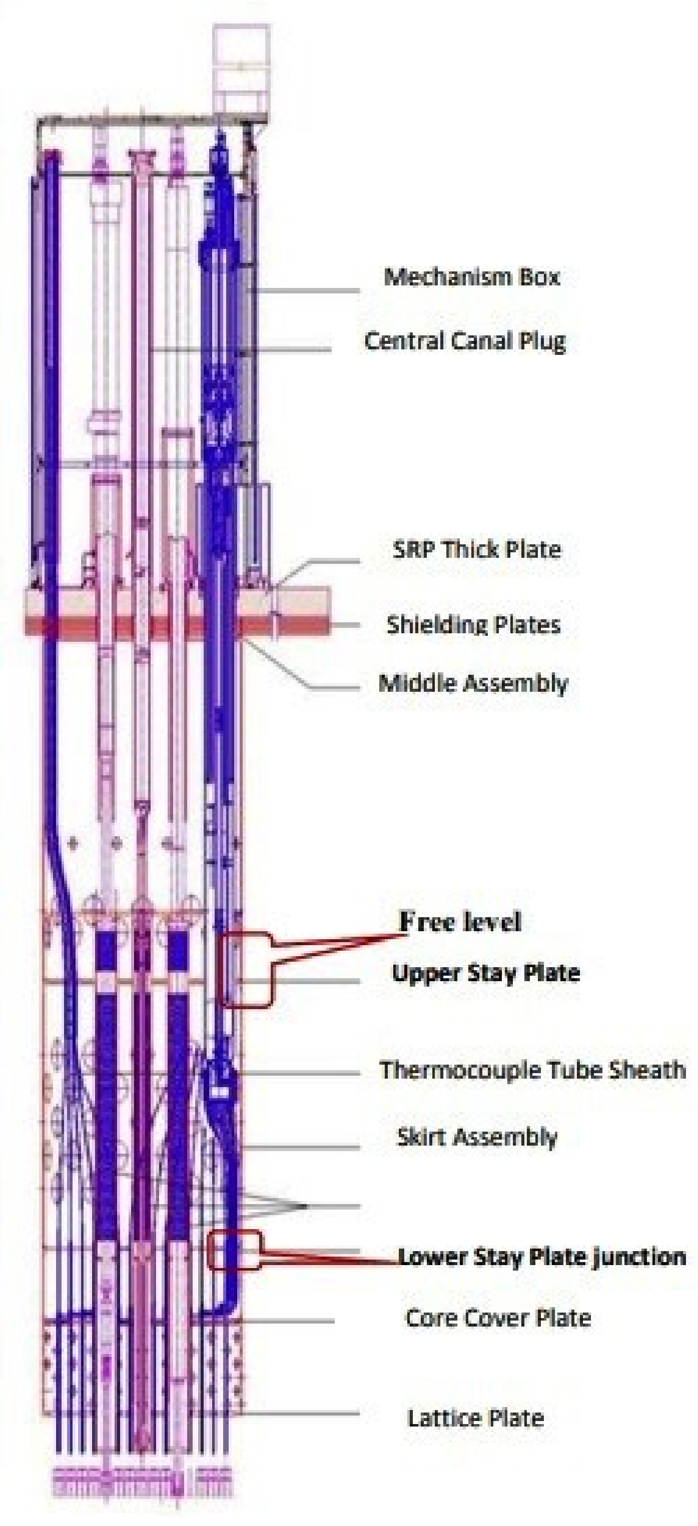

Figure 1.6 Vertical section of control plug in PFBR [10]

The USP and LSP are thick plates that are welded to the outer shell of CP. In the shutdown condition, the USP is above the sodium level and the LSP is submerged in sodium. On power raising, the sodium level rises and submerges the USP. Hence the USP-CP junction, is the free level of sodium location. Also, the thick plate, LSP, which is immersed in sodium throughout, can develop high thermal stresses at the junction. Thus, the LSP-CP junction is the critical submerged location.

1.1.7.2. Inner vessel

The function of the inner vessel is to serve as a leak tight barrier between the hot and cold pools of primary sodium with minimum heat transfer between pools. It consists of an upper cylindrical shell and a lower cylindrical shell connected by a conical shell (for PFBR). Apart from this, inner vessel has six stand pipes (4 for IHXs and 2 for PSPs) in the redan portion for providing passages for four IHX and two primary pumps. A schematic of inner vessel is shown in Figure 1.7. The free level interface of sodium, inner vessel curvature, and the inner vessel-IHX standpipe junctions (submerged in sodium) are the critical locations.

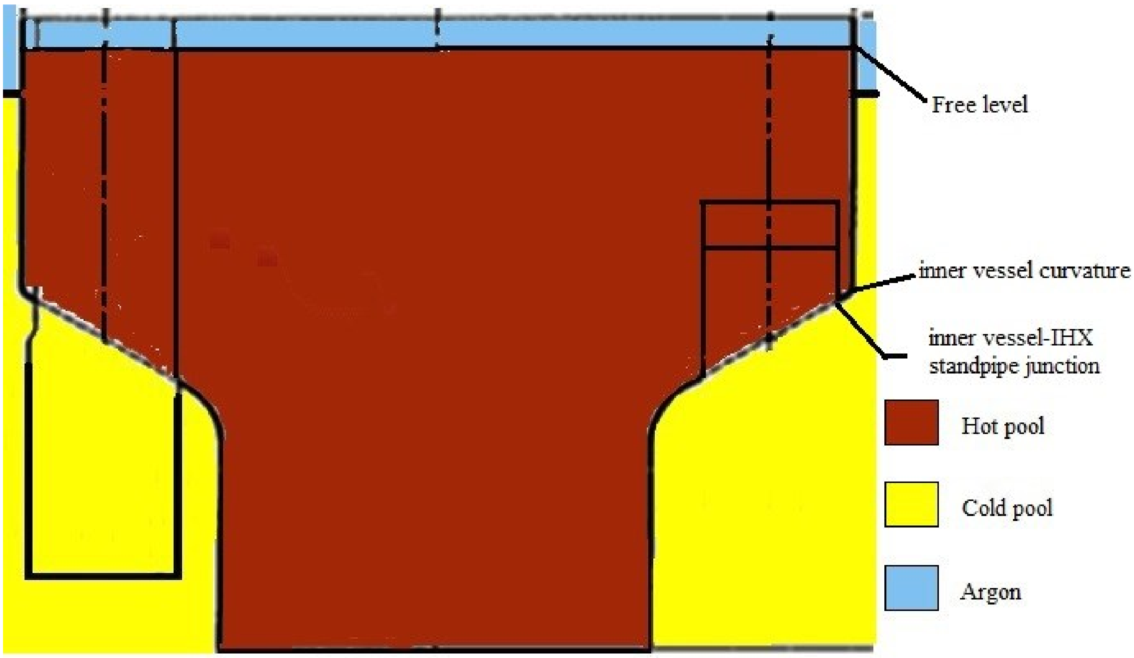

Figure 1.7 Inner vessel of PFBR with hot and cold pool sodium levels

1.1.7.3. Intermediate heat exchanger

IHX is a vertical counter-current, shell and tube heat exchanger. The function of IHX is to transfer thermal power from the radioactive primary sodium to the non-radioactive secondary sodium [11]. It also takes part in the decay heat removal and provides a leak tight barrier between primary and secondary sodium. It prevents the effects of sodium water reaction in steam generator from reaching the core. The geometrical details of IHX are given in Figure 1.8 [14].

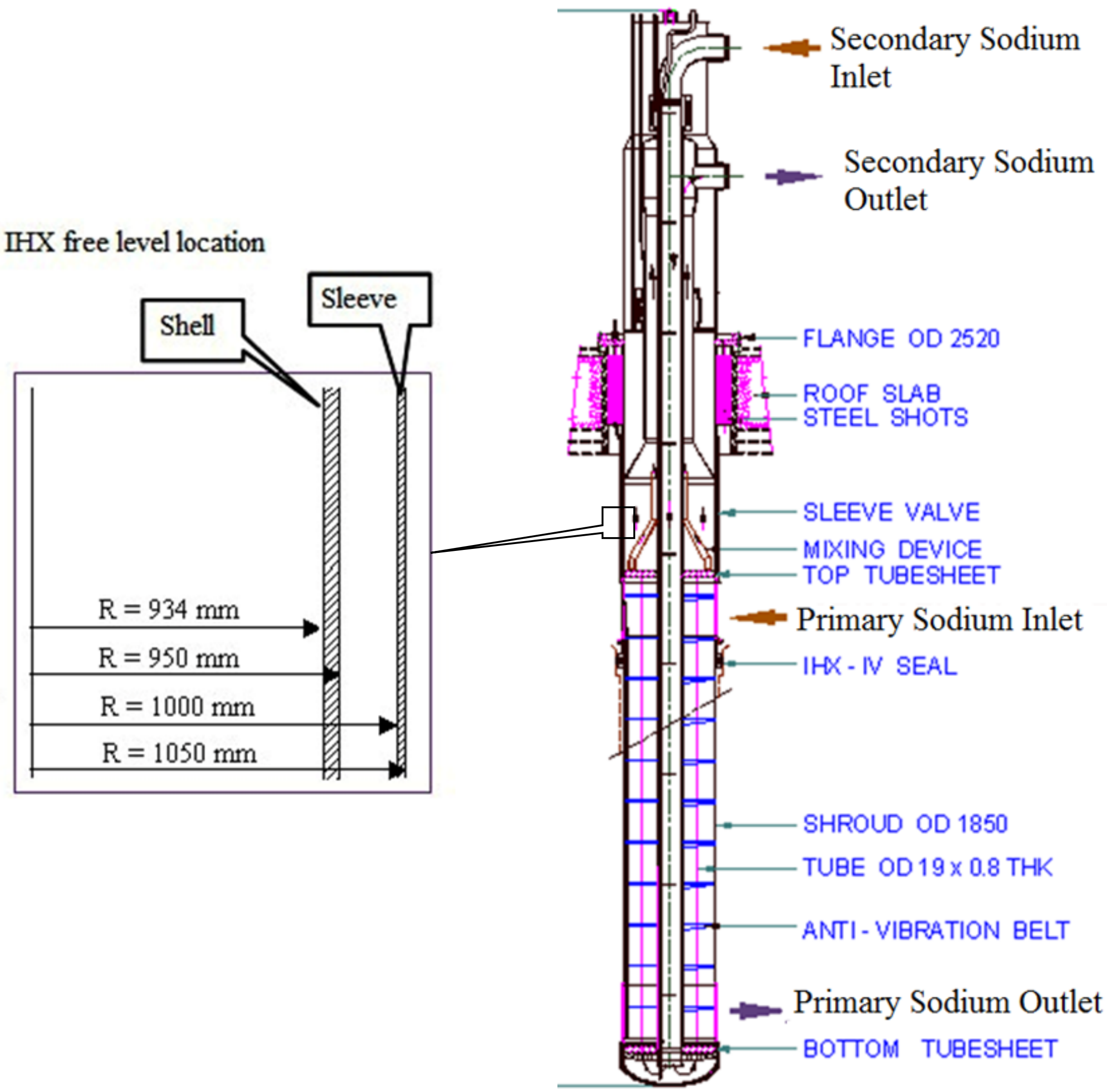

Figure 1.8 Geometrical details of IHX [11]

The tube bundle consists of 3600 straight tubes of outer diameter 19 mm and 0.8 mm thickness. The front and top view of the IHX are shown in Figure 1.9 and Figure 1.10 respectively [11].

Figure 1.9 Front view of IHX [11]

Figure 1.10 Top view of IHX [11]

The tubes are rolled and welded to the top and bottom tube sheets. The tube bundle consists of 3600 straight tubes of outer diameter 19 mm and 0.8 mm thickness. Figure 1.11

shows the primary and secondary sodium flow across the IHX. The secondary sodium enters through the down comer to the secondary sodium inlet plenum and flows upwards on the tube side to the outlet plenum and exits to the steam generator through the secondary sodium outlet. The primary sodium enters through the IHX top windows, travels from top to bottom on the shell side and exits to the cold pool sodium in the main vessel through the IHX bottom windows. Manually operated sleeve valve is provided to close the primary sodium inlet windows to permit operation of reactor with one secondary loop. When the windows are open, the sleeves are parked at the level of IHX free level location. The sleeve and shell are shown in the inset of Figure 1.8.

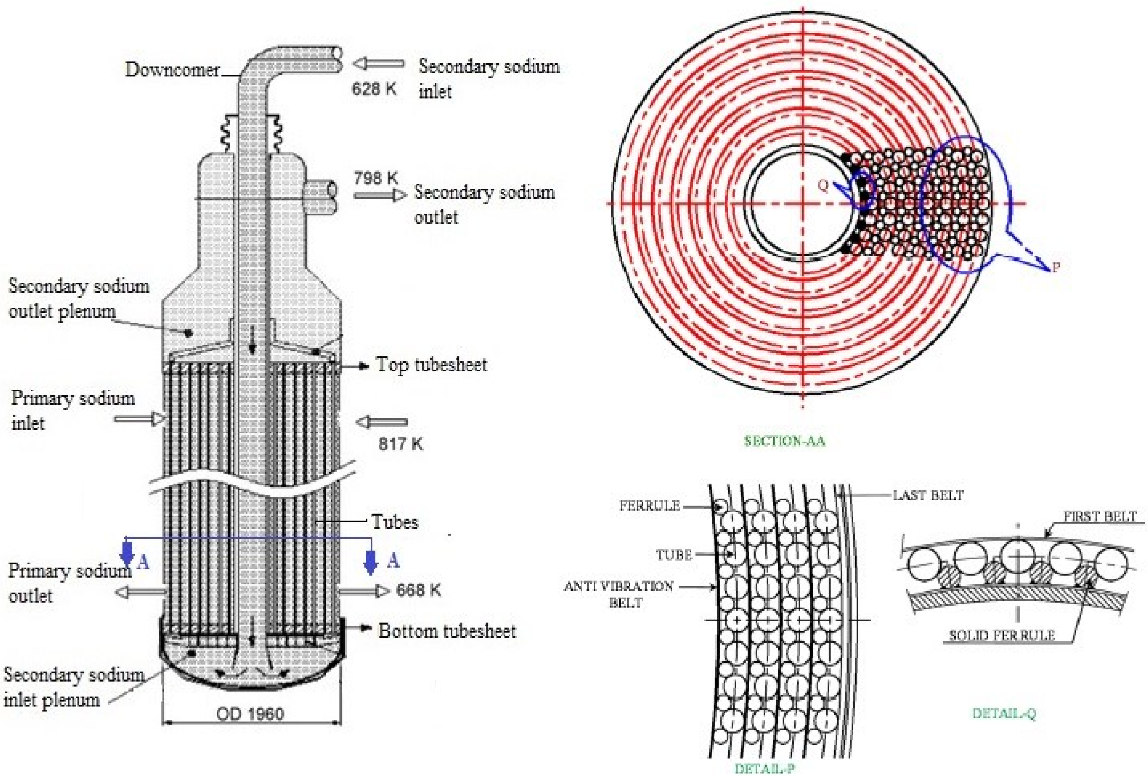

Figure 1.11 Sodium flow in IHX and tube sheets details [12], [13]

The top tubesheet is an annular plate of OD 1900 mm with 3600 holes arranged in concentric rows. The bottom tubesheet is also an annular plate of OD 1900 mm with corresponding perforations. The bottom dished end (ellipsoidal) collects the cold secondary sodium from downcomer and distributes into various rows of tubes. The circumferential pitch in any row is ~26.4 mm and radial pitch between rows is 25 mm. The pitch of the holes is 26.61 mm. The minimum ligament width is 6.8 mm. The ligament efficiency is 0.2555 [15]. The tube sheets are the critical submerged locations and the other perspective critical location is at the free level of sodium which is depicted in the inset of Figure 1.8.

1.1.7.4. Primary sodium pump standpipe

PSP is a centrifugal, mechanical, and vertical type pump with a single stage top suction impeller [16]. The PSP circulates sodium from the cold pool to the core to remove the nuclear heat. The principal material of construction of the pump components is SS 304 LN [17]. The PSP is partly submerged in the cold pool sodium, partly in the argon space and partly in the RCB ambient conditions. The overall height of PSP is ~ 20 m and it is supported at the roof slab. The PSPs are contained in the PSP standpipes as shown in Figure 1.12. PSP standpipe is an integral part of the inner vessel and it provides necessary head to PSP. The PSP standpipe and inner vessel junction, and the free level location of PSP standpipe are the perspective critical locations in view of thermal loadings.

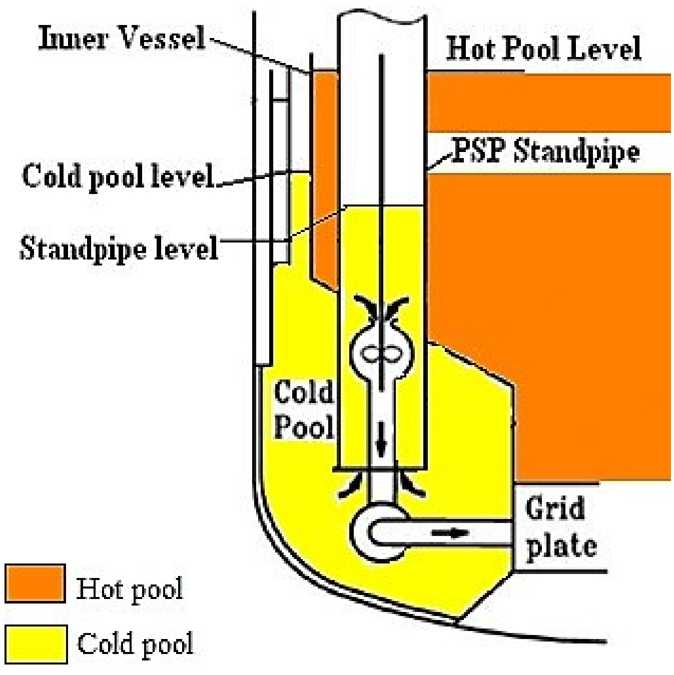

Figure 1.12 PSP standpipe of PFBR with hot and cold pool sodium levels

A pressure head of 0.5 m is maintained between the cold pool (outside inner vessel) and the cold sodium level in the standpipe to aid the sodium flow. Hot pool sodium is outside the standpipe and there is cold pool sodium within the PSP standpipe as shown in Figure 1.12. During start-up and normal operation, there is 1.5 m difference between hot pool sodium and cold pool sodium. Hence the difference in between the sodium levels inside and outside the PSP standpipe is 2 m. During shutdown, there is 75 mm difference between hot pool sodium and cold pool sodium. As a constant pressure head of 500 mm is maintained to aid the sodium flow, the difference between the sodium levels during shutdown condition is 575 mm.

With this background regarding various reactors and PFBR components, the objective of the thesis is defined in the next section.

1.2. Objective and scope of the thesis

In pool-type fast reactors, the structural design and life assessment of the reactor components are done by considering the steady-state and transient thermal loadings. The thermal transients are covered by the umbrella of main transients such as secondary sodium pump trip, loss of feed water and spurious scram. However, the transients namely power raising (during start-up) and crash cooling (during shutdown) have been included with normal operation and is considered as a cycle (as shown in Figure 1.13). In actual case, the start-up of the reactor is done from T_1 to T_2 at the rate of 20 K/h (slow heating) in t_p hours. It is then held at normal operating conditions for t_n hours. The time taken for shutdown is t_c. But the total time spent in creep regime of t_h has been taken for analysis of normal operating condition, and the rates of heating and cooling of primary sodium have been ignored. Thus, there is a need for a detailed analysis for power raising and crash cooling, at various possible heating/cooling rates, towards optimization and simplification of the existing schemes.

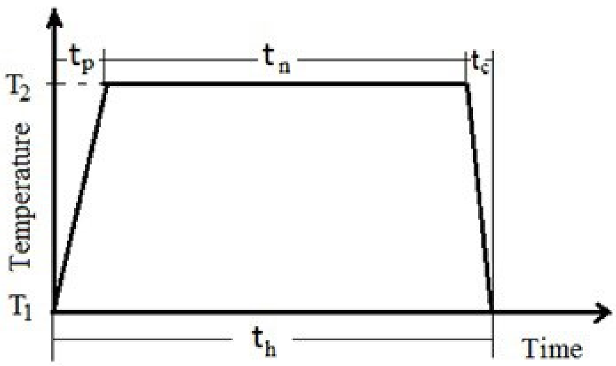

Figure 1.13 Startup-normal operation-shutdown cycle

Following a reactor SCRAM, the primary sodium rapidly cools from 823 K to 623 K, through the main condenser path; and at 623 K, it is envisaged to deploy OGDHR, for controlled cooling at 20 K/h. However, controlled cooling requires a higher capacity OGDHR, and makes the design of seal in the recirculation pump a critical challenge due to its operation at varying pressure. Hence, the objective of the thesis is to study the possibility of eliminating controlled cooling, and quantifying the structural damage in the components, to arrive at an economic shutdown scheme. The investigation involves in-house development of a numerical model to simulate the complex thermo-mechanical behavior at the free level locations. The generalized numerical model can be used to study the physics of partially immersed components of any system.

The numerical model has also been applied to simulate the power raising operation at free level interface of sodium. Power raising operation is one of the three stages during reactor start-up, namely, decay heat removal, approach to criticality, and power raising. The power raising is the most extended operation, and a slow heating rate is not economical due to the long time spent in creep regime. On the other hand, speeding up the process can result in high thermal stresses. Hence, the objective of the thesis is to arrive at an optimum heating rate by detailed analysis and to substantiate the integrity of all the components in contact with primary sodium.

The components that are in contact with primary sodium are CP, inner vessel, IHX, PSP standpipe, and the fuel clad (effect on fuel SAs is less severe and is neglected). Therefore, the thesis includes the studies in a sequential manner to examine the:

(i) Effect of crash cooling on reactor components

(ii) Effect of power raising on reactor components and fuel clad tubes

The critical locations in the reactor components are broadly classified as free level locations and locations that are submerged in sodium (Figure 1.5). Thermo-mechanical analysis of the reactor components that are submerged in sodium has been done using conventional FE codes. However, due to the complex loading at the free level locations, the conventional codes are modified by a numerical algorithm and used.

Fuel clad tubes are also in contact with primary sodium. The rate of heating of primary sodium affects the integrity and coolability of the clad tubes. Fuel clad failure during transients can be detected and rectified, but excessive dilation of the clad that can lead to coolant flow blockage, termed as 'ballooning' [18], should be avoided at all conditions. Figure 1.14 shows the schematic of clad ballooning phenomenon.

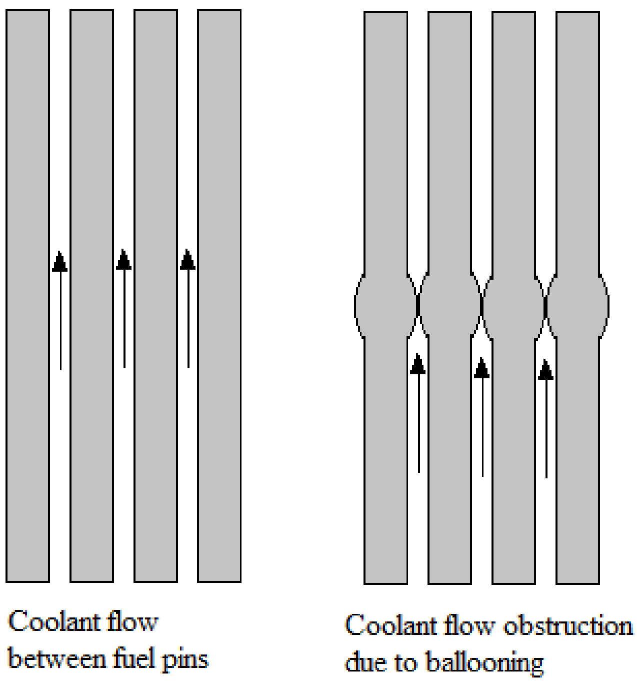

Figure 1.14 Schematic of fuel clad ballooning

Hence, investigation of the possibility of ballooning during power raising at various heating rates is a part of the objectives.

The main focus of the thesis being crash cooling and power raising in primary system components and fuel clad tubes, the chapters are organized accordingly as discussed in the next section.

1.3. Organization of the thesis

The thesis is organized into seven chapters. Chapters 1, 2 and 3 give an overview of the background, concepts, problem statement and literature survey. Chapters 4, 5 and 6 are the working chapters that give the details of the work and results. Chapter-7 summarizes the thesis, and gives a direction for future work. The following sections describe the highlights of each chapter.

(i) Chapter 1: Introduction

In this chapter, the background of nuclear reactors technology and their significant features are described. This chapter also deals with the objective and scope of the research work, and organization of the thesis.

(ii) Chapter 2: Background to structural integrity

In this chapter, the concepts relating to the structural integrity of the reactor components, the various high-temperature failure modes in fast reactors, and the procedure to estimate the creep-fatigue damage have been briefed. The terms used in structural integrity, failure theories and stress classification have also been included for better understanding of the concepts of structural mechanics. The fundamentals of creep, fatigue, ratcheting, and buckling have been described.

(iii) Chapter 3: Literature survey

This chapter presents the detailed literature review on thermo-mechanical models, start-up, shutdown and ballooning in fuel clad tubes. It is found that the numerical model for partially immersed components for simulating the thermo-mechanical behavior at the free level locations is not addressed in the literature. Literature survey on power raising during start-up suggests that the reactor components, and the fuel clad tubes, are the critical components during power raising operation that need to be investigated. Ballooning in fast reactors has not been addressed in the literature. The high burn-up and narrow coolant flow path between the fuel pins call for a need for the investigation of ballooning in fast reactors. These gap areas were identified from the literature survey and formed the basis and objective of the Ph. D thesis.

(iv) Chapter 4: Effect of crash cooling on reactor components

In-house development of the computational procedure to study the thermo-mechanical behavior of partially immersed structures during transients has been carried out. The generalized numerical model can be used to study the physics of partially immersed components of any system. The developed model has been used to obtain the thermal stresses at free level locations of sodium during crash cooling operation. Detailed studies for various shutdown schemes have been carried out to arrive at a simplified shutdown scheme. Based on this study, it is concluded that for the future design of fast reactors with 60 years of design life, controlled cooling is not essential from the structural damage point of view. The recommendation simplifies the design of decay heat removal system.

(v) Chapter 5: Effect of power raising on reactor components

In this chapter, the possibility of increasing the primary sodium heating rate for reducing the heating time with minimal structural damage has been explored. Thermo-mechanical analysis has been carried out at the free level interface of sodium and locations submerged in sodium with the developed numerical model and conventional FE analysis respectively. The structural damage has been estimated and an optimum heating rate has been recommended. The study forms a benchmark for other fast reactors for deciding upon the heating rate during start-up of the reactor.

(vi) Chapter 6: Fuel clad behavior during transients

This chapter describes the fuel clad tube behavior during transients. Experimental facilities have been developed to study ballooning in fuel clad tubes. Experiments have been carried out to find the rate of heating at which clad tubes can balloon and when it can rupture. It is found that ballooning is a plastic instability that can occur at slow heating rates and block the coolant flow in the reactor core. A hypothetical power raising case has been studied to see whether ballooning can take place during power raising operation. Fractography and optical imaging studies have been done to investigate the metallurgical changes that take place in the material when there is ballooning.

(vii) Chapter 7: Conclusions and future works

The concluding remarks and the scope for future work have been presented in this chapter.

1.4. Closure

In this chapter, the various types of nuclear reactors, reactor transients, introduction to PFBR geometry and its primary system components have been discussed. The objective and scope of the thesis have been brought out. It is highlighted that structural analysis of reactor components towards simplification of the shutdown schemes, development of a numerical model to study the physics of partially immersed components and its application, optimization of primary sodium heating rate are the objectives of the thesis. As fuel clad tubes are also in contact with primary sodium, investigation of fuel clad tube behavior during transients is also an indispensable part of the objectives. In the next chapter we will discuss the background to structural integrity to understand the concepts and procedure for structural damage assessment.

References

[1] Saroja Saibaba. Presentation on structural materials for nuclear reactors. HBNI, Engg Sciences, (2016).

[2] Baldev Raj, P. Chellapandi, P.R.Vasudeva Rao. Sodium Fast Reactors with closed fuel cycle. ISBN-13:978-1-4665-8769-4 (2015).

[3] Eduard Khodarev. Liquid Metal Fast Breeder Reactors. IAEA BULLETIN-VOL 20, NO.6, December (1978).

[4] R.G.Rangasamy, Prabhat Kumar. Quality Management during Manufacture of Block Pile Components for 500MWe Prototype Fast Breeder Reactor. International Journal of Engineering Research and Reviews ISSN 2348-697X (Online), Vol. 4, Issue 2, pp: (45-51), Month: April - June (2016).

[5] Haihua Zhao, Hongbin Zhang. An Innovative Hybrid Loop-Pool Design for Sodium Cooled Fast Reactor. 2007 ANS/ENS International Meeting, November (2007).

[6] K.V. Suresh Kumar, A. Babu, B. Anandapadmanaban & G. Srinivasan. Twenty five years of operating experience with the Fast Breeder Test Reactor. Asian Nuclear Prospects 2010. Energy Procedia 7 (2011) 323–332.

[7] U. Parthasarathy. Thermal Hydraulic Studies for PFBR using PHOENICS. IGCAR, Kalpakkam, May 3-5th (2004).

[8] RCC-MR, Section III - Tome 1 - Subsection Z: Technical Appendix A3, (2012).

[9] Event Analysis. PFBR/PSAR/Rev.0/24.03.04.

[10] P. Chellapandi, Amitava Sur, S.B. Bhoje. Stress analysis of bottom portion of control plug. PFBR/31410/DN/1013/R-A (1991).

[11] Prabhat Kumar and Aravinda Pai. An overview of welding aspects and challenges during manufacture of Intermediate Heat Exchangers for 500 MWe Prototype Fast Breeder Reactor. 1st International Conference on Structural Integrity, ICONS-2014, Procedia Engineering 86 (2014) 173 – 183.

[12] R. Gajapathy, K. Velusamy, P. Selvaraj, P. Chellapandi, S. C. Chetal, T. Sundarajan. Thermal hydraulic investigations of intermediate heat exchanger in a pool –type fast breeder reactor. Nuclear Engineering and Design, Volume 238, Issue 7, July (2008), pages 1577-1591.

[13] S. Athmalingam. Intermediate heat exchanger for PFBR and future FBR.. Technical Meeting on Innovative Heat Exchanger and Steam Generator Designs for Fast Reactors, 21-22 December (2011) at IAEA Headquarters.

[14] S. Athmalingam. Intermediate heat exchanger for PFBR and future FBR. Technical Meeting on Innovative Heat Exchanger and Steam Generator Designs for Fast Reactors, 21-22 December (2011) at IAEA Headquarters.

[15] R. Srinivasan, P. Chellapandi. Stress analysis of IHX under mechanical loading. PFBR/32130/DN/1045/R-A (2002).

[16] K.V. Sreedharan, Bhagwana Ram Manda, S.Athmalingam,V.Balasubramaniyan, .Chellapandi. Design and manufacture of sodium pumps of 500 MWe prototype fast breeder reactor. Pumps India, Vol. 17 No.1, October (2010), Pages 11-24.

[17] P.Chellapandi, R.Suresh Kumar, S.Jalaldeen, P.Selvaraj, S.C.Chetal. Evaluation of speed lowering of primary sodium pump into sodium pool for 500 MWe PFBR based on creep damage. Procedia Engineering, Volume 55, (2013), Pages 451-456.

[18] M. Ragheb, Internet, (2010) mragheb.com/Clad%20Ballooning%20Accident.pdf.

Web references

[1] https://www.nuclear-power.net/nuclear-power/fission/

[2] https://www.nrc.gov/reading-rm/basic-ref/glossary/transient.html

Chapter 2

Background to Structural Integrity

2.1. Background

The various types of nuclear reactors, reactor transients, details of PFBR geometry and its primary system components have been discussed in the previous chapter. In this chapter, the concepts relating to the structural integrity of the reactor components, the various high-temperature failure modes in fast reactors, the procedure to estimate the creep-fatigue damage have been briefed. The terms used in structural integrity, failure theories and stress classification have been included for better understanding of the concepts of structural mechanics. The fundamentals of creep, fatigue, ratcheting, buckling, thermal striping, stratification, FIV and free level fluctuations have also been described.

2.2. Structural integrity and design codes

Structural integrity is defined as the ability of a structure to support the designed load, including its own weight, without excessive deformation and rupture [3 web ref]. Structural material can fail to perform their intended functions in three general ways: a) excessive deflection under stable equilibrium or sudden deflection or buckling (unstable equilibrium), b) yielding or excessive plastic deformation, and c) fracture. The various factors influencing the integrity of a component are temperature, load, material, environment (corrosion, irradiation) and time (at high temperature).

Considering the above factors, a component can be designed to perform its functions, in two ways, namely, 'Design by rule' and 'Design by analysis'. The former is done based on operating experience and theoretical equations/formulas available in codes like ASME BVP Section VIII Division 1 [19]. This procedure is very conservative and can be used for simpler geometry and loading conditions. Complex design problems (complex geometry, material and loading conditions) can be analyzed using finite element analysis with sufficient accuracy.

ASME Section VIII Div II, ASME Section III Division 5 Subsection HB and RCC-MR RB 3200 are the design codes that include design procedure based on numerical codes [20]. The selection of design codes are based on application. ASME Section III Division 5 Subsection HB and RCC-MR RB 3200 are the codes used for high temperature components. RCC-MR is a French code that is used for the design of fast reactor components operating at low pressure and high temperature.

Some of the terms used in structural integrity assessment are given below.

2.2.1. Types of forces

Force is defined as the push or pull of an object with mass, which causes acceleration in the object. There are basically four types of forces, namely: axial, shear, torsion and bending. Stress is defined as force per unit area (N/m^2) and strain is the ratio of change in length and its original length (dimensionless). Force is a vector that is defined by its magnitude and direction, whereas stress is a tensor that has magnitude, direction and the plane at which the stress acts.

2.2.1.1. Axial force

Axial force is the force that acts along the axis of a part or structural element. When the force is applied away from the surface, the force is tensile and it results in positive elongation of the rod. When the force is applied towards the surface, it is compressive and gives negative elongation (compression). Axial forces cause only change in volume (dilation) and no change in shape. The energy developed in the rod due to axial force is called *'Dilation energy'*. The ratio of axial stress and axial strain is the Young's Modulus (E), which is the property of a material.

2.2.1.2. Shear force

Shear force is the force acting tangential to the surface, which results in change in shape and angle (distortion). The resulting energy produced in the body is called *'Distortion energy'*.

The ratio of shear stress and shear strain is the Rigidity Modulus (G), which is the property of a material.

2.2.1.3. Torsional shear force

Torsional shear is defined per unit rotation per unit twist. It is the twisting of an object due to an applied torque. The simple torsion equation is given in equation 2.1.

$$\frac{T}{J} = \frac{\tau}{r} = \frac{G\theta}{l} \tag{2.1}$$

Similar to shear, torsion also results in distortion. The energy produced in the body is called '*Torsional Distortion Energy*'.

2.2.1.4. Bending moment (M)

Bending of a component is defined by bending moment. Bending moment is the reaction induced in a structural element when an external force or moment (product of a distance and a physical quantity) is applied to the element, causing it to bend. Bending moment in a body results in rotation, which is defined by its neutral plane. Due to this rotation, bending energy is produced. Bending moment is given by equation 2.2, which gives the 'Flexural formula' (σ is the bending stress).

$$\frac{M}{I} = \frac{E}{R} = \frac{\sigma}{y} \tag{2.2}$$

2.2.2. Failure theories

In an xyz coordinate system, when various forces act on a component, the state of stress at a point is designated by 9 components (i.e. σ_{xx}, τ_{xy}, τ_{xz}, τ_{yx}, σ_{yy}, τ_{yz}, τ_{zx}, τ_{zy}, σ_{zz}). The 9 components are reduced to 6 components as $\tau_{xy} = \tau_{yx}$; $\tau_{xz} = \tau_{zx}$; $\tau_{yz} = \tau_{zy}$. The state of stress with the 6 stress components is the multi-axial state of stress, which are extracted from any analysis method, for example, FE analysis. The stress components are combined to give equivalent stresses called stress intensity. The failure theories are used to find the equivalent stresses to relate with the allowable stresses. The allowable stresses of a material are available in the codes that are based on standard tensile test results.

A material can fail in two ways: by yielding or fracture. A ductile material fails by yielding whereas a brittle material fails by fracture. The various failure theories are summarized in Figure 2.1[21], and the details [22], [23] are briefed in the subsequent sections.

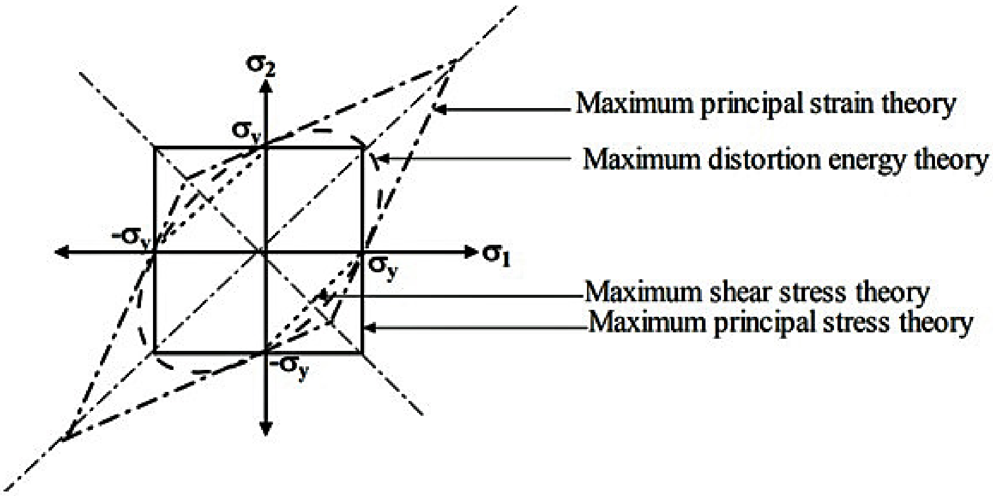

Figure 2.1 Comparison of different failure theories [21]

2.2.2.1. Maximum principal stress theory (Rankine theory)

According to this theory, failure in the component is predicted when either of the principal stresses, σ_1 or σ_2, equals or exceeds the yield strength, σ_y, of the material.

$$\sigma_1 \; or \; \sigma_2 \; < \sigma_y \tag{2.3}$$

2.2.2.2. Maximum shear stress theory (Tresca theory)

According to this theory, failure by yielding would occur when the maximum shearing stress ($\tau_{\max}$) in the material reaches a value equal to the shear stress at the tensile yield point.

$$\tau_{\max} \; = \frac{(\sigma_{max} - \; \sigma_{min})}{2} < \frac{\sigma_y}{2} \tag{2.4}$$

Where, σ_{max} and σ_{min} are the maximum and minimum stresses respectively, among the three principal stresses.

2.2.2.3. Maximum distortion energy theory (von-Mises yield criterion)

According to this theory, failure by yielding would occur when the distortion energy associated with principal stresses exceeds the distortion energy corresponding to that for the tensile yield point.

$$\frac{1}{\sqrt{2}}\sqrt{(\sigma_1 - \sigma_2)^2 + (\sigma_2 - \sigma_3)^2 + (\sigma_3 - \sigma_1)^2} < \sigma_y \tag{2.5}$$

2.2.2.4. Maximum principal strain theory (St. Venant's theory)

According to this theory, failure is predicted by yielding when the maximum principal strain resulting from the principal stresses, $\sigma_{1,2}$, just exceeds the maximum strain corresponding to the yield strength, σ_y, of the material in uniaxial tension or compression.

$$\sigma_1 - \nu(\sigma_2 + \sigma_3) < \sigma_y \tag{2.6}$$

2.2.3. Stress classification

The total stress is the combination of primary stress and non-primary stress as per RCC-MR [24]. The classification of stresses is given in Figure 2.2.

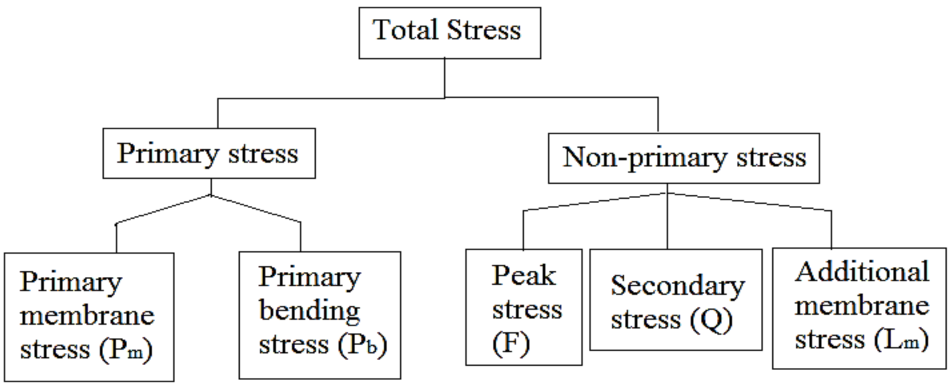

Figure 2.2 Classification of stresses [24]

The stresses across the thickness can be classified into membrane stresses and bending stresses that are primary stresses as shown in Figure 2.3.

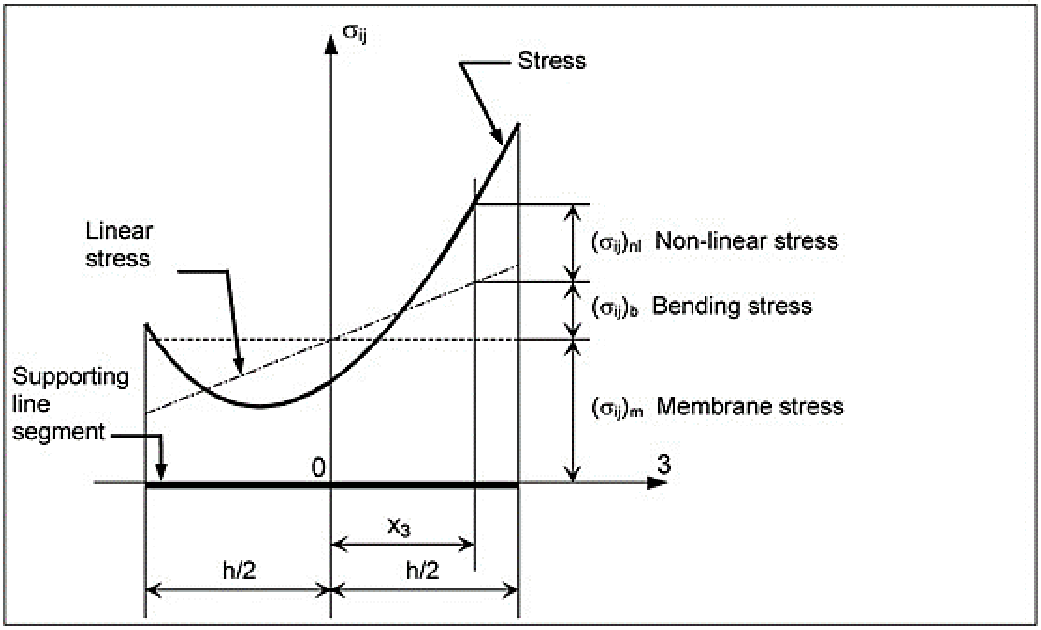

Figure 2.3 Breakdown of stresses across the thickness [24]

The non-linear portion is called peak stress. The peak stress, secondary stress and additional local membrane stress are non-primary stresses. The details of the types of stresses are discussed below in detail.

2.2.3.1. Primary stress

Primary stress is defined as the fraction of the stress that does not disappear after a small scale permanent deformation in the structure. Any normal or shear stress developed by an imposed loading, that is necessary to satisfy the laws of equilibrium of external and internal forces and moments is called primary stress. Primary stresses satisfy the equilibrium equations. The stress is not self-limiting. Local yielding of the component will not change the primary stress value. If the stress is greater than yield stress, failure or at least gross deformation of the component takes place. Pressure and mechanical loads are the examples of primary stresses.

A) Primary membrane stress (P_m)

Primary membrane stress (general) is the component of normal stress that is equal to the average value of stress across the thickness and is distributed such that no redistribution in stress occurs as the result of yielding. The membrane stress tensor is the tensor whose components are equal to the mean value of stresses along the support line segment, where, the support line segment (h) is the shortest segment which joins the two sides of the wall. Primary membrane stress is given by equation 2.7.

$$(\sigma_{ij})_m = \frac{1}{h}\int_{-\frac{h}{2}}^{+\frac{h}{2}} \sigma_{ij} dx_3 \qquad \textbf{2.7}$$

Where, x_3 is the abscissa of the point of the supporting line segment (shown in Figure 2.3).

B) Primary bending stress (P_b)

Primary bending stress is the stress across the thickness that is produced by pure bending. It is distributed linearly within the thickness, which has the same moment as the primary stress. The bending stress tensor indicated in Figure 2.3 is the tensor whose components are defined by equation 2.8.

$$(\sigma_{ij})_b = \frac{12\mathrm{x}_3}{h^3}\int_{-\frac{h}{2}}^{+\frac{h}{2}} \sigma_{ij}.x_3 dx_3 \qquad \textbf{2.8}$$

P_m and P_b are global properties (net section properties), that do not vary point by point.

2.2.3.2. Secondary stress

Secondary stresses are the normal stresses or shear stresses developed by the constraint of adjacent material or by self-constraint of the structure. The stress is self-limiting. Secondary stresses disappear if deformation is allowed or by local yielding. Failure from one application of secondary stress is not to be expected. Secondary stresses satisfy the compatibility equations, and respect the internal or boundary conditions. Examples of secondary stresses are thermal and discontinuity stresses.

2.2.3.3. Peak stress (F)

Peak stress is the additional stress applied by a geometrical discontinuity of a structure or by non-linearity in the stress distribution across the thickness. It is a local stress which can only affect fatigue damage, and thus the life of the component. Skin stresses caused by thermal shocks are also classified as peak stresses.

2.2.3.4. Additional local membrane stress (L_m)

The additional local membrane stress (L_m) is the difference between local primary membrane stress (P_L) and primary membrane stress (P_m). P_L is the mechanical stress that is in the vicinity of a shape or loading discontinuity, i.e., in a small zone adjoining the discontinuity. L_m produces excessive deformation (distortion) in the transfer of load to other portions of the structure. At the junctions, it adjusts itself by compatibility. Thus the nature of this type of stress is secondary. Though the characteristics of P_L are secondary in nature, it is conservatively classified as local primary membrane stresses. P_L is uniform across the thickness, unlike peak stress.

2.3. Failure modes in a typical fast reactor

An SFR contains liquid sodium as a coolant and it is operated at high temperatures. As there is no need to pressurize the sodium to maintain their liquid state, fast reactors have thin-walled components that are economical and have low thermal stresses. The details of SFRs and the working of pool-type fast reactors are explained in sections 1.1.3 and 1.1.4. The cold pool sodium enters the fuel subassemblies and absorbs the heat from fuel and comes out as hot pool sodium. There is a high temperature gradient between the hot pool and cold pool sodium. Due to the high heat transfer characteristics of sodium, the rapid changes in coolant temperature are transmitted to the structure with insignificant film drop. The structural material chosen for the design of reactor components have low thermal conductivity, low thermal diffusivity and large thermal expansion coefficients. All the above factors are responsible for causing certain structural mechanics failure modes as shown in Figure 2.4 [25]. Some of the terms are discussed in the subsequent sections.

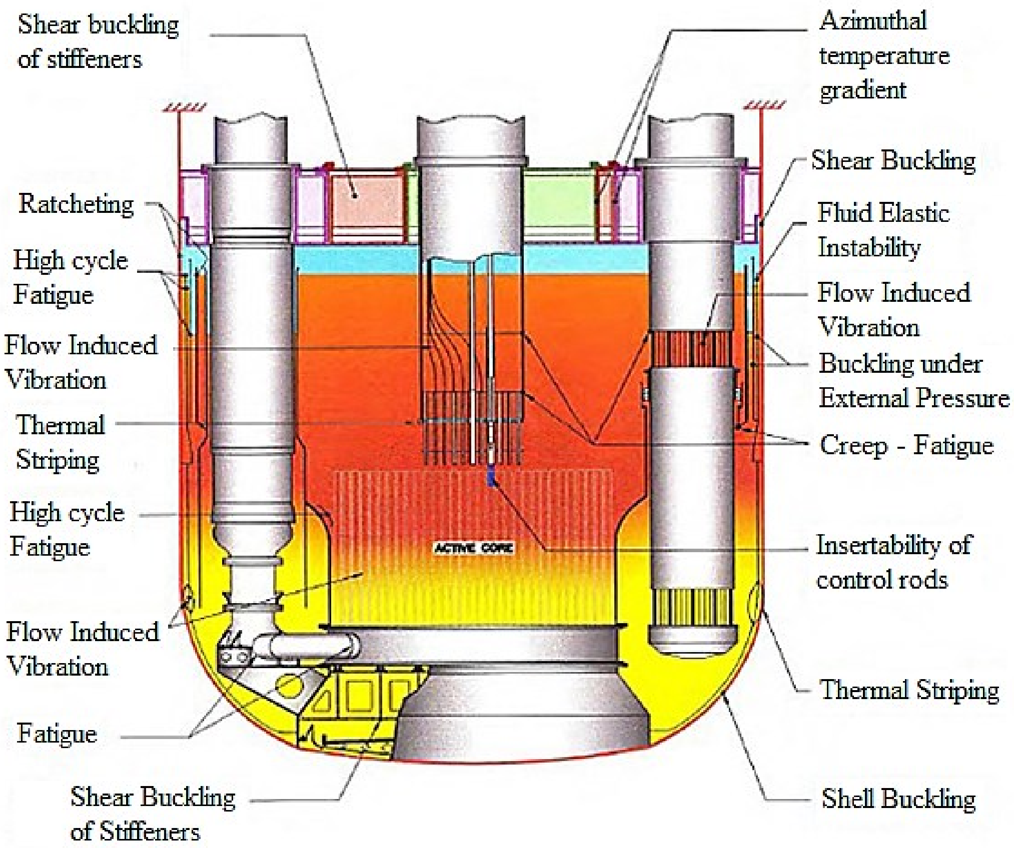

Figure 2.4 Failure modes considered in the design of pool type reactors [25]

2.3.1. Buckling

Buckling is a sudden deformation in a structure, which is caused when the load reaches a critical level, resulting in bowing of a column under compression or wrinkling of a plate under shear [4 web ref]. Large diameter vessels in SFR have higher slenderness ratio and are prone to buckling. The nature of buckling of thin shells of SFR are classified as shear buckling, shell mode buckling, localized shell mode buckling, progressive buckling, creep buckling and bowing mode buckling. The details are discussed in [25]. Buckling studies based on RCC-MR code has been extensively carried out by [26].

2.3.2. Flow induced vibration

As the name indicates, FIV is the vibration induced in slender structures when there is turbulence in the process fluid. In SFRs, slender components like CP, IHX, SG etc., are prone to FIV due to the presence of free liquid sodium surfaces, which is the source of sloshing. The operation of PSP also causes vibration in reactor components [27]. Some of the vibration excitation mechanisms in the CP components are fluid-elastic instability, vortex shedding, turbulence buffeting etc. The FIV tests for CP and IHX have been carried out by [27] and [28] respectively and it is demonstrated that the design is safe against FIV.

2.3.3. Thermal striping

In the reactor core, the blanket SAs are positioned adjacent to the fuel SAs. The temperature of the sodium jet from the fuel SAs are higher than that from blanket SAs (since low heat is generated within blanket SAs). When the sodium jets emerging from the SAs hit the structure above it (i.e., CCP in CP), the mixing would not be complete. The temperature fluctuation in the non-mixing zone is of the frequency range of 1-10 Hz. Due to the high heat transfer coefficient of liquid sodium, the temperature fluctuations are transmitted to the structure with minimal attenuation [29]. This phenomenon namely, thermal striping induce high cycle fatigue in the component. This phenomenon is depicted in Figure 2.5.

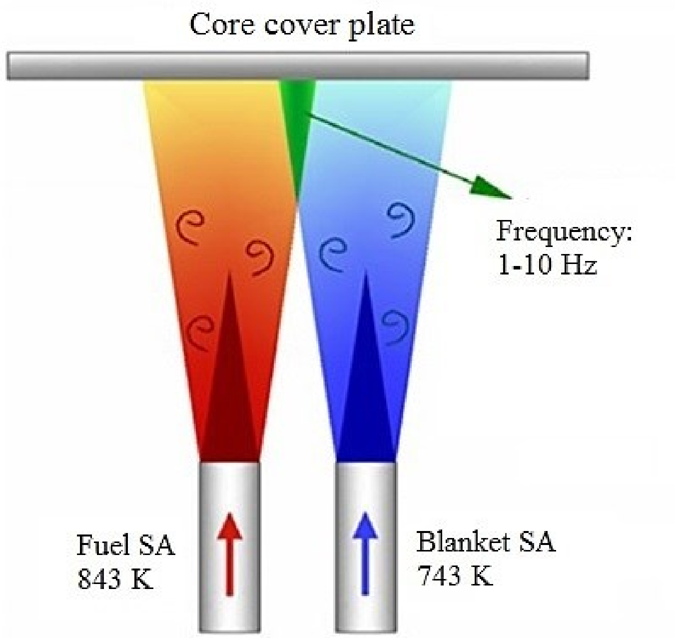

Figure 2.5 Thermal striping phenomenon at core cover plate [25]

2.3.4. Thermal stratification

The pool-type fast reactors consist of sodium jets ejecting from fuel, breeder and spent SAs, with a large temperature difference. Due to the large size of reactor with high thermal expansion coefficient of sodium, the Richardson number in the pool is of the order of unity [30]. As the buoyancy force and inertial forces are of similar magnitude, a stratification interface is developed at the zones where there is high temperature difference over a short length [31]. This phenomenon called stratification leads to low frequency (~0.01 – 2 Hz) temperature oscillations of high amplitude, which are transmitted to the adjoining structures causing high cycle fatigue. The flow field in hot pool that causes stratification is depicted in Figure 2.6 [30].

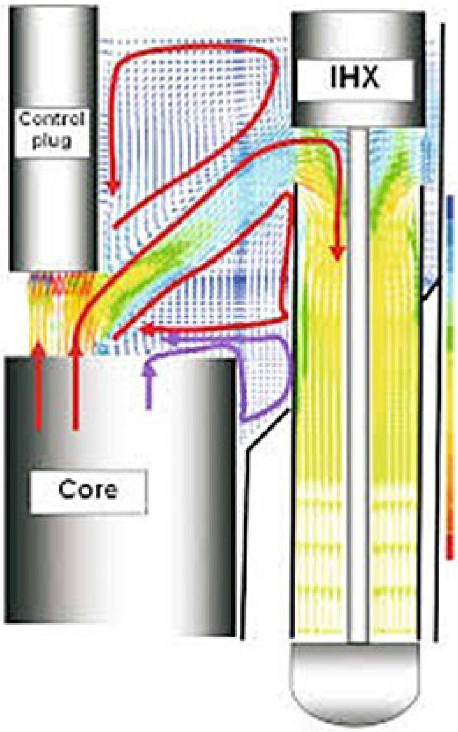

Figure 2.6 Flow field in hot pool at full power causing stratification [30]

2.3.5. Free level fluctuation

There is a presence of free level of sodium in some components in SFRs, and inert gas above sodium to accommodate thermal expansion of sodium during temperature transients. The reactor pool is not static and it is associated with vertical and horizontal velocities, resulting in free level fluctuations, causing HCF at the vicinity of the free level. The structures that are in contact with sodium at the free level interface see alternating temperatures resulting in ratcheting [32]. Furthermore, the free surface oscillations of the sodium level results in the formation of vortices, which are sources for gas entrainment in sodium pools. Mechanisms of gas entrainment, agglomeration of gas inside grid plate etc., have been studied by [30].

At the free level, there is another phenomenon apart from HCF that takes place. During the reactor start-up and shutdown, the level of sodium changes corresponding to the sodium temperature, depending upon the expansion coefficient of sodium and its density. The structure that is in contact with sodium at the free level, can experience a thermal shock due to an abrupt change in the ambient temperature. In this case the free level fluctuation is not rapid and it is not oscillation of the free level. The sodium level increases gradually during power raising, and falls gradually during shutdown. Hence this is considered as LCF and is studied in detail in the present thesis.

2.3.6. Ratcheting

Ratcheting is a progressive incremental inelastic deformation or strain which can occur in a component that is subjected to repetitive loading paths. When the material is cyclically loaded at constant stress amplitude with a non-zero mean stress, ratcheting occurs. During the cyclic loadings, the hysteresis loop displaces forward at a decreasing rate. Ratcheting generally occurs in the direction of mean stress. The unsymmetrical loading due to mean stress leads to material hardening, and non-linear kinematic hardening is attributed to be the primary reason for ratcheting [33]. If ratcheting ceases after a few cycles of load application, it leads to shakedown. Pure elastic behavior, elastic shakedown, low cycle fatigue, plastic cycling and ratcheting are the various component behavior under various combinations of primary and secondary stresses.

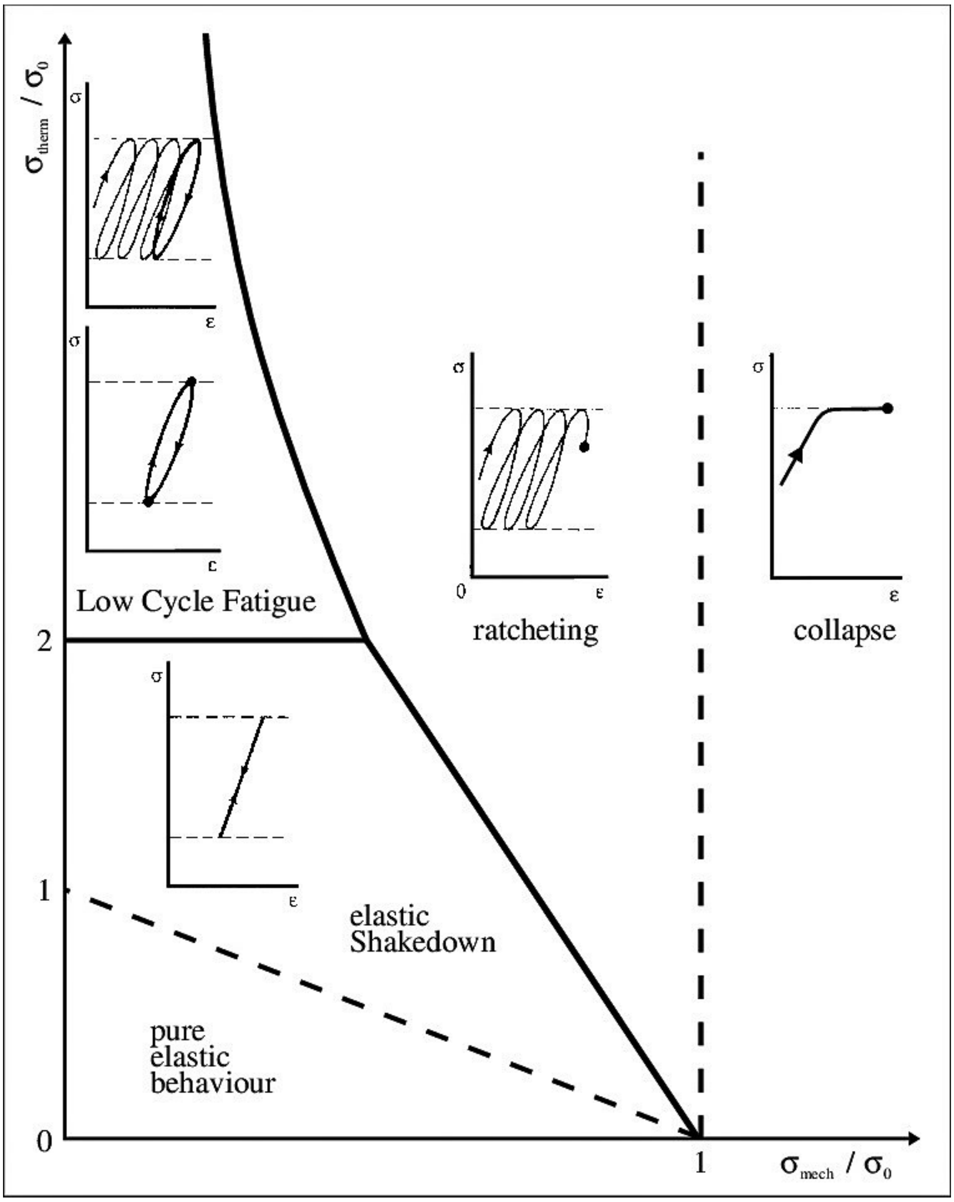

Figure 2.7 Bree diagram in cylindrical shells under pressure and cyclic thermal stresses [34]

Figure 2.7 shows the bree diagram, which depicts the various behaviors of the components when there is a combination of primary and secondary stresses. The x-axis is the ratio of primary stress and ultimate stress, and the y-axis is the ratio of secondary stress and yield stress. When the primary stress is equal to the ultimate stress, the component collapses. It may be noted that the component ratchets only when there is considerable primary stress. In the absence of primary stress, when the secondary stress is high, there is plastic cycling but no ratcheting. Ratcheting is a gross failure across the thickness whereas fatigue is a local failure which initiates at the surface and propagates as discussed in the next section.

2.3.7. Fatigue

Fatigue is the progressive accumulation of deformation or damage under cyclic loading. The fatigue damage mechanisms, S-N curve, LCF, HCF, design fatigue curves are discussed in the subsequent sections.

2.3.7.1. Fatigue damage mechanisms

The fatigue damage occurs in three distinct stages as shown in Figure 2.8. The damage initiates and the fatigue cracks are initiated in the first stage (I). Fatigue crack growth takes place in the second stage (II) and cyclic tearing leading to instability or rupture occurs in the third stage (III). The details are illustrated below.

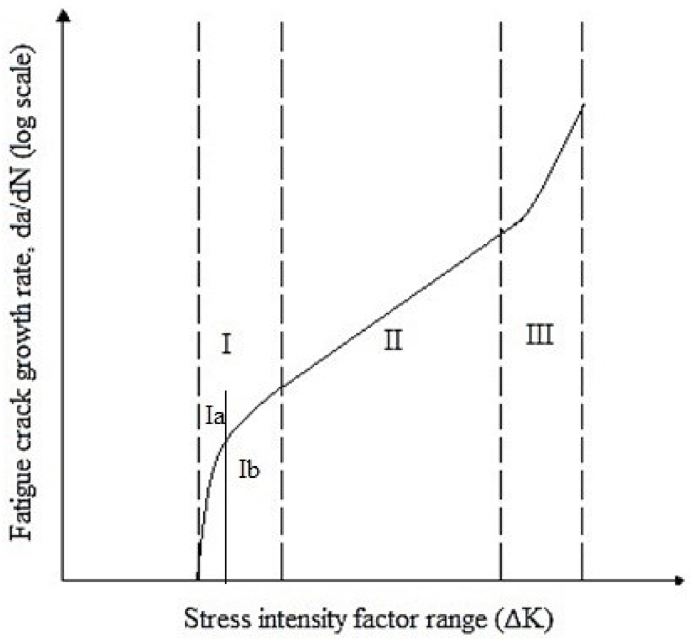

Figure 2.8 Fatigue crack propagation curve [5 web ref]

1. **Ia-Initial damage**

In this stage, there are changes in material’s stress/strain response under cyclic loading, and there is cyclic softening or cyclic hardening in the material. Cyclic stress-strain curve, which is obtained by joining the tips of the hysteresis loops can be generated at this stage, as depicted in Figure 2.9.

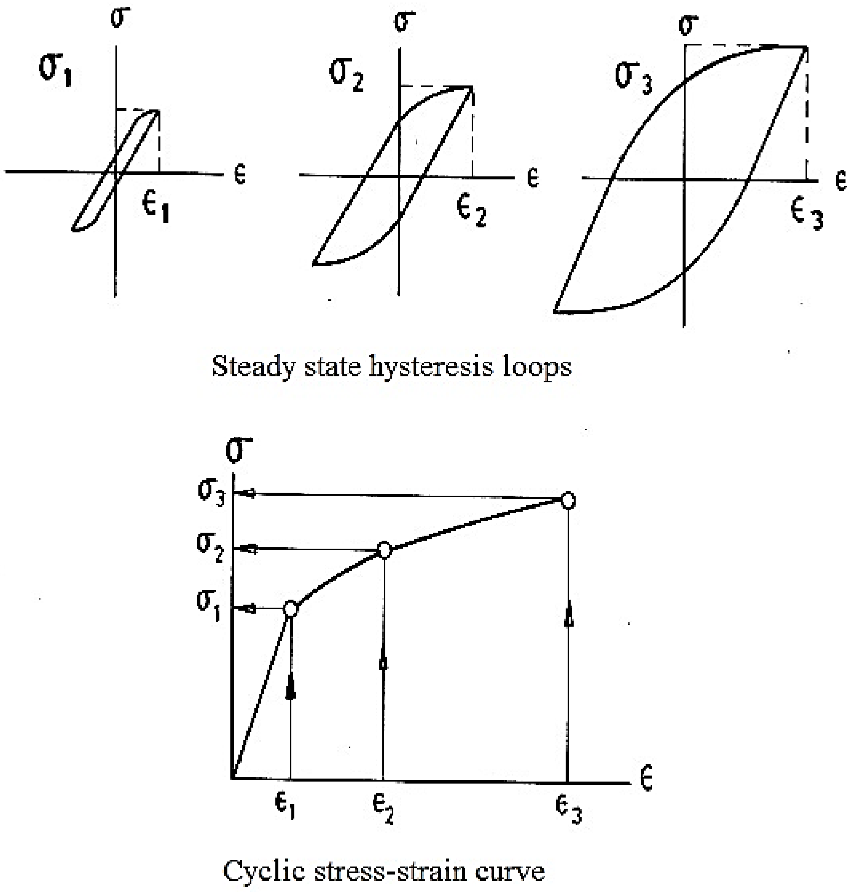

Figure 2.9 Cyclic stress-strain curve [35]

2. **Ib-Initiation of fatigue cracks**

Once the material harden/softens, micro crack nucleation takes place due to slip band extrusions and intrusions as shown in Figure 2.10. The slip bands movement due to the cyclic loads results in crack nucleation. After nucleation the crack deepens to an easily observable size.

3. **II- Fatigue crack growth**

When a crack is initiated, the crack grows cycle by cycle in the direction normal to maximum tensile stress. The crack propagation at the crack tip is controlled by highly concentrated cyclic plastic deformation. The rate of fatigue crack growth is given by Paris Power Law.

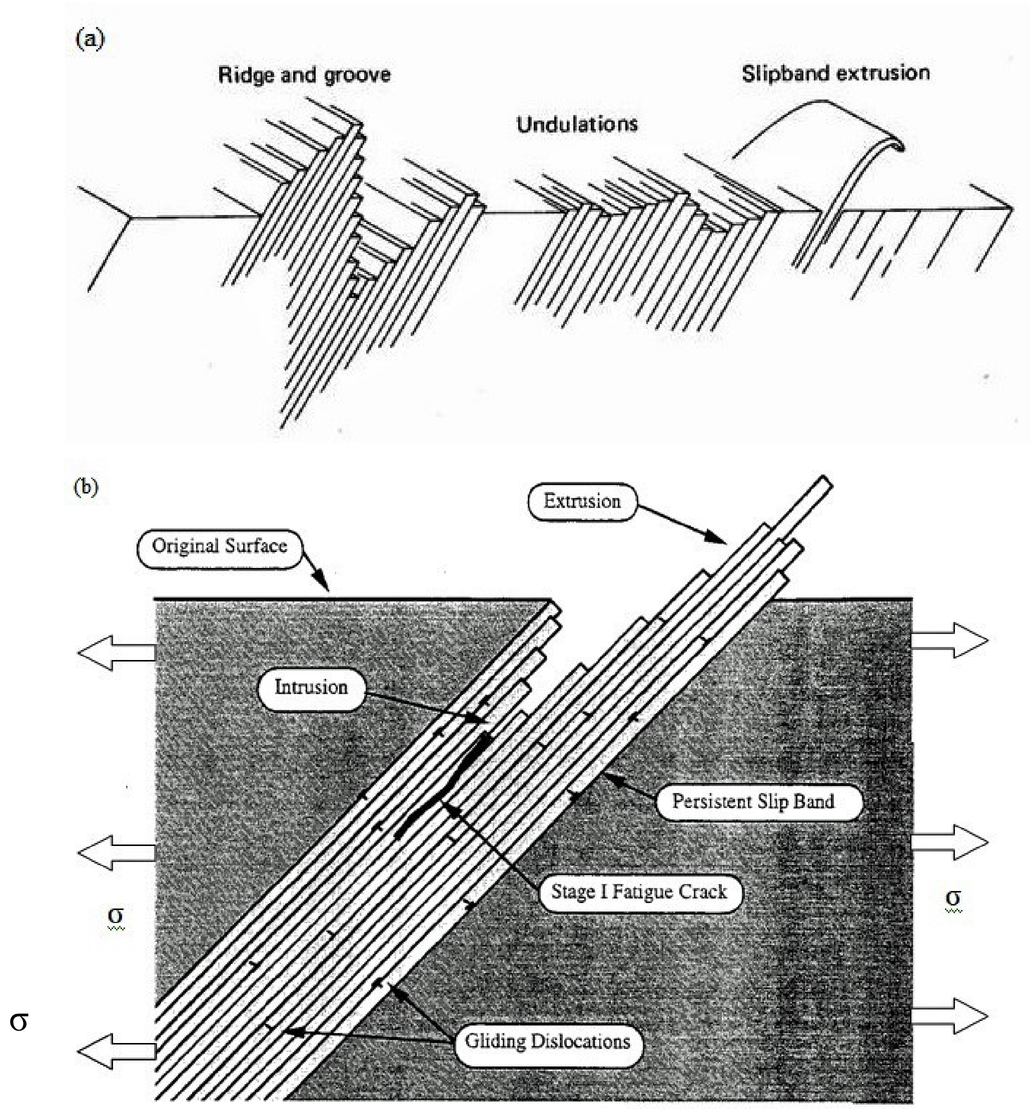

Figure 2.10 Early stages of fatigue crack formation [36]

4. **III- Cyclic tearing leading to instability / rupture:**

The fatigue crack growth continues along with stable tearing in each load cycle and ends up in unstable fracture. Stable tearing is analogous to tearing under monotonic loads. Unstable fracture is observed in this stage. (Tearing / Region-III in Figure 2.8).

2.3.7.2. S-N curve

S-N curve for a material is the plot of the magnitude of the cyclic stress/strain amplitude versus the number of cycles to failure, as depicted in Figure 2.11. Typically, both the axes are on logarithmic scales. Figure 2.11 shows the endurance limit, LCF and HCF. The differences between LCF and HCF are given in Table 2.1.

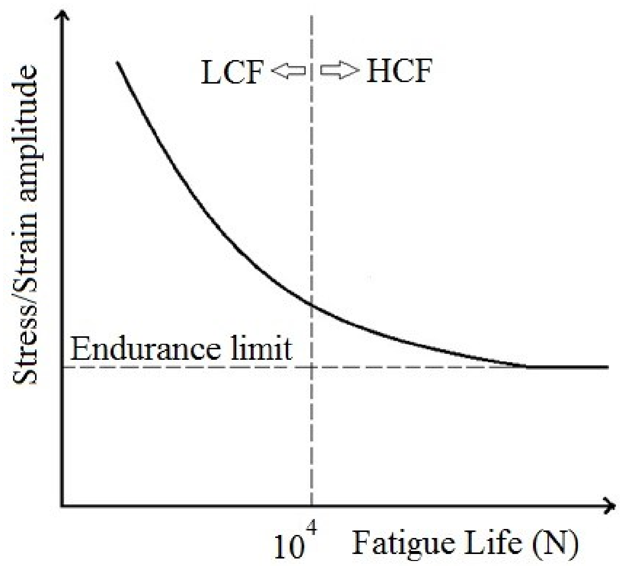

Figure 2.11 Schematic of S-N curve

Table 2.1 Differences between low cycle fatigue and high cycle fatigue

Low Cycle Fatigue (LCF)	**High Cycle Fatigue (HCF)**
Strain cycling above yield point	Stress cycling below the yield point
Thermal gradients in thick components	Vibrations
Strain controlled tests	Stress controlled tests
Frequency of Testing <1Hz	Frequency of testing about 50 Hz
Cycles to failure < 10^4	Cycles to Failure > 10^4

The endurance limit, also known as fatigue limit or fatigue strength is the stress amplitude below which an infinite number of loading cycles can be applied to a material without causing fatigue failure.

2.3.7.3. Design fatigue curve

The fatigue experiments are carried out to generate the raw fatigue curve. The DFC is obtained by applying a factor of safety of 2 on strain and 20 on cycles. The modified DFC for a material is obtained with maximum mean stress correction as shown in Figure 2.12. This modified DFC is available in codes for fatigue life evaluation.

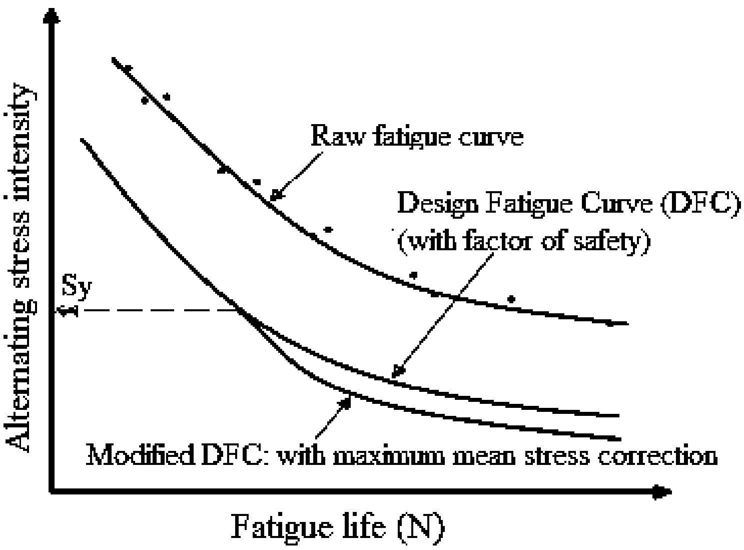

Figure 2.12 Design fatigue curve [35]

2.3.8. Creep

Creep is defined as the tendency of a solid material to slowly move or deform permanently under the influence of stress. It is a time-dependent deformation under a certain applied load. Creep is a function of time, temperature, stress (below yield strength), and material properties (composition). Higher the temperature, higher is the creep damage.

When we say that a component is not meeting the creep limits, what is the kind of damage we expect in the component?

- ✓ It means, the component is going to deform excessively leading to mismatch of the sub-components or contact between moving parts causing severe damage.
- ✓ Further, it may (not always) lead to crack initiation leading to component failure.

2.3.8.1. Stages of creep deformation

The application of load naturally leads to an instantaneous elastic strain (ε_0). This is followed by a primary creep regime in which the strain rate decreases with time due to strain hardening (strengthening by plastic deformation because of dislocation movement). In the second stage, the material settles down towards the steady state regime, where there is a balance between dynamic recovery and strain hardening. This secondary creep is the limiting factor for creep life design. The creep accelerates during tertiary creep. The strain rate increases exponentially with stress, due to necking induced by the accumulation of creep damage (voids). The creep deformation stages are shown in Figure 2.13.

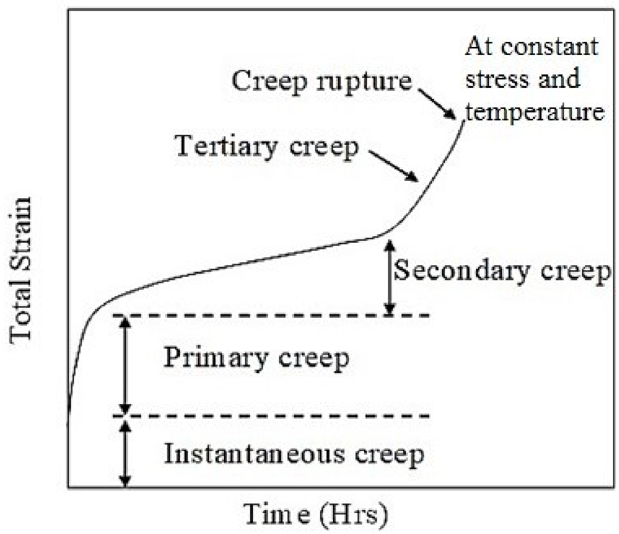

Figure 2.13 Stages of creep deformation [37]

2.3.8.2. Creep mechanisms

There are three basic mechanisms that can contribute to creep in metals, namely:

(i) Dislocation creep. (ii) Grain boundary sliding. (iii) Diffusion flow

(i) Dislocation Creep

Dislocations are line defects that slip through a crystal lattice when a minimum shear stress is applied. At low strain rates and relatively low temperatures, creep occurs by the glide of slip locations. When the glide process is obstructed by, for example, the presence of precipitates in the glide plane, an applied stress assists the climb process to push the dislocation onto a parallel plane, bypassing the particle (Figure.2.15).

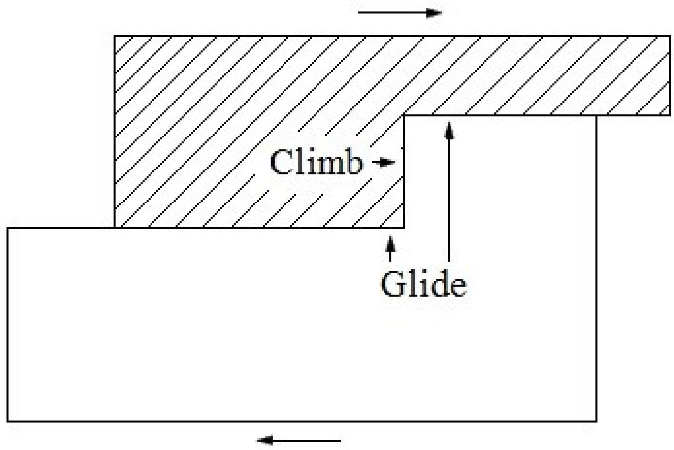

Figure 2.14 Dislocation creep [38]

(ii) Grain boundary sliding

The onset of tertiary creep is a sign that structural damage has occurred in an alloy. Rounded and wedge shaped voids are seen mainly at the grain boundaries as depicted in Figure 2.15. When these grain boundaries coalesce, creep rupture occurs. The mechanism of void formation involves grain boundary sliding which occurs under the action of shear stresses acting on the boundaries.

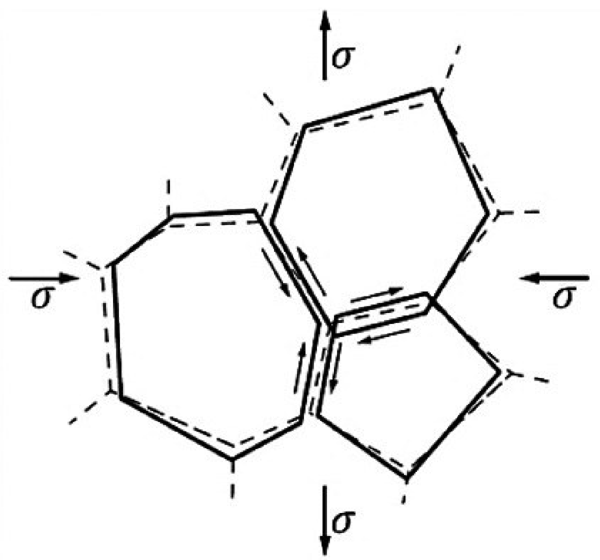

Figure 2.15 Grain boundary sliding [39]

(iii) Diffusion Creep

Diffusion creep occurs by transport of material via diffusion of atoms within a grain. The gradient of free energy is created by the applied stress. There are two ways in which diffusion creep can take place (Figure 2.16).

a) Nabarro-Herring diffusion through grains. This is at a sufficiently high temperature and low strain rate.

b) Coble creep-diffusion along grain boundaries. This occurs at low strain rate and low temperature.

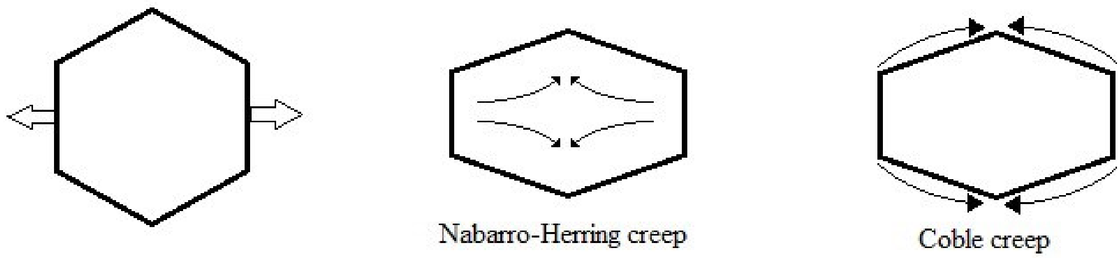

Figure 2.16 Diffusion creep [6 web ref]

The mechanisms of creep are summarized in Figure 2.17 (Asby map).

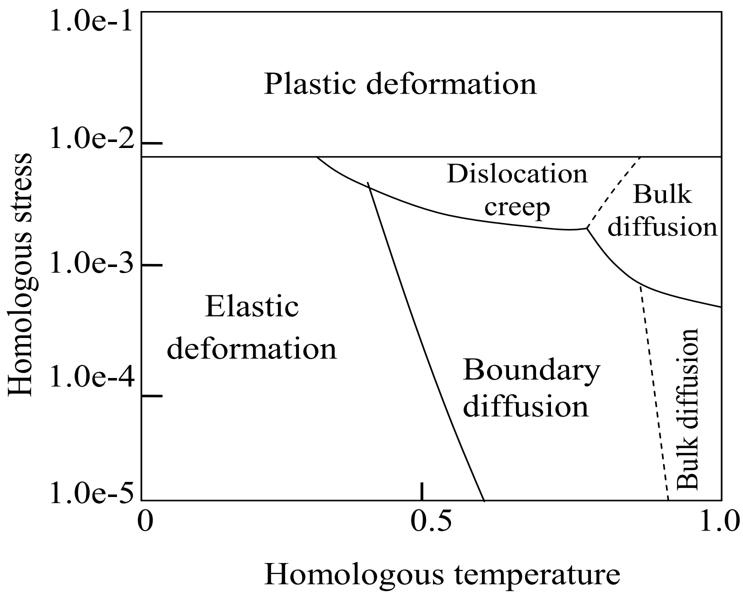

Figure 2.17 Creep deformation map (Ashby map) [37]

2.4. Creep-fatigue damage estimation as per RCC-MR

The creep and fatigue damage estimation is done in RCC-MR [24] as per the procedure briefed in Figure 2.18 [41].

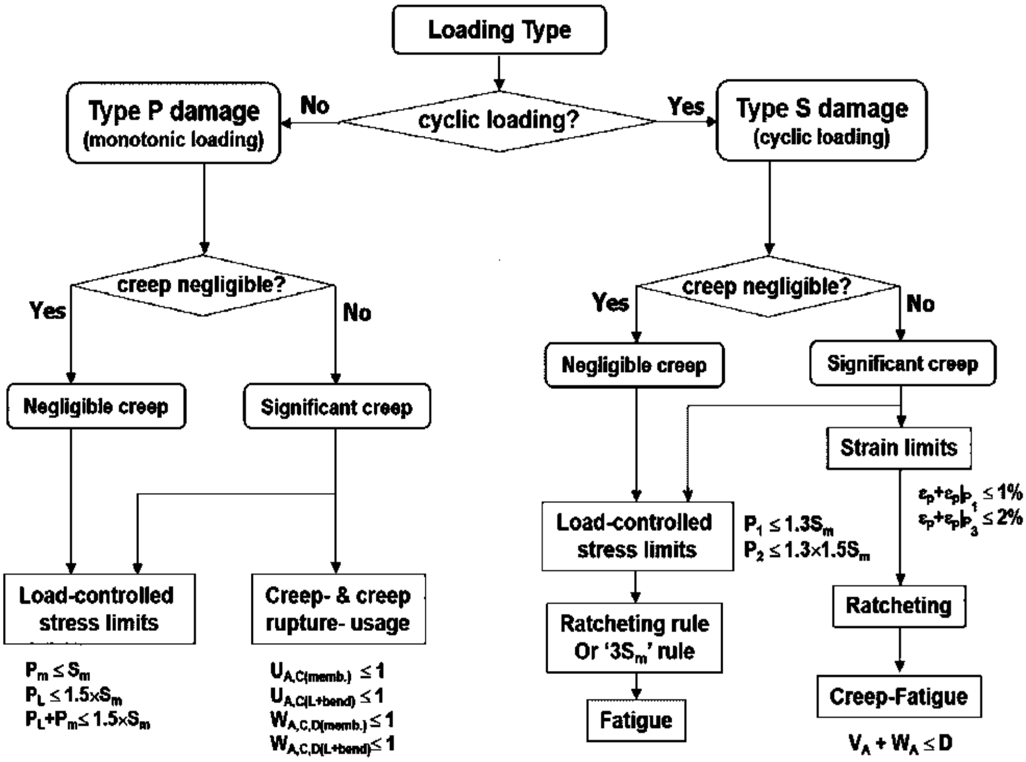

Figure 2.18 Flow diagram of RCC-MR for elevated temperature design [41]

RCC-MR distinguishes between two broad types of possible damages, P-type and S-type. The P-type damage results from the application of a steadily increasing load or constant load. The S-type damages occur due to repeated application of loading (cyclic loads). The procedure to deal with monotonic loads and cyclic loads with and without creep are discussed in the subsequent sections.

SS 316 LN (1S) is the material generally used for class-1 components in Indian fast breeder reactors. The curves shown in this material are from Section III – Tome 1 – Subsection Z – Appendix A3.1S [42]. Based on the material selected, other appendices may be used.

2.4.1. Negligible or significant creep

Creep cross over curve (CCOC) is used to check whether creep is negligible or significant. A CCOC is shown in Figure 2.19.

Table A3.1S.311: negligible creep and thermal ageing curve

θ (°C)	450	475	500	525	550	575	600	625	650
T (h)	$1.6.10^6$	$1.5.10^5$	17000	2000	270	50	10.5	3.5	1.3

Figure A3.1S.311: negligible creep and thermal ageing curve

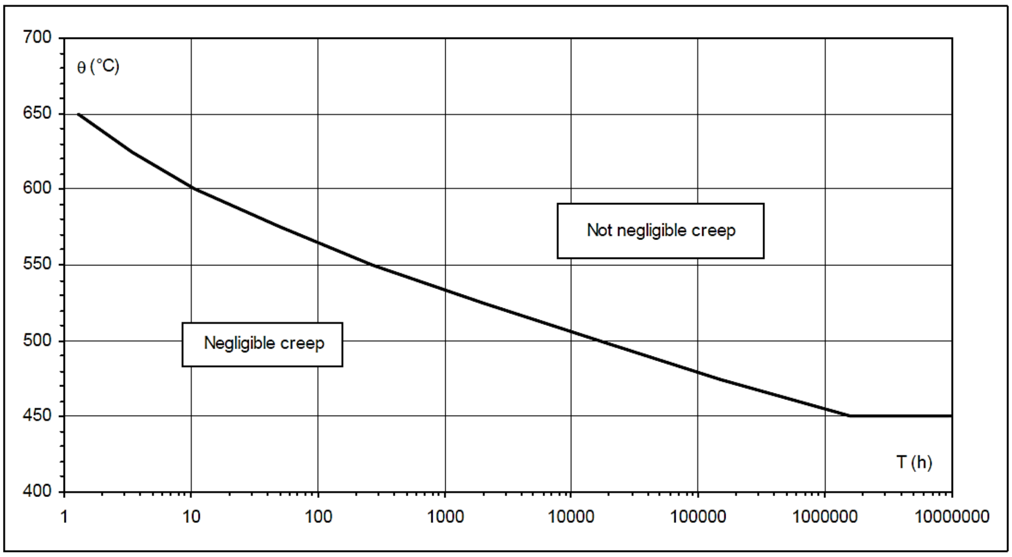

Figure 2.19 Creep cross over curve [42]

CCOC is generated experimentally by the following procedure [40].

i) Select a temperature θ_1 ^{0}C.

ii) Find S_m at temperature θ_1 ^{0}C (S_m is the material property, which is the minimum of two-thirds yield strength or one-third ultimate strength).

iii) Generate mean relaxation data at θ_1 from appropriate creep law assuming strain hardening hypothesis.

iv) Start with stress = 1.5 S_m.

v) Record the time (t_1) which can cause 20 % relaxation of the starting stress (=1.2 S_m). Creep is significant at temperature θ_1 beyond time (t_1).

vi) Repeat the procedure with temperature θ_2, θ_3, θ_4, and so on, and find the corresponding time t_2, t_3, t_4, and so on, to generate the CCOC for that material.

In practical application we may come across two kinds of cases. One is the case at constant temperature and the other is variable temperature case. CCOC is used in both the cases as illustrated below.

2.4.1.1. Constant temperature

If the temperature (θ) is constant throughout the operating period (t), the point (t, θ) is plotted in the CCOC, and it is checked whether the point is in the negligible creep region or not negligible creep region.

2.4.1.2. Variable temperature

We may come across certain cases, like for example, during start-up of a reactor, the power raising is done by slowly raising the coolant temperature. In this case, the temperature at a particular location varies with time, as shown in Figure 2.20.

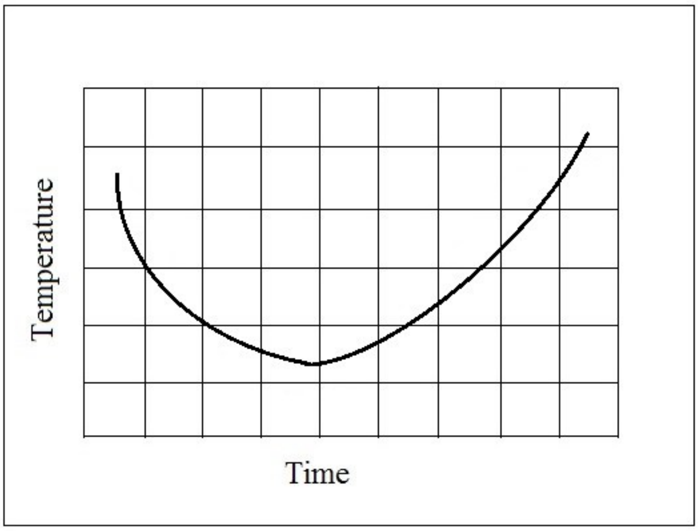

Figure 2.20 Example of temperature variation with time

The significance of creep is estimated by dividing the total operating period into 'N' intervals of time of duration t_i and of maximum temperature θ_i. The time T_i is then determined from the CCOC for each θ_i. If the equation 2.9 is satisfied, creep is negligible, else creep is significant.

$$\sum_{i=1}^{N} \frac{t_j}{T_j} \leq 1$$

2.9

2.4.2. Creep without fatigue [P-type]

When a constant load (P-type) is applied on a component, the limits given below have to be checked for both negligible creep and significant creep.

$$P_m \leq S_m$$

2.10

$$P_L \leq 1.5\ S_m$$

2.11

$$P_L + P_b \leq 1.5\ S_m$$

2.12

In case of significant creep, creep usage fraction (section 2.4.2.1) shall also be checked along with the above criteria (equation 2.10 to equation 2.12). The procedure to check the creep usage fraction is explained below in detail.

2.4.2.1. Creep usage fraction

Creep usage fraction is the fraction of damage that occurred in the material at a constant load, in given time. Equation 2.13 and equation 2.14 are the rules for primary membrane, and primary membrane and bending stresses respectively.

A) For primary membrane:

$$U_A\ (\Omega.\ P_m) = \frac{t_j}{T_j} \leq 1$$

2.13

where, *Creep Correction Factors*, $\Omega_1 = 1 + 0.2\ (\frac{L_m}{P_m})$, $\Omega_2 = (\frac{\sigma_1}{P_m})$, $\Omega = \Omega_1 * \Omega_2$

σ_1 is the largest tensile component of the principal stress,

t_j is the application time,

T_j is the maximum allowable time (from RCCMR- S_t curve) [shown in Figure 2.21].

The purpose of the creep correction factors are:

(a) Coefficient Ω_1 takes into account, the possible underestimation of general primary membrane stress intensity by elastic analysis when in the same part of the component there is also a primary local stress. Due to the stress redistribution under creep, some part of the primary local stress is to be considered acting as a general primary membrane stress.

(b) Von-Mises or Tresca equivalent stresses are used in RCC-MR code, Ω_2 factor is used to correct that discrepancy.

B) For primary membrane and bending:

$$U_A\,(P_L + \Phi\, P_b) = \frac{t_j}{T_j} \leq 1 \tag{2.14}$$

Where coefficient, Φ depends on the geometry of the cross section concerned. It is equal to 0.8 for plate elements and thin-walled shells with a rectangular cross-section. Coefficient Φ is used to correct the overestimation of the elastic bending stress.

2.4.2.2. S_t curve

S_t curve for SS 316 LN is shown in Figure 2.21.

Figure A3.1S.52: values of S_t

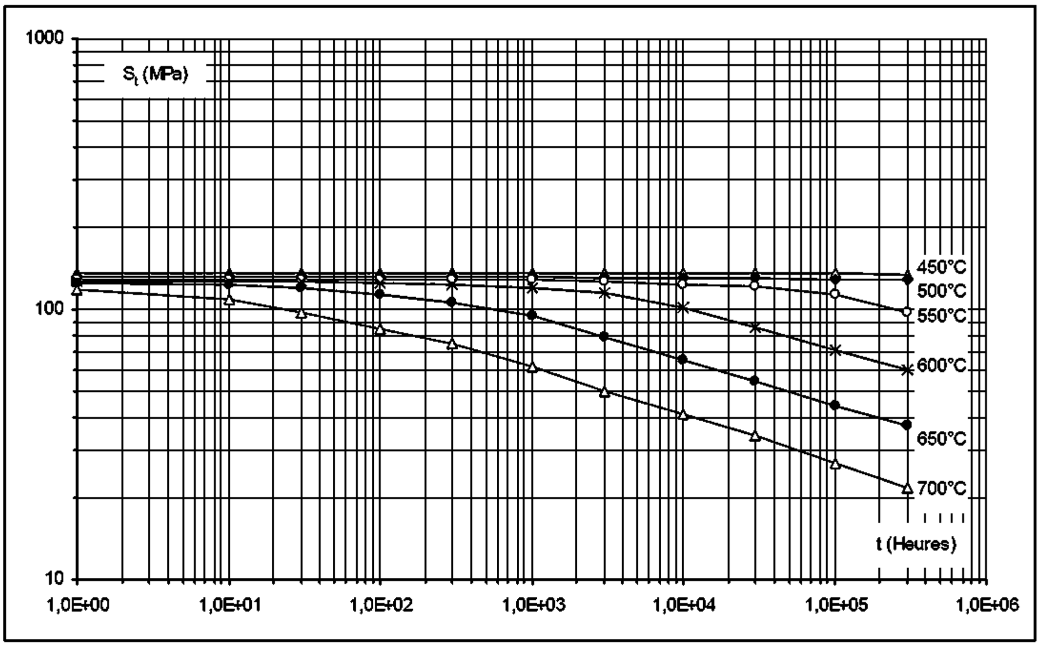

Figure 2.21 S_t curve for SS 316 LN material [42]

S_t is the minimum of

- 100% of the average stress required to obtain a total (elastic, plastic, primary creep, and secondary creep) strain of 1%;
- 80% of the minimum stress to cause initiation of tertiary creep; and
- 67% of the minimum stress to cause creep-rupture.

2.4.3. Creep-fatigue damage interaction [S-type damage]

The damage caused due to fatigue loadings is S-type damage. The rules for the S-type damage apply only if the rules for the prevention of P-type damage are satisfied. In S-type, two types of damages are looked at under level-A criteria.

A) Progressive deformation and

B) Creep-fatigue

The code explicitly says that the check of creep fatigue rules is valid only if the check of no progressive deformation has been performed. However, no requirement exist under level C and D criteria. We shall distinguish the case where the creep effect is negligible from the case where it is significant, in the subsequent sections and bring out the damage estimation procedure for each case.

2.4.3.1. Negligible creep condition [only fatigue]

The CCOC is checked to find whether creep is significant or negligible, as discussed in section 2.4.1. When creep is negligible, the progressive deformation and fatigue damage are estimated as illustrated below.

A) Progressive deformation

Progressive deformation occurs if an increase in deformation appears at each cycle under the effect of cyclic loads. Once we have P_m, $P_m + P_b$, P_L, $P_L + P_b$ and ΔQ, the shakedown criteria is checked as per equation 2.15.

$$\text{Max}\,(P_m+P_b) + \Delta Q \le 3\ Sm \qquad \textbf{2.15}$$

If equation 2.15 is satisfied, there is no ratcheting for the given loading, else, efficiency index method is followed.

i) Efficiency index method

The shakedown criteria is the sum of the primary and secondary stresses. However, there are cases where the primary stress is negligible and the secondary stress is high, resulting in plastic cycling, but no ratcheting (as discussed in section 2.3.6). Hence, efficiency index method, which considers the contribution of primary and secondary stresses is used to check the possibility of ratcheting.

The effective primary stress is determined from the efficiency index diagram, and the limits are checked as per equations 2.18 and 2.19. The effective primary stress is the primary stress which, if applied alone in the same condition of time and temperature, would lead to the same accumulated strain obtained under a constant primary stress (P) combined with a cyclic secondary stress range (ΔQ). The steps to calculate the progressive deformation damage are given below.

The secondary ratio (SR_1) in relation to the primary membrane stress (P_m) and the secondary ratio (SR_2) in relation to the sum of the primary stresses ($P_L + P_b$) are determined.

$$SR1 = \frac{\Delta Q}{\text{Max (Pm)}} \qquad \textbf{2.16}$$

$$SR_2 = \frac{\Delta Q}{\text{Max (PL + Pb)}} \qquad \textbf{2.17}$$

The efficiency indicies (ν_1 & ν_2) are obtained from the efficiency diagram (Figure 2.22). Using these values, the effective stress intensities (P_1 and P_2) are calculated

$$P_1 = \frac{\text{Max (Pm)}}{\nu 1} \text{ (MPa)} < 1.3 * S_m \qquad \textbf{2.18}$$

$$P_2 = \frac{\text{Max (PL + Pb)}}{\nu 2} \text{ (MPa)} < 1.3 * 1.5 * S_m \qquad \textbf{2.19}$$

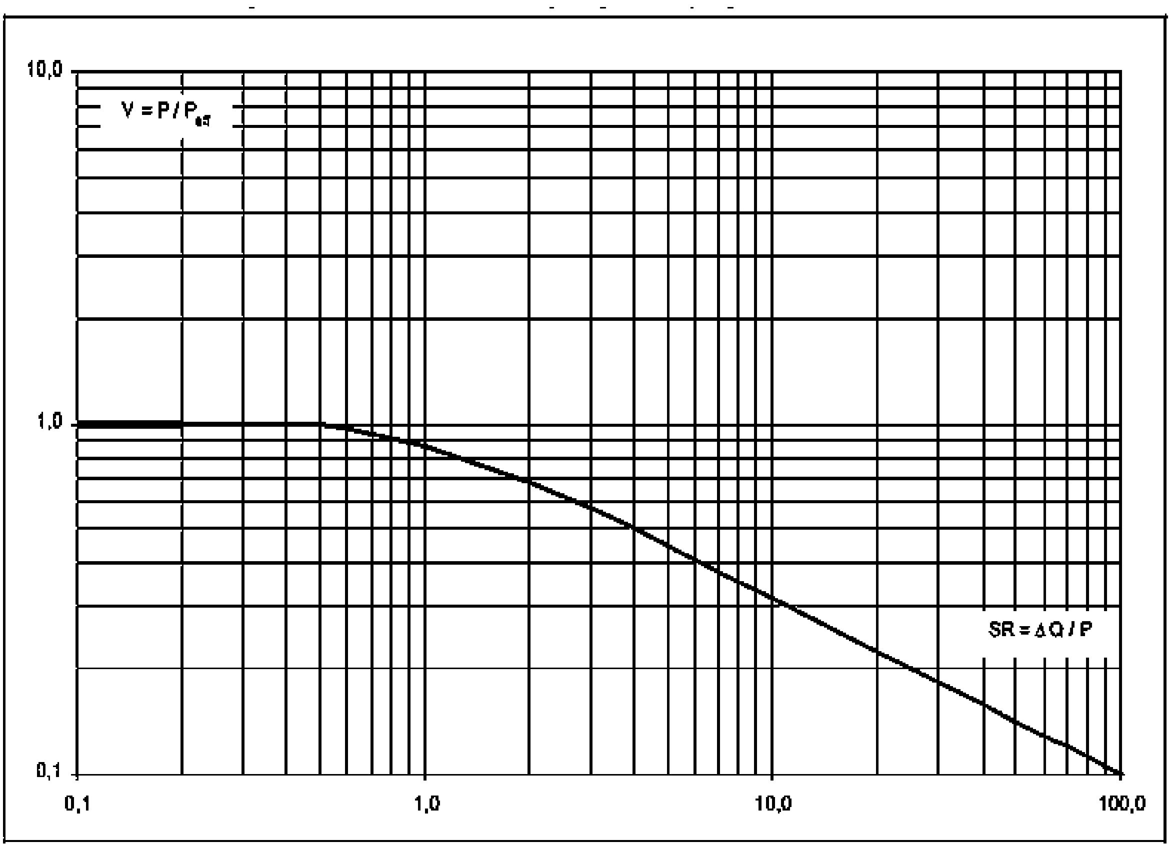

Figure 2.22 Efficiency index diagram as per RCC-MR [24]

B) Fatigue rules

When using elastic analysis to calculate the response of a structure, the range of strains thus obtained does not take account of plastic strain which would occur if the real behavior of the material were to be modeled. The method proposed below in RCC-MR is thus aimed at providing an estimate of the 'real' strain range $\overline{\Delta\varepsilon}$ on the basis of the results of the elastic analysis [24].

(i) Amplification due to plasticity- Calculation of total strain $(\overline{\Delta\varepsilon})_{el+pl}$

$$\Delta\sigma_{tot} = \Delta(P + Q + F) \tag{2.20}$$

$$(\overline{\Delta\varepsilon})_{el+pl} = (\overline{\Delta\varepsilon_1} + \overline{\Delta\varepsilon_2} + \overline{\Delta\varepsilon_3} + \overline{\Delta\varepsilon_4}) \tag{2.21}$$

$(\overline{\Delta\varepsilon})_{el+pl}$ is the strain given by elastic calculation, corrected by Neuber term of amplification and increase of poisson's ratio in plastic behavior.

(ii) ***Calculation of*** $\overline{\boldsymbol{\Delta\varepsilon_1}}$

$$\overline{\Delta\varepsilon_1} = \frac{2}{3}(1+\nu)\left(\frac{\Delta\sigma_{tot}}{E}\right)$$

2.22

Elastic strain range $\overline{\Delta\varepsilon_1}$

Where E: Youngs Modulus and ν: poissons ratio

(iii) ***Calculation of*** $\overline{\boldsymbol{\Delta\varepsilon_2}}$

$\overline{\Delta\varepsilon_2}$ is the plastic increase in strain due to the primary stress range (ΔP) equal to

$$\Delta P = \Delta\left[\overline{P_m + 0.67\,(P_b + P_L - P_m)}\right]$$

2.23

$\overline{\Delta\varepsilon_2}$ =0, if primary stresses are small. However, when there is an appreciable elastic follow-up, the secondary stresses are taken as primary, and $\overline{\Delta\varepsilon_2}$ is not negligible.

(iv) ***Calculation of*** $\overline{\boldsymbol{\Delta\varepsilon_3}}$

$\overline{\Delta\varepsilon_3}$ is the plastic amplification strain established with the Neuber's Method (stress × strain = constant).

$$\overline{\Delta\varepsilon_3} = (K_\varepsilon - 1)\,\overline{\Delta\varepsilon_1}$$

2.24

K_ε is the amplification coefficient to compute elastically computed stress or strain into real stress or strain [42].

(v) ***Calculation of*** $\overline{\boldsymbol{\Delta\varepsilon_4}}$

$\overline{\Delta\varepsilon_4}$ is the plastic amplification strain due to triaxiality and Poisson's coefficient variation in the plastic domain.

$$\overline{\Delta\varepsilon_4} = (K_\nu - 1)\,\overline{\Delta\varepsilon_1}$$

2.25

K_ν is the amplification coefficient [42].

The total elasto-plastic strain is calculated from equation 2.21.

The summary of the calculation of $(\overline{\Delta\varepsilon})_{el+pl}$ is given in Figure 2.23 [24].

With $(\overline{\Delta\varepsilon})_{el+pl}$, find the number of cycles allowable (N_d), from the fatigue curve of the material.

$$\text{Fatigue Damage (V)} = \frac{\text{N}}{N_d} \tag{2.26}$$

where N is the applied number of cycles.

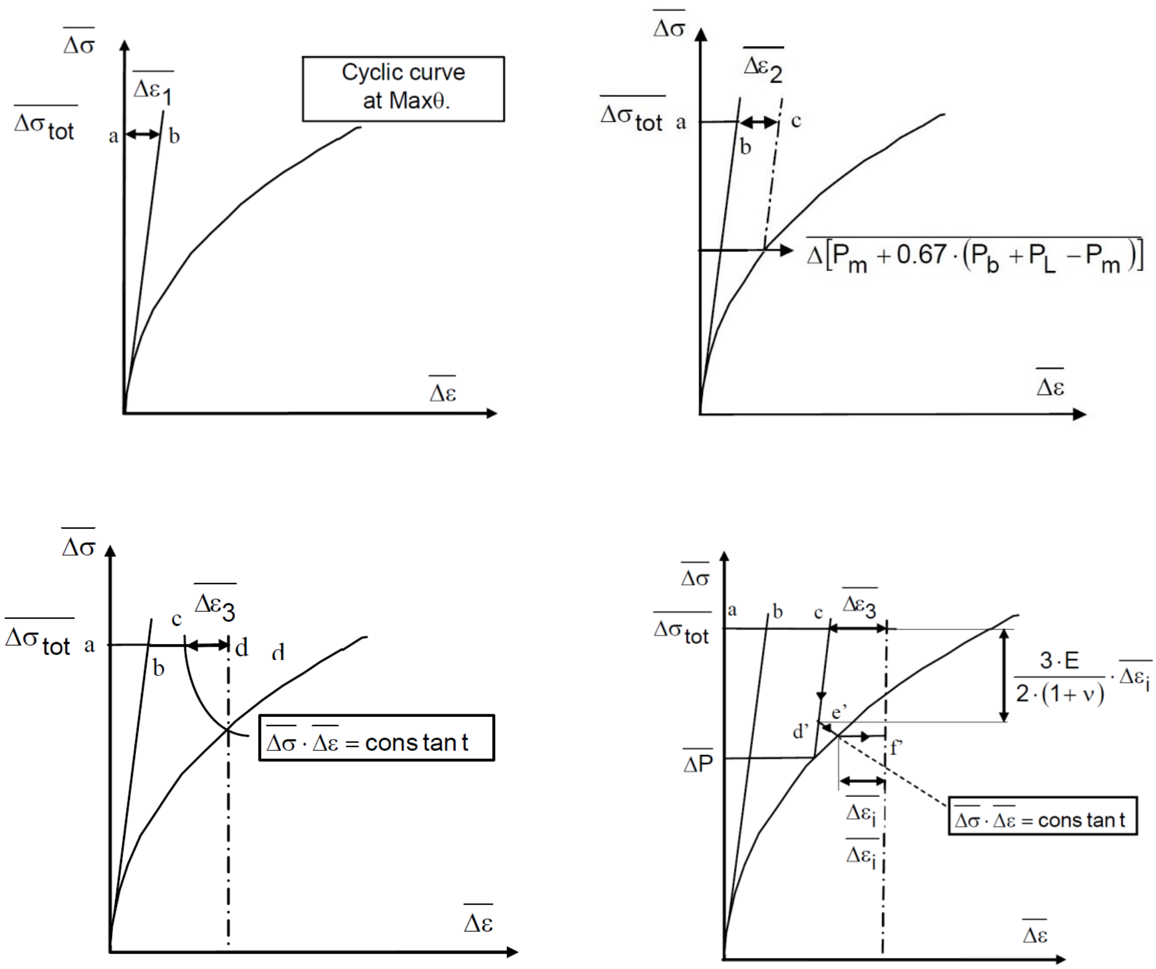

Figure 2.23 Calculations of strain ranges as per RCC-MR [24]

2.4.3.2. Significant creep condition [creep and fatigue]

A) Assessment of progressive deformation

In high temperature structural design, it is very important to prevent progressive deformation in the points of functional requirements and structural integrity. When there is significant creep, the progressive deformation designates the increase in deformation due to loads caused by imposed cyclic deformation such as thermal deformation.

With P_m, $P_m + P_b$, P_L, $P_L + P_b$ and ΔQ, equation 2.15 is checked, and if the limits are met, there is no progressive deformation as discussed in section 2.4.3.1. If the limit is not met, efficiency index method is used as follows.

(i) Efficiency index method:

The secondary ratio (SR_1) in relation to the primary membrane stress (P_m) and the secondary ratio (SR_2) in relation to the sum of the primary stresses ($P_L + \Phi P_b$) are determined as per equations 2.27 and 2.28.

$$SR_1 = \frac{\Delta Q}{\text{Max (Pm)}} \tag{2.27}$$

$$SR_3 = \frac{\Delta Q}{\text{Max (PL} + \Phi \text{ Pb)}} \tag{2.28}$$

The efficiency indicies (ν_1 & ν_3) are obtained from the efficiency diagram (Figure 2.22). Using these values, the effective stress intensities (P_1 and P_3) are calculated as per equations 2.29 and 2.30.

$$P_1 = \frac{\text{Max (Pm)}}{\nu 1} \text{ (MPa)} < 1.3 * S_m \tag{2.29}$$

$$P_3 = \frac{\text{Max (PL} + \Phi \text{ Pb)}}{\nu 3} \text{ (MPa)} < 1.3 * 1.5 * S_m \tag{2.30}$$

Also, the following conditions are checked.

$$\varepsilon_p + \varepsilon_c \text{ (for } \sigma = 1.25\ P_1\text{) (\%)} < 1\% \tag{2.31}$$

$$\varepsilon_p + \varepsilon_c \text{ (for } \sigma = 1.25\ P_3\text{) (\%)} < 2\% \tag{2.32}$$

$$\text{Where, creep strain, } \varepsilon_c \text{ (\%)} = C_1\ T_H^{C2}\ (\sigma)^{n1} \tag{2.33}$$

(T_H and σ are time spent in creep regime and stress respectively. C_1, C_2 and n_1 are material constants [42]).

and plastic strain, ε_p (%)= $(\sigma / [C_o*(R^t_{p,0.2})_{moy}])^{(1/n0)}$ *(up to 1.5 % plastic strain)*

2.34

$[(R^t_{p,0.2})_{moy}]$ is the average yield stress, C_o = 1.198, n_0 = 0.1125.

For plastic strain > 1.5 %, use the curves given in [42].

B) Assessment of creep-fatigue damage

Due to the low frequencies ($\leq 10^4$ cycles) and the time spent in creep regime at high temperatures, a severe interaction between creep and fatigue occurs. Equation 2.35 presents the limit rule of the accumulated creep and fatigue damage for the total design life time.

$$\sum_{j=1}^{p}\left(\frac{N}{N_d}\right)_j + \sum_{k=1}^{q}\left(\frac{T_H}{T_d}\right)_k \leq D$$

2.35

Where D is the total creep-fatigue damage, which is different for different materials. For example its value is 0.3 for SS 316 LN and 0.1 for 2.25 Cr-1Mo steel.

(i) Calculation of fatigue damage

Fatigue damage is calculated from fatigue curve when the total strain is known. The total strain is the elasto-pastic strain (equation 2.21), when there is no creep. In the presense of creep, the creep strain is included in the total strain as per equation 2.36.

$$(\overline{\Delta\varepsilon}) = (\overline{\Delta\varepsilon})_{el+pl} + (\overline{\Delta\varepsilon})_{cr}$$

2.36

Creep strain (held for time T_H at temperature $\theta*$) is defined in equation 2.33. To substitute creep strain in equation 2.36, σ and T_H in equation 2.33 are σ_k and time spent in creep regime per cycle respectively.

$$\text{Time spent in creep regime per cycle} = \frac{\text{Total life time}}{\text{number of cycles}}$$

2.37

$$\sigma_k = \bar{P}_{max} + K_s\,\overline{\Delta S}^*$$

2.38

$$\text{where, } \bar{P}_{max} = \text{Max}\,[\overline{P_m + 0.66\,(P_b + P_L - P_m)}]$$

2.39

$$\overline{\Delta S}^* = \overline{\Delta\sigma}^* - \overline{\Delta P} \quad \textbf{2.40}$$

$\overline{\Delta\sigma}^*$ is from cyclic curve for ($\overline{\Delta\varepsilon}$) (shown in Figure 2.24) [42].

Symmetrization coefficient, K_s value is got from $R = \overline{\Delta\sigma}^* / 2(R^t_{p0.2})_{min}$

$(R^t_{p0.2})_{min}$ is the minimum yield stress.

Using ($\overline{\Delta\varepsilon}$), the number of cycles is obtained from fatigue curve of the material, and the fatigue damage is calculated as per equation 2.26.

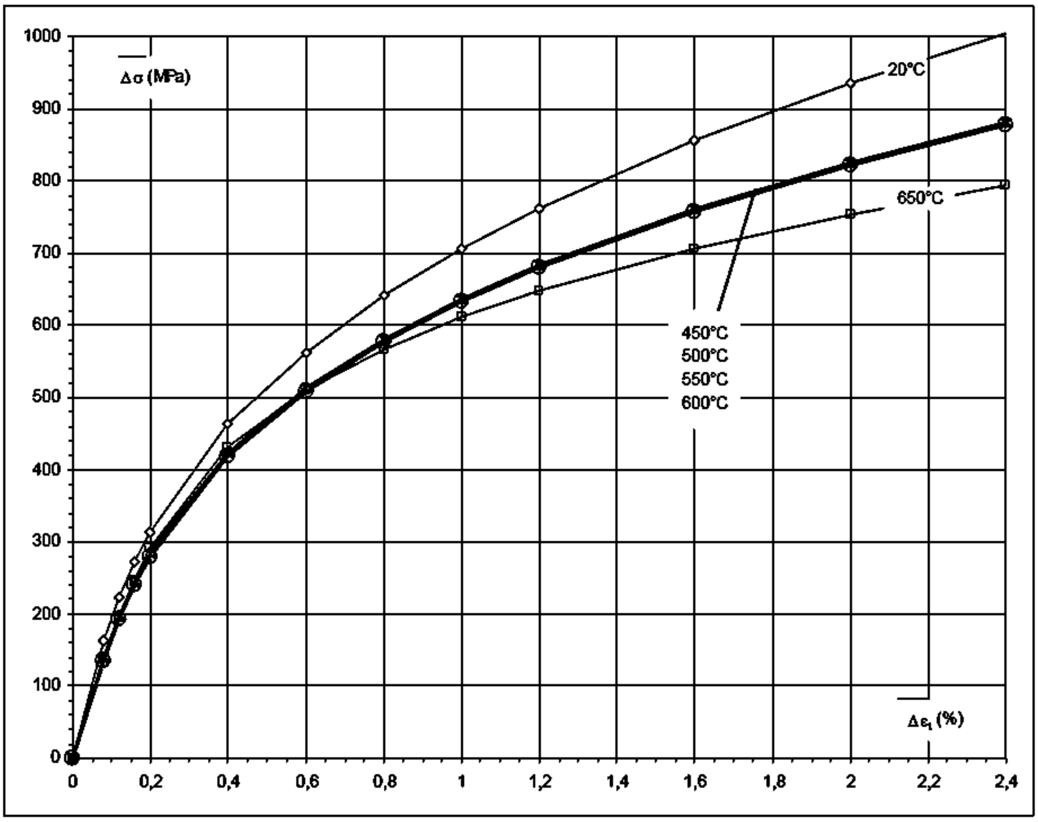

Figure 2.24 Cyclic curve for austenitic stainless steel as per RCC-MR [42]

(ii) Calculation of creep damage

For the creep damage evaluations, the maximum time, T_d, corresponding to the stress (σ_k / 0.9) is determined on the basis of the minimum value of the creep rupture stress, S_r curves given in A3.1S.53 in RCC MR (Figure 2.25) [42].

The creep damage (W) is calculated using

$$W = \frac{T_H}{T_d}$$ **2.41**

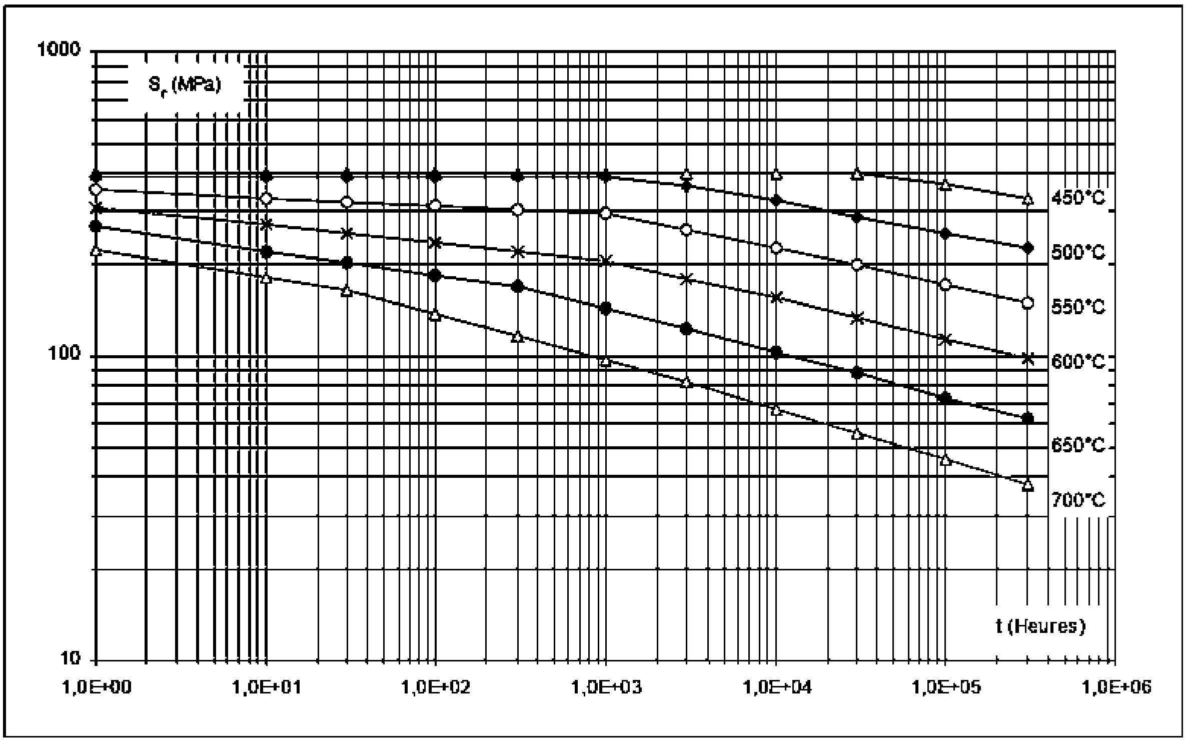

Figure 2.25 Minimum creep rupture stress (Sr) curve [42]

(iii) Estimation of effective damage

The effective damage (D_{eff}) is the equivalent damage expressed by considering the bilinear interaction between creep and fatigue. If the total life of the component is 1, D_{eff} is the fraction of damage occurred due to the transient considered. The D_{eff} for each case is calculated using (V) and (W) values. The creep-fatigue interaction diagram for SS 316 LN is shown in Figure 2.26. The life of the component is estimated by predicting the number of cycles allowable by calculating the D_{eff}. The procedure is shown below.

w-creep damage per cycle, v-fatigue damage per cycle.

From Figure 2.26, When w>v, OP cuts AB at Q.

$Q = (\frac{3w}{3w+7v}, \frac{3v}{3w+7v})$

Derivation:

Equation of line is given by equation 2.42.

$$(y - y_1) = \frac{(y_2 - y_1)}{(x_2 - x_1)}(x - x_1) \tag{2.42}$$

Equation of line AB: Substituting A (1,0), B (0.3, 0.3), in equation 2.42, equation of line AB is 3x + 7y = 3. Similarly, when O (0,0), P (w,v), equation of line OP is wy = vx.

The point of intersection of line OP and AB is Q. Solving both the line equations of AB and OP, Q = $(\frac{3w}{3w+7v}, \frac{3v}{3w+7v})$. Hence,

$$D_{eff} = \frac{OP}{OQ} = \frac{3w+7v}{3} \tag{2.43}$$

Similarly, when w'<v', OP' cuts BC at Q'.

Q' = $(\frac{3w'}{7w'+3v'}, \frac{3v'}{7w'+3v'})$. Hence,

$$D_{eff} = \frac{OP'}{OQ'} = \frac{3v'+7w'}{3} \tag{2.44}$$

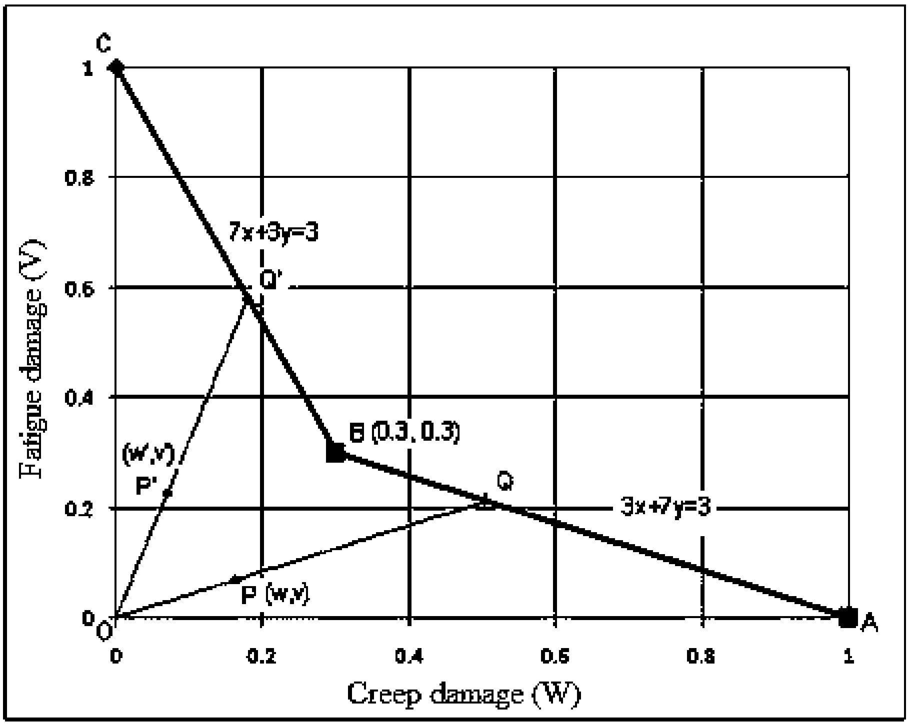

Figure 2.26 Creep fatigue interaction diagram for SS 316 LN material

2.5. Closure

In this chapter, the design codes used for various applications have been discussed. The types of forces, failure theories and the stresses developed in the component on application of various kinds of loads have been illustrated. The failure modes in a typical fast reactor has been briefed and creep, fatigue damage mechanisms have been highlighted. The procedure to estimate the creep-fatigue damage and ratcheting have been detailed, as it is used to determine the effective damage at each location during power raising and crash cooling operations. With this background, the next chapter represents the detailed literature survey on fast reactor transients and bring out the gap areas.

References

[19] BPVC Section VII Rules for construction of pressure vessels. Division 1, BPVC-VIII-1-(2019), Publisher ASME, ISBN 9780791872871.

[20] R P Pandey. Fundamentals of Design by Analysis. National workshop on High Temperature Design (2016).

[21] Nptel. Design for static loading, Module 3 Design for Strength, Version 2 ME, IIT Kharagpur (2016).

[22] J. Bodig & B.A. Jayne. Mechanics of Wood and Wood Composites. Krieger Publishing, (1993), pp. 314-5.

[23] Failure Prediction and Avoidance. Experimental Stress Analysis Notebook, Issue 22, Dec. (1993), Measurements Group, pp. 6-11.

[24] RCC-MR Section III - Tome-1-Subsection B: Reactor components and supports (2012).

[25] Baldev Raj, P. Chellapandi, P.R.Vasudeva Rao. Sodium fast reactors with closed fuel cycle. ISBN-13:978-1-4665-8769-4 (2015).

[26] Ashok Kumar and Anindya Chatterjee. On One Imperfection Estimation Method for Thin Shell Buckling in the Design Code RCC-MR. Journal of Nuclear Engineering and Radiation Science OCTOBER 2019, Vol. 5 / 042001-1.

[27] V. Prakash, P. Anup Kumar,M. Anandaraj, M. Thirumalai, C. Anandbabu, K.K. Rajan. Flow induced vibration studies on PFBR control plug components. Nuclear Engineering and Design 250 (2012) 725– 734.

[28] V. Prakash, M. Thirumalai, R. Prabhakar, G. Vaidyanathan..Assessment of flow induced vibration in a sodium–sodium heat exchanger. Nuclear Engineering and Design 239 (2009) 169–179.

[29] Wakamatsu M, Nei H, Hashiguchi K. Attenuation of temperature fluctuations in thermal stripping.Nuclear Sci. and Technol. 32(8): 752–762 (1995).

[30] K. Velusamy, P. Chellapandi, S. C. Chetal and Baldev Raj. Overview of pool hydraulic design of Indian prototype fast breeder reactor. Sadhana Vol. 35, Part 2, April (2010), pp. 97–128.

[31] M. Azarian, J. C. Astegiano, D. Tenchine, M. Lacroix, M. Vidard. Sodium thermal-hydraulics in the pool LMFBR primary vessel. Nuclear Eng. and Design 124: 417–430 (1990).

[32] Ashutosh Mishra, R. Suresh Kumar and P. Chellapandi. Progressive deformation behaviour of thin cylindrical shell. Latin American Journal of Solids and Structures 11 (2014) 980-992.

[33] R. Suresh Kumar. High temperature design as per ASME section III - Division 1- Subsection NH. National workshop on High Temperature Design (2016).

[34] M. Heitzer and M. Staat. Direct static FEM approach to limit and shakedown analysis. IASS-IACM 2000 Fourth International Colloquium on Computation of Shell & Spatial Structures June 5–7, (2000) Chania – Crete, Greece.

[35] R Sandhya. Presentation on Mechanical behavior of Engineering materials. HBNI, Engg Sciences, (2016).

[36] G. Glinka. ME 322-Mechanical Design 1. University of Waterloo, Department of Mechanical Engineering, Partial notes –Part 4 (Fatigue), Fall (2005).

[37] Mahendra Kumar Samal. Creep design of pressure vessel and piping as per codes. INS workshop on Structural integrity assessment procedure for pressure vessel and piping, Mumbai 5-9 September, (2011).

[38] Sinisa Dj. Mesarovic. Dislocation Creep: Climb and Glide in the Lattice Continuum. School of Mechanical and Materials Engineering, Washington State University, Pullman, WA 99164, USA, August (2017).

[39] J. Roesler, H. Harders, M. Baeker. Mechanical Behaviour of Engineering Materials: Metals, Ceramics, Polymers, and Composites, SpringerVerlag Berlin Heidelberg, pp. 383-401 (2007).

[40] P. Chellapandi. Training school material, HBNI, IGCAR (2009).

[41] Hyeong-Yeon Lee, Min-Gu Won, Nam-Su Huh, "HITEP_RCC-MRx Program for the support of Elevated Temperature Design Evaluation and Defect Assessment", Journal of Pressure Vessel Technology, vol.14, October 2019.

[42] RCC-MR Section III - Tome 1 - Subsection Z : Technical Appendix A3, (2012).

Web references

[3] https://en.wikipedia.org/wiki/Structural_integrity_and_failure

[4]https://en.wikipedia.org/wiki/Buckling#:~:text=In%20structural%20engineering%2C%20buckling%20is,of%20a%20plate%20under%20shear.

[5]https://www.engineersedge.com/material_science/fatigue_crack_growth_analysis_review_10071.htm

[6]https://www.tectonique.net/MeansCD/contribs/jessell/lectures/lec1.html

Chapter 3

Literature Survey

3.1. Background

The introduction to fast reactors components and the concepts for the assessment of structural damage in the reactor components have been discussed in the previous chapters. In this chapter, the literature survey of the thermal aspects, reactor physics and instrumentation, and structural aspects in reactors during thermal transients has been carried out to identify the critical components that decide the rate of power raising of sodium. Literature on the thermo-mechanical behaviour of structures and the various thermo-mechanical models developed for various applications has been surveyed to explore the availability of a numerical model to study the behaviour of partially immersed components. The failure modes in fuel clad tubes during thermal transients have also been investigated and the gap areas have been identified.

3.2. Thermal transients in reactors

A reactor transient is said to occur when there is a change in the reactor coolant temperature, pressure or both, and affects the reactor's power [7web ref]. Some of the examples of thermal transients in PFBR are PSP trip, PSP seizure, primary pipe rupture, start-up, shutdown of the reactor and so on. The objective of the thesis is to simplify the start-up and shutdown schemes in PFBR and future fast reactors. Hence literature survey on various aspects of start-up and shutdown in reactors is presented below.

3.2.1. Thermal aspects

Thermal analysis on temperature-raising phase and power-raising phase of start-up are carried out with a developed computation code for SWCR. The findings show that the cladding temperature difference could be reduced by adjusting flow rate distribution in different fuel assemblies or changing power setting during start-up [43].

The start-up system of a supercritical pressure light water cooled fast reactor (Generation IV concept) has been studied by time dependent thermal-hydraulic analysis. The maximum cladding surface temperature is the critical parameter and accordingly, a power raising rate of ~ 50 K/h has been identified [44].

3.2.2. Reactor physics and instrumentation

The nuclear aspects during power raising have been extensively studied. Spatial kinetic model during the start-up transient is studied. The response in reactors during short time transients has been done using developed codes namely WIMS and CITATION [45]. Simulation of start-up measurements with the KIKO3D code has been carried out and the time and space dependent neutron flux in the core during these measurements have been calculated [46].

The instrumentation is classified as that for control and that for protection. The control instrumentation is used in reactor start-up, steady-state operation and normal shutdown. During start-up and shutdown of a reactor, the reactor must be responsive to changes in energy demand. The rate of heat generation is controlled by controlling the neutron generation. This is done by the reactor control system in conjunction with the load demand program [47]. The power evolution during start-up and shutdown procedures of the IPR-R1 triga reactor was performed and the behavior is found to be sigmoidal [48].

3.2.3. Structural aspects

The structural integrity of the core and all components should be ensured so that the reactor core can be safely controlled, shutdown and cooled under operational states accident conditions [49]. The structural aspect, i.e., the effect on the reactor components that are surrounded by sodium, which is an excellent heat transfer medium, has been highlighted by B. L. Eyre et al. [50]. When there is a large change in the coolant temperature during a transient, the temperature changes are rapidly experienced by all hot pool structures. In the thicker sections of stainless steel these rates can induce significant temperature gradients.

3.2.4. Critical locations

It is observed from [44] that fuel clad tubes can be the critical component that decide the rate of power raising of sodium. Also, from [50] it is observed that the reactor components that are in contact with primary sodium can experience high thermal stresses during power raising and crash cooling operations.

3.3. Thermo-mechanical behavior of structures

The reactor components in the pool-type fast reactors are partially immersed in sodium, i.e., parts of the components are submerged in sodium and the rest is above the sodium level, in the argon cover gas ambience. Thus, the critical locations in the reactor components that are in contact with primary sodium are broadly categorized as submerged locations and free level locations. Literature survey on thermo-mechanical analysis at both the locations and various applications has been carried out in this section.

3.3.1. Thermo-mechanical analysis

Thermo-mechanical analyses for various applications like composites, ceramics, reactor vessels and functionally graded materials have been performed in literature. A detailed stress analysis has been carried out to account for the transients during various operating conditions of the reactor, and the structural integrity of a reactor pressure vessel has been demonstrated [51]. Thermo-mechanical analyses of concrete in LMFBR programs and multi-layered coatings in solar thermal applications have been carried out by [52] and [53] respectively. Coupled thermo-mechanical creep analysis has been carried out for boiling water reactor pressure vessel lower head during severe accidents [54]. Thermo-mechanical analysis of inner vessel in fast reactors has been done with mechanical and thermal loads to bring out an optimized geometry [55]. Thermo-mechanical analyses for other material have been done in [56], [57], [58], [59] and [60]. All the above-mentioned thermo-mechanical analyses have been carried out for various applications using the existing FE codes. Thermo-mechanical analysis for special applications have been done by developing numerical models as discussed below.

3.3.2. Thermo-mechanical models developed

Various numerical models were developed in order to simulate the thermo-mechanical behaviour of materials under various loading and operating conditions. A three-dimensional explicit Lagrangian hydro code has been used to develop a computational procedure to solve the coupled thermo-mechanical equations [61]. Novascone et al., have done the evaluation of coupling approaches for thermo-mechanical simulations involving coupling between the thermal and mechanical response of an engineered system [62]. A stochastic multiscale computational method for predicting the thermo-mechanical coupling properties of porous materials has been developed [63]. Ozdemir et al. developed a cohesive zone formulation that is suitable for the thermo-mechanical analysis of heterogeneous solids and structural systems with contacting/interacting components [64]. Zhu and Poh, 2017 compared the numerical predictions of thermo-mechanical models with the experimental data for 316 L stainless steel [65]. A 3D coupled thermo-mechanical multiscale model for alumina ceramics has been developed to simulate thermally induced fractures [66]. Syed and Jongmin, 2017, investigated the heating effects of high level radioactive wastes in the intact rock by using coupled thermo-mechanical process [67].

Though there is a lot of literature on thermo-mechanical models developed, a numerical model for partially immersed components for simulating the thermo-mechanical behavior at the free level locations is not addressed anywhere, to the best of author's knowledge. Hence there is a need to develop a numerical model for the locations at the free level interface of sodium.

3.4. Effect of heating rate on fuel clad tubes

The power raising operation involving heating rate of sodium, affects all the components in contact with sodium. Fuel clad tubes are one of the crucial structural components in contact with sodium, and its temperature can shoot up with that of sodium, due to the meager temperature difference between hot pool sodium and fuel clad tubes, as shown in Figure 3.1. Thus the behavior of clad tubes during various transients is of paramount importance to ensure the integrity of the reactor core.

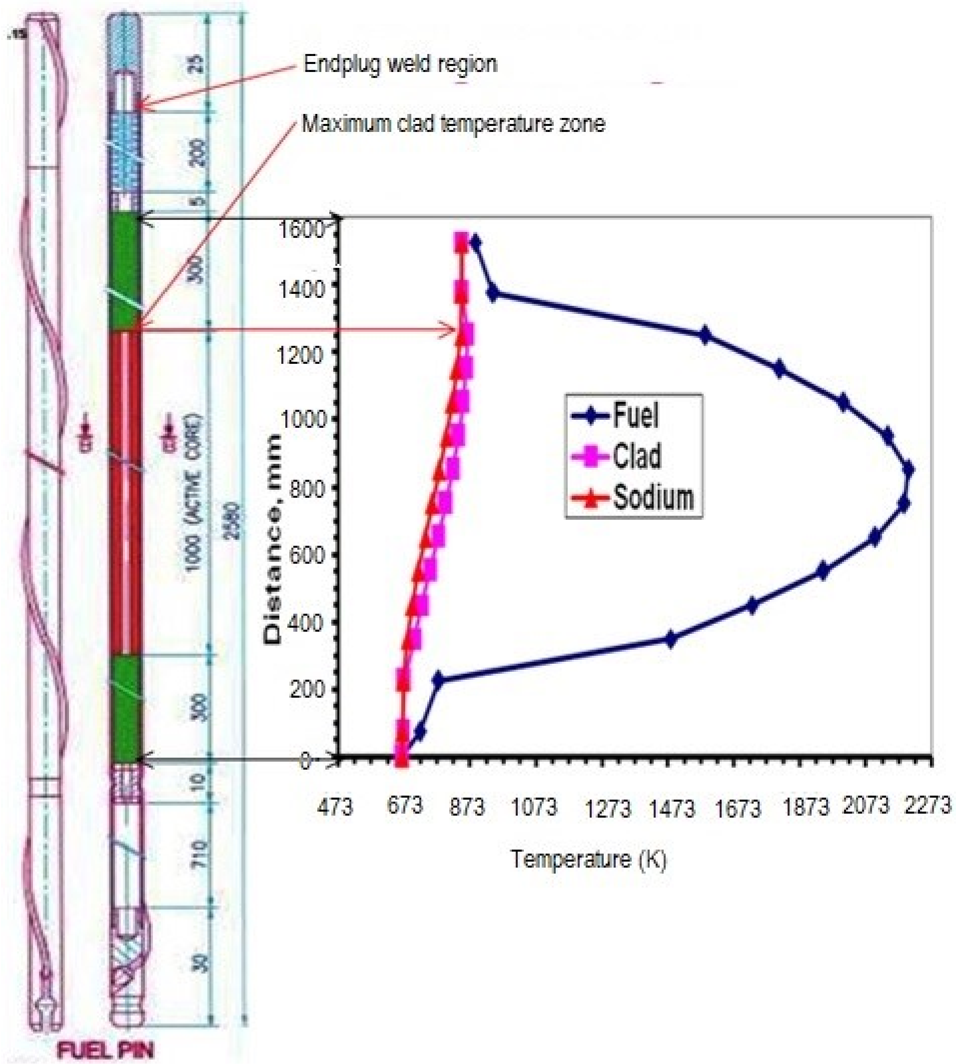

Figure 3.1 Axial temperature distribution of the PFBR fuel pins [70]

During transients, if there is a clad rupture, it can be detected using detectors, and a safety action can be initiated. However, if there is a large plastic deformation in the adjacent clad tubes, which is known as ballooning [68], there can be a blockage of coolant flow in the subassemblies [69]. This flow blockage goes unnoticed as the total flow reduction is low at the subassembly exit, where flow detectors are available. When the damage progresses further to other fuel pins and subassemblies, it can lead to a severe damage in the reactor core. Hence, the possibility of ballooning in fuel clad tubes during power raising has been investigated.

Literature survey has been carried out to understand the ballooning phenomenon, the studies made so far in thermal reactors, the possibility of ballooning in fast reactors, effect of radiation on ballooning and so on.

3.4.1. Review on ballooning

During certain conditions of temperature and pressure difference across the clad, the stresses developed in the fuel clad shoots up to cause plastic deformation which leads to ballooning and burst. The ballooning can potentially be detrimental to cooling of the fuel assemblies. A coolant flow restriction results in an increase in the cladding and fuel temperatures leading to severe fuel damage [69]. Figure 3.2 shows a schematic of the blockage caused by ballooning [71].

Ballooning starts as a combined effect of temperature maxima and wall thickness minima [72]. Viswanathan et al. [73] described ballooning of the cladding as a phenomenon that occurs due to an increase in the internal pressure of the fuel pin and also due to the decrease in the cladding strength. It is observed that the differential pressure is one of the critical parameters which contribute to ballooning [74], [75]. Rapid pressurization test carried out to evaluate the mechanical behavior of a cladding under a fast strain rate inferred that the maximum hoop stress increases with the pressurization rate [76]. With creep being a strong function of temperature and pressure, ballooning is a highly non-linear phenomenon and the small differences in conditions can have large effects on the time of onset and degree of ballooning. Nevertheless, ballooning ceases to increase on rupture due to release of the pressure developed [77].

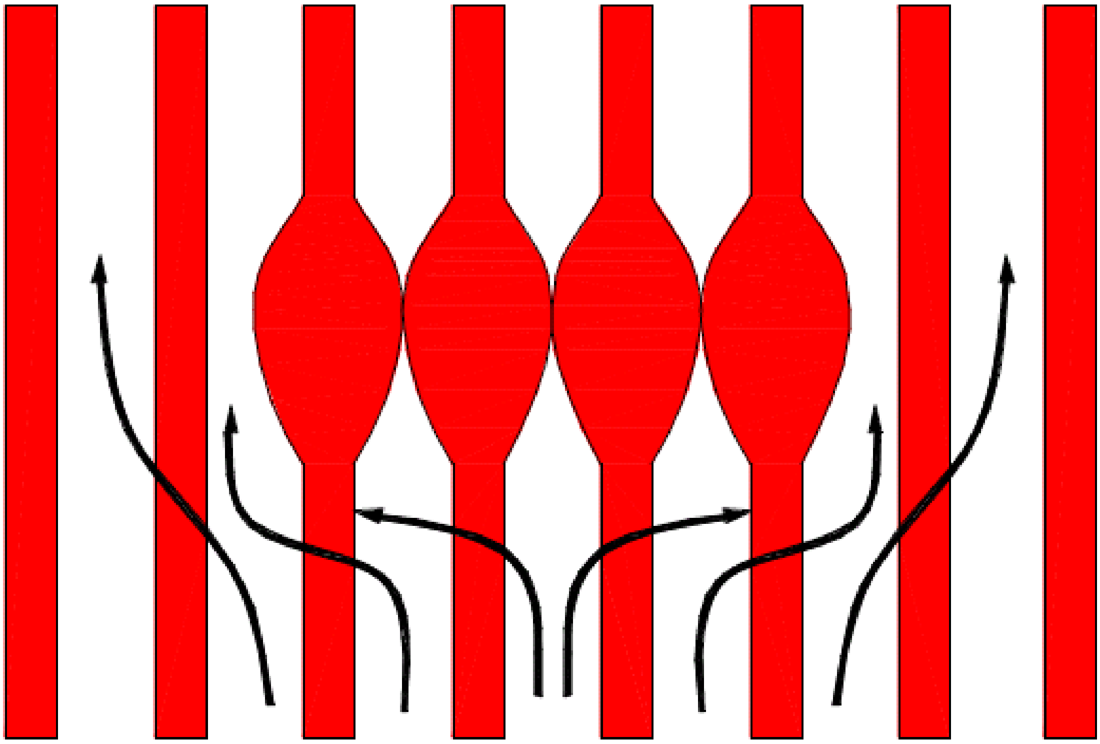

Figure 3.2 Blockage caused by ballooning in fuel clad tubes [71]

The VVER (E110 type) cladding tubes have been tested with single-rod and bundles. It is observed that the mechanical behavior of the fuel rods was predominantly influenced by the pressurization rate when compared to temperature increase and iodine pretreatment [78]. A significant difference in the clad behavior at 1073 K and 1273 K has also been observed in E110 and Zircaloy-4 material. Thus Zoltan [78] emphasized the need to perform ballooning experiments with new or less studied cladding materials because their behavior may differ from the well-investigated Zircaloy cladding.

3.4.2. Numerical models on ballooning

Various numerical models have been developed to study clad ballooning. A multi-pin code MATARE has been developed for ballooning transient analysis and to reproduce the flow diversion [79], [80]. The code simulates the deformation of wide regions of a fuel assembly under reflood conditions. It has shown how differences in pin pressure and power also contribute to incoherent ballooning [81]. A high-temperature clad ballooning failure model named BALON2 has been developed to model ballooning, and FRAPTRAN, which is an analytical tool is used to predict the occurrence of clad failure [82]. Alain et al. assessed the safety criteria of reactivity initiated accidents using the code SCANAIR, which features thermal dynamics, structural mechanics until the prediction of the clad failure and the gas behavior modeling [83]. An extended mechanical algorithm for large creep strains was developed and implemented in the TRANSURANUS fuel performance code. A sensitivity analysis was carried out in order to address the effect of a geometry change in the creep flow law [84]. Leridon proposed a burst model which is coupled to a visco-plastic deformation law for Zircaloy at high temperatures [85].

3.4.3. Ballooning as a plastic instability

Ballooning, which is an abrupt local deformation, is a plastic instability. When thin walled metallic cylindrical tubes are subjected to internal pressure, failure may occur when the hoop stress exceeds a certain critical value and result in various types of non-uniform deformation modes [86]. Various theories have been proposed to identify the critical value at which ballooning can initiate [87]. Lin [88], [89] has analyzed ballooning deformation of internally pressurized tubes and has given the plastic instability criteria for necking of bars and ballooning of tubes. Hill and Hutchinson [90] have done a complete bifurcation analysis including material and geometric instabilities. The material instability leads to shear banding, and the geometric instability can lead to either necking or bulging [86 (cf [91, [92])].

3.4.4. Effect of thermal hydraulics on ballooning

When the coolant flow reduces due to LOCA in thermal reactors or due to LOFA, sodium void etc in fast reactors, there is a local rise in clad temperature which can trigger ballooning and result in permanent deformation or distortion of the clad geometry. Ballooning once occurred poses a severe threat on coolability of blocked regions.

An analytical model was developed based on the COBRA-TF computer code, to simulate the thermo-hydraulic behavior of a water reactor assembly during a LOCA reflood scenario [93]. Claude Grandjean [93] confirms the absence of penalizing temperatures for short blockages and moderate blockage ratios (<60%), and corroborates the fact that significant increase in blockage wall temperatures, may threaten the coolability of the blockage. Ardron and Fairbaurn developed a method for predicting the temperature response of clad at the constricted part of an obstruction and observed that strong axial temperature gradients will develop within a blockage if a significant clad strain occurs over an appreciable distance [94]. The effect of fuel relocation on the reflood phenomena in a partially-blocked rod bundle has been experimentally studied and compared with the numerical predictions from the MARS code [95], [96].

3.4.5. Ballooning in thermal reactors

During a LOCA, which results due to a rupture in the primary heat transport system including the headers, feeders, coolant tubes, etc., depressurization occurs in a few seconds, depending on the break size. Rapid coolant depressurization results in a decrease in heat removal from the fuel with a consequent increase in cladding temperature and an increase in the internal to the external pressure differential across the clad wall. This pressure differential leads to increased biaxial stresses in the cladding. With time, the combination of hoop stress and high temperature reaches a point beyond which the fuel cladding begins to increase in diameter and then deform locally, which is known as ballooning [97].

Ballooning of clad can result in partial blockage of the coolant channel which may impair further heat transfer when emergency core cooling system comes into operation [98]. Besides, the pressure tube (which houses the fuel pins) is also expected to sag and balloon coming into contact with the calandria tube [99]. A considerable international effort has been spent in investigating ballooning in thermal reactors [100], [101], [102], [103], [104], [105], [106], [107], but there is no literature available on ballooning in fast reactor clad tubes.

3.4.6. Ballooning in fast reactors in comparison with thermal reactors

Ballooning in fast reactors is quite distinct when compared to that in thermal reactors. The failure mechanisms of the Zr-based alloys, which are the clad material in thermal reactors, are strongly influenced by time and temperature dependent creep and oxidation, while Fe-based alloys used as a clad material in fast reactors is not dominated by the thermal creep. The later demonstrated around 10 % higher temperature (and thus time to burst) at the onset of burst, in comparison to the former [108]. Thus the onset of clad ballooning in fast reactors is not expected at lower burn-up. Nevertheless, when an increase in the burn-up of the fuel is envisaged, the higher power generation and the tight packing of fuel pins, in combination with severe thermal transients can have a synergistic effect on the fuel clad leading to clad ballooning. Though the cause for ballooning in fast reactors is different from that of thermal reactors, the consequences are equally damaging and need intensive research to prevent it.

3.4.7. Effect of irradiation on structural material

Due to the intense neutron flux and high temperature that prevails in a nuclear reactor, core structural materials in a fast reactor are prone to dimensional instability due to void swelling, irradiation creep and change in material properties like irradiation hardening and embrittlement [109]. Irradiation-induced loops and voids result in significant hardening accompanied with losses in both uniform and total elongation [110].

Figure 3.3 shows the microstructural changes in 20 % cold worked 316 SS wrapper irradiated in a 40MWt/13MWe FBTR at Kalpakkam, India. $\Delta V/V$ %

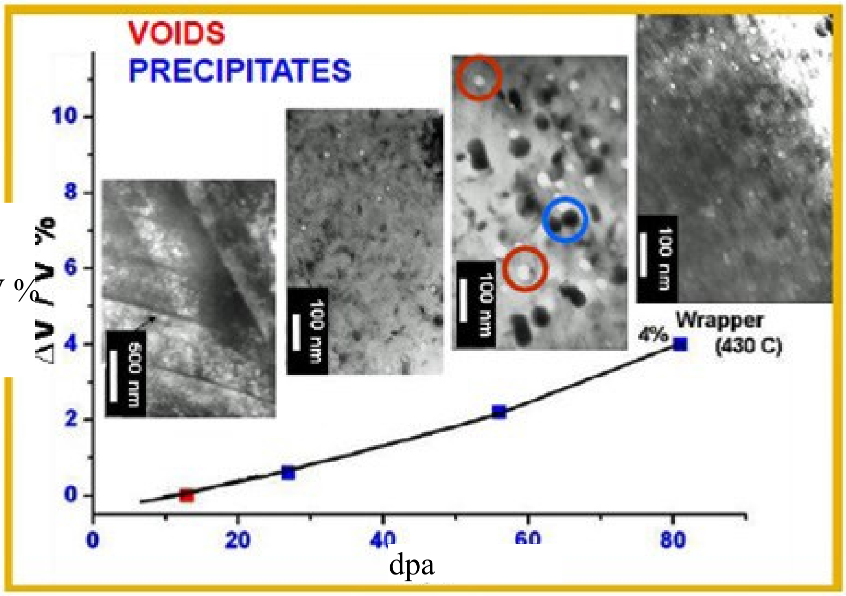

Figure 3.3 Structure at various dpa on the swelling curve [111]

The hexagonal wrapper is subjected to different displacement damages up to a maximum of 83 dpa at an operating temperature of about 673 K. Density measurements on the specimen from various portions of the irradiated wrapper showed a peak volumetric swelling of about 3.5 % at a damage of 83 dpa. Transmission electron microscopy studies showed extensive void formation at 40 dpa and beyond in addition to extensive precipitation and formation of dislocation loops [69]. Nanoscale precipitation of TiC promotes the void swelling resistance in alloy D9 in the austenite matrix [70].

Takehiko, et.al., observed that the unirradiated fuel pins fail after ballooning late in the transient when the cladding temperature was high. The used (irradiated) fuel clad tube fails early in the transient with brittle fracture [113]. Hence, out of pile tests are conducted in the present investigation because ballooning in fuel clad is expected in the beginning of life, when the material is ductile. The material becomes brittle due to irradiation at the end of the life (in reactor), which results in clad tube rupture.

3.5. Intention of the present work

This chapter presents the detailed literature review on thermal transients in reactors, thermo-mechanical models, and effect of heating rate on fuel clad tubes. Literature survey on start-up and shutdown of reactors suggests that the reactor components and the fuel clad tubes are the critical components during the transients considered, and need to be investigated. Many thermo-mechanical models have been developed for various applications, but a numerical model for partially immersed components for simulating the thermo-mechanical behavior at the free level interface location is not available in literature. Ballooning is one of the failure modes that can take place at certain combinations of heating rates and pressure. Ballooning in thermal reactor clad and pressure tubes have been extensively researched, but that in fast reactor has not been addressed. Nevertheless, due to the high burn-up and narrow coolant flow path between the fuel pins in fast reactors, the onset of ballooning at various combinations of pressure and heating rate needs to be investigated to ensure that ballooning does not take place during the reactor operating conditions. These gap areas were identified from the literature survey and formed the basis and objective of the Ph. D thesis. The structural damage in reactor components during shutdown of the reactor, and development of a numerical model for partially immersed components have been discussed in the next chapter.

References

[43] Chen Juan, Zhou Tao, Hou Zhousen, Cheng Wanxu. Thermo-hydraulic analysis for SCWR during power-raising phase of startup. Nuclear Science And Techniques, 23, Issue 3 (2012) 181 –192 .

[44] Sutanto and Yoshiaki Oka. Time dependent start-up thermal analysis of a Super Fast Reactor. Nuclear Engineering and Design 263 (2013) 129– 137.

[45] Samira Kashi, Nader Maleki Moghaddam, Majid Shahriari. A spatial kinetic model for simulating VVER-1000 start-up transient. Annals of Nuclear Energy, 38 (2011) 1300–1309.

[46] Gy Heygi, A. Keresztúri, Cs. Maráczy, Gabor Hordósy, E. Temesvári. Simulation of start-up measurements with the KIKO3D code and its application for determining the scram rod worth uncertainty in the VVER-440 reactor. Annals of Nuclear Energy, 38 (2011) 694–704.

[47] Lynn E.Weaver. Reactor control. Nuclear Power Safety, (1976), Pages 169-208.

[48] Dante M. Zangirolami, Amir Z. Mesquita, Andréa V. Ferreira. Evaluation of power behavior during startup and shutdown procedures of the IPR-R1 triga reactor. 2009 International Nuclear Atlantic Conference - INAC 2009 Rio de Janeiro,RJ, Brazil, September27 to October 2, (2009), ISBN: 978-85-99141-03-8.

[49] Design of the Reactor Core for Nuclear Power Plants, IAEA Safety Standards for protecting people and the environment, Safety Guide No. NS-G-1.12 (2004).

[50] B. L. Eyre, B. Tomkins, J. D. Lewins, M. Kohler, J. Spence, K. Q. Bagley and D. Broadley. Structural Integrity of Fast Reactor Components. Philosophical Transactions of the Royal Society of London. Series A, Mathematical andPhysical Sciences, Vol. 331, No. 1619, The Fast-Neutron Breeder Fission Reactor (Jun. 28,1990), pp.419-434.

[51] V.Chaudhry, A.Kumar, S.M.Ingole, A.K.Balasubramanian, U.C.Muktibodh. Thermo-mechanical Transient Analysis of Reactor Pressure Vessel. Procedia Engineering, Volume 86, (2014), Pages 809-817.

[52] Marchertas. Thermo-mechanical analysis of concrete in LMFBR programs. Nuclear Engineering and Design, Volume 82, Issue 1, 1 October (1984), Pages 47-62.

[53] F. Montero-Chacón, S. Zaghi, R. Rossi, E. García-Pérez, I. Heras-Pérez, X. Martínez, S. Oller, M. Doblaré. Multiscale thermo-mechanical analysis of mulit-layered coatings in solar thermal applications. Finite Elements in Analysis and Design, Volume 127, May (2017), Pages 31–43.

[54] Walter Villanueva, Chi-Thanh Tran1, Pavel Kudinov. Coupled thermo-mechanical creep analysis for boiling water reactor pressure vessel lower head. Nuclear Engineering and Design, Volume 249, August (2012), Pages 146–153.

[55] Rosy Sarkar, Kulbir Singh, S. Jalaldeen, K. Velusamy and P. Selvaraj. Design and life assessment of inner vessel for FBR-1&2. Transactions of the Indian Institute of Metals, March (2016), Volume 69, Issue 2, pp 543–547. doi:10.1007/s12666-015-0778-3.

[56] Lin Qiliang, Chen Fangliang, Yin Huiming. Experimental and theoretical investigation of the thermo-mechanical deformation of a functionally graded panel. Engineering Structures, Volume 138, 1 May (2017), Pages 17–26.

[57] Albert Noumowé, Rafat Siddique, Guillaume Ranc. Thermo-mechanical characteristics of concrete at elevated temperatures up to 310 °C. Nuclear Engineering and Design, Volume 239, Issue 3, March (2009), Pages 470–476.

[58] Mustapha Boumhaout, Lahcen Boukhattem, Hassan Hamdi, Brahim Benhamou, Fatima Ait Nouh. Thermomechanical characterization of a bio-composite building material: Mortar reinforced with date palm fibers mesh. Construction and Building Materials, Volume 135, 15 March (2017), Pages 241–250.

[59] P. Vidal, L. Gallimard, I. Ranc, O. Polit. Thermal and thermo-mechanical solution of laminated composite beam based on a variables separation for arbitrary volume heat source locations. Applied Mathematical Modelling, volume 46, June (2017), pages 98–115.

[60] Zhi Yong Ai, Zhen Zhao, Lu Jun Wang. Thermo-mechanical coupling response of a layered isotropic medium around a cylindrical heat source. Computers and Geotechnics, Volume 83, March (2017), Pages 159–167.

[61] Itoh Masaharu, Katayama Masahide, Obata Hideo, Moriya Kouki and Murakami Sumio. Introduction of coupled thermomechanical equations into a hydrocode. Nuclear Engineering and Design, Volume 138, Issue 1, 2 November (1992), Pages 117-122.

[62] S.R. Novascone, B.W. Spencer, J.D. Hales, R.L. Williamson. Evaluation of coupling approaches for thermomechanical simulations. Nuclear Engineering and Design, Volume 295, 15 December (2015), Pages 910–921.

[63] Zhiqiang Yang, Junzhi Cui, Yi Sun, Yizhi Liu, Youcai Xiao. A stochastic multiscale method for thermo-mechanical analysis arising from random porous materials with interior surface radiation. Advances in Engineering Software, 104 (2017) 12-27.

[64] I. Özdemir, W. Brekelmans, M. Geers. A thermo-mechanical cohesive zone model. Comput. Mech., 46 (5) (2010), pp. 735–745.

[65] Zhu Yilin, Poh Leong Hien. On an energetic or dissipative isotropic hardening mechanism for thermo-mechanical models in cyclic loading. International Journal of Mechanical Sciences, Volume 122, March (2017), Pages 297–307.

[66] X. Dong, Y. Shin. Coupled thermomechanical multiscale modeling of alumina ceramics to predict thermally induced fractures under laser heating. J. Am. Ceram. Soc., 98 (3) (2015), pp. 920–928.

[67] Syed Danial Ali, Jongmin Kim. A numerical simulation of thermo-mechanical behaviour of the intact rock in response to the Borehole Heater Test. Annals of Nuclear Energy, Volume 101, Pages:301-311, March (2017).

[68] Jun Hwan Kim, Myoung Ho Lee, Yong Hwan Jeong, Jae Gwan Lim. Behavior of zirconium fuel cladding under fast pressurization rates. Nuclear Engineering and Design, 238 (2008) 1441–1447.

[69] M. Ragheb. Internet, (2010) mragheb.com/Clad%20Ballooning%20Accident.pdf.

[70] Rosy Sarkar. Investigation of structural integrity of fuel cladding under normal and extreme loading conditions. MTech thesis, HBNI (2012).

[71] Luca Ammirabile. Coupled Mechanical-Thermohydraulic Multi-pin Deformation Analysis of a PWR Loss of Coolant Accident. A Thesis submitted for the degree of Doctor of Philosophy at the University of London and Diploma of Membership of the Imperial College London. September (2003).

[72] M. Chung Hee. Fuel behavior under Loss-Of-Coolant accident situations. Nuclear Engineering and Technology, vol.37, No.4, (2005).

[73] U.K. Viswanathan, K. Unnikrishnan, Prerna Mishra, Suparna Banerjee, S. Anantharaman, D.N. Sah. Behaviour of irradiated PHWR fuel pins during high temperature heating. Journal of Nuclear Materials, 383 122–127, (2008).

[74] D. O. Hobson. Ductile-brittle behavior of Zircaloy fuel cladding. Proc. ANS Topical Mtg. on Water Reactor Safety, Salt Lake City, March 26, pp. 274-288, (1973).

[75] H.J. Neitzel, H.E. Rosinger. The development of a burst criterion for zircaloy fuel cladding under LOCA conditions. Institute for Reaktorbauelemente, (1980).

[76] Jun Hwan Kima, Myoung Ho Lee, Yong Hwan Jeong , Jae Gwan Lim. Behavior of zirconium fuel cladding under fast pressurization rates. Nuclear Engineering and Design 238 (2008) 1441–1447.

[77] Luca Ammirabile and S.P. Walker. Analysis of the MT3 clad ballooning reflood test using the multi-rod coupled MATARE code. Nuclear Engineering and Design 240(5):1121-1131 · May (2010). DOI: 10.1016/j.nucengdes.2009.12.038.

[78] Zoltán Hózer, Csaba Gyuőri, Márta Horváth, Imre Nagy, László Maróti, Lajos Matus, Péter Windberg & József Frecska. Ballooning Experiments with VVER Cladding. ISSN: 0029-5450, (2017).

[79] Luca Ammirabile, Simon Walker. Large-break loca studies: computational analysis of clad ballooning and thermohydraulics in a PWR. International Conference Nuclear Energy for New Europe (2002), September 9-12.

[80] Luca Ammirabilea, Simon P. Walker. Analysis of the MT-3 clad ballooning reflood test using the multi-rod coupled MATARE code. Nuclear Engineering and Design 240 (2010) 1121–1131.

[81] Luca Ammirabile and Simon P. Walker. Dynamic ballooning analysis of a generic PWR fuel assembly using the multi-rod coupled MATARE code. Nuclear Engineering and Design 268 (2014) 24– 34.

[82] K.J. Geelhood, W.G. Luscher, C.E. Beyer, J.M. Cuta Pacific N. FRAPTRAN 1.4: A Computer Code for the Transient Analysis of Oxide Fuel Rods (2011).

[83] Alain Moal, Vincent Georgenthum, Olivier Marchand. SCANAIR: A transient fuel performance code Part One: General modelling description. Nuclear Engineering and Design, Volume 280, December (2014), Pages 150-171.

[84] Valentino Di Marcello, Arndt Schubert, Jacques van de Laar, Paul Van Uffelen. The TRANSURANUS mechanical model for large strain analysis. Nuclear Engineering and Design, Volume 276, September (2014), Pages 19-29.

[85] A. Leridon. One and two dimension analysis of the clad ballooning in pressurized fuel rods. Nuclear Engineering and Design 61 (1980) 143-149.

[86] Anurag Gupta. Ballooning in fuel clads: A study in the constitutive theory and stability of thermoplastic response. IGCAR – IIT Kanpur Collaborative Project, (2018).

[87] R. Hill. A general theory of uniqueness and stability in elastic-plastic solids. Journal of Mechanics and Physics of Solids, 6:236-249, (1958).

[88] E. I. H. Lin. Analysis of the ballooning deformation of an internally pressurized thin-wall tube during fast thermal transients. In 4th International Conference on Structural Mechanics in Reactor Technology, San Francisco, CA, (1977).

[89] I. H. Lin, J. P. Hirth, and E. W. Hart. Plastic instability in uniaxial tension tests. Acta Metallurgica, 29:819-827, (1981).

[90] R. Hill and J. W. Hutchinson. Bifurcation phenomenon in the plane tension test. Journal of Mechanics and Physics of Solids, 23:239-264, (1975).

[91] M. Larsson, A. Needleman, V. Tvergaard, and B. Storakers. Instability and failure of internally pressurized ductile metal cylinders. Journal of Mechanics and Physics of Solids, 30:121-154, (1982).

[92] R. Hill, S. S. Hecker, and M. G. Stout. An investigation of plastic flow and differential work hardening in orthotropic brass tubes under fluid pressure and axial load. International Journal of Solids and Structures, 31:2999-3021, (1994).

[93] Claude Grandjean. Coolability of blocked regions in a rod bundle after ballooning under LOCA conditions. Main Findings From A Review Of Past Experimental Programmes. Nuclear Engineering and Design, Elsevier, 237, pp. 1872-1886, (2007).

[94] K.H Ardon, S.A Fairbaurn. A method of predicting the temperature response of ballooning fuel rod cladding for PWR LOCA conditions. Nuclear Engineering and Design, Volume 72, Issue 3, 1 October (1982), Pages 391–409.

[95] Byoung Jae Kim, Jongrok Kim, Kihwan Kim, Sung Won Bae, Sang-Ki Moon. Effects of fuel relocation on reflood in a partially-blocked rod bundle. Nuclear Engineering and Design,Volume 312, February (2017), Pages 239-24.

[96] J.J. Jeong, K.S. Ha, B.D. Chung, W.J. Lee. Development of a multi-dimensional thermal-hydraulic system code. MARS 1.3.1. Ann. Nucl. Energy 26, 1611–1642, (1999).

[97] M.E. Markiewicz, F.J. Erbacher. Experiments on ballooning in pressurized and transiently heated Zircaloy-4 tubes. vol 43 of Kernforschungszentrum Karlsruhe, (1988).

[98] K. Sawarn Tapan, Banerjee Suparna, K.M Pandit, S. Ananatharaman. Study of clad ballooning and rupture behavior of fuel pins of Indian PHWR under simulated LOCA condition. Nuclear Engineering and Design, 280 (2014) 501-510.

[99] A.K. Dureja, D.N. Pawaskar, P. Seshu, S.K. Sinha, R.K. Sinha. Experimental determination of thermal contact conductance between pressure and calandria tubes of Indian pressurised heavy water reactors. Nuclear Engineering and Design 284, 60–66, (2015).

[100] R.S.W. Shewfelt. The ballooning of fuel cladding tubes: theory and experiment. Res Mechanica, 25:261-294. (1988).

[101] H.M. Chung, A.M. Garde, T.F. Kassner. Deformation characteristics of Zircaloy cladding in vacuum and steam under transient heating conditions. In: Summary Report, NUREG/CR-0344 ANL-77-31, (1978).

[102] S. Sagat, H.E. Sills, J.A. Walsworth. Deformation and failure of Zircaloy fuel sheaths under LOCA conditions. American Society for Testing and Materials, pp.709-733, ASTM STP 824 (1984).

[103] F. Erbracher, H.J. Neitzel, K. Wiehr. Studies on Zircaloy fuel clad ballooning in a Loss-of-Coolant Accident-Results of Burst Tests with indirectly heated fuel rod simulators. American Society for Testing and Materials pp.429-446, ASTM STP 681 (1979).

[104] C. Grandjean. A state of the art review of past programs devoted to fuel behaviour under LOCA conditions—part 1: clad swelling and rupture; assembly flow blockage. IRSN/DPAM/SEMCA -313, http://net-science.irsn.org/, (2005).

[105] C. Grandjean. A state of the art review of past programs devoted to fuel behaviour under LOCA conditions— part 2: impact of clad swelling upon assembly cooling. IRSN/DPAM/SEMCA -183, http://net-science.irsn.org/, (2006).

[106] C. Grandjean and G. Hache. A state of the art review of past programs devoted to fuel behaviour under LOCA conditions—part 3; cladding oxidation, resistance to quench and post quench loads. IRSN/DPAM/SEMCA -093, http://net-science.irsn.org/, (2008).

[107] D.N Sah, U.K. Viswanathan and S. Anantharaman. Study of creep deformation of irradiated zircaloy cladding by isothermal heating of irradiated PHWR fuel pins in temperature range 700 ℃ – 900 ℃, Transactions of the Indian Institute of Metals, vol 63, Issues 2-3, pp. 467-471 (2010).

[108] P. Massey Caleb, A. Terrrani Kurt, N. Dryepondt Sebastine, A. Pint Bruce. Cladding burst behavior of Fe-based alloys under LOCA. Journal of Nuclear Materials 470 (2016) 128-138.

[109] F.A. Garner. Comprehensive nuclear materials, in: Rudy Konings (Ed.), Radiation Damage in Austenitic Steels, Elsevier, pp. 33-95, (2012).

[110] S.I. Porollo, A.M. Dvoriashin, Yu.V. Konobeev, A.A. Ivanov, S.V. Shulepin, F.A. Garner. Microstructure and mechanical properties of austenitic stainless steel 12X18H9T after neutron irradiation in the pressure vessel of BR-10 fast reactor at very low dose rates. Journal of Nuclear Materials 359 (2006) 41–49.

[111] C.N. Venkiteswaran, V. Karthik, Parameswaran Padmanabhan, N. G. Muralidharan, V. AnandaRaj, Saroja Saibaba, Viggneshwar Venugopal, M. Vijayalakshmi, K. V. Kasi Viswanathan, Baldev Raj, Jeremy T. Busby, Brady Hanson. Study of Microstructure and Property Changes in Irradiated SS316 Wrapper of Fast Breeder Test Reactor. J. ASTM International 6(7) (2009).

[112] Baldev Raj, Divakar Ramachandran, M. Vijayalakshmi. Development of cladding materials for sodium-cooled fast reactors in India. Transactions of the Indian Institute of Metals 62(2):89-94 (2009).

[113] Takehiko Nakurama, Toyoshi Fuketa, Tomoyuki Sugiyama and Hideo Sasajima. Failure thresholds of high burnup BWR fuel rods under RIA Conditions. Japan Atomic Energy Research Institute, Tokai-mura, Ibaraki 319-1195, (2004).

Web references

[7] https://www.nrc.gov/reading-rm/basic-ref/glossary/transient.html#:~:text=A%20change%20in%20the%20reactor,or%20(3)%20accident%20conditions.

Chapter 4

Effect of Crash Cooling on Reactor Components

4.1. Background

The gap areas from literature have been identified in the previous chapter. In this chapter, a numerical model has been developed to simulate the thermo-mechanical behavior of partially immersed components. The generalized numerical model can be used to study the physics of partially immersed components of any system. The developed model has been used to obtain the thermal stresses at free level locations of sodium, during shutdown of the reactor. Detailed studies for various shutdown schemes have been carried out to arrive at a simplified shutdown scheme. The various shutdown schemes and its problem statement is illustrated in section 4.2.

4.2. Problem statement

4.2.1. Shutdown schemes

In sodium-cooled fast reactors, during emergency condition, the control rods are dropped instantaneously to shutdown the reactor. It is known as SCRAM. Following such a reactor SCRAM, the OGDHR comes into operation to remove the decay heat of the core [114]. There are two options possible for the decay heat removal, following a SCRAM. One option is to immediately switch over to OGDHR. This option will require a large capacity OGDHR system as the decay power is large just after the SCRAM. This has economic implications and it calls for a complex design of the pumps used in OGDHR system. Further, if a lower capacity OGDHR system is deployed, the hot pool temperature will shoot up initially due to its lower capacity and the pool temperature will start to decrease whenever the decay heat decreases below the OGDHR system capacity. This system is cost effective when compared to the larger capacity system. Nevertheless, the initial increase in sodium temperature is not preferable due to the structural damage considerations.

The second option, which is the existing scheme, is to use the main condenser and the boiler feed pump to bring down the sodium temperature to the saturation temperature at the corresponding pressure (I-phase) and thereafter deploy OGDHR system for controlled cooling to the cold shutdown condition (II-phase). In such a design, as the sodium temperature and hence the water temperature decreases, the pressure of the steam generator reduces. For example, the pressure reduces from 16.7 MPa at normal condition to 1.5 MPa for cold shutdown condition [115]. This reduces the onus on the OGDHR capacity but still makes the design of seal in the recirculation pump a critical challenge due to its operation at varying pressure.

The possibility of making the future design of the pool type fast reactors simple by designing a highly reliable OGDHRS has been studied. It is envisaged to eliminate control cooling and to deploy OGDHRS only after reaching cold shutdown condition to avoid its operation at varying pressure. This proposal will require a lower capacity OGDHR system and a constant pressure recirculation pump, making the design simple and reliable. The temperature evolution of the hot and cold pool temperatures for the proposed scheme is given in Figure 4.1[116].

In the proposed shutdown scheme, it is envisaged to cool the sodium from 823 K to 453 K (includes I-phase and II-phase of cooling) using main condenser path, and deploy OGDHR after reaching cold shutdown condition. During the phase when the reactor systems are at high temperature (820 K), the cool down takes place at a high rate (~480 K/h) and subsequently, when the reactor systems are at low temperature (623 K), the cool down is performed at lower rate (100 K/h), when main condenser is used for cool down. It may be noted that I-phase and II-phase of cooling have been defined for better understanding of the problem. I-phase of cooling is to bring down the primary sodium temperature from 823 K to 623 K. II-phase of cooling is to bring down the primary sodium temperature from 623 K to 453 K.

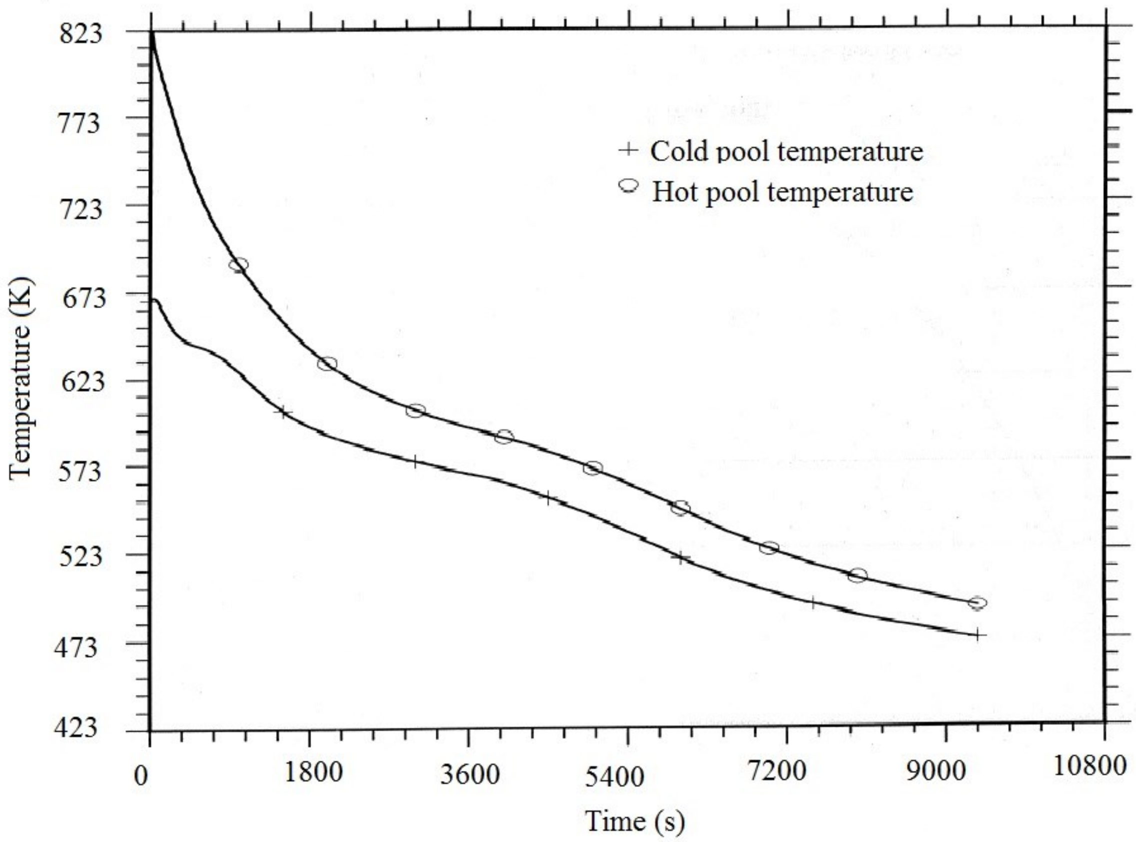

Figure 4.1 Evolution of hot and cold pool temperature following SCRAM in the case without the deployment of OGDHRS [116]

A simplified temperature profile of sodium cooling with the existing and proposed schemes is shown in Figure 4.2. The I-phase of cooling is the same in both the schemes. In the II-phase, controlled cooling is done until cold shutdown at 20 K/h in the existing scheme, whereas the proposal to use main condenser for cooling of hot pool sodium temperature from 623 K to 453 K leads to a maximum cooling rate of 100 K/h.

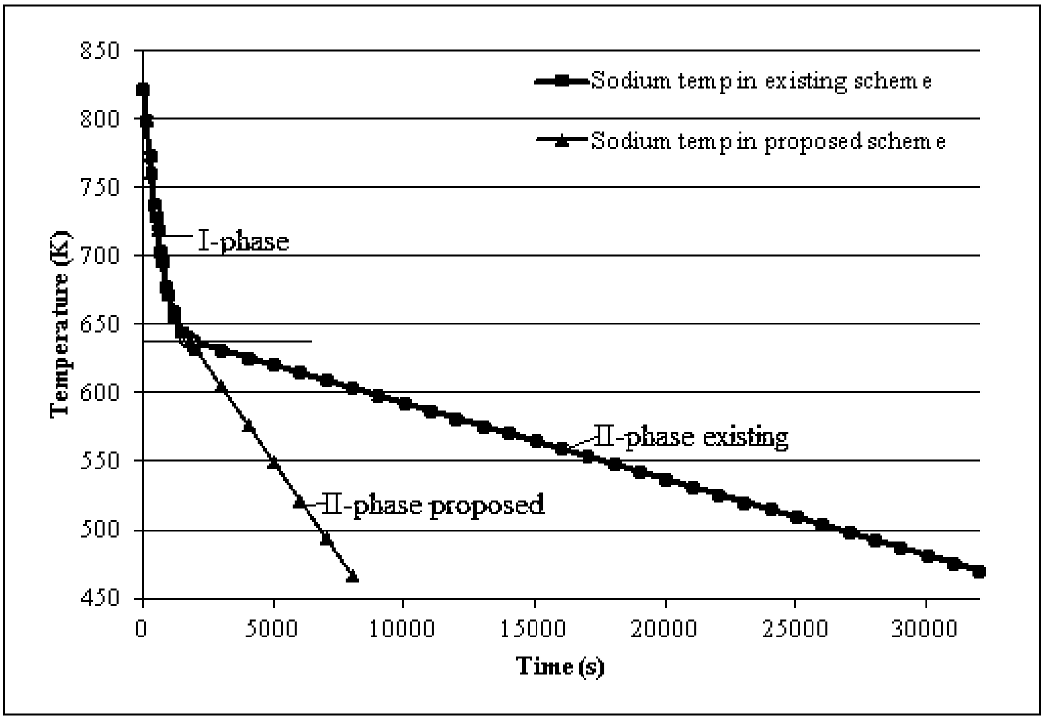

Figure 4.2 Cooling rate of sodium in existing and proposed schemes

4.2.2. Structural damage

As sodium is a good heat transfer medium with high thermal conductivity, high specific heat and high density, it causes rapid changes in surface temperatures of stainless steel structures during fast transients. This can lead to thermal shock loading on reactor SCRAM and such shock is experienced by all hot pool components [117]. Hence a thermo-mechanical analysis has been carried out in the present chapter to estimate the structural damage caused to the hot pool components during I-phase and II-phase of cooling for both the schemes. The computer code used for the FE analysis of structures of Indian fast reactor components is CAST3M [118]. CAST3M is the latest version of CASTEM, which is in GIBIANE language developed by CEA - Saclay, France.

The critical locations in the hot pool components are broadly classified into two types. One is the junctions and curvatures submerged in sodium, and the other is the locations at the free level interface of sodium and argon gas. The thermo-mechanical analysis of the former is carried out by transient analysis in FE software. Further, the creep-fatigue damage at the junctions is estimated. Nevertheless, for the latter case, the loading conditions are complex due to the rise in sodium level with temperature rise, and the conventional FE software does not have the provision to model this behavior.

The crash cooling transient takes place for 861 cycles during the life time of the reactor. The sodium level falls by 700 mm with a fall in sodium temperature. The mean value of fluctuation and temperature are changing. There is no appropriate provision in the available FE codes to analyze the above discussed behaviour. Efforts have been made for the in-house development of the computational procedure to study the thermo-mechanical behaviour of partially immersed structures during transients.

The numerical model is validated with an analytical model and the overall heat balance equations. The dimensions and loading conditions of PFBR hot pool components such as CP, inner vessel, IHX and PSP standpipe have been considered for the transient analysis. The associated damage of these components for submerged and free level locations has been computed and the results are presented in the subsequent sections.

4.3. Thermo-mechanical analysis at the locations submerged in sodium

When the primary sodium is cooled down at high cooling rates, a thermal shock is experienced by all the hot pool components. The high cooling rate can develop high thermal stresses at the thicker junctions that are immersed in sodium, due to a lower Fourier number and a higher Biot number, which results in higher Fitz number. Thermo-mechanical analysis of various critical locations within sodium with the transient loading, and parametric studies with varying cooling rates and varying thicknesses has been carried out. The details of PFBR and its critical locations are given in Figure 1.5. The primary system components are introduced in section 1.1.7. Three critical locations of the components submerged in sodium have been identified in the analysis and are given below.

i) Control plug-lower stay plate junction

ii) Inner vessel junctions

iii) IHX tubesheets

The maximum stresses at the critical location of each component, and the associated damages are evaluated in the subsequent sections.

4.3.1. Control plug - lower stay plate junction

The CP, which is located right above the core SAs, is a hollow cylindrical shell structure that provides passages and support for the absorber rod drive mechanisms (details in section 1.1.7.1). It consists of a CCP, which forms the bottom end, two intermediate support plates, i.e., LSP and USP. The LSP (20 mm thick) and the CP shell (10 mm thick) junction is submerged in sodium. Thermo-mechanical analysis of the CP-LSP junction (B1 in Figure 1.5) for I-phase of crash cooling, which is to bring down the hot pool temperature from 823 K to 623 K in 25 minutes (1500 s) has been carried out. The temperature contour and the stress contour at the instance where the stresses are maximum are shown in Figure 4.3a and Figure 4.3b respectively.

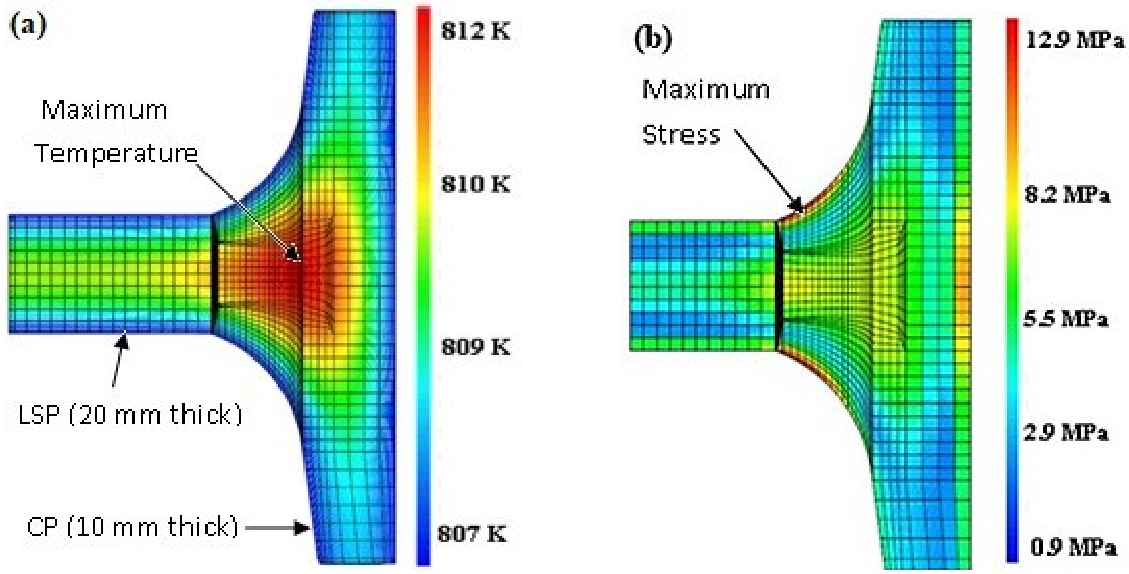

Figure 4.3 CP-LSP junction: a) Temperature contour b) Stress (equivalent) contour

It is observed that the maximum stress developed at the CP-LSP junction due to crash cooling is 12.9 MPa, which is negligible.

4.3.1.1. Parametric study for various cooling rates

In order to study the effect of cooling rate on the stress developed at the bend, a parametric study has been carried out at the CP-LSP junction at various cooling rates. The peak stresses varying with cooling rate are plotted in Figure 4.4.

It may be observed that there is an escalation in the magnitude of the stress when the cooling rate augments. The rationale for this behavior is attributed to the deprival of time for the removal of heat from the inner layers of the component to the surface. This contemplation suggests a need for the study of the effect of thickness of the component on the stress developed.

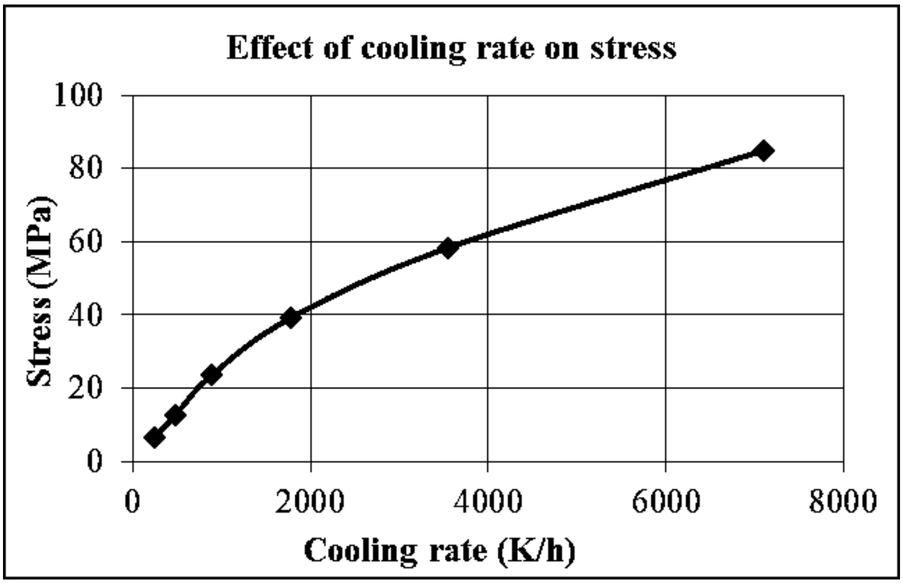

Figure 4.4 Effect of cooling rates on the stress developed

4.3.1.2. Parametric study for various thicknesses of LSP

To study the effect of various thicknesses on the stresses developed, the initial geometry is considered. The thickness of the horizontal portion of the geometry, which is the LSP thickness is varied from 20 mm to 60 mm in steps of 10 mm. The thickness of the control plug (the vertical portion of the geometry), is retained as 10 mm. Thermal analysis has been carried out with the conditions of I-phase of crash cooling. The maximum stresses found in each case are plotted in Figure 4.5.

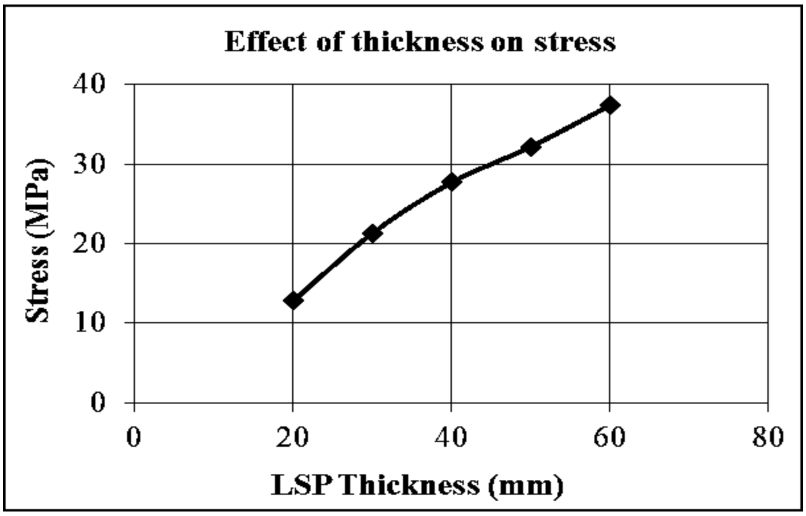

Figure 4.5 Effect of thickness of LSP on the stress developed

The results show that as the thickness of the LSP increases, the stress at the junction escalates. It may be noted that there is a difference in the thicknesses of the LSP and CP, yet the stresses are lower (38 MPa) due to the dissipation of heat from the thinner structure.

4.3.1.3. Parametric study for various thicknesses of LSP and CP

The thicknesses of the LSP and CP are simultaneously varied to investigate the effect of thickness on heat dissipation and thereby stress aggregation. The results are plotted in Figure 4.6.

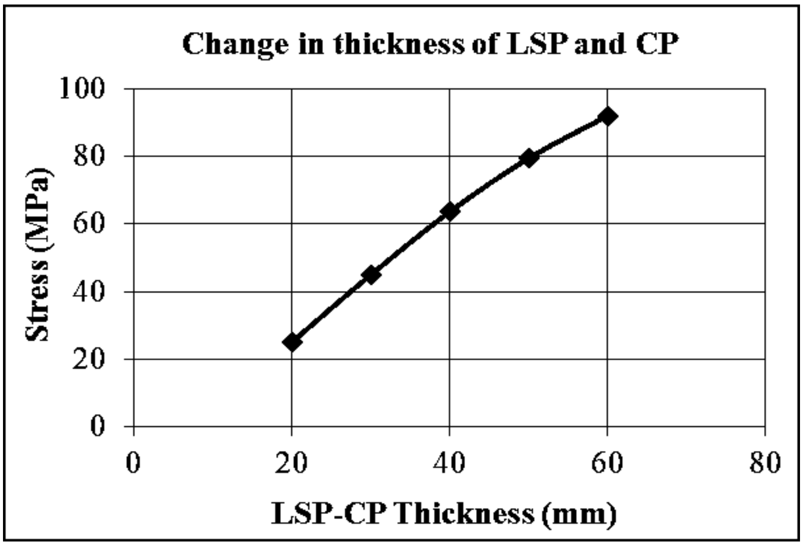

Figure 4.6 Effect of thicknesses of LSP and CP on the stress developed

The trend in the plot is similar to that which is observed in Figure 4.5. Nevertheless, the magnitude of the stress is significantly higher when the thicknesses of LSP and CP are simultaneously altered. The rationale for this upsurge in stress is the widespread heat transfer barriers on both the possible heat dissipation sites.

4.3.2. Inner vessel junctions

Inner vessel separates the hot pool sodium (823 K) and the cold pool sodium (673 K), which entails significant thermal stresses during normal operating conditions, due to the large thermal gradient across the thickness. Two critical locations namely inner vessel upper cylinder-redan curvature and inner vessel-IHX standpipe junction have been analysed below.

4.3.2.1. Inner vessel upper cylinder and redan junction

During shutdown, the effect of crash cooling of hot and cold sodium with distinct cooling rates on either side of the component poses an added damage to the component. This study has been carried out to quantify the additional stress developed in the inner vessel during crash cooling. The curvature connecting the upper cylinder and the conical redan portion (location B2 in Figure 1.5) is modelled using CAST3M (FE software).

Various cases have been analyzed and the results are summarized below.

- When the temperatures on both the sides of the bend are at 823 K, the stresses developed are 1.6 MPa and 6.0 MPa at the cooling rates of 240 K/h and 888 K/h respectively. These stresses are insignificant. The corresponding times in operation are 0.83 h (49.8 min) and 0.225 h (13.5 min).
- When the inner surface of the inner vessel bend is at 823 K and the outer surface at 673 K, and both the surfaces are cooled to 453 K within 25 minutes, maximum stress have been observed, the value being 252 MPa.
- The actual temperature distribution of hot and cold pool temperature varies with height. The inner and outer surface temperatures at the height of the curvature are 815 K and 741 K respectively. Both the pools are cooled to 623 K in 25 minutes and the maximum stress

is 118 MPa. The temperature and stress contours at the instance of maximum stress are shown in Figure 4.7Figure 4.7a and Figure 4.7b respectively.

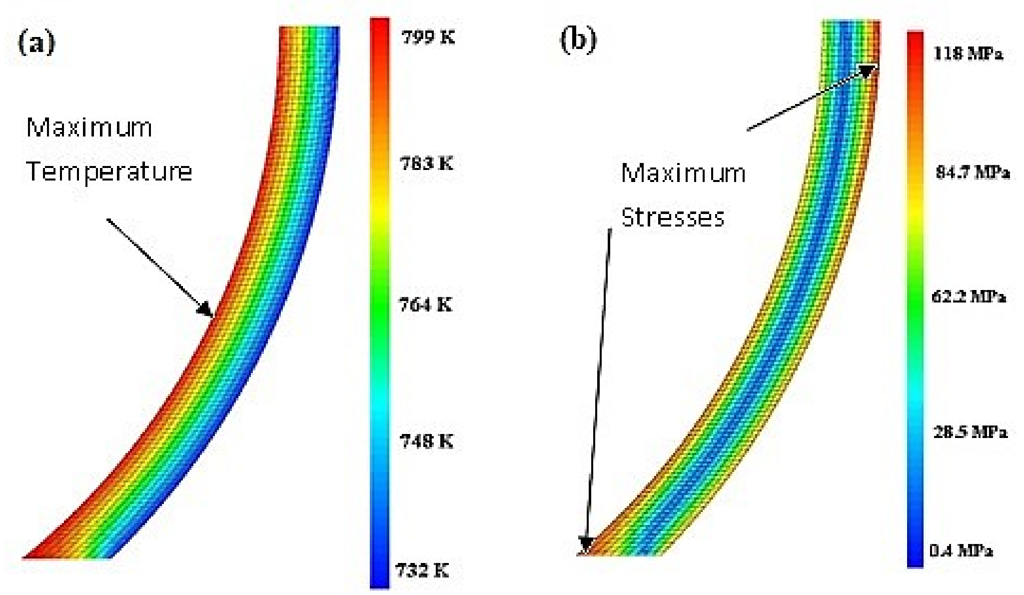

Figure 4.7 Inner vessel curvature: a) Temperature distribution b) stress (equivalent) distribution

The creep and fatigue damage values are 0.088 and 2.35 E-09 respectively.

4.3.2.2. Inner vessel-IHX junction

The most critical junction, which is the inner vessel-IHX junction, location B3 in Figure 1.5 has been analyzed for the I-phase of crash cooling condition. The inner and outer surfaces of the junction are at 815 K and 741 K respectively and are cooled to 623 K in 25 minutes (1500 s). The temperature and stress contours at the instance of maximum stress, i.e., 166 seconds, are shown in Figure 4.8a and Figure 4.8b respectively.

The maximum stress developed is 179 MPa. The creep and fatigue damages at a more conservative value of time spent in creep regime, i.e., 25 minutes (1500 s) (823 K to 623 K), are 0.186 and 2.5 E-04 respectively and at a less conservative time spent in creep regime, i.e., 12 minutes (720 s) (823K to 723 K) are 0.093 and 7.9 E-05 respectively. Creep is significant in SS 316LN material above 723 K. The above results indicated that the creep and fatigue damage caused during crash cooling at various critical locations that are immersed in sodium are acceptable.

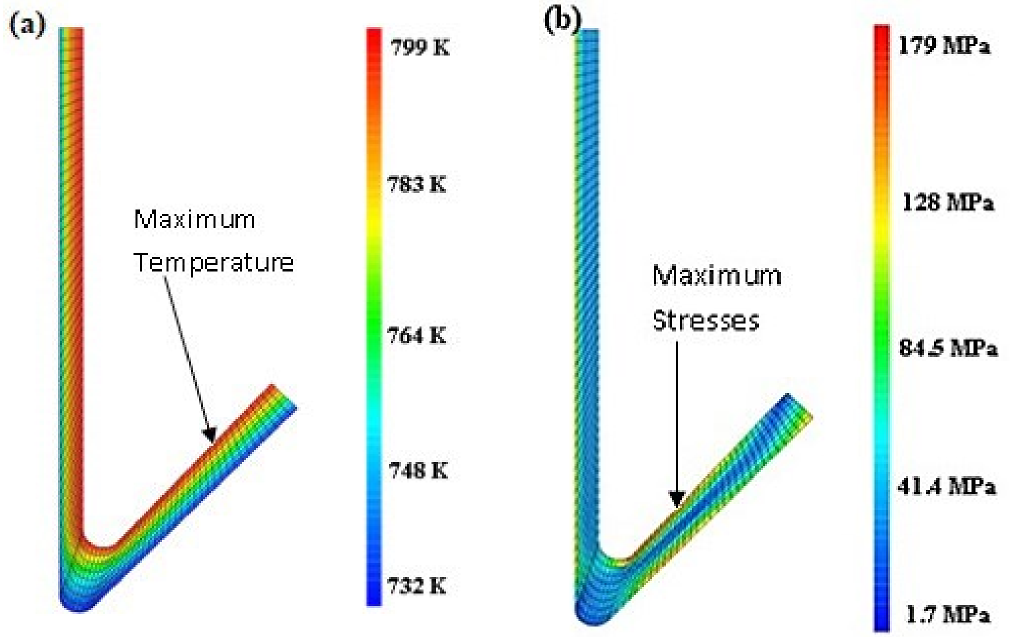

Figure 4.8 Inner vessel-IHX junction: a) Temperature b) equivalent stress contour

4.3.3. IHX tubesheets

IHX tubesheets are submerged in sodium, and are the perspective critical locations. The top and bottom tubesheets of the IHX are annular plates with perforations connected by the tube bundles. The geometrical details of the IHX tubesheets are illustrated in section 1.1.7.3. Thermo-mechanical analysis for the IHX tubesheets has been carried out using ESP concept.

4.3.3.1. Equivalent solid plate concept and application

The FE analysis of the tube sheets has been carried out using ESP concept. As per the ESP, the perforated region of the tube plate is idealized by a homogeneous solid plate, thus taking care of the increased flexibility resulting from perforations. Such an analysis provides the true deflections of the tube plate but the stresses obtained are only exact in the truly solid areas of the structure. In the next step, analysis procedure requires the calculation of physically meaningful stresses in the perforated region of the tube plate from the ESP stress. This is obtained by applying stress multipliers to the ESP stresses. The resulting stresses are called the "true" stresses for the perforated area [121].

A) Perforated region

The stress multipliers are considered pessimistic for 'skin thermal' type loadings which only generate stresses near the surface, where the loading is applied. An alternate method is to multiply the principal stresses calculated on the faces of the ESP by FE analysis, by the stress multiplier K_{skin} to obtain the skin thermal stresses. These skin stresses are then used in equation 4.1, to get the total stressses.

At the perforated region, maximum total stresses at periphery of a hole, at angular position ϕ is given by

$$\sigma_\phi\ (t) = \ Y_1\left(\frac{P}{L}\right)\sigma_1{}^*\ (t) + Y_2\left(\frac{P}{L}\right)\sigma_2{}^*\ (t) \qquad \textbf{4.1}$$

where, σ_1^* (t) – radial stress, σ_2^* (t) – hoop stress, Y_1 and Y_2 from graphs

Y_1=1.2, Y_2=2.25, P=26.61, L=6.8 [120].

B) Junction between perforated plate and solid rim

Total hoop stress is given by

$$\sigma_\phi(t) = K_{r1}\ (\sigma_{1cnt}) + \ K_{r2}\ (\sigma_{2cnt}) \qquad \textbf{4.2}$$

where, σ_{1cnt} – nominal hoop stress, σ_{2cnt} – nominal radial stress, K_{r1} from [121].

C) Rim region

The stress components are extracted from the FE analysis, and the equivalent stress is the vonMises stress or Tresca stress, as defined in sections 2.2.2.3 and 2.2.2.2 respectively.

4.3.3.2. Thermo-mechanical analysis for tubesheets

The temperature evolution of the tubesheets is taken as 823 K in the beginning and 623 K at the end of the I-phase of crash cooling (1500 s). An axi-symmetric model of the IHX top and bottom tube sheets with 2421 elements has been employed for the FE analysis. The IHX is supported at the roof slab. Thus, as the IHX is hanging from the top, the axial displacement has been arrested for simulating the boundary conditions. The FE mesh of the IHX, and the critical locations are shown in Figure 4.9.

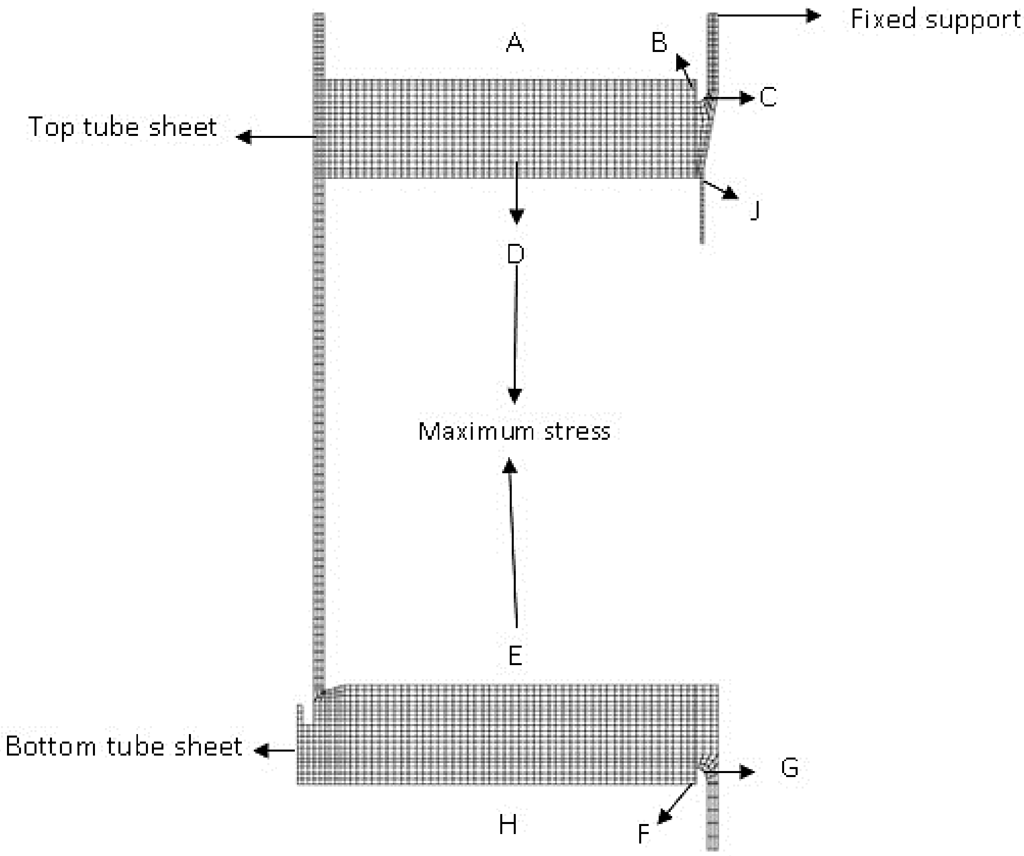

Figure 4.9 FEM mesh of IHX tubesheets

Thermo-mechanical analysis of the IHX top and bottom tube sheets with the above-mentioned loading and boundary conditions has been carried out. It is found that the stresses increased with time. The temperature distribution at the instance corresponding to maximum stress is shown in Figure 4.10. The temperature at the surfaces decrease, corresponding to sodium temperature. However, the decrease in temperature in the interior (bulk) of the tubesheets is lower when compared to that on the surfaces, as shown in Figure 4.10. The temperature is low on the surface, the stresses are maximum, and are tensile in nature. The radial and hoop stress distribution of top tubesheet at the maximum stress instance is shown in Figure 4.11.

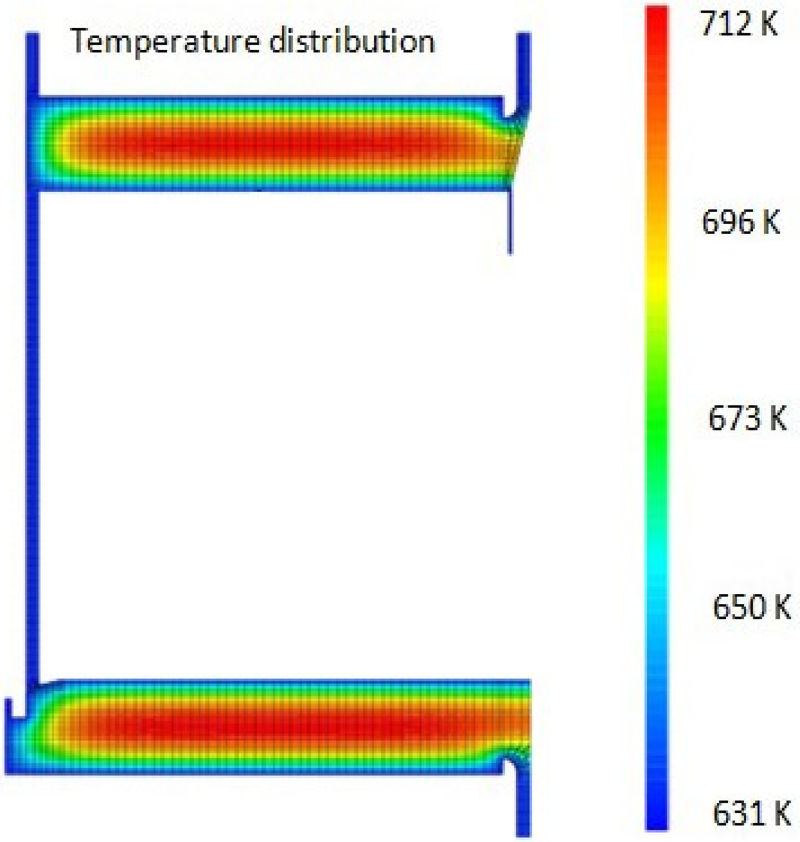

Figure 4.10 Temperature distribution in IHX tubesheets during crash cooling

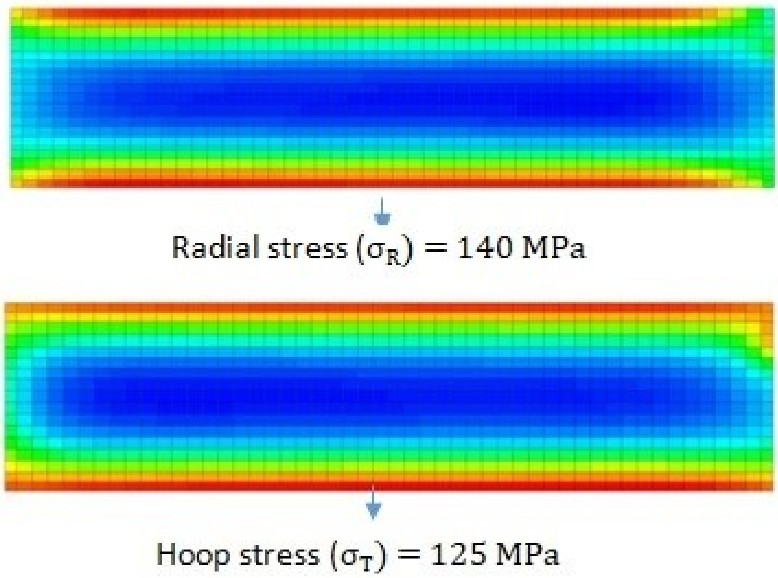

Figure 4.11 Radial and hoop stress in top tubesheet during crash cooling

The elemental stresses are extracted (at all locations of IHX tubesheets) to get the real stresses. This is because, the nodal stresses at interface are very high, due to large differences between elastic properties of perforated regions and solid regions [122].

A) Perforated region

From Figure 4.9, it may be observed that the perforated regions are Locations- A, D, E, and H, where A and D are maximum stress locations at the top and bottom sides of the top tube sheet. Locations- E and H are the maximum stress locations at the top and bottom sides of the bottom tube sheet. The maximum stress locations have been selected after taking many locations and calculating their equivalent stresses.

The radial, hoop and axial stresses are extracted from the FE analysis using ESP concept. The principal stresses extracted from the analysis are multiplied with stress multiplier (K_{skin} = 0.22 at L/P = 0.2555 [120]), to get the skin thermal stresses. Equation 4.1 is used to arrive at the equivalent true stress. The values of Y_1 and Y_2, corresponding to the ligament efficiency of 0.25 are 1.2, and 2.25 respectively [121]. The stresses obtained and the equivalent true stresses are given in Table 4.1.

B) Junction between perforated plate and solid rim

From Figure 4.9, it may be observed that the Locations- B and F are the interface locations, where B is the interface location of the top tube sheet, and F is the interface location of the bottom tube sheet. The radial, hoop and axial stresses (elemental) are extracted from the FE analysis. Equation 4.2 is used to arrive at the equivalent true stress. The K_{r1} and K_{r2} values are obtained at a hole diameter of 19 mm and rim width of (950 – 905) = 45 mm, from [121], and the values are, K_{r1} = 2.35 and K_{r2} = -1.

C) Rim region

From Figure 4.9, it may be observed that the Locations- C, J and G are the maximum stress locations in the solid rim portion, where C is at the top portion of the top tube sheet, J is at the bottom side of the top tube sheet, and G is at the bottom side of the bottom tube sheet. The radial, hoop and axial stresses (elemental) are extracted from the analysis, and the equivalent stress (Tresca) is evaluated. The tresca theory is more conservative than the vonMises theory, and it is safer from the design point of view. Table 4.1 shows the stresses obtained from the analysis and the equivalent stresses at all the locations.

Table 4.1 Stresses in IHX tubesheets during crash cooling

Location		Radial (MPa)	Hoop (MPa)	Axial (MPa)	Equivalent stress (MPa)
Perforated (skin) Eqn-4.1	A	28.60	22.11	0.00	328.98
	D	29.57	26.53	0.00	372.46
	H	27.52	23.21	0.00	333.60
	E	**29.88**	**27.37**	**0.00**	**381.26**
Interface Eqn-4.2	B	-0.2845	133.2	1.82	313.30
	F	0.1543	139.6	3.833	327.91
Solid rim (Tresca)	C	-17.29	107.1	-39.83	146.93
	J	-7.798	142.9	-0.08485	150.70
	G	-6.057	102.2	-68.33	170.53

Table 4.1 shows that the maximum stress is at location-E (perforated region in Figure 4.9). Thermo-mechanical analyses for all the three cases, namely I-phase, II-phase (proposed scheme) and II-phase (existing scheme) have been carried out and the maximum thermal stress values (at location-E) are 386.4 MPa, 86 MPa and 17.2 MPa respectively.

The time spent in creep regime (823 K to 723 K) for 861 cycles is 173 hours. From CCOC for SS316LN at 823 K, min time for creep to occur is 270 h (Figure 2.19). So, creep is neglected. It may be noted that the creep damage is calculated for other locations and components as a conservative approach (considering creep throughout the crash cooling operation). However, the stresses at IHX tubesheets are high and the calculations have been carried out more realistically. The fatigue damage calculations are done with P_{max} = 42 MPa [122]. Fatigue damage values with and without considering the presence of welds at the maximum stress locations are 0.175 and 0.077 respectively and are acceptable (< allowable limit 1). The fatigue damage for the II-phase for both existing and proposed schemes are negligible. Hence it is concluded that the I-phase of crash cooling is governing, and the II-phase of cooling, i.e., to bring down the primary sodium temperature from 623 K to 423 K is not of concern.

4.4. Development of numerical model to simulate the thermo-mechanical behaviour of partially immersed components

4.4.1. Formulation of the numerical model at the free level interface of sodium

It is inferred from the previous section that the damage at the locations immersed in sodium is acceptable. The other critical location, which is the free level interface of sodium has been considered for analysis in this section. During crash cooling, the sodium temperature drops down, which results in a fall in the sodium level. As the sodium level falls, the location that is in sodium environment suddenly comes into argon environment, entailing a high thermal stress at that location.

Numerical discretization adopted for applying the variation in sodium temperature and its level is presented in Figure 4.12. It is basically a solid axisymmetric section of a cylinder. The section is divided into small segments and the inner side of the segments are named as li.1, li.2, and so on. The outer side of the segments are named as lo.1, lo.2, and so on. The material details are given in section 1.1.5.

A simple case where the sodium temperature and sodium level inside and outside the cylinder are the same is illustrated below. The structure is modeled such that li.i is known and can be called for (.i is the number given to the element, as shown in Figure 4.12). The inner and outer surfaces of the length of the structure immersed in sodium are defined as lbi and lbo respectively. The structure above the sodium is in argon gas ambience and the inner and outer surfaces are lti and lto respectively.

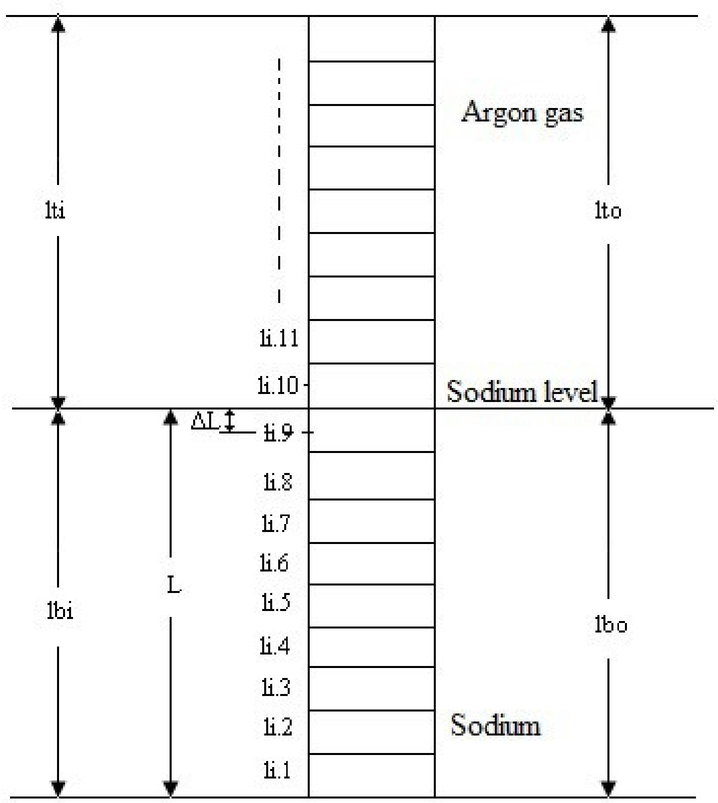

Figure 4.12 Conceptual drawing of the procedure to develop a numerical model

Figure 4.13 shows the process flowchart for the development of the numerical model. An FE code named CAST3M has been used for the in-house development of the computational procedure [118].

To start the iterations, j=0, where j represents time in minutes. The I-phase of crash cooling takes 25 minutes. Hence the number of iterations are taken as 25 and the loop continues 25 times. The initial sodium level is (L). After 1 iteration, the sodium level comes down by (ΔL). If the element (li.i), i.e., li.9 in Figure 4.12 is above the current sodium level (L-j*ΔL), the lengths lbi, lbo, lti and lto are updated as in Figure 4.13 (lti = lti + li.i, lto = lto + lo.i, lbi = lbi - li.i, lbo = lbo - lo.i). The sodium temperature (T_{Na}) and the argon temperature (T_{Ar}) are given for each component according to the respective loading conditions.

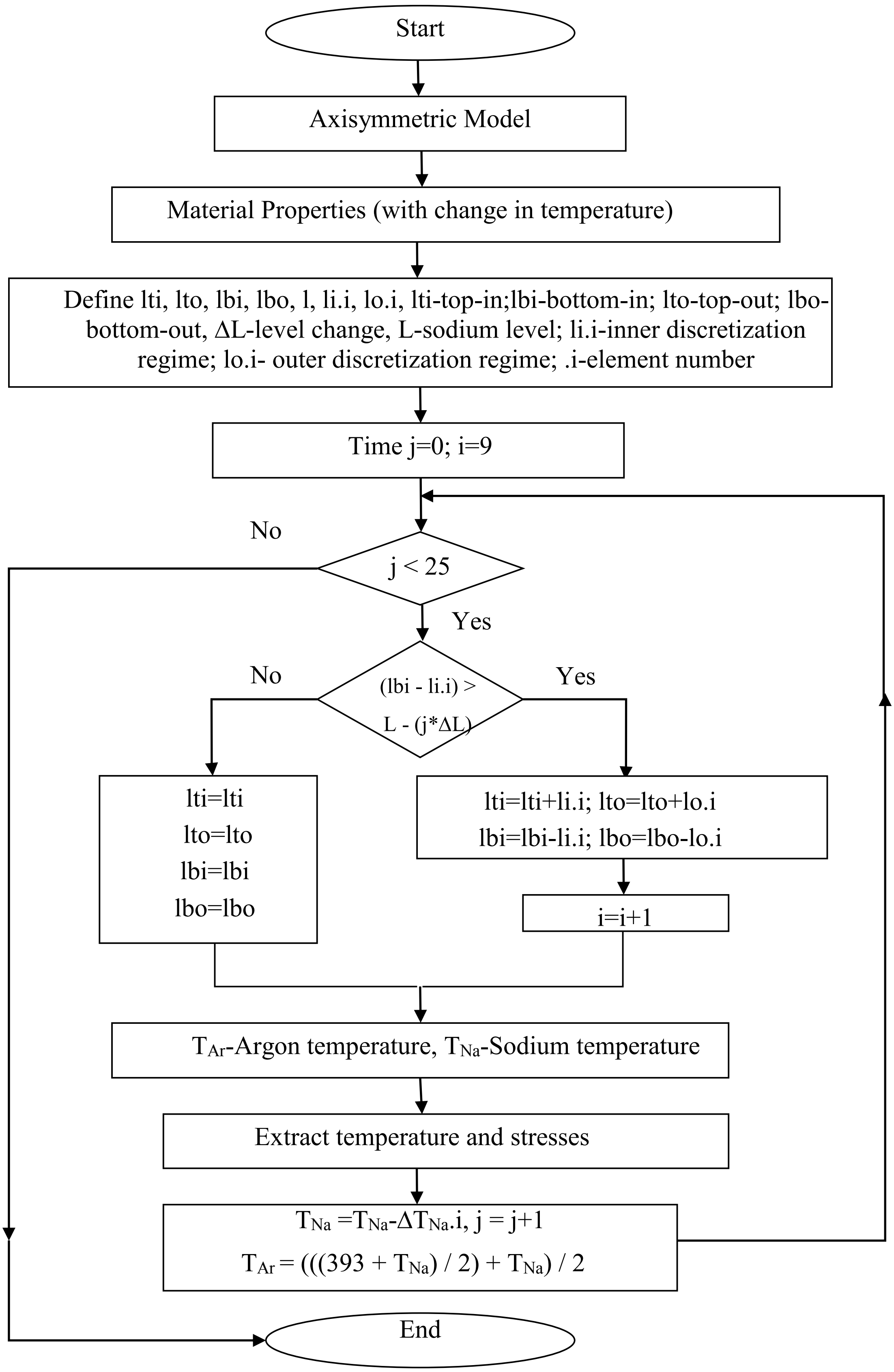

Figure 4.13 Process flow chart for the development of the numerical model

Convection heat transfer is considered, with h = 10 W/m^{2}K at the top region of the component that is surrounded by argon cover gas. Conduction heat transfer is deemed for the bottom portion which is surrounded by sodium, which has a very high heat transfer coefficient.

4.4.2. Stress analysis of crash cooling for control plug using numerical model

Stress analysis of free level location of CP, (F1 in Figure 1.5, CP - USP junction) has been carried out using the developed numerical model. During I-phase, there is a ~400 mm fall in sodium level as shown in Figure 4.14. The loading condition during I-phase, which constitutes the maximum cooling rate is considered for the analysis.

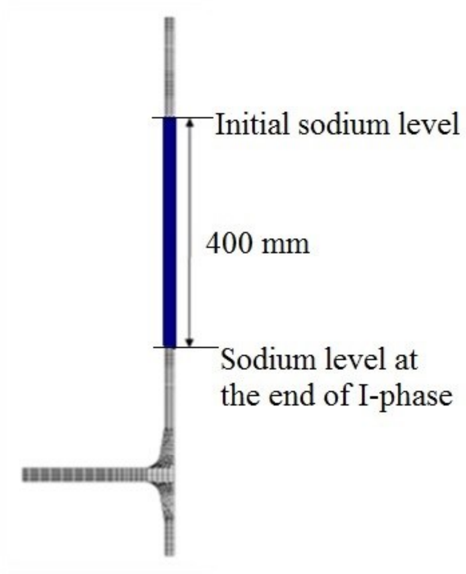

Figure 4.14 Fall in sodium level in CP during I-phase

4.4.2.1. Loading conditions

During I-phase, the sodium level falls by 400 mm and the average rate of change in the sodium level is 16 mm/min. During II-phase, the sodium level drops by 300 mm at 100 K/h. Thus the average rate of change in sodium level is 3 mm/min.

The inner and outer surfaces of the CP (10 mm thick) are in contact with hot pool sodium. The hot sodium (T_{Na}) is encompassed by argon cover gas (T_{Ar}), whose temperature varies with that of the hot pool sodium as per 4.3 [119].

$$T_{Ar} = \frac{\frac{393+T_{Na}}{2}+T_{Na}}{2} \tag{4.3}$$

4.4.2.2. Results from the numerical analysis

Thermo-mechanical analysis of the CP with the above-mentioned loading and boundary conditions has been carried out. The evolution of temperature and equivalent stresses are shown in Figure 4.15 and Figure 4.16 respectively. The horizontal lines in the figures indicate the sodium level.

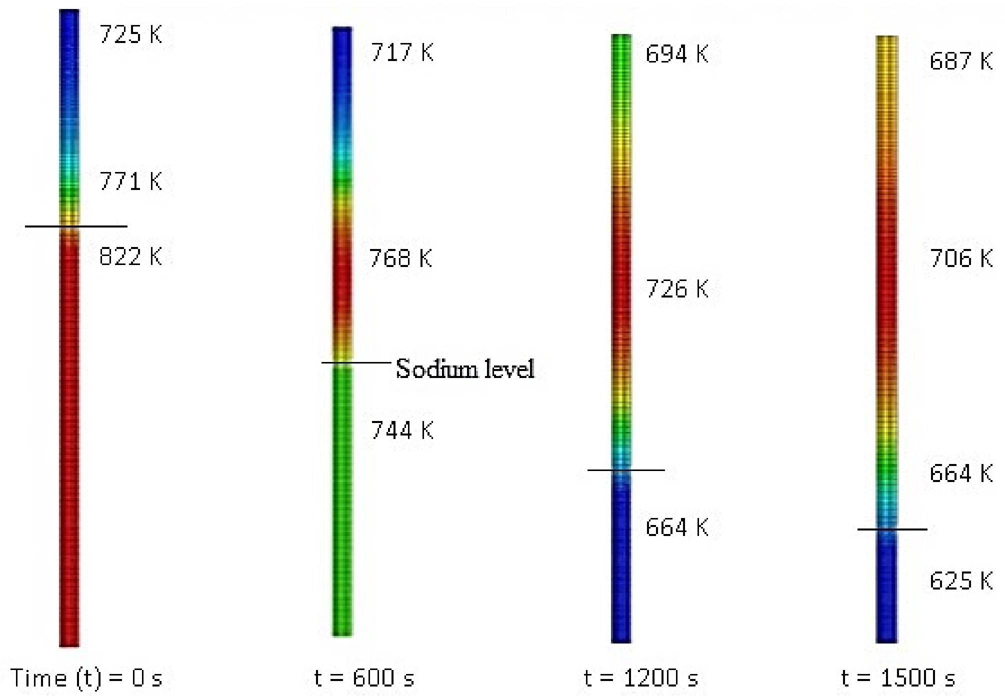

Figure 4.15 Temperature evolution in CP during I-phase shutdown

The maximum stresses are obtained at the location which is at the sodium level at the initial condition (t=0) due to the maximum axial thermal gradient. The stress and temperature distribution curves at the maximum stress location is shown in Figure 4.17.

It is observed from Figure 4.17 that the maximum stress is 98.0 MPa at 823 K, which is in the significant creep temperature. For the conservative creep-fatigue damage estimation, the maximum stress is considered to be at 823 K throughout the time of occurrence of the transient. The creep and fatigue damage calculations are done as per RCC MR-RB [121]. The creep and fatigue damage values are 1.2 E-04 and 2.65 E-14 respectively.

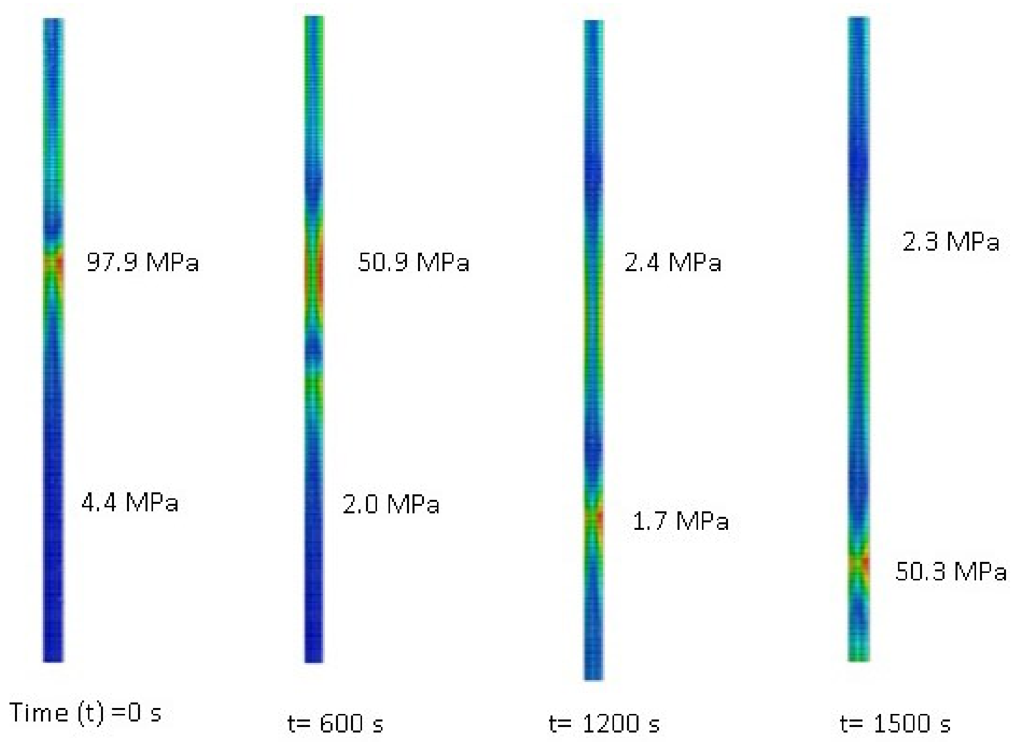

Figure 4.16 Stress evolution in CP during I-phase shutdown

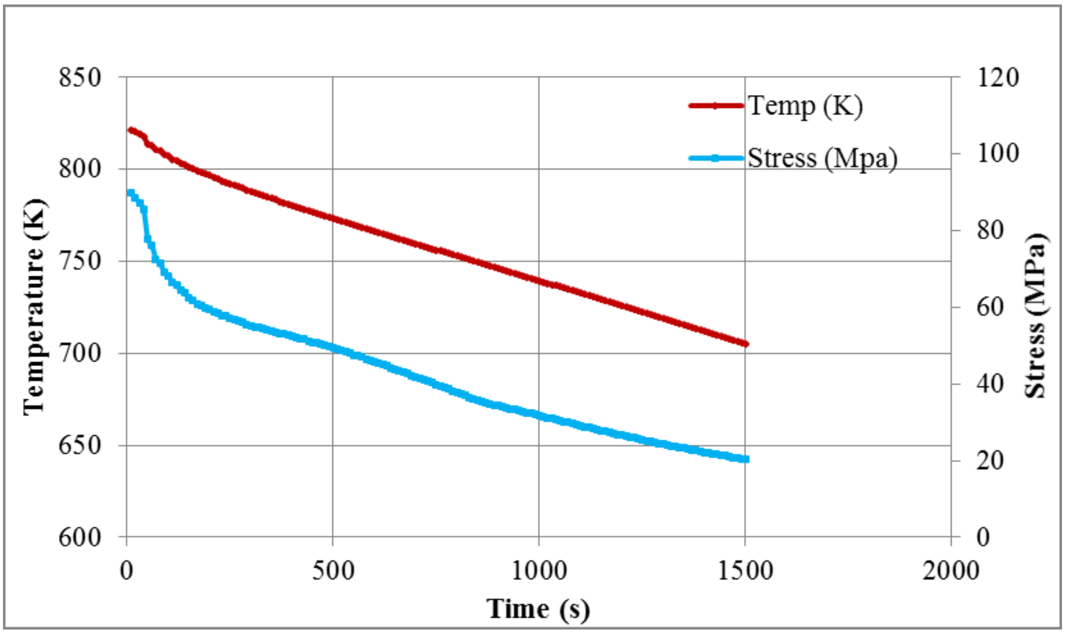

Figure 4.17 Temperature and stress vs. time at the initial free level

4.4.3. Formulation of the analytical model

4.4.3.1. Governing equations

The heat transfer equations used to arrive at the final solution are discussed in this section. All the equations given below are taken from text book [123].

(i) The initial variation in temperature at the locations in the argon gas at a distance 'y' from the sodium level is represented by the fin equation as given in equation 4.4. The temperature of all the locations below the sodium level is at the sodium temperature.

$$T_s - T_\infty = (T_{s1} - T_\infty)\ \exp\left(-\sqrt{\left(\frac{hP}{KA}\right)}y\right) \quad \textbf{4.4}$$

(ii) The part of the component that is above the sodium level is in the argon environment. The heat transfer coefficient of argon gas is 10 W/m^2K, which is calculated based on the correlations provided in [124]. The wall thicknesses of the components are less when compared to the other dimensions, giving lower volume to surface area ratio and thus lower characteristic length. Biot number (Bi), which is the ratio of the internal resistance to the convective resistance is given by equation 4.5.

$$Bi = \frac{h\,L_c}{K} \quad \textbf{4.5}$$

$$L_c = \frac{\text{volume of the body (V)}}{\text{surface area of the body (A)}} \quad \textbf{4.6}$$

As the Bi < 0.1, lumped heat analysis is used. The interior temperature remains essentially uniform at all times during the heat transfer process.

The temperature distribution for a solid initially kept at a temperature (T_0) which is placed in a convective environment at a temperature (T_∞) is given by equation 4.7.

$$\frac{T - T_\infty}{T_0 - T_\infty} = \exp\left(-\frac{hA}{\rho C_p V}\,t\right) \quad \textbf{4.7}$$

(iii) The part of the component that is immersed in sodium, which has a very high heat transfer coefficient is a system with negligible surface resistance, compared to the overall resistance. The mathematical formulation of this problem is given by equation 4.8.

$$\frac{\partial^2 \mathrm{T}}{\partial x^2} = \frac{1}{\alpha}\frac{\partial \mathrm{T}}{\partial \mathrm{t}} \text{ for } (0 \leq \mathrm{x} \leq \mathrm{z}) \tag{4.8}$$

The temperature distribution for a solid initially at a temperature (T_0) which is suddenly placed in an environment which is at a temperature (T_∞) is given by equation 4.9.

$$\frac{\mathrm{T}-\mathrm{T}_\infty}{\mathrm{T}_0-\mathrm{T}_\infty} = \frac{4}{\Pi}\sum_{n=1,3,5}^{\infty}\left(\frac{1}{n}\sin\frac{n\pi x}{L}\exp(-\left(\frac{n\pi}{L}\right)^2 \alpha t\right) \tag{4.9}$$

As the thickness is low (10 mm) in the cases referred in the analysis, the exponential terms is negligible. Thus the temperature across the thickness of the component is constant.

(iv) The conduction heat transfer within the body, from the region which is in argon gas ambience, to the region which is in sodium ambience is given by the general heat conduction equation 4.10.

$$\frac{1}{r}\frac{\partial}{\partial r}\left(r.\frac{\partial T}{\partial r}\right) + \frac{1}{r^2}\frac{\partial}{\partial \phi}\left(\frac{\partial T}{\partial \phi}\right) + \frac{\partial}{\partial z}\left(\frac{\partial T}{\partial z}\right) + \dot{q} = \frac{1}{\alpha}\frac{\partial \mathrm{T}}{\partial \mathrm{t}} \tag{4.10}$$

Equation 4.4 is used to get the initial temperatures at each location above sodium, and the temperature below sodium is the same as sodium temperature. For the next iteration, the sodium temperature (known) and the argon temperature (equation 4.3) decrease and there is a location which experiences the abrupt change in the ambience. The locations below sodium are maintained at the sodium temperature at all iterations and the locations in argon ambience follow equation 4.7. Equations 4.8 and 4.9 have been used initially to check the temperature distribution across the thickness, and it is found that the temperature across the thickness is negligible. Equation 4.10 has been neglected and compared with the results predicted by the code. It is found that its contribution (conduction) within body is negligible.

4.4.3.2. Analytical validation of the numerical model

Analytical validation of the numerical model has been done by considering a rectangular slab, which is divided into small segments. Figure 4.18 shows the conceptual drawing of the model considered for the analysis.

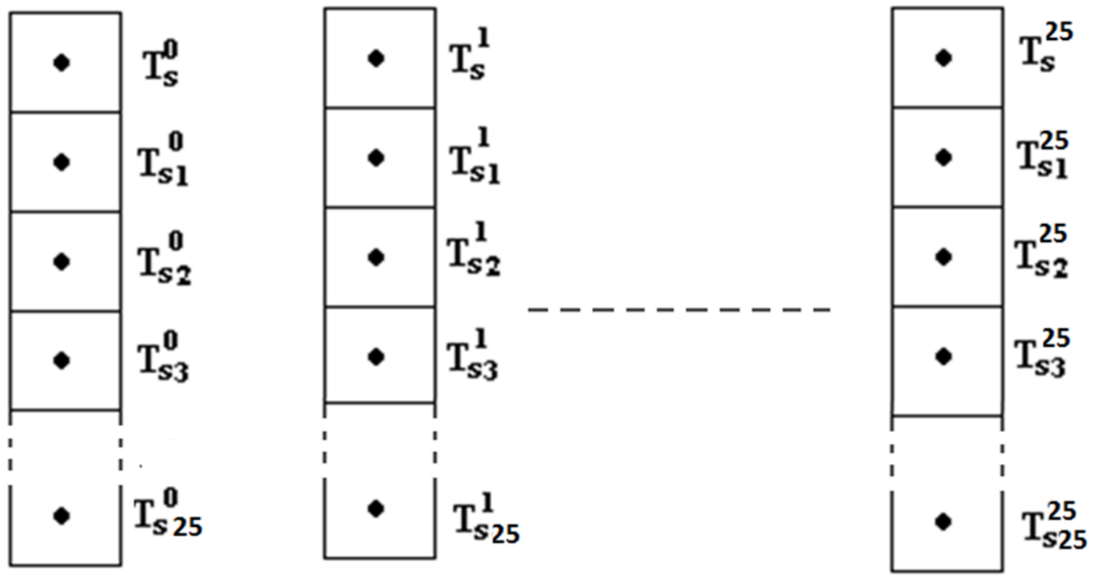

Figure 4.18 Conceptual drawing considered for the analytical model

The temperature of the region which is in argon ambience is T_s^0 and that at the initial sodium level is T_{s1}^0, and T_{s2}^0 , T_{s3}^0 , and so on up to T_{s25}^0 are the locations below T_{s1}^0, under sodium. It may be noted that, the subscript denotes the location number and the superscript denotes the iteration number.

The iterations are carried out at every 60 seconds interval for the validation (The time interval in the code model, CAST3M, is taken at every 10 seconds). The distance between two points is taken as 16 mm, which is the fall in sodium level in 60 seconds.

The temperature of all the locations below the sodium level is at the sodium temperature. The initial variation in temperature at the locations in the argon gas at a distance 'y' from the sodium level is represented by the fin equation as given in equation 4.4. As the locations are selected such that they are 16 mm apart, the initial temperature at the location above the sodium level (at y = 16 mm), is T_s^0 = 806.2 K, where, T_∞ (initial) = 715.5 K and T_{s1}^0 = 823 K.

At the second instance, the sodium temperature decreases by 8 K and the sodium level falls by 16 mm to T_{s2}^1. T_{s3}^1 , T_{s4}^1 ,and so on are below the sodium level and is at the sodium temperature of 815 K. T_s^1 , T_{s1}^1 are evaluated using equation 4.7.

Where, T is the temperature at the desired location

To evaluate T_s^1, the initial temperature $T_0 = T_s^0$,

To evaluate T_{s1}^1, the initial temperature $T_0 = T_{s1}^0$ and so on.

The temperatures at the next instance are evaluated following the same procedure. Thus T_s^0, T_{s1}^0, T_{s2}^0, up to, T_{s25}^0 to T_s^{25}. T_{s1}^{25}, T_{s2}^{25}, up to, T_{s25}^{25} are determined. The results are plotted and compared with that of the numerical model in section 4.4.5. It is observed that curve plotted from the analytical expressions overlap (match) on the curve plotted from the numerical model run in the CAST3M code.

4.4.4. Formulation of overall heat balance model

Another approach for addressing the problem is by balancing the heat input and output at the location considered. Figure 4.19 shows the conceptual drawing for heat balance, where, T_{s1}^o, which is the location above sodium level (in argon gas medium), T_{s2}^o, location in sodium and T_s^o, location above T_{s1}^o. Consider the location T_{s1}^0, the amount of heat stored in the material is equal to the difference in the heat added to the element by conduction and that removed by convection. It is assumed that heat is added to the system by conduction, and removed by convection. Thus the heat balance equation is written as follows.

$$\frac{K\delta(T_s^o - T_{s1}^o)\Delta t}{L} + \frac{K\delta(T_{s2}^o - T_{s1}^o)\Delta t}{L} - 2hL(T_{s1}^o - T_\infty^o)\Delta t = \rho L\delta C_p(T_{s1}^n - T_{s1}^o)$$

The superscript 'o' denotes the temperature in the previous step (old) and the superscript 'n' denotes the temperature in the present (new) step.

On rearranging, the equation takes the form as shown below.

$$T_{s1}^{n} = \frac{\Delta t}{\rho L \delta C_p}\left[\frac{K\delta(T_s^o + T_{s2}^o)}{L} + 2hLT_\infty^o\right] + T_{s1}^{0}\left[1 - \frac{2K\delta\Delta t}{\rho\delta C_p L^2} - \frac{2h\Delta t}{\rho\delta C_p}\right]$$

4.11

The time step for each iteration is determined by ensuring that the coefficient of T_{s1}^{0} in equation 4.11 is positive.

$$\Delta t < \frac{\rho L \delta C_p}{2[\frac{K\delta}{L} + hL]}$$

4.12

The time step is determined using equation 4.12.

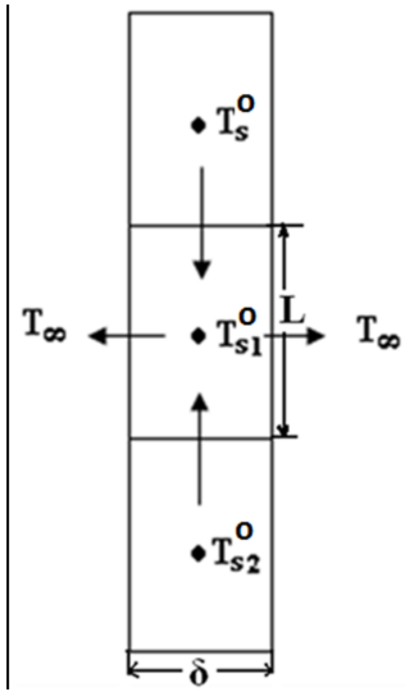

Figure 4.19 Conceptual drawing for heat balance

4.4.5. Comparison of the results

The curve plotted using the heat balance equation, which considers the heat conduction across the length, matches with the curves obtained by analytical model and the numerical model in Figure 4.20. The results infer that the heat conducted within the body from the region at argon gas ambience to the region at sodium ambience is removed by the sodium, resulting in negligible heat addition in the body. As all the three curves almost overlap with each other, we can use the numerical model developed to predict the thermo-mechanical behavior at free level interfaces, with high confidence.

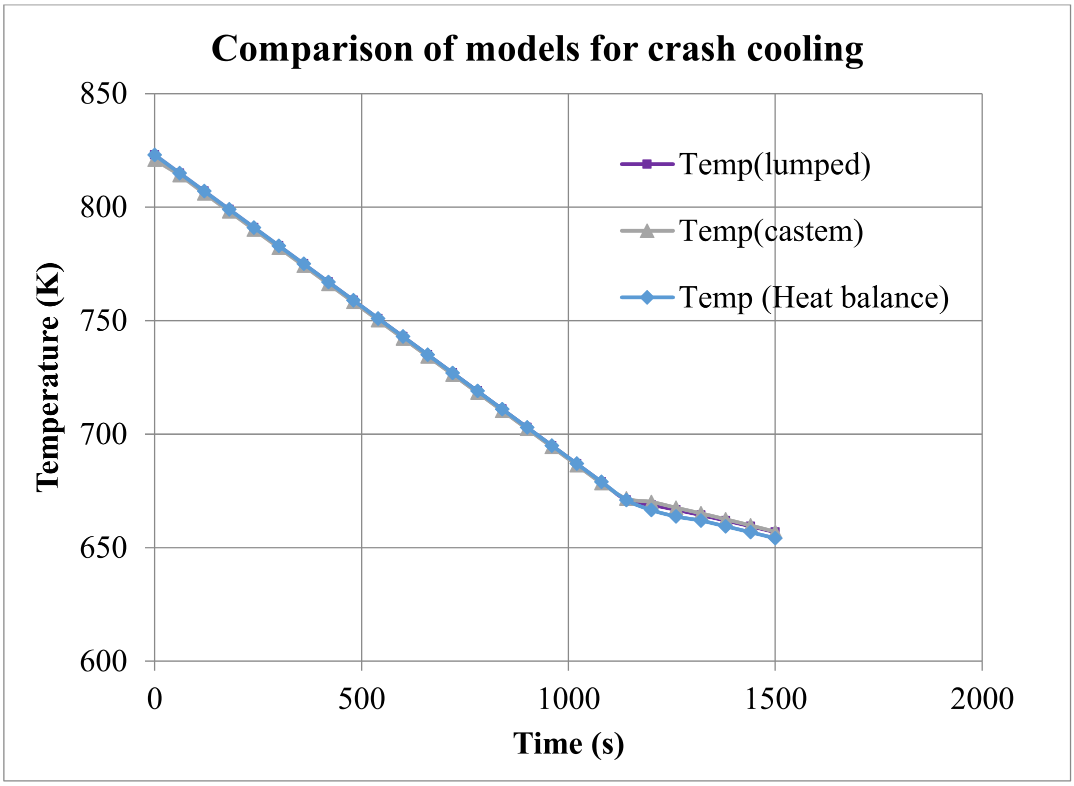

Figure 4.20 Comparison of temperature evolution: Numerical code, analytical and heat balance

4.5. Thermo-mechanical analysis at the free level interface of sodium

The numerical model developed has been used for all the locations at the free level interface of sodium. The evolution of temperature with time at each location is predicted by the logics of the numerical model and the thermal stresses (secondary stresses) are extracted from the FE code CASTEM. The primary stresses are taken from the references where mechanical loadings are considered. With these primary and secondary stresses, ratcheting check is done using 3Sm limit and efficiency index diagram (section 2.4.3.2). Ratcheting limits are met for all the cases considered in the thesis. In the next step, creep-fatigue damage assessment has been carried out and the values are presented in the subsequent sections. Time spent in creep regime of I-phase of cooling is taken as 16 minutes (time taken for sodium temperature to cool from 823 K to 698 K).

4.5.1. Assessment of damage in CP - USP junction

The temperature and stress evolution in CP (at location F1 in Figure 1.5) during I-phase are shown in Figure 4.15 and Figure 4.16 respectively. The maximum stress obtained is 98 MPa. The P_{max} value is 7.5 MPa [125]. The creep and fatigue damage for I-phase are 1.2 E-04 and 2.65 E-14 respectively. The maximum stress during II-phase at a cooling rate of 100 K/h is 50 MPa and at 20 K/h is 50 MPa. As the temperature in II-phase is not in the creep range, the fatigue damage alone is evaluated, and the values are 1.78 E-26 and 1.78 E-26 for 100 K/h and 20 K/h respectively. The combined creep and fatigue damage values (I-Phase + II-Phase) for CP during crash cooling are 1.2 E-04 and 2.65 E-14 respectively.

4.5.2. Assessment of damage in inner vessel

The maximum stress and temperature distribution for the I-phase of cooling in inner vessel (at location F2 in Figure 1.5) are shown in Figure 4.21.

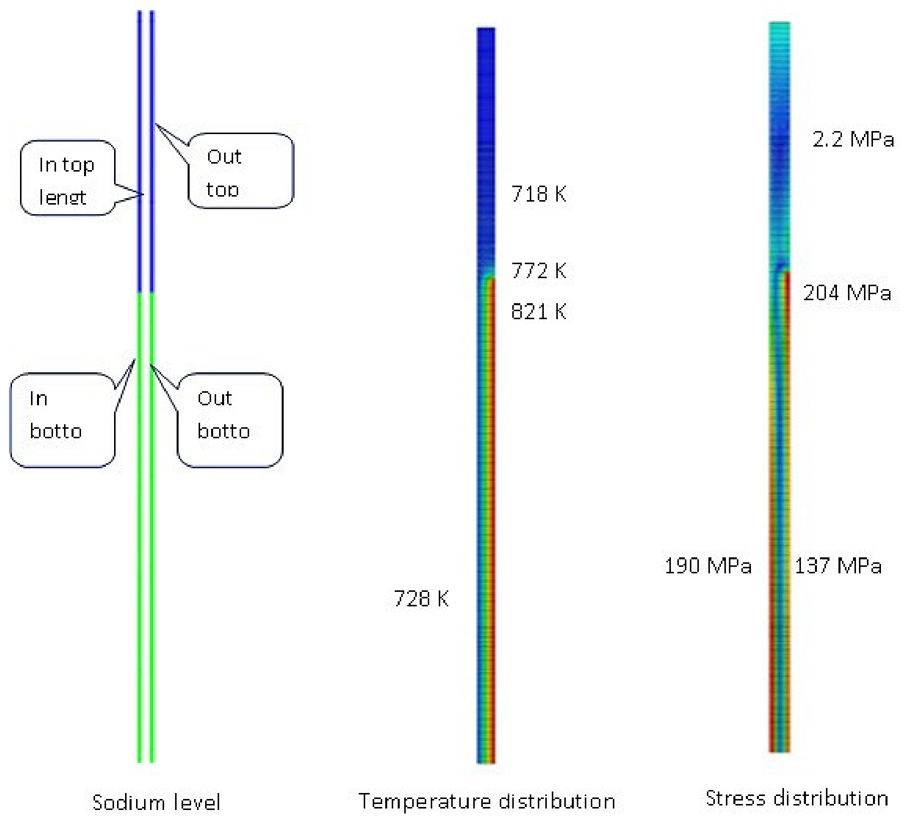

Figure 4.21 Temperature and equivalent stress distribution in inner vessel during I-phase of crash cooling

The maximum stress obtained is 204 MPa. P_{max} at free level interface is taken as 10 MPa (section 5.4.3.1). The creep and fatigue damage for I-phase are found to be 1.5 E-03 and 5.37 E-05 respectively. The maximum stress during II-phase at a cooling rate of 100 K/h is 60 MPa and at a cooling rate of 20 K/h is 58 MPa. As the temperature in II-phase is not in the creep range, the fatigue damage alone is evaluated and the values are 2.08 E-21 and 8.35 E-22 for 100 K/h and 20 K/h respectively. The combined creep and fatigue damage values (I-Phase + II-Phase) for inner vessel during crash cooling is 1.5 E-03 and 5.37 E-05 respectively.

4.5.3. Assessment of damage in IHX

The free level of sodium as indicated in Figure 1.5 (at location F3), is in the upper secondary sodium header. It consists of two concentric cylinders, the inner one being the IHX outer shell and the outer cylinder being the sleeve valve. Thermo-mechanical analysis has been carried out for IHX and the temperature and maximum stress distribution of the axi-symmetric model are shown in Figure 4.22.

The maximum stress obtained is 95 MPa. The P_{max} value is taken as 42 MPa [122]. The creep and fatigue damage for I-phase are found to be 1.0 E-04 and 1.12 E-14 respectively. The maximum stress during II-phase at a cooling rate of 100 K/h is 40 MPa and at a cooling rate of 20 K/h is 40 MPa. As the temperature in II-phase is not in the creep range, the fatigue damage alone is evaluated and the values are 4.4 E-29 and 4.4 E-29 for 100 K/h and 20 K/h respectively. The combined creep and fatigue damage values (I-Phase + II-Phase) for IHX during crash cooling is 1.0 E-04 and 1.12 E-14 respectively.

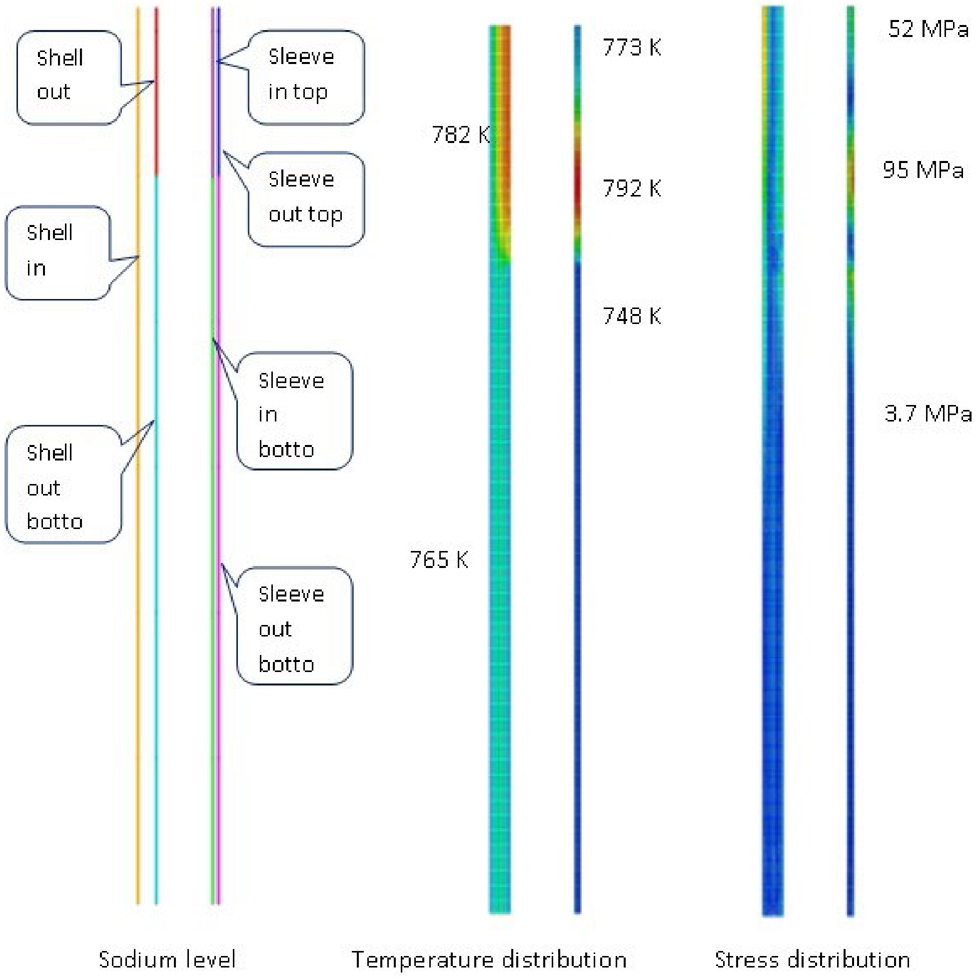

Figure 4.22 Temperature and equivalent stress at IHX free level

4.5.4. Assessment of damage in PSP standpipe

The PSP standpipe is a part of inner vessel which is one of the major components immersed in the primary sodium, and its details are in section 1.1.7.4. The thickness of the PSP standpipe is 12 mm and its outer diameter is 2062 mm. The difference in sodium height has been modeled in the analysis. Transient analysis has been carried out for PSP and the temperature and maximum stress distribution (at location F4 in Figure 1.5) are shown in Figure 4.23. The maximum stress obtained is 259 MPa. The creep and fatigue damage for I-phase are found to be 3.0 E-03 and 2.9 E-03 respectively. The maximum stress during II-phase at a cooling rate of 100 K/h is 50 MPa and at a cooling rate of 20 K/h is 50 MPa. As the temperature in II-phase is not in the creep range, the fatigue damage alone is evaluated and the values are

1.78 E-26 and 1.78 E-26 for 100 K/h and 20 K/h respectively. The combined creep and fatigue damage values (I-Phase + II-Phase) for PSP standpipe during crash cooling is 3.0 E-03 and 2.9 E-03 respectively.

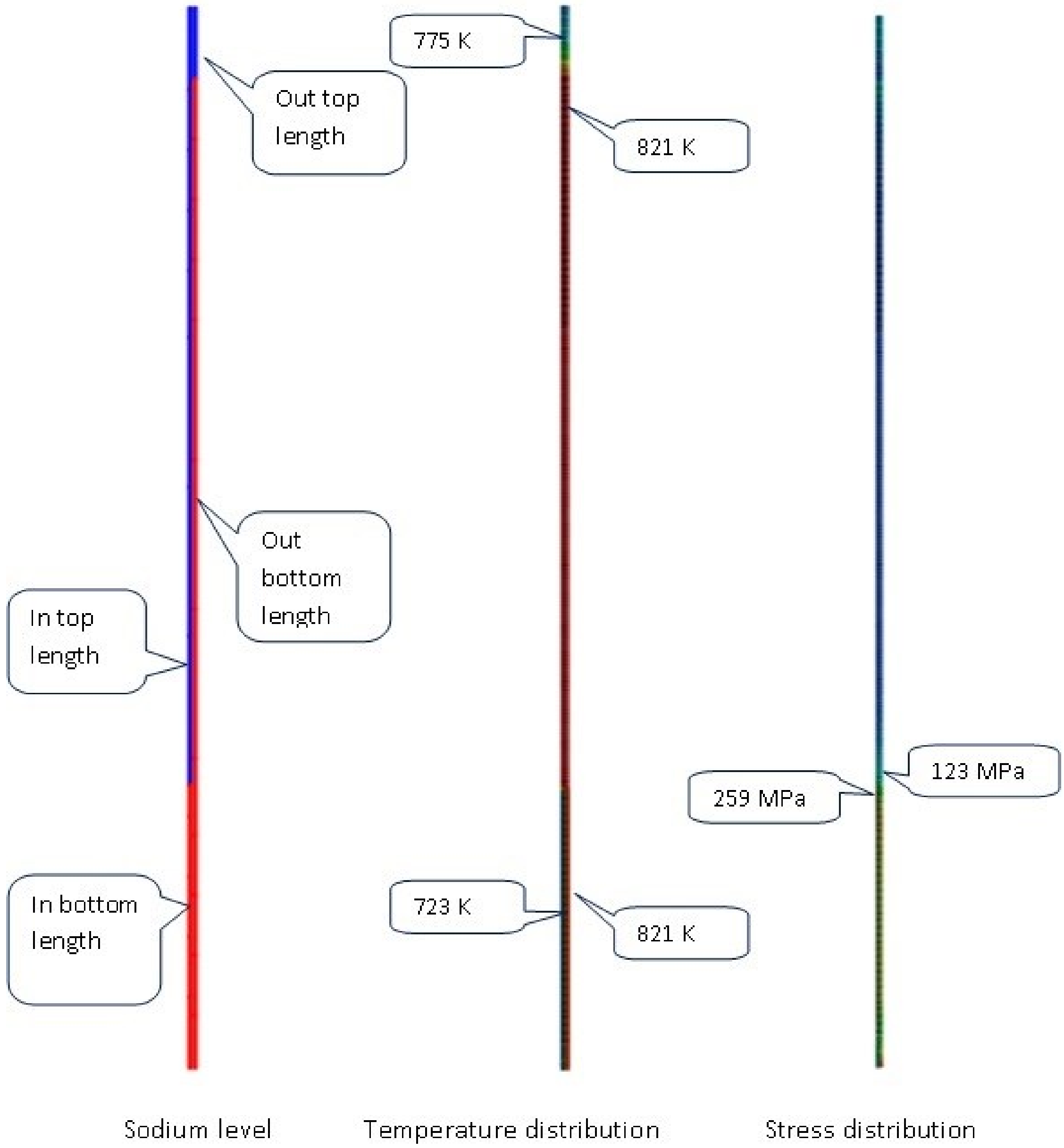

Figure 4.23 Temperature and equivalent stress distribution at PSP standpipe free level location

4.5.5. Damage estimation in future FBR

Creep-fatigue damage estimation in future reactors has been done using the stress values obtained above for PFBR. The future fast breeder reactors are designed to operate for

60 years [126]. The number of cycles for PFBR with design life of 40 years, with a load factor 75 % is 861 cycles. In future FBR, the number of cycles during life time of 60 years and load factor 85 % is 1459 cycles. The creep fatigue damage at the free level locations during crash cooling (I and II phase – combined) for 1459 cycles are presented in Table 4.2.

Table 4.2 Creep-fatigue damage during crash cooling at free level interface locations in future fast reactors

Component	Creep Damage	Fatigue Damage
Control Plug	1.58 E-04	3.5 E-14
Inner vessel	1.98 E-03	7.11 E-05
IHX	1.32 E-04	1.48 E-14
PSP standpipe	3.97 E-03	3.84 E-03

It is observed from Table 4.2 that the creep-fatigue damage caused in fast reactors during crash cooling in 1459 cycles is negligible at the free level locations. However, as the submerged locations, IHX tubesheets in particular are critical, thermo-mechanical analysis at submerged locations for crash cooling needs to be carried out with exact FBR geometry and loading conditions. Nevertheless, this analysis shows that free level locations are not critical for crash cooling condition.

4.6. Closure

Thermo-mechanical analysis during crash cooling of primary sodium has been carried out at thick junctions that are immersed in sodium, and the following are the observations.

- The maximum stress at LSP-CP junction is 12.9 MPa.
- Parametric study with varying cooling rates shows that there is an escalation in the magnitude of stresses when the cooling rate augments.

- Parametric study with various thicknesses of LSP shows that the stress escalates with an increase in thickness. The magnitude of stress is higher when the thicknesses of both CP and LSP are increased.
- The inner vessel upper cylinder and redan junction, with inside and outside temperatures of 815 K and 741 K respectively is analyzed for I-phase of crash cooling. The maximum stress is 118 MPa and the creep and fatigue damage values are 0.08 and 2.35 E-09 respectively.
- With the same loading conditions, the inner vessel-IHX junction has been analyzed and the maximum stress is found to be 179 MPa. The creep and fatigue damage values are 0.093 and 7.9 E-05 respectively.
- IHX tubesheets are analyzed using ESP concept, and it is found that the maximum stress (381.3 MPa) is at the perforated region. As the stresses are very high, the conservative approach has not been used to estimate the creep and fatigue damages. The time spent in creep regime (823 K to 723 K) for 861 cycles is 173 h. From CCOC for SS316LN at 823 K, min time for creep to occur is 270 h. So, creep is neglected. The fatigue damage calculations are done at the stress value of 381.26 MPa, and its value with and without considering the presence of welds at the maximum stress locations are 0.175 and 0.077 respectively and are acceptable (< allowable limit 1).

The free level interface of sodium is another critical location which has a complex loading condition due to change in sodium level with change in sodium temperature. A numerical model has been developed to predict the thermo-mechanical behavior of partially immersed components and the model is validated both analytically and with overall heat balance equations.

Transient analysis has been performed for the hot pool components at the free level for I-phase and II-phase at 100 K/h and 20 K/h, and the following are the observations for PFBR.

- The maximum creep and fatigue damage values for CP are 1.2 E-04 and 2.65 E-14 respectively.
- The maximum creep and fatigue damage values for inner vessel are 1.5 E-03 and 5.37 E-05 respectively.
- The maximum creep and fatigue damage values for IHX are 1.0 E-04 and 1.12 E-14 respectively.
- The maximum creep and fatigue damage values for PSP standpipe are 3.0 E-03 and 2.9 E-03 respectively.

The creep-fatigue damage is considerable in submerged locations. It is inferred from this investigation that the crash cooling at 480 K/h from 823 K to 623 K is the governing phase, which contributes to maximum damage. The damage caused in the subsequent phases of cooling from 623 K to 453 K (in the non-creep regime) at 100 K/h and 20 K/h is insignificant. Thus the proposal to eliminate controlled cooling and to deploy OGDHR after reaching cold shutdown condition is recommended, which leads to simplification of the OGDHR design. The numerical model developed has been used in the next chapter to investigate the optimum heating rate during power raising.

References

[114] U. Parthasarathy, T. Sundararajan, C. Balaji, K. Velusamy, P. Chellapandi, S.C. Chetal. Decay heat removal in pool type fast reactor using passive systems. Nuclear Engineering and Design, 250 (2012), 480– 499.

[115] L. Satish Kumar, K. Natesan, A. John Arul, V. Balasubramaniyan, S.C. Chetal. Design and evaluation of Operation Grade Decay Heat Removal System of PFBR. Nuclear Engineering and Design, 241 (2011), 4953–4959.

[116] K. Natesan, K. Velusamy, P. Selvaraj, P. Chellapandi. (2011), Integrated Plant Operations, PFBR/01151/DN/1018/Rev-C.

[117] B. L. Eyre, B. Tomkins, J. D. Lewins, M. Kohler, J. Spence, K. Q. Bagley and D. Broadley. Structural Integrity of Fast Reactor Components. Philosophical Transactions of the Royal Society of London. Series A, Mathematical andPhysical Sciences, Vol. 331, No. 1619, The Fast-Neutron Breeder Fission Reactor (Jun. 28,1990), pp.419-434.

[118] Cast3M, 2008: www-cast3m.cea.fr.

[119] Pranav Paliwal, U. Parthasarathy, K. Velusamy, T. Sundararajan, P. Chellapandi. Characterization of cellular convection of argon in top shield penetrations of pool type liquid metal fast reactors. Nuclear Engineering and Design 250 (2012) 207-218.

[120] R. Srinivasan and P. Chellapandi. Stress Analysis of IHX under Mechanical Loading. PFBR/32130/DN/1045/R-A (2002).

[121] RCC-MR Section III - Tome-1 - Subsection B: Class N1Rx reactor components and supports (2012).

[122] Suman Gupta and P. Chellapandi. Application of RCC-MR for the structural design of tubesheet of Intermediate Heat Exchanger for a sodium cooled fast reactor. Nuclear Engineering and Design, 280 (2014) 181-200.

[123] R.C. Sachdeva. Fundamentals of Engineering Heat and Mass Transfer. Revised Second Edition, New Age International Publishers (2006).

[124] Cengel Yunus, Ghajar Afshin. Heat and Mass Transfer: Fundamentals and Applications. McGraw Hill Education, (2010).

[125] P. Chellapandi and S.C. Chetal. Life Prediction of Control Plug. PFBR/RG/31410/DN/1022/R-A (1996).

[126] P. Chellapandi, P. Puthiyavinayagam, V. Balasubramaniyan, S. Ragupathy, V. Rajanbabu, S. C. Chetal, Baldev Raj. Design concepts for reactor assembly components of 500 MWe future SFRs. Nuclear Engineering and Design, 240 (10). pp. 2948-2956. ISSN 0029-5493 (2010).

Chapter 5

Effect of Power Raising on Reactor Components

5.1. Background

The numerical model to study the physics of partially immersed components has been developed in the previous chapter. The developed numerical model has been used to explore the possibility of simplifying the power raising operation by arriving at an optimum heating rate. The fuel clad and the primary system components are the critical components that are affected by the power raising rate of sodium. The former is dealt in Chapter 6, and the latter is studied in the present chapter. The primary system components include CP, inner vessel, PSP standpipe, and IHX. The heating rates considered for the parametric study are 20 K/h, 40 K/h, 60 K/h, 80 K/h, 100 K/h and 120 K/h. Thermal ratchetting, creep damage, fatigue damage, and creep-fatigue damage interaction have been estimated for each location to arrive at an optimum heating rate.

5.2. Power raising operation in PFBR

In the Indian pool-type sodium-cooled fast reactors, the reactor system temperatures are at 453 K in the cold shutdown condition, and the decay heat is removed continuously using OGDHR and SGDHR systems. From this condition, the reactor start-up operation is done in three stages [127]. The first stage is to terminate the decay heat removal, and the feedwater is injected into the steam generator. The second stage is to approach to criticality by the movement of control rods. The DSRs are raised to the topmost position, and the CSRs are raised to the defined height to attain criticality [128]. The details of DSRs and CSRs are given in [129] and [130] respectively. The third stage is the power raising in the reactor core by raising the CSRs in wait and raise mode.

The final activity, i.e., the power raising by CSR movement, is the most extended operation in the reactor startup. The control rod is raised by a certain distance, which is called the step movement. This step value is fixed based on the worth of control rods (pcm/mm) at the calculated critical level, which in turn depends on the core configuration (beginning/end of equilibrium cycles). The wait time between the movements of two control rods is decided based on the allowable sodium heating rate. The hot pool sodium heating rate of 20 K/h has been conservatively chosen to avoid thermal shocks to various components. Thus the total time required to reach the full power is 20 h for the chosen heating rate.

The power raising duration can be optimized by detailed structural damage investigation of the reactor components in sodium that is at a high temperature, and bring down the power raising time, with minimal structural damage. Thus, the optimization of hot pool heating rate is done in the present chapter.

5.3. Critical locations in primary system components

The fast reactor geometry and material details considered are discussed in section 1.1.5. The critical locations are broadly categorized to submerged locations and free level locations as shown in Figure 1.5. Conventional FE analysis in coupled-temperature displacement mode gives the thermal stresses at the submerged critical locations. The stresses at the free level locations cannot be estimated using the conventional FE code due to the intricate loading conditions at the sodium free level. Hence a numerical model has been established in-house to account for the abrupt shift from argon ambience to sodium ambience at a local region (section 4.4).

Structural damage investigations have been carried out for all the critical locations including free level and submerged locations, to arrive at the optimum heating rate.

5.4. Effect of power raising at the locations submerged in sodium

During power raising, the primary sodium heating rate can develop high thermal stresses at the locations such as joints and thick plates in the reactor components, due to higher Fitz number. Conventional method of thermo-mechanical analysis has been carried out in CASTEM code to obtain the thermal stresses at the submerged locations.

5.4.1. Boundary conditions

The CP, PSP standpipe, and IHX hang from the top and the inner vessel is bolted at the bottom, at the grid plate. Thus the boundary condition is considered as Uz = 0 (i.e., the axial displacement has been arrested).

5.4.2. Thermo-mechanical analysis at CP-LSP junction

The LSP is a thick plate that is welded to the outer shell of CP. The LSP that is immersed in sodium can develop high thermal stresses at the junction. The FE mesh of the axi-symmetric model of the CP-LSP junction (B1 in Figure 1.5) is shown in Figure 5.1.

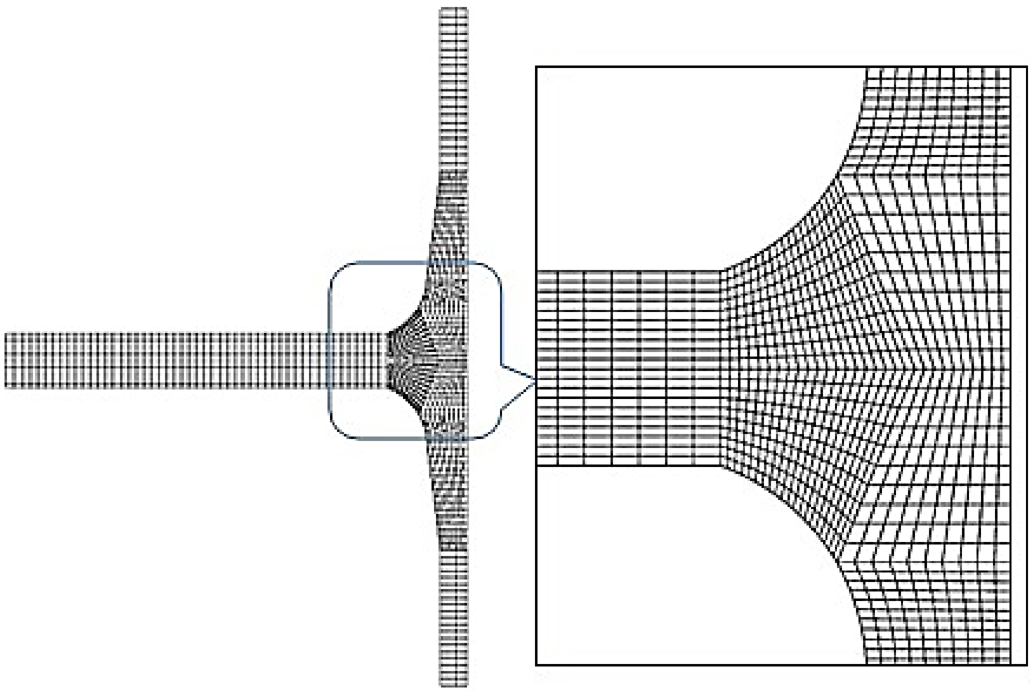

Figure 5.1 FE mesh of CP at the junction of CP-LSP junction

The temperature of the inner surface of CP is 7 K higher than that of the outer surface temperature. Thermo-mechanical analysis of the CP-LSP junction has been carried out for all the heating rates considered. The temperature and stress contours at the maximum stress instance at 20 K/h are shown in Figure 5.2. The maximum stress value of 23.2 MPa is observed at all the heating rates considered. The P_{max} value is taken from [131], from the calculations for stay-plate to outer shell junction.

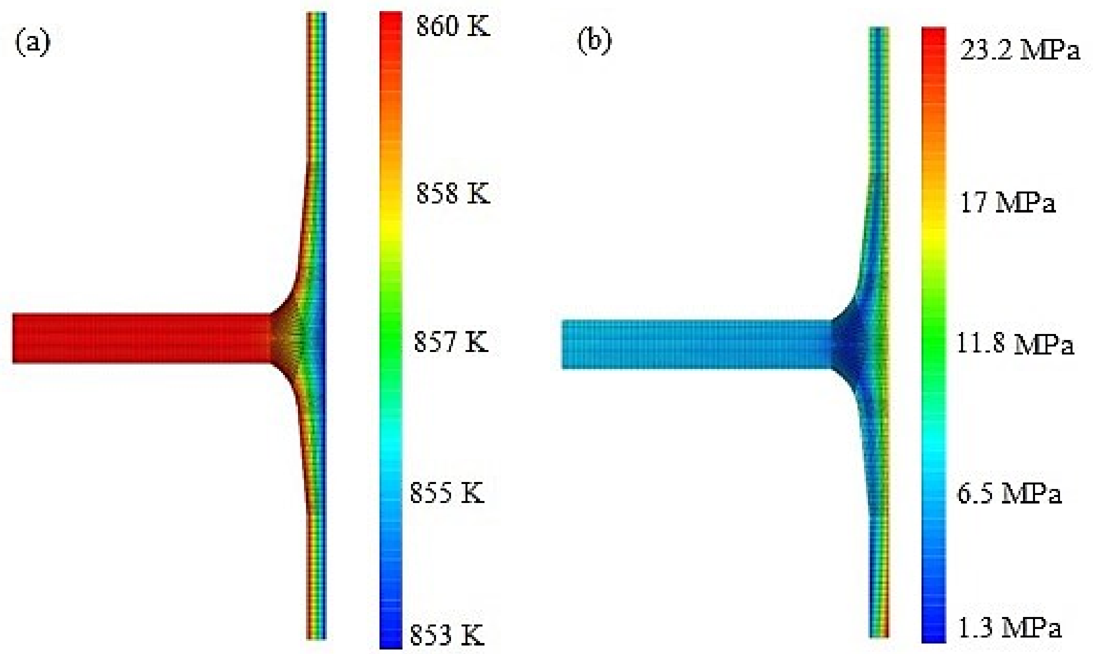

Figure 5.2 CP-LSP junction: a) Temperature b) Stress contour

The effective creep-fatigue damage values at the maximum stress location due to power raising at 20 K/h, 60 K/h, and 120 K/h are 1.95 E-07, 6.48 E-08, and 3.24 E-08 respectively. The effective damage decreases with an increase in heating rates due to the reduction in the time spent in creep regime. Nevertheless, the creep and fatigue damage during power raising is negligible at CP-LSP junction, for all the heating rates considered. Hence, it can be concluded that this location is not of concern and any of the six heating rates is acceptable at this location.

5.4.3. Thermo-mechanical analysis at inner vessel-IHX junction

5.4.3.1. Stress analysis with mechanical loading

In order to estimate the creep and fatigue damages of inner vessel at the free level, the mechanical stresses are essential. Towards this, a stress analysis has been carried out on inner vessel based on mechanical loading. Self-weight of inner vessel along with the weights of stand pipes and sodium pool pressure head constitute normal operating condition mechanical loads acting on the inner vessel. Pressure loading is due to the differential head (1.5 m in PFBR) between the sodium free surface levels in the hot and adjacent cold pools. Stress analysis of the inner vessel geometry has been performed and the von-Mises stress distribution is shown in Figure 5.3.

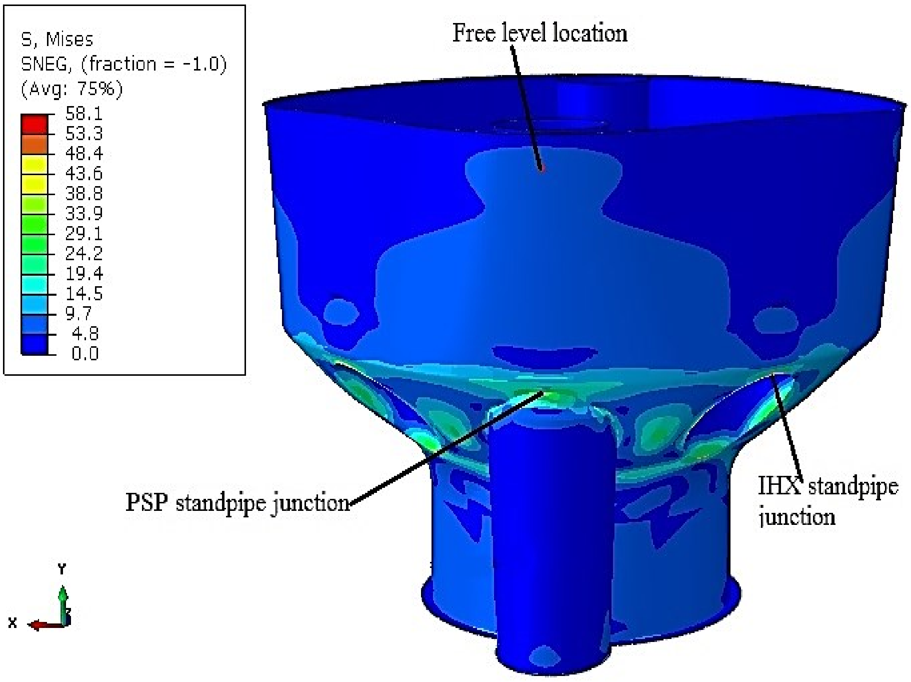

Figure 5.3 Stress distribution in inner vessel due to mechanical loading

The maximum stress is at the IHX standpipe junction. The mechanical stresses at the free level are very less. The stresses extracted at the IHX standpipe junction, PSP standpipe junction and the free level and the P_{max} values are calculated as shown in Table 5.1.

The P_{max} value is calculated using equation 2.39, and the values at inner vessel-IHX standpipe location and at free level location are 54.5 MPa and 10.1 MPa respectively. The P_{max} value for other components have been taken from references, unlike inner vessel.

Table 5.1 Mechanical stresses at critical locations

Location	**Max. Primary Stress Intensities - MPa**		**P_{max} = Max [P_m + 0.66 (P_b + P_L – P_m)] MPa**
IHX	P_L	69.8	54.5
	$P_L + P_b$	138.7	
PSP	P_L	40.3	35
	$P_L + P_b$	90.5	
Free Level	P_m	2.5	10.1
	$P_m + P_b$	14.0	

5.4.3.2. Stress analysis with thermal loading

The inner vessel-IHX standpipe junction (B3 in Figure 1.5) is one of the critical locations in inner vessel. There is hot pool and cold pool sodium on the interior side and exterior sides of the inner vessel respectively. The evolution of temperature during start-up at the inner (hot) and outer (cold) surfaces of the inner vessel at the junction location is shown in Figure 5.4. The temperatures then reach steady state.

Thermo-mechanical analysis has been carried out at the inner vessel - IHX junction at all the heating rates considered. The temperature distribution and the equivalent stress distribution at 20 K/h are shown in Figure 5.5.

The maximum stress value is 176 MPa, which is the same for all the heating rates considered. Ratcheting check is done by checking the 3Sm limit. As the 3Sm limits are not met, efficiency index method is used as per section 2.4.3.2 , and it is found that the limits of progressive deformation are met. Thus, creep-fatigue damage is estimated further.

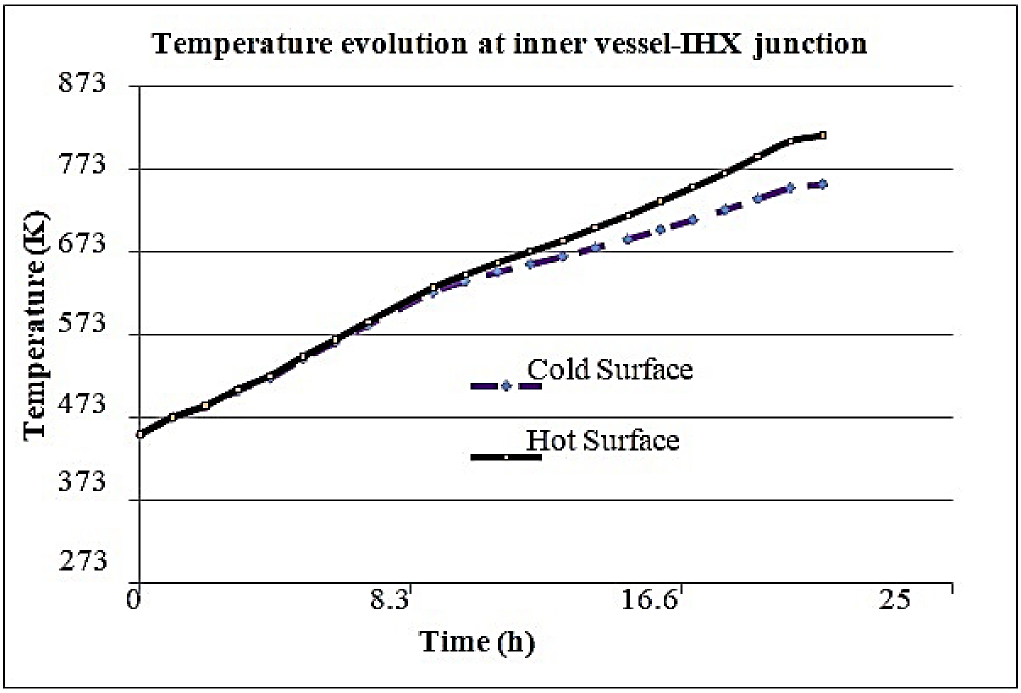

Figure 5.4 Temperature evolution at inner vessel-IHX junction

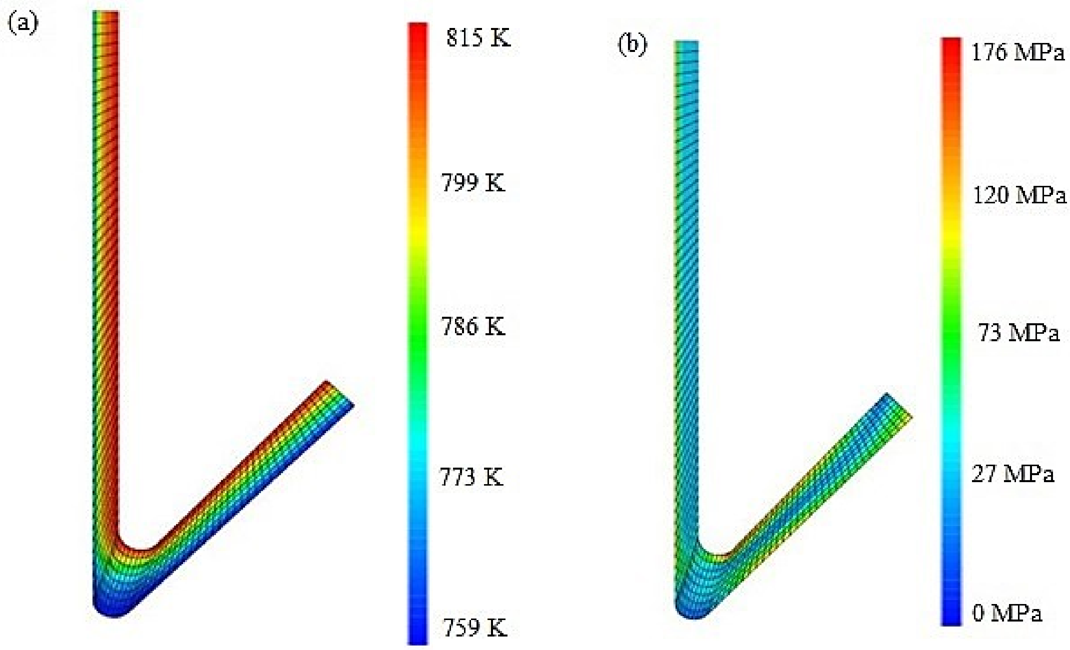

Figure 5.5 Inner vessel-IHX junction: a) Temperature b) Equivalent stress contour

The creep-fatigue damage calculations are shown in Table 5.2 (All the terms are explained in section 2.2 and 2.4). The value of P_{max} is taken from Table 5.1. The effective damage values at inner vessel – IHX junction are 0.23, 0.076, and 0.038 at 20 K/h, 60 K/h, and 120 K/h, respectively.

Table 5.2 Creep-fatigue calculations for inner vessel-IHX junction during power raising

Parameter	**20 K/h**	**60 K/h**	**120 K/h**
$\Delta\sigma_{Tot}$ (MPa)	176	176	176
$\overline{\Delta\varepsilon}_1$ (%)	0.098	0.098	0.098
$\overline{\Delta\varepsilon}_2$ (%)	0	0	0
$\overline{\Delta\varepsilon}_1 + \overline{\Delta\varepsilon}_3$ (%)	0.1	0.1	0.1
$\overline{\Delta\varepsilon}_4$ (%)	3.2 E-05	3.2 E-05	3.2 E-05
$(\overline{\Delta\varepsilon})_{el+pl}$ (%)	0.106	0.106	0.106
$\bar{P}_{max}$ (MPa)	54.5	54.5	54.5
$\overline{\Delta\sigma}^*$ (MPa)	176	176	176
$\overline{\Delta S}^* = \overline{\Delta\sigma}^* - \overline{\Delta P}$ (MPa)	176	176	176
R	0.822	0.822	0.822
K_s	0.738	0.738	0.738
σ_k (MPa) $= \bar{P}_{max} + K_s\,\overline{\Delta S}^*$	184.4	184.4	184.4
Time spent in creep regime per cycle (h)	***6.25***	***2.08***	***1.04***
$(\overline{\Delta\varepsilon})_{cr}$ (%)	0.022	0.013	0.01
$(\overline{\Delta\varepsilon})$ (%) $= (\overline{\Delta\varepsilon})_{el+pl} + (\overline{\Delta\varepsilon})_{cr}$	0.128	0.12	0.116
No. of cycles allowable (N_d)	5.0 E+06	3.0 E+07	6.7 E+07
$S_r = \sigma_k / 0.9$ (MPa)	204.8	204.8	204.8
t_r (hours)	2.3 E+04	2.3 E+04	2.3 E+04
FD (861 cycles)	**1.69 E-04**	**2.85 E-05**	**1.28 E-05**
CD (861 cycles)	**0.23**	**0.076**	**0.038**
Deff (861 cycles)	**0.23**	**0.076**	**0.038**

The effective damage curves with and without the presence of welds is shown in Figure 5.6. It is observed that, though the stresses are constant, the effective damage decreases with an increase in heating rate due to a decrease in time spent in creep regime.

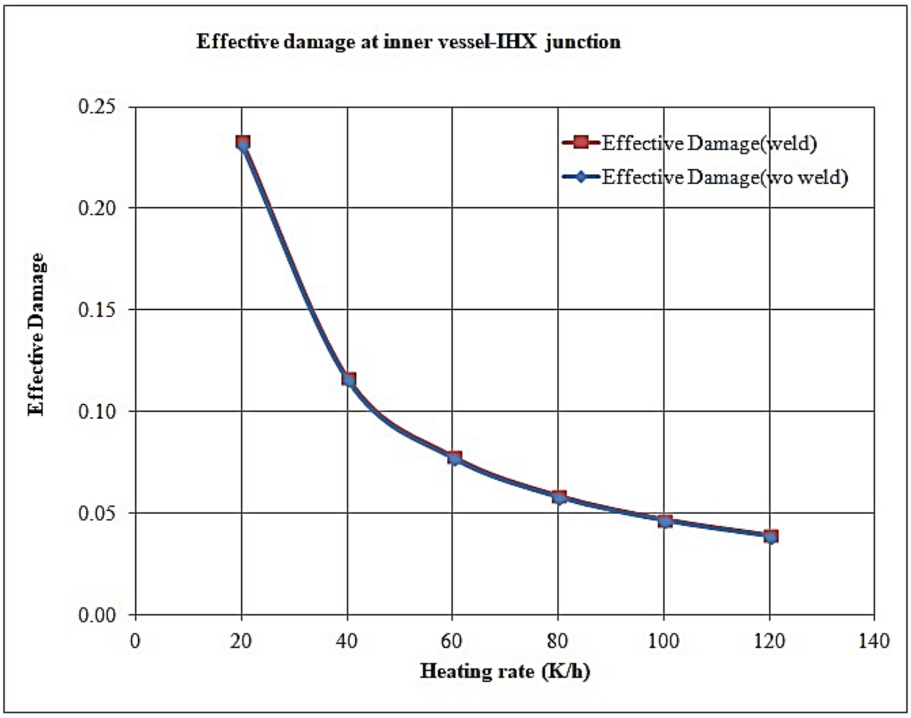

Figure 5.6 Effective damage at inner vessel-IHX junction

5.4.4. Thermo-mechanical analysis at IHX tubesheets

The geometrical details of IHX has been described in section 1.1.7.3 and specific details on IHX tubesheets in section 4.3.3.1. The temperature evolution at the tubesheets is taken as 453 K at the start of power raising and reaches 823 K. The top and bottom tubesheets which are submerged in sodium have been analyzed for all the heating rates considered.

The FE analysis of the tubesheets has been carried out using ESP concept. The procedure is given in section 4.3.3.2. As the IHX is hanging from the top, the axial displacement has been arrested for simulating the boundary conditions. Thermo-mechanical analysis of the IHX top and bottom tube sheets with the above-mentioned loading and boundary conditions has been carried out. The temperature distribution at the instance corresponding to maximum stress is shown in Figure 5.7. The temperature at the surfaces increases with increase in sodium temperature, whereas, the temperature within the tubesheets increase at a comparatively slower rate. Hence, the surface temperature is higher than the bulk temperature, and the stresses at the surfaces are compressive.

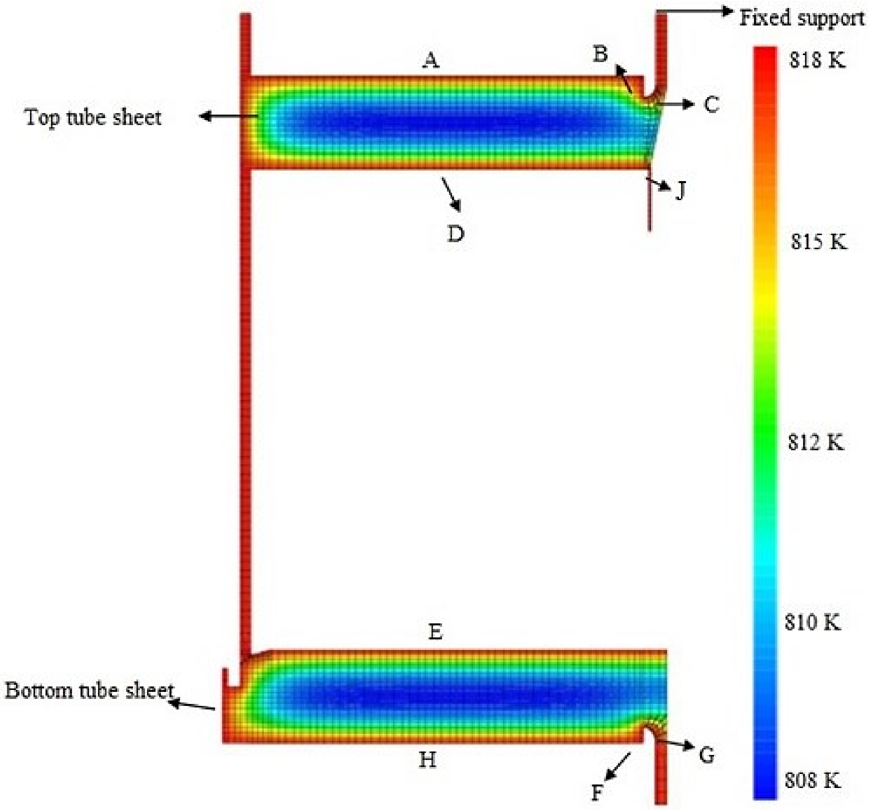

Figure 5.7 Temperature distribution at the maximum stress instance

5.4.4.1. Perforated region

From Figure 5.7, it may be observed that the perforated regions are Locations- A, D, E, H, where A and D are maximum stress locations at the top and bottom sides of the top tube sheet. Locations- E and H are the maximum stress locations at the top and bottom sides of the bottom tube sheet. The maximum stress locations have been chosen after taking many locations and calculating equivalent stress.

The radial, hoop and axial stresses are extracted from the FE analysis using ESP concept. The stresses are compressive due to higher temperature at the surface. The principal stresses extracted from the analysis are multiplied with stress multiplier (K_{skin} = 0.22 at L/P = 0.2555 [132]), to get the skin thermal stresses. Equation 4.1 is used to arrive at the equivalent true stress. The values of Y_1 and Y_2, corresponding to the ligament efficiency of 0.25 are 1.2, and 2.25 respectively [133]. The stresses obtained and the equivalent true stresses at all the locations for the heating rate of 20 K/h are given in Table 5.3.

5.4.4.2. Junction between perforated plate and solid rim

From Figure 5.7, it may be observed that the Locations- B and F are the interface locations, where B is the interface location of the top tube sheet, and F is the interface location of the bottom tube sheet. The radial, hoop and axial stresses are extracted from the analysis. Equation 4.2 is used to arrive at the equivalent true stress. The K_{r1} and K_{r2} values are obtained with hole diameter of 19 mm and rim width of (950 – 905) = 45 mm, and the values are 2.35 and -1 respectively [133].

5.4.4.3. Rim region

From Figure 5.7, it may be observed that the Locations- C, J and G are the maximum stress locations in the solid rim portion, where C is at the top portion of the top tube sheet, J at the bottom side of the top tube sheet and G is at the bottom side of the bottom tube sheet. The radial, hoop and axial stresses are extracted from the analysis. The stress components, and the equivalent stress (Tresca), are given in Table 5.3.

Table 5.3 Stresses in IHX tubesheets during power raising at 20 K/h

Location		Radial (MPa)	Hoop (MPa)	Axial (MPa)	Equivalent stress (MPa)
Perforated (skin) Eqn-4.1	A	-1.19	-0.91	0.00	-13.63
	D	-1.21	-1.08	0.00	-15.13
	H	-1.12	-0.94	0.00	-13.54
	E	-1.21	-1.10	0.00	**-15.35**
Interface Eqn-2	B	0.009	-5.556	-0.08	-13.07
	F	-0.006	-5.66	-0.16	-13.29
Solid rim (Tresca)	C	0.745	-4.362	1.78	-6.14
	J	0.30	-5.77	0.003	-6.08
	G	0.24	-4.12	2.82	-6.95

Thermo-mechanical analysis has been carried out for all the other heating rates considered. As Location-E is the maximum stress location, the equivalent stresses at this location for all the heating rates considered, and time spent in creep regime are given in Table 5.4.

Table 5.4 Max thermal stresses during power raising at various heating rates

Heating Rate (K/h)	**Time spent in creep regime per cycle (h)**	**Equivalent stress (MPa) at Location-E**
20	6.25	15.35
40	3.125	30.74
60	2.08	46.15
80	1.56	61.55
100	1.25	76.93
120	1.04	92.34

The time spent in creep regime considered is the time taken for the primary sodium temperature to rise from 698 K to 823 K. It is assumed conservatively that the temperature is held at 823 K throughout the time spent in creep regime.

5.4.4.4. Creep-fatigue damage estimation

The creep and fatigue damage at location-E for all the heating rates considered has been estimated as per the procedure discussed in section 2.4. The fatigue damage values are calculated with weld and without weld. The creep damage is the same even with the presence of welds as the weld strength reduction factor is 1 up to a time spent in creep regime of 10 hours. The creep and fatigue damage values are calculated considering $\bar{P}_{max}$ = 42 (MPa) [134], and the values are given in Table 5.5.

Table 5.5 Damage values at various heating rates at Location-E

Heating rate (K/h)	**Fatigue damage (welds)**	**Creep damage**	**Effective damage**
20	3.36E-33	1.85 E-05	1.85 E-05
40	4.21E-25	6.2 E-05	6.2 E-05
60	2.68E-20	0.000195	0.000195
80	7.53E-17	0.0005	0.0005
100	3.88E-14	0.0013	0.0013
120	2.80E-03	0.0028	0.0028

The above results show that the effective creep-fatigue damage for 861 cycles is low for all the heating rates considered. The curves showing the creep and fatigue damages at the IHX tubesheets due to power raising for 861 cycles (considering welds) are shown in Figure 5.8 and Figure 5.9 respectively.

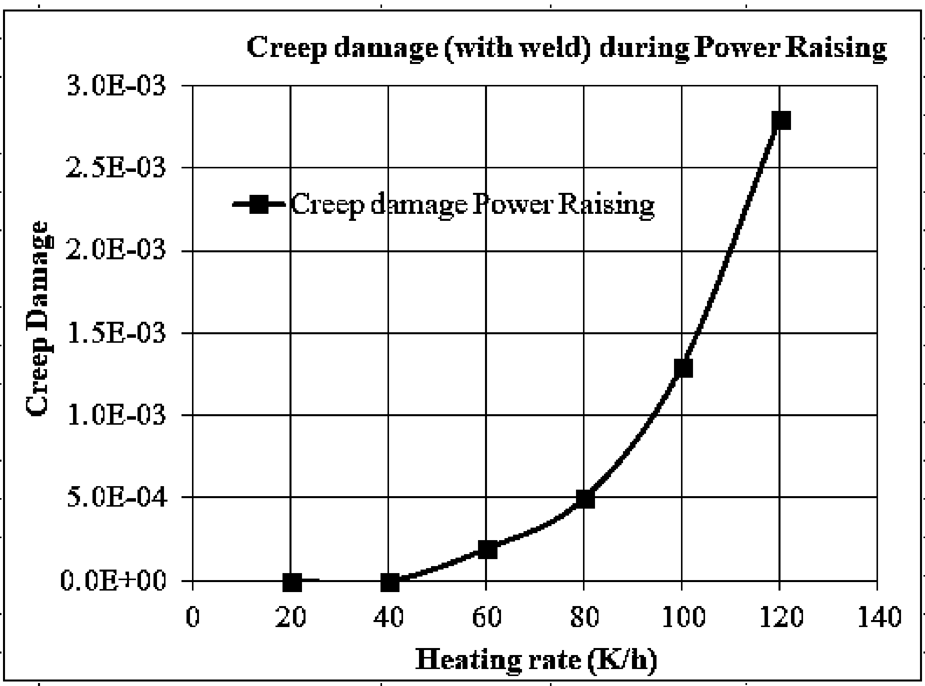

Figure 5.8 Creep damage (with weld) at IHX tubesheet during power raising

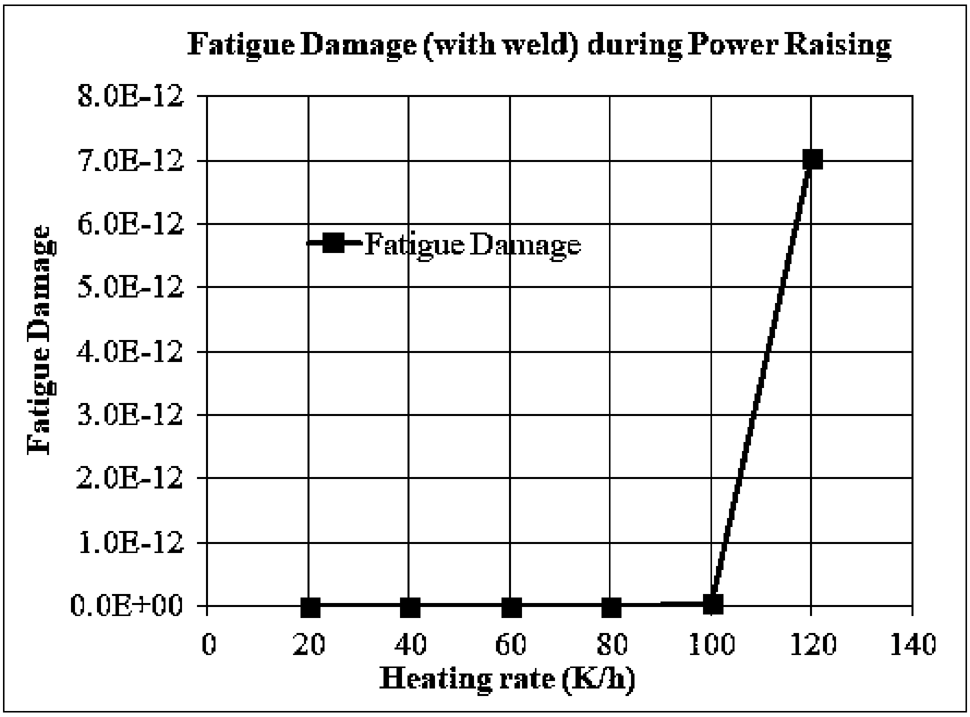

Figure 5.9 Fatigue damage (with weld) at IHX tubesheet during power raising

Figure 5.8 shows that the creep damage is almost constant initially and then increases with an increase in heating rate. Figure 5.9 shows that fatigue damage increases as the heating rate increases due to high thermal stresses due to power raising. The effective damage curve is same as that of the creep damage curve. It is observed that the effective damage increases with increase in heating rate. The damage at 120 K/h is 0.0028, which is very less than its allowable limit, 1.

5.5. Effect of power raising at the free level interface of sodium

It is observed that the creep and fatigue damage values at the critical locations submerged in sodium are below the limit, 1. The locations of the primary system components that are at the free level interface of sodium are analyzed in this section.

5.5.1. Application of numerical model for power raising case

During power raising, the sodium level increases along with an increase in sodium temperature. When an element is considered, we find that there is an abrupt shift from argon gas ambience to sodium ambience, which can result in high thermal stresses. As there is no conventional code available to tackle such intricate loading conditions, a numerical model developed in section 4.4 has been used to estimate the thermal stresses for partially immersed components. The same numerical model has been used for power raising application with a change in the logic in the flowchart. The basic difference between the flowcharts for crash cooling case and power raising case is that the sodium level and temperature fall in crash cooling case, whereas they rise in power raising case. The numerical discretization adopted for imposing the variation in sodium temperature and level during power raising is presented in Figure 5.10, with a view of a solid axisymmetric section of a shell. Figure 5.11 shows the process flowchart used for power raising case.

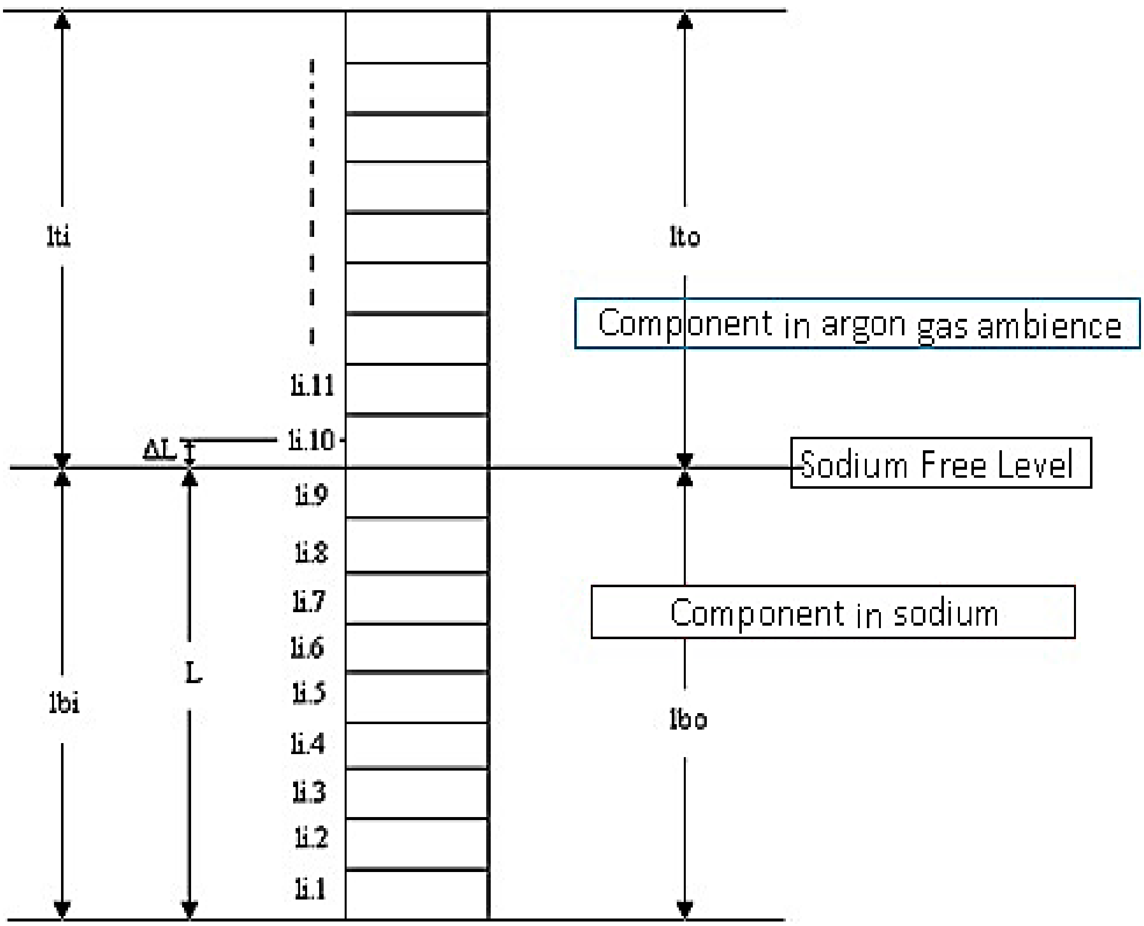

Figure 5.10 Schematic of the numerical discretization for power raising case

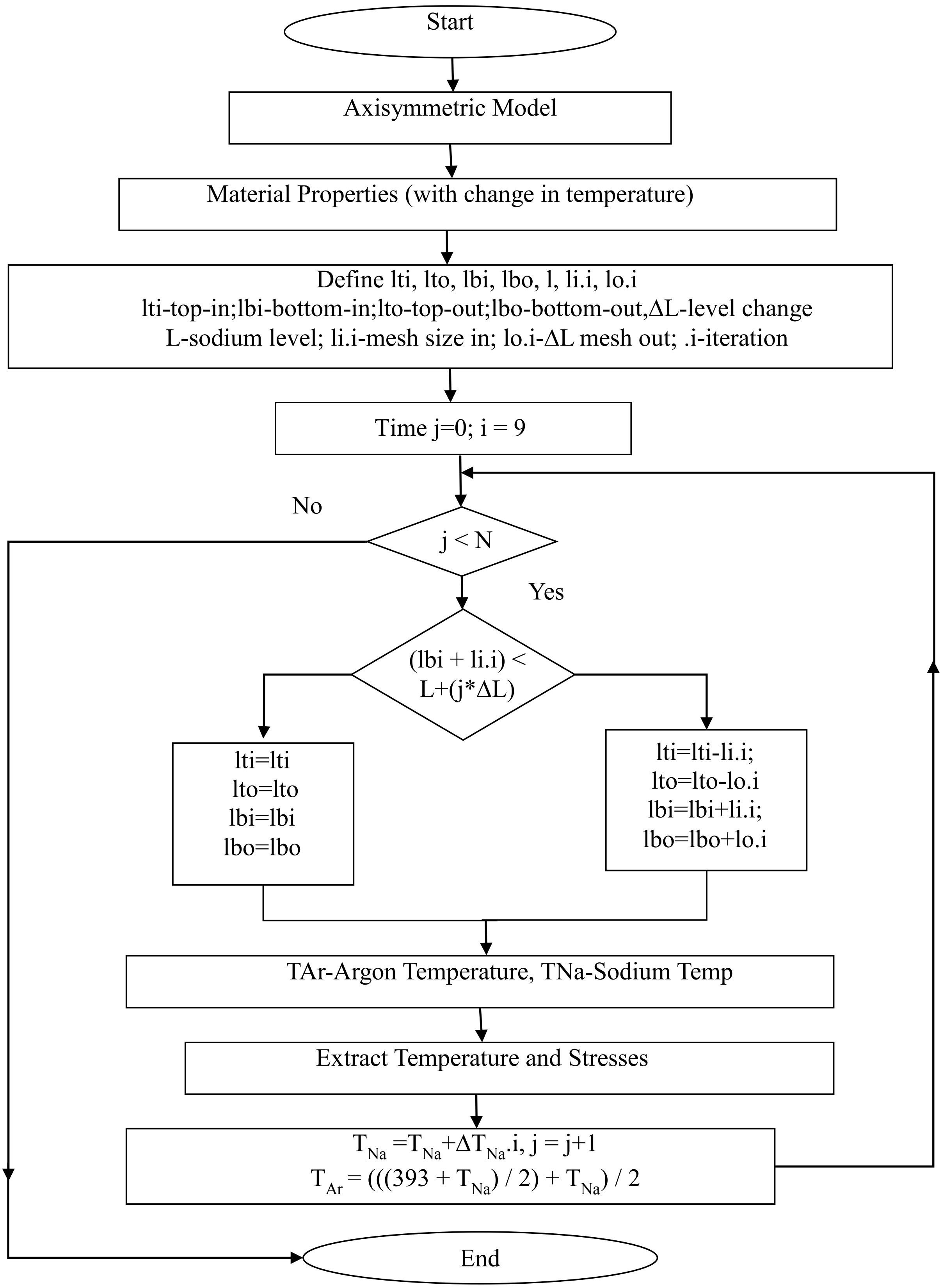

Figure 5.11 Flowchart for power raising used in the numerical model

Figure 5.10 illustrates the sectional view of a cylindrical component, indicating the sodium free level. The portion of the cylinder that is below the free level (lbi and lbo, where ‘i’ and ‘o’ stand for in and out respectively), is in the ambience of sodium and that above (lti and lto, where ‘t’ stands for top and ‘b’ for bottom) is enveloped by argon cover gas. The component is modeled into fine segments (li.i), where .i is the number given to a particular segment and can be invoked.

To start the iterations, j=0, where j represents time in minutes. The initial sodium level is (L). In the next iteration, the sodium level increases by (ΔL). When (lbi + li.i), i.e., (lbi + li.10) in Figure 5.10 is less than the updated sodium level (L+ (j*ΔL)), it implies that the sodium level has raised above the element (li.10). Thus the lengths lti, lto, lbi and lbo are updated (lti = lti - li.i; lto = lto - lo.i; lbi = lbi + li.i; lbo = lbo + lo.i) as shown in the flowchart, Figure 5.11.

The temperatures of argon gas (T_{Ar}) and sodium (T_{Na}) are provided to the code as per the loading conditions for each component. As the top portion is surrounded by argon gas, h = 10 W/m^{2}K is deduced based on the correlations provided in [20]. Due to the high heat transfer coefficient of sodium, conduction heat transfer is contemplated for the portion under sodium.

5.5.2. Boundary conditions

The CP, PSP standpipe, and IHX hang from the top and the inner vessel is bolted at the bottom, at the grid plate. Thus the boundary condition is considered as Uz = 0 (axial displacement has been arrested).

5.5.3. General loading conditions

The reactor main vessel is filled with primary sodium. The inner vessel separates the hot pool sodium from the cold pool sodium. The level of hot pool sodium (at 453 K) at the start of power raising is 26700 mm. After reaching full power (823 K), the hot pool sodium level reaches 27400 mm. The maximum sodium temperature is taken as 833 K (conservatively). Thus, the sodium expands to a height of 700 mm while gaining 380 K temperature rise. The height above the hot pool is encompassed by argon gas, whose temperature (T_{Arh}) changes, as per equation 5.1, given in [136].

$$\mathrm{T_{Arh}} = \frac{\frac{393 + \mathrm{T_{Nah}}}{2} + T_{Nah}}{2}$$

5.1

The length above the cold pool (lto) is enveloped by argon gas whose temperature (T_{Arc}) changes as per equation.

$$\mathrm{T_{Arc}} = \frac{T_{Nah} + T_{Nac}}{2}$$

5.2

T_{Nah} and T_{Nac} are hot pool and cold pool sodium temperatures respectively.

The time taken to heat the primary sodium and the raise in sodium level at all the heating rates considered are given in Table 5.6.

Table 5.6 Input parameters used in the analysis

Heating rate	Heating time	Raise in sodium level in 1 hour
20 K/h	20 h	35 mm
40 K/h	10 h	70 mm
60 K/h	6.6 h	105 mm
80 K/h	5 h	140 mm
100 K/h	4 h	175 mm
120 K/h	3.3 h	210 mm

Thermo-mechanical analysis has been carried out for all the heating rates considered, as per the input parameters given in Table 5.6, at the free level location for all the reactor components. The loading conditions that are specific to each component are given in their corresponding sections.

5.5.4. Thermo-mechanical analysis at free level of CP

The geometrical details of the CP are given in section 1.1.7.1. The hot pool sodium is initially below the USP and CP outer shell junction. On power raising, the sodium level rises by 700 mm, covering the CP-USP junction. The temperature of sodium within the CP is 7 K more than that outside. The argon gas temperature is calculated using equation 5.1.

Thermo-mechanical analysis of the CP at the free level location, with the above mentioned loading and boundary conditions has been carried out for all the heating rates considered. The evolution of temperature of the CP and the corresponding stress distribution (Tresca) are shown in Figure 5.12a, and Figure 5.12b, respectively, for the case of heating rate at 20 K/h. The maximum thermal stresses increase with increase in heating rate.

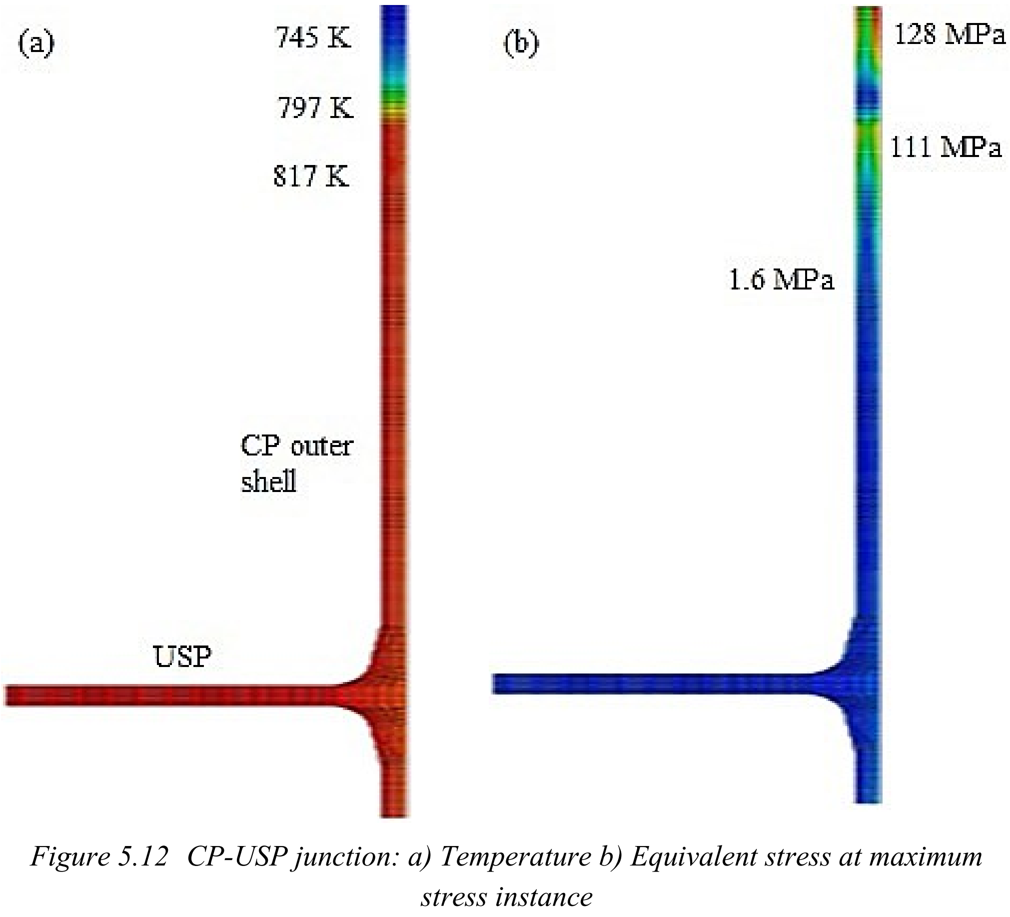

Figure 5.12 CP-USP junction: a) Temperature b) Equivalent stress at maximum stress instance

The creep-fatigue damage calculations for power raising has been carried out for all the heating rates considered. Table 5.7 shows some of them.

Table 5.7 Creep-fatigue damage in CP at various heating rates

Cases	**20 K/h**	**60 K/h**	**120 K/h**
$\Delta\sigma_{Tot}$ (MPa)	128	168	250
P_{max} (MPa) [131]	7.5	7.5	7.5
Total strain (%)	0.079	0.1	0.16
Fatigue damage	3.53E-10	7.59E-07	2.19E-03
Time spent in creep regime per cycle (h)	6.25	2.08	1.04
S_r (MPa)	135.2	150.1	173.5
Creep damage	0.0078	0.006	0.0096

The D_{eff} curve as a function of various heating rates is shown in Figure 5.13. The effective damage at CP free level is the least at 60 K/h, and the damage value is 0.006. It may be observed from Figure 5.13, that the Deff decreases initially and then increases because of the following reason. The creep damage is a function of stress and hold time. The maximum thermal stresses increase with an increase in heating rate, as shown in Table 5.7. The time spent in the creep regime decreases as the heating rate increases. Thus, the creep damage decreases initially due to lower hold time, after a heating rate of 60 K/h, the creep damage increases due to higher thermal stresses.

When the presence of welds at the maximum stress location is considered, the fatigue damage values are considerable. The creep damage values remain the same, as the weld strength reduction factor is 1 up to 10 hours of time spent in creep regime. The effective damage curve at the CP free level, considering the presence of welds is shown in Figure 5.13. It may be observed that the damage increases with increase in heating rate because of the combined effect of creep and fatigue. When the welds are not considered, the fatigue damage is negligible and the effective damage curve follows the behavior of creep damage curve.

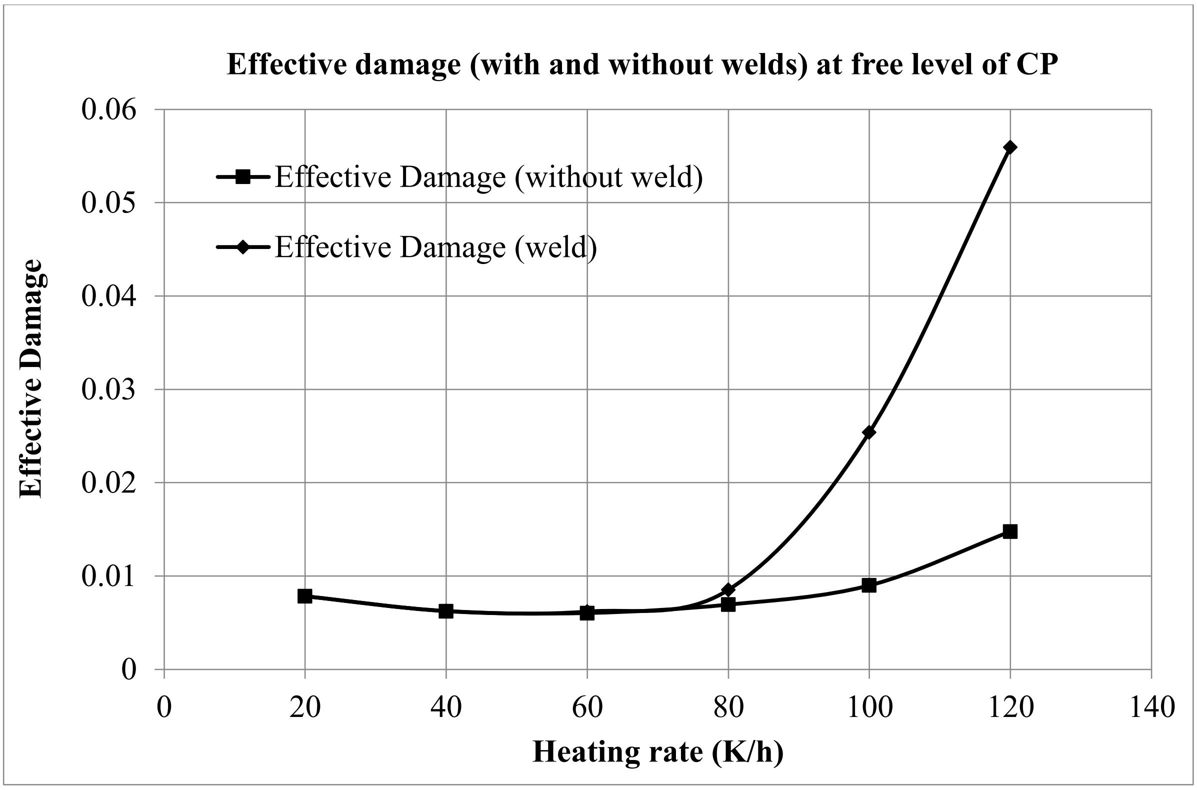

Figure 5.13 Effective damage at CP free level location (with and without welds)

5.5.5. Thermo-mechanical analysis at free level of inner vessel

The geometrical details of inner vessel and its functions are given in section 1.1.7.2. The temperature difference between the hot and cold pool sodium that changes with time constitutes the thermal loading. The evolution of sodium temperature at the hot (inner) and cold (outer) surfaces of the inner vessel for heating rate 20 K/h is shown in Figure 5.14 [137].

As the temperature of sodium rises, the sodium level in the hot and cold pools also rise, and the difference in height (of 1.5 m) is maintained during power raising. The argon cover gas above hot pool sodium changes as per equation 5.1, and that above cold pool sodium varies as per equation 5.2. Thermo-mechanical analysis of the inner vessel at the free level location has been carried out for all the heating rates considered. The maximum temperature and the corresponding equivalent stress distribution (Tresca stress) of the inner vessel during power raising at 20 K/h are shown in Figure 5.15. The maximum secondary stress (ΔQ) at 20 K/h, 40 K/h, 60 K/h, 80 K/h, 100 K/h and 120 K/h are 210 MPa, 239 MPa, 261 MPa, 280 MPa, 302 MPa and 323 MPa respectively.

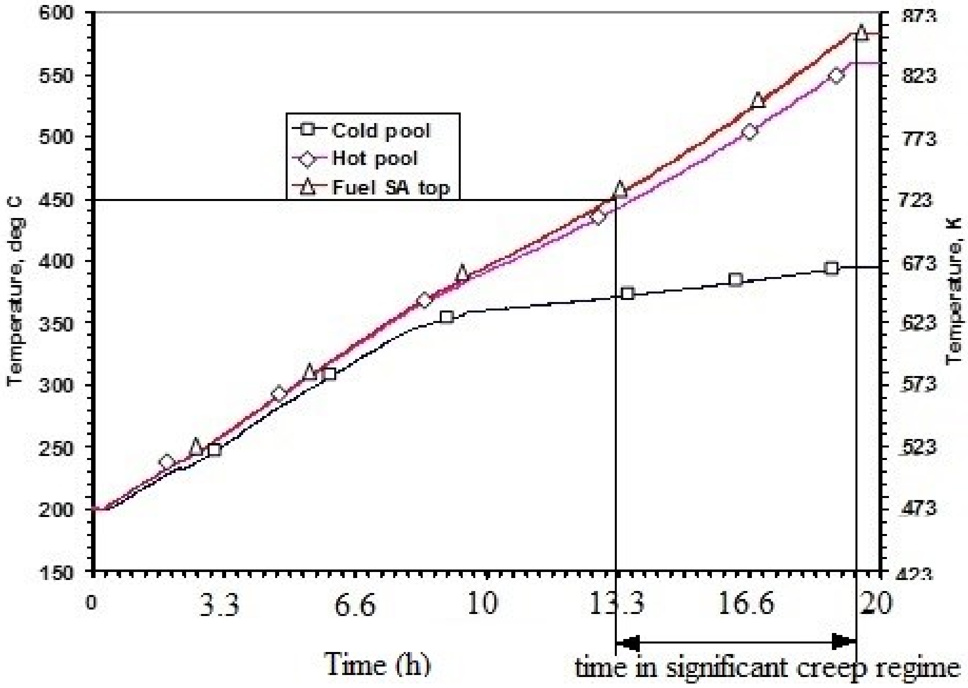

Figure 5.14 Evolution of primary circuit temperatures during wait and raise mode of plant startup [137]

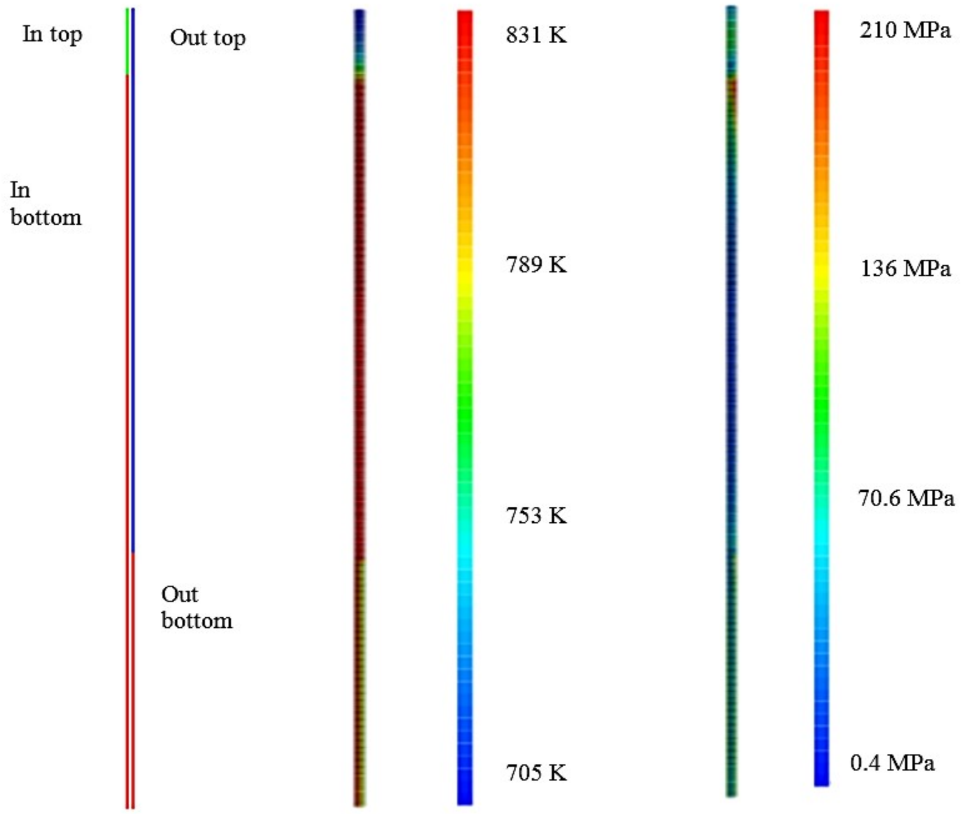

Figure 5.15 Temperature and equivalent stress distribution in inner vessel at free level at 20 K/h

5.5.5.1. Shake down criteria check

The progressive deformation has been checked using the shake down criteria in Table 5.8 as per equation 2.15.

Table 5.8 Shakedown criteria check at the free level location

Heating Rate (K/h)	**Max ($P_L + P_b$) (MPa)**	**ΔQ (MPa)**	**3Sm (MPa)**	**Max ($P_L + P_b$) + ΔQ < 3Sm**
20	14.0	210	288	224 < 288
40	14.0	239	288	253 < 288
60	14.0	261	288	275 < 288
80	14.0	280	288	**294 > 288**
100	14.0	302	288	**316 > 288**
120	14.0	323	288	**337 > 288**

It is observed from Table 5.8, that the shake down criteria limits are not met for the heating rates 80 K/h, 100 K/h and 120 K/h. Hence efficiency index method is followed to check the progressive deformations for the above three heating rates.

5.5.5.2. Efficiency index method

The effective stress intensities (P1 and P3) and the sum of creep strain and plastic strain are compared with their allowable values as shown in Table 5.9

Table 5.9 Design check for progressive deformation

Cases	**80 K/h**	**100 K/h**	**120 K/h**	**Allowable**
P_1	26.6	27.7	28.7	124.8
P_3	58.5	59.7	61.5	187.2
$\varepsilon_p + \varepsilon_c$ (for 1.25 P_1) (%)	3.21 E-05	3.63 E-05	3.98 E-05	1
$\varepsilon_p + \varepsilon_c$ (for 1.25 P_3) (%)	7.33 E-04	8.67 E-03	1.0 E-02	1*

* Conservatively allowable values of weld are used, anticipating the presence of weld at peak stress location.

Table 5.9 shows that the sum of plastic strain and creep strains are well below the limit, 1. The low values are attributed to the low primary stresses though the secondary stresses are high.

5.5.5.3. Effective creep-fatigue damage

The D_{eff} curve with and without considering the presence of welds is given in Figure 5.16. When the presence of welds is not considered, it is observed that the lowest damage of 0.031 is at a heating rate of 40 K/h. The D_{eff} decreases initially due to decrease in the time spent in creep regime and then increases due to high secondary stresses (similar to CP). The fatigue damage is negligible when the welds are not considered. Hence the behavior of the D_{eff} curve is similar to that of creep damage curve.

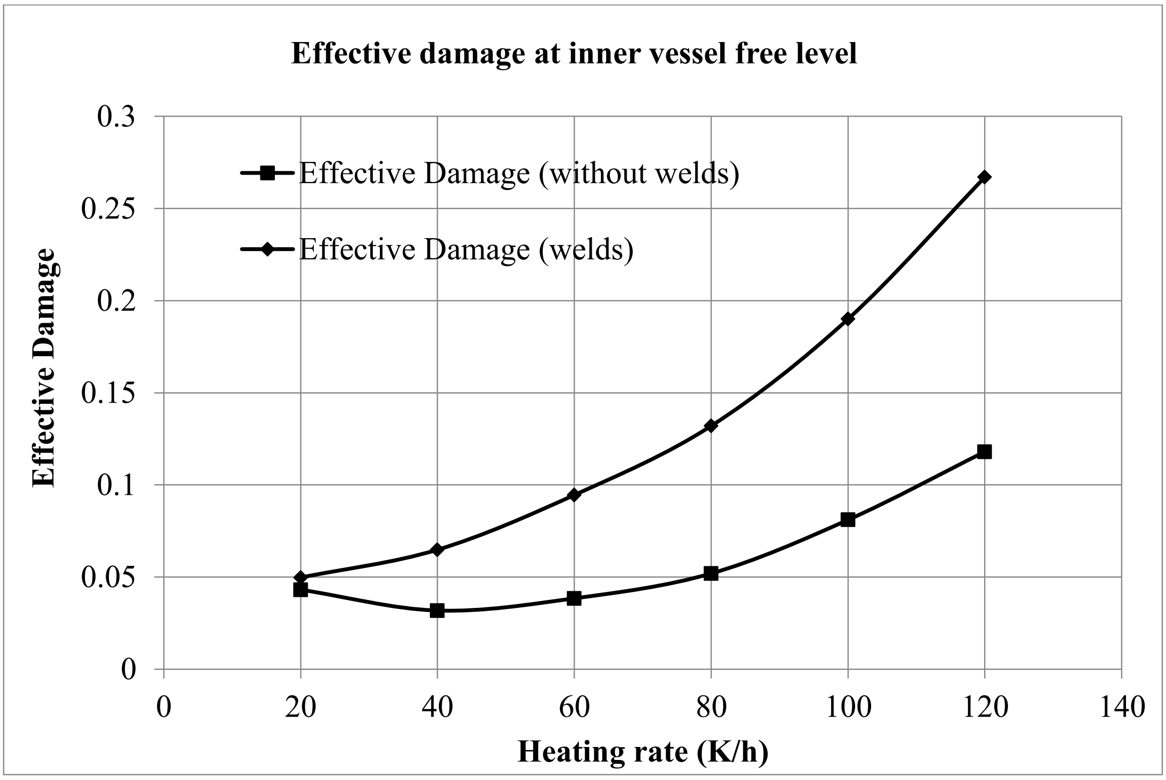

Figure 5.16 Effective damage at free level of inner vessel during power raising with and without the presence of welds

The fatigue damage increases with an increase in heating rates is all cases. This is due to the increase in stress with an increase in heating rate. Unlike fatigue damage, creep damage may increase or decrease with an increase in heating rate due to the decrease in time spent in creep regime. Creep damage behavior depends on whether the stresses or governing or the time spent in creep regime is governing.

When the presence of welds is considered, the fatigue damage values are considerable. Hence the effective damage curve does not behave similar to creep damage curve. The combined effect of creep damage and fatigue damage results in the effective damage behavior as shown in Figure 5.16.

5.5.6. Thermo-mechanical analysis at free level of PSP standpipe

The PSP standpipe is a part of inner vessel which is one of the major components in contact with the primary sodium. The geometric details are given in section 1.1.7.4. Unlike inner vessel, the PSP standpipe has hot pool sodium on the exterior side, and cold pool sodium on the interior side (Figure 1.12). The difference in the height of hot and cold pool sodium is 2.0 m. The evolution of sodium temperature at the hot and cold surfaces of inner vessel for heating rate 20 K/h, as shown in Figure 5.14 is also used for PSP standpipe. The argon gas temperature is calculated using equation 5.1.

Thermo-mechanical analysis has been carried out at the free level location at all the heating rates considered. The maximum temperature and the corresponding stress distribution (Tresca) at 20 K/h are shown in Figure 5.17.

The maximum secondary stress due to power raising at 20 K/h is 123 MPa. The effective damage at PSP standpipe free level is the least at 40 K/h, and the value is 0.0053, when the presence of welds is not considered. Its value is 0.00534 when the presence of welds is considered. The effective damage curve at the free level of PSP standpipe, considering the presence of welds is shown in Figure 5.20. The magnitude of the D_{eff} is very less due to the lower diameter of PSP standpipe (1019 mm), when compared to that of inner vessel (6093 mm). Lower diameter of PSP standpipe results in lower thermal stresses, and hence lower D_{eff} (when compared to inner vessel).

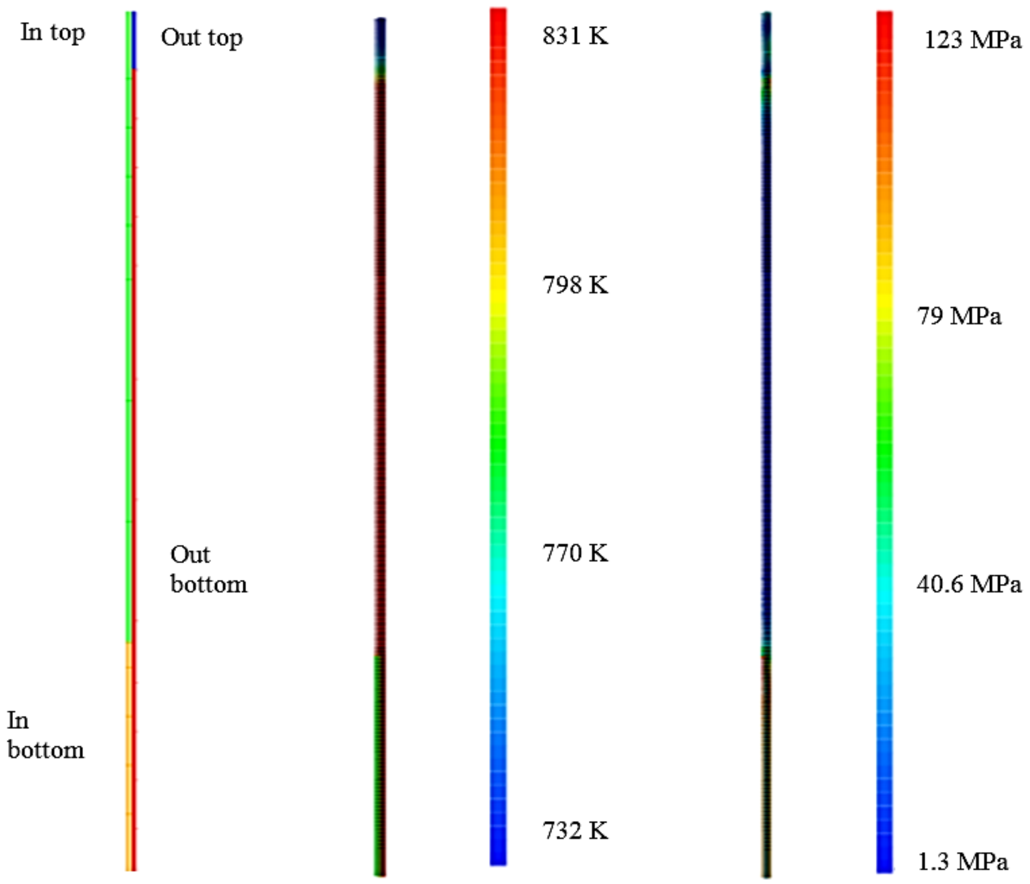

Figure 5.17 Temperature and stress distribution at PSP standpipe free level

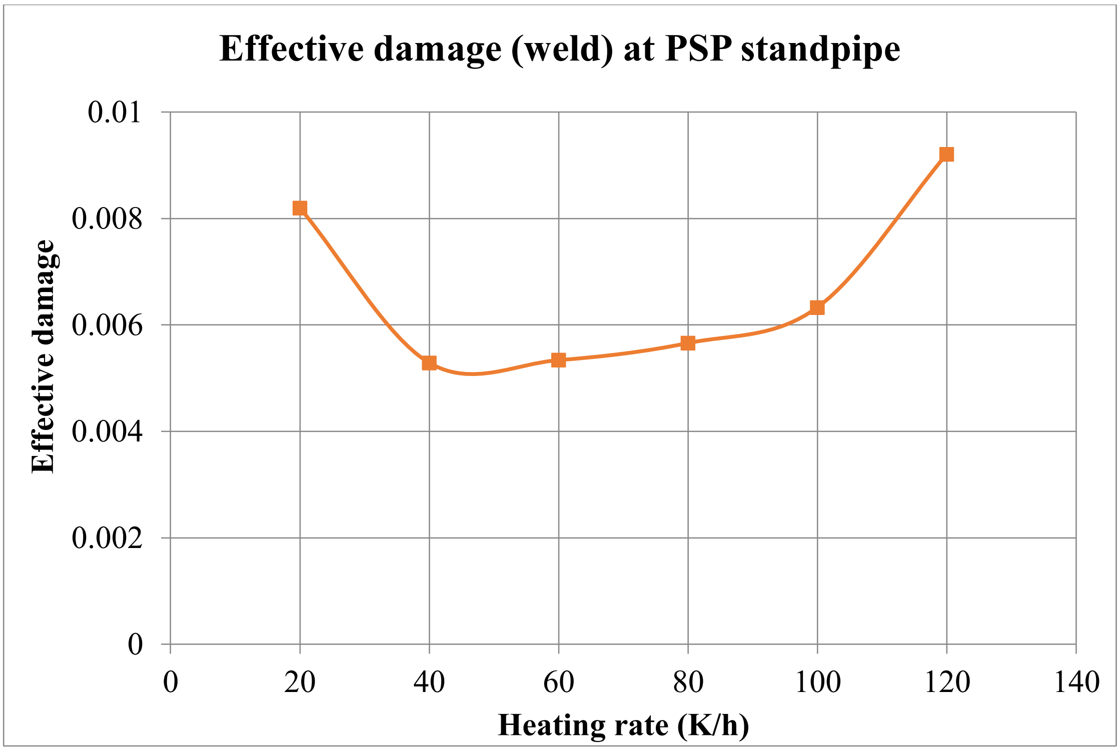

Figure 5.18 Effective damage (weld) at free level of PSP standpipe

5.5.7. Thermo-mechanical analysis at free level of IHX

The geometrical details of IHX are given in section 1.1.7.3. The free level of sodium is at the upper secondary sodium header. It consists of two concentric cylinders, the inner one being the IHX outer shell and the outer cylinder being the sleeve valve as depicted in the inset of Figure 1.8.

The inner side of IHX shell is surrounded by secondary sodium. The outer side of the IHX shell is surrounded by primary sodium at the bottom and argon cover gas at the top. The sleeve is surrounded by primary sodium at the bottom and argon cover gas at the top (both inside and outside). The evolution of sodium temperature at various locations namely, IHX shell inside (secondary sodium outlet), IHX shell out, IHX sleeve inside and IHX sleeve out (primary sodium inlet) for heating rate 20 K/h is shown in Figure 5.19. The argon gas temperature is taken the same for all the three top regions (top of shell out, sleeve in and sleeve out) and is calculated using equation 5.1.

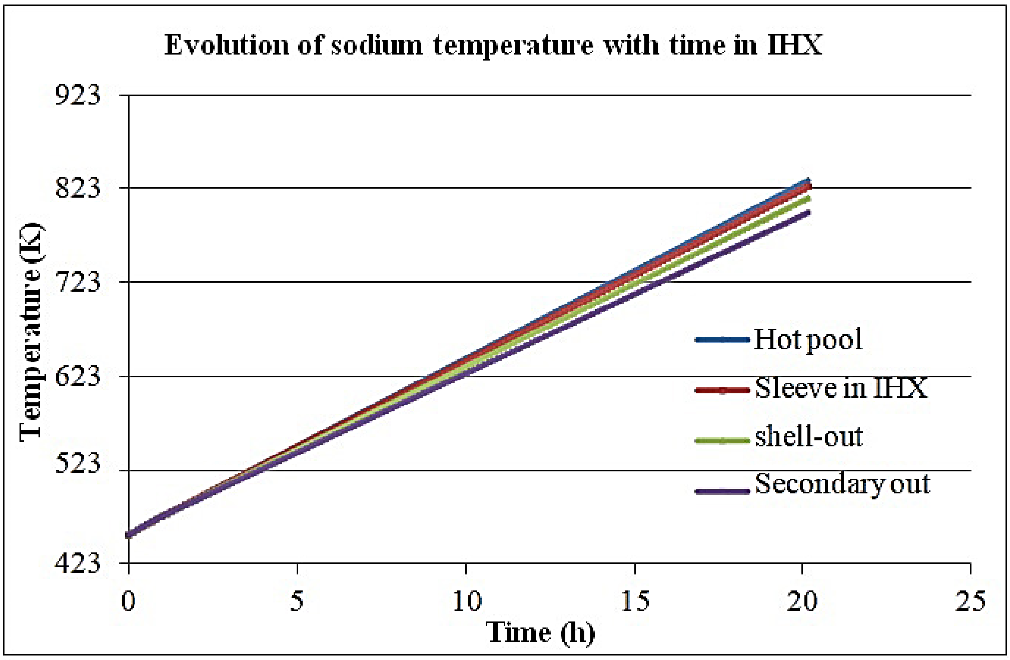

Figure 5.19 Evolution of sodium temperature with time at IHX free level location

Thermo-mechanical analysis of the IHX free level location has been carried out at all the heating rates considered. The maximum temperature and the corresponding equivalent stress distribution (Tresca) are shown in Figure 5.20. The maximum secondary stress due to power raising at 20 K/h is 96 MPa. It is observed that the maximum stress location is the sleeve valve. The reason is that, there is continuous sodium in the inner side of the IHX shell, resulting in lower axial temperature gradient, when compared to sleeve, which has sodium argon interface on both the sides.

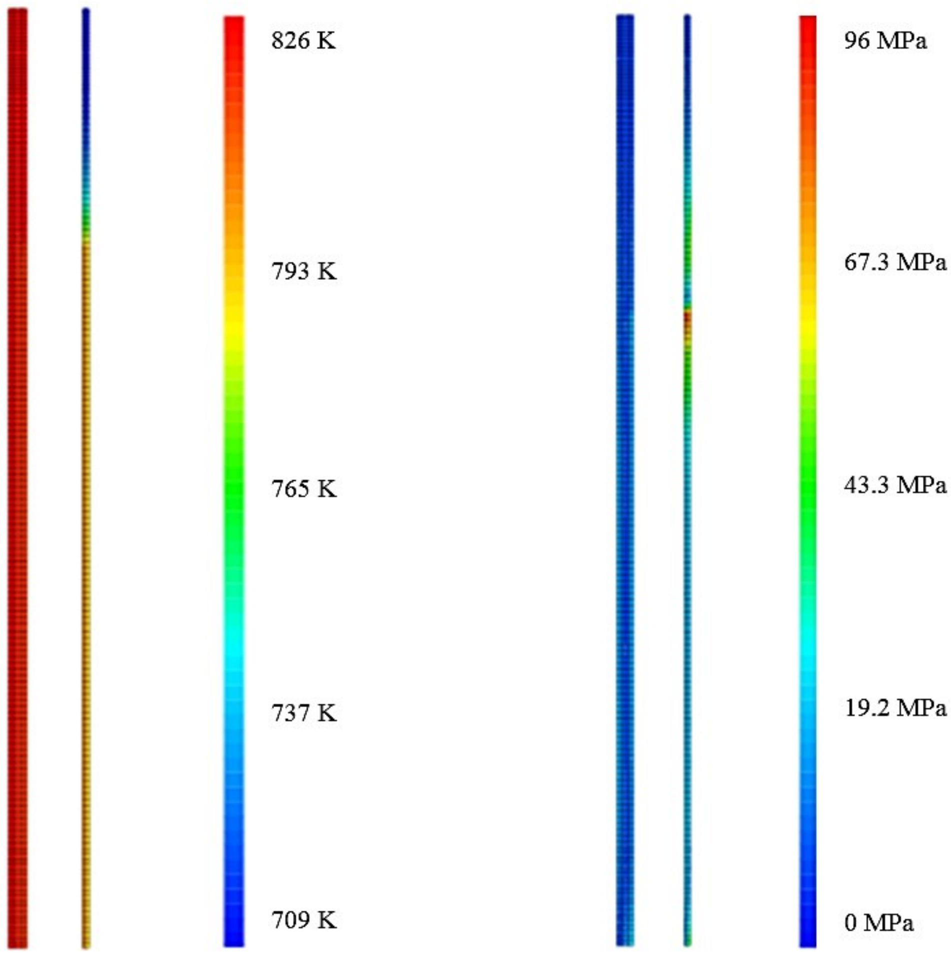

Figure 5.20 Temperature and stress distribution at IHX free level during power raising

The effective damage values at IHX free level with and without considering the presence of welds are almost the same. The D_{eff} curve considering the presence of welds is shown in Figure 5.21. The D_{eff} values for IHX free level are low when compared to other components due to lower diameter and thickness.

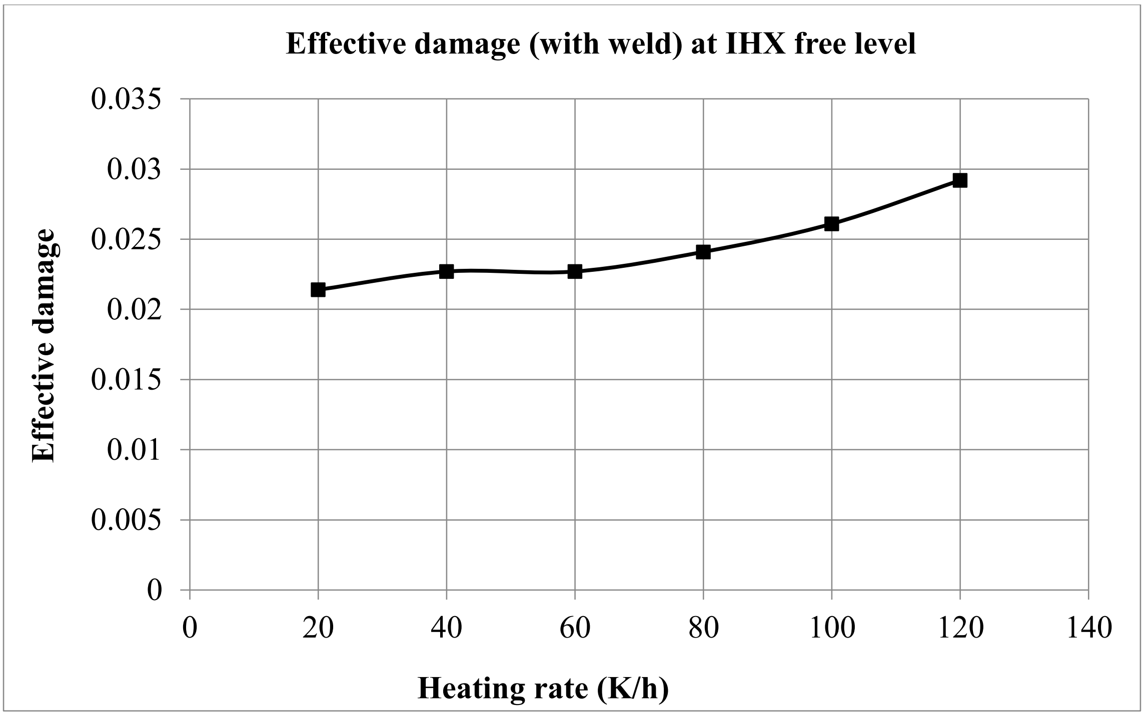

Figure 5.21 Effective damage (weld) at IHX free level

5.6. Discussion and recommendation

The creep-fatigue damage estimation has been done for all the primary system components with and without considering the presence of welds at the maximum stress locations. The comparison of all the components has been done to arrive at the optimum heating rate.

5.6.1. Comparison of stresses

The maximum stresses at the free level locations of the reactor components have been given in Table 5.10. The diameter and thickness details are given in Table 5.11. The following are the observations:

- The stresses increase with increase in heating rate.
- Stresses are the least in IHX sleeve due to lower diameter and thickness. It is followed by PSP standpipe and CP due to lower diameter and thicknesses.
- Maximum stresses are observed in inner vessel due to higher diameter, higher thickness and difference in hot and cold pool sodium levels.

- Inner vessel is the critical component.

Table 5.10 Comparison of maximum stresses (MPa) at free level locations

Component	**20 K/h**	**40 K/h**	**60 K/h**	**80 K/h**	**100 K/h**	**120 K/h**
Control Plug	128	148	168	195	225	250
IHX sleeve	96	116	136	156	176	194
PSP Standpipe	123	133	152	170	186	203
Inner Vessel	210	239	261	280	302	323

Table 5.11 Diameter and thickness of primary system components

Component	**Diameter (mm)**	**Thickness (mm)**
Control Plug	1110	10
IHX (sleeve)	1000	5
PSP Standpipe	1019	12
Inner Vessel	6093	15

5.6.2. Comparison of effective damage

The creep damage, fatigue damage and effective damage are estimated for all the reactor components. It is observed that the fatigue damage increases with increase in heating rate. The creep damage decreases initially due to decrease in time spent in creep regime with increase in heating rate, and then increases with increase in stresses. When the stresses are constant, creep damage decreases as the time spent in creep regime decreases with increase in heating rate. The behavior of creep damage curve depends on the values of stresses and time spent in creep regime.

The behavior of effective damage curves depend on the magnitude of creep and fatigue damage values. If the fatigue damage values are negligible, its behavior is similar to creep damage curve, and if the fatigue damage values are considerable, then its behavior is similar to that of fatigue damage curve. When both the creep and fatigue damage values are considerable, the effective damage curve behaves as a combination of both the curves.

5.6.2.1. Without considering the presence of welds

The D_{eff} values without considering the presence of welds at the critical locations, for all the components are given in Table 5.12 and is shown graphically in Figure 5.22.

Table 5.12 Effective damage values at all locations without considering welds

Heating rate (K/h)	CP_FL	IV_FL	PSP_FL	IHX-free level	CP_sub	IV_sub	IHX-TS (sub)
20	7.8E-03	4.3E-02	8.2E-03	2.1E-02	1.9E-07	2.3E-01	1.9E-05
40	6.2E-03	3.2E-02	5.3E-03	2.3E-02	9.7E-08	1.2E-01	6.2E-05
60	6.0E-03	3.8E-02	5.3E-03	2.3E-02	6.5E-08	7.7E-02	2.0E-04
80	6.9E-03	5.2E-02	5.5E-03	2.4E-02	4.9E-08	5.8E-02	5.0E-04
100	9.0E-03	8.1E-02	5.6E-03	2.6E-02	3.9E-08	4.6E-02	1.3E-03
120	1.5E-02	1.2E-01	6.0E-03	2.7E-02	3.2E-08	3.8E-02	2.8E-03

Figure 5.22 shows that the maximum D_{eff} values are at inner vessel submerged location (inner vessel - IHX junction) and inner vessel free level locations. The maximum stress is constant at the inner vessel-IHX junction for all the heating rates considered. However, as the time spent in creep regime decreases with increase in heating rate, the creep damage and thereby, the effective damage decreases as depicted in the curve. The curves intersect at 83 K/h, which is the optimum heating rate when the presence of welds at the maximum stress location is not considered. The maximum D_{eff} at 83 K/h is 0.055, which is less than its allowable limit, 1.

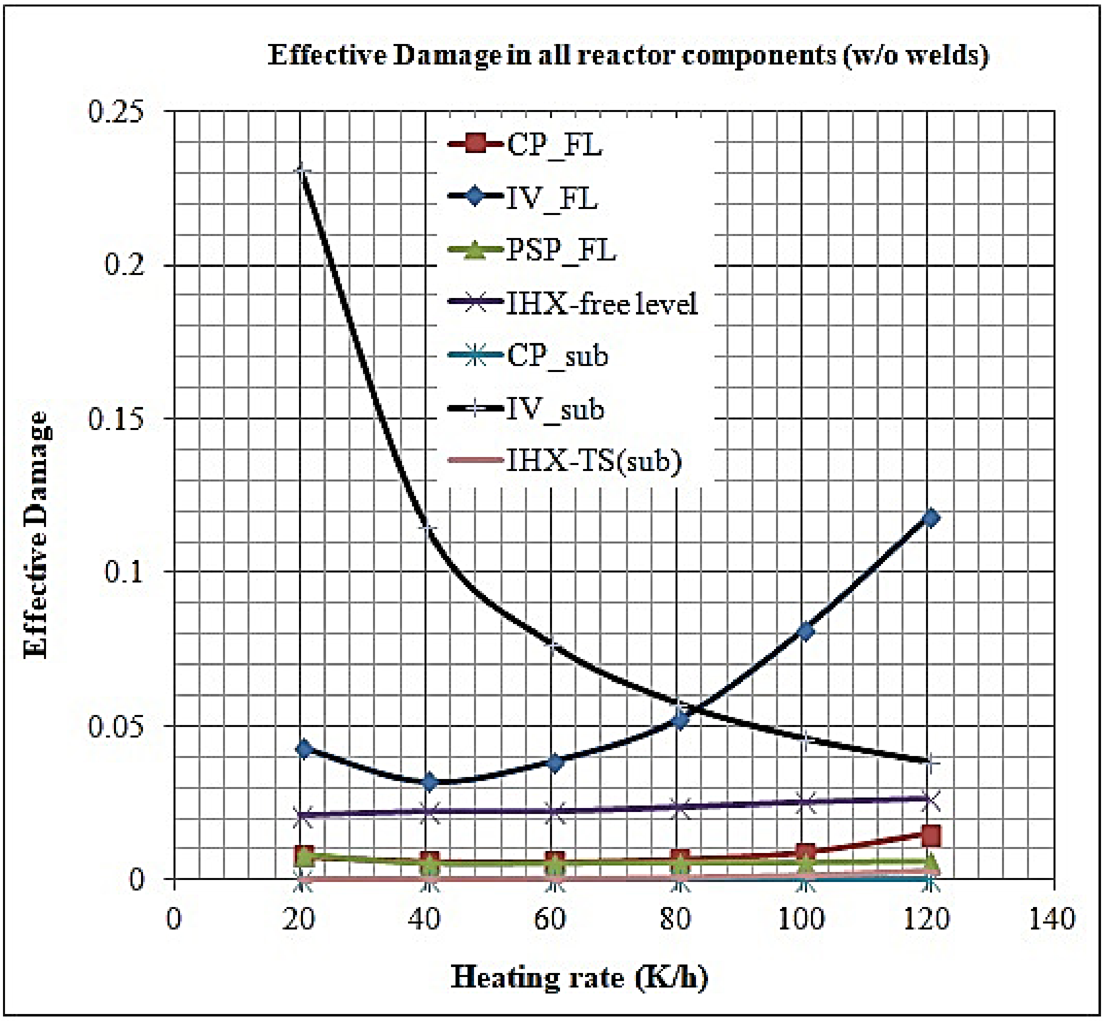

Figure 5.22 Effective damage in all components without considering the presence of welds

5.6.2.2. Considering the presence of welds

In practical application, there can be welds at the critical locations, thus it is a safe practice to account for the presence of welds. The D_{eff} values for all the components are given in Table 5.13 and is shown graphically in Figure 5.23. The maximum D_{eff} values are at inner vessel submerged location (inner vessel- IHX junction) and inner vessel free level locations. The curves intersect at 56 K/h, which is the optimum heating rate when the presence of welds at the maximum stress location is considered. The maximum D_{eff} at 56 K/h is 0.085, which is less than its allowable limit, 1.

Table 5.13 Effective damage at all locations considering the presence of welds

Heating rate (K/h)	CP_FL	IV_FL	PSP_FL	IHX-free level	CP_sub	IV_sub	IHX-TS(sub)
20	7.8E-03	5.0E-02	8.2E-03	2.1E-02	1.9E-07	2.3E-01	1.9E-05
40	6.3E-03	6.5E-02	5.3E-03	2.3E-02	9.7E-08	1.2E-01	6.2E-05
60	6.2E-03	9.5E-02	5.3E-03	2.3E-02	6.5E-08	7.8E-02	2.0E-04
80	8.5E-03	1.3E-01	5.7E-03	2.4E-02	4.9E-08	5.8E-02	5.0E-04
100	2.5E-02	1.9E-01	6.3E-03	2.6E-02	3.9E-08	4.7E-02	1.3E-03
120	5.6E-02	2.7E-01	9.2E-03	2.9E-02	3.2E-08	3.9E-02	2.8E-03

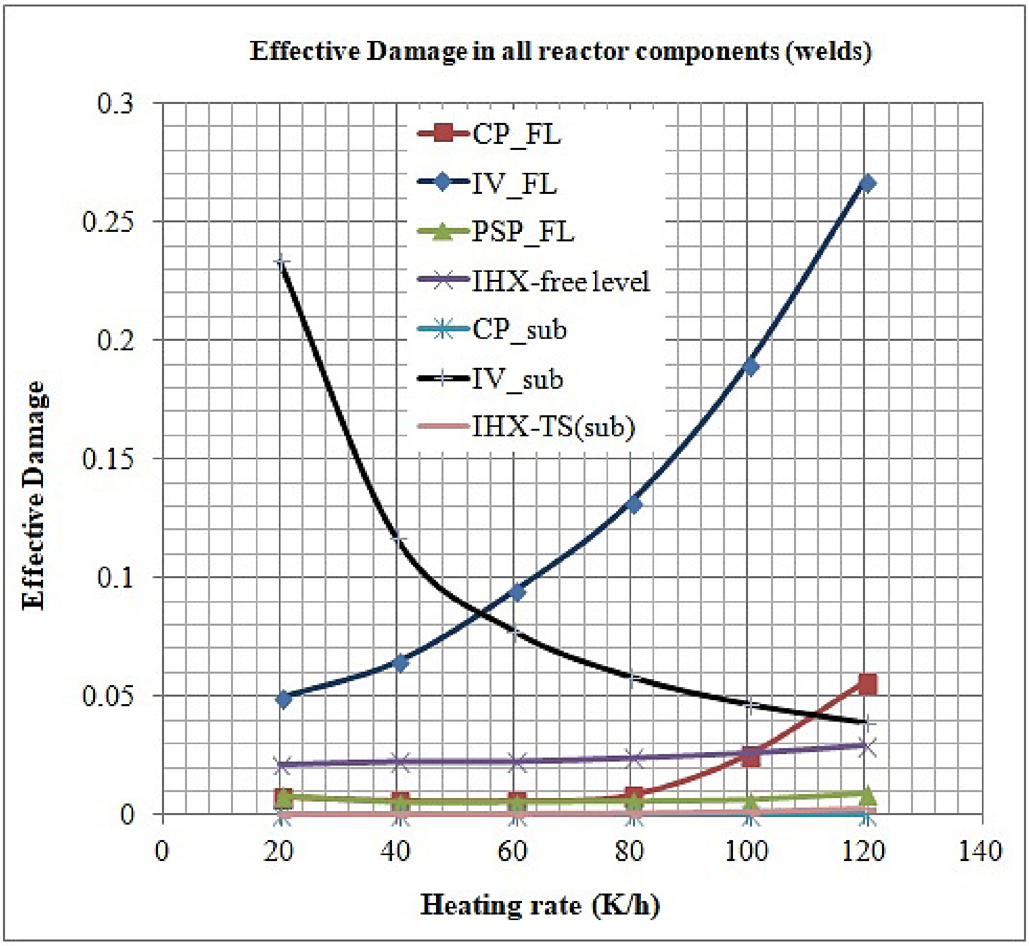

Figure 5.23 Effective damage in all components considering the presence of welds

5.6.3. Recommendation

The optimum heating rates in view of all the critical locations, with and without considering the presence of welds are 56 K/h and 83 K/h respectively. However, the inner vessel is the critical component in both the cases. The presence of welds is expected at both the submerged and free level locations of inner vessel. Hence, the heating rate of 56 K/h is recommended during power raising operation of PFBR. The effective damage in inner vessel during power raising operation is 0.085. The D_{eff} in inner vessel during normal operation is 0.183. Thus there is enough margin for reaching its allowable limit, 1.

5.7. Closure

The effect of heating rate during power raising operation on the primary system components that are in contact with primary sodium has been investigated. Parametric studies are carried out to find the optimum heating rate with minimal structural damage and minimal start-up time, and a heating rate of 56 K/h is recommended. The study forms a benchmark for other fast reactors for deciding upon the heating rate during start-up of the reactor. Besides the reactor components, fuel clad tubes are also the critical components that are affected by the primary sodium heating rate. Hence, the integrity of fuel clad tubes at this range of heating rates is studied in the next chapter.

References

[127] K. Natesan, K. Velusamy, P. Selvaraj, P. Chellapandi. Integrated Plant Operations. PFBR/01151/DN/1018/Rev-C, (2011).

[128] K. Devan, A. Riyas, M. Alagan, P. Mohanakrishnan. A new physics design of control saftery rods for prototype fast breeder reactor, Annals of Nuclear Energy, 35, 1484-1491, (2008).

[129] R. Vijayashree, R. Veerasamy, Sudheer Patri, P. Chellapandi, G. Vaidyanathan, S. C. Chetal, Baldev Raj. Design, development, testing & qualification of diverse safety rod & drive mechanism for prototype fast breeder reactor, (2010), J. Eng. Gas Turbines Power, 132, pp.102921-102929.

[130] V. Rajan Babu, R. Veerasamy, Sudheer Patri, S. Ignatius Sundar Raj, S.C.S.P. Kumar Krovvidi, S.K. Dash, C. Meikandamurthy, K.K. Rajan, P. Puthiyavinayagam, P. Chellapandi, G. Vaidyanathan, S.C. Chetal, C. Babu Rao. Testing and qualification of Control & Safety Rod and its drive mechanism of Fast Breeder Reactor, Nuclear Engineering and Design 240, 1728–1738 (2010).

[131] P. Chellapandi and S.C. Chetal. Life Prediction of Control Plug. PFBR/RG/31410/DN/1022/R-A (1996).

[132] R. Srinivasan and P. Chellapandi. Stress Analysis of IHX under Mechanical Loading. PFBR/32130/DN/1045/R-A (2002).

[133] RCC-MR Section III - Tome-1 - Subsection B: Class N1Rx reactor components and supports (2012).

[134] Suman Gupta and P. Chellapandi. Application of RCC-MR for the structural design of tubesheet of Intermediate Heat Exchanger for a sodium cooled fast reactor. Nuclear Engineering and Design, 280 (2014) 181-200.

[135] Cengel Yunus, Ghajar Afshin. Heat and Mass Transfer: Fundamentals and Applications. McGraw Hill Education, (2010).

[136] Pranav Paliwal, U. Parthasarathy, K. Velusamy, T. Sundararajan, P. Chellapandi. Characterization of cellular convection of argon in top shield pen etrations of pool type liquid metal fast reactors. Nuclear Engineering and Design 250 (2012) 207-218.

[137] K. Natesan, K. Velusamy, P. Selvaraj, P. Chellapandi. Integrated Plant Operations, PFBR/01151/DN/1018/Rev-C (2011).

Chapter 6

Fuel Clad Behavior during Transients

6.1. Background

Detailed investigation on primary system components has been carried out in the previous chapter to arrive at the optimum heating rate, and a heating rate of 56 K/h is recommended. Besides primary system components, heating rates can affect the integrity of fuel clads as well. Hence the integrity of fuel clad tubes at various heating rates has been investigated in this chapter. During transients like power raising, the fuel clad may balloon and obstruct the coolant flow. As ballooning in fast reactor clad tubes is not reported in literature, the key question is whether ballooning is likely to occur in fast reactors. The associated questions are: what is the temperature range at which it can occur? What is the role of pressure in ballooning? What is the range of heating rates at which ballooning can occur? If ballooning can occur at slow heating rates, power raising operation is done at slow heating rates, so is there a risk of ballooning during power raising? All these points are addressed in this chapter in a step by step way.

6.2. Development of experimental facilities

Two experimental facilities namely HTCTTF and RABITS have been indigenously developed to simulate the transient events at high temperature and pressure. The latter is the extended version of the former.

The objectives for developing the testing facilities are

- To identify the zones where the clad would either rupture or undergo ballooning by conducting experiments at various combinations of pressure, temperature and heating rates.
- To predict the possibility of ballooning during the design basis events.

- Repeatability of the tests to gain confidence in the results.

Presently, experiments are being conducted using single pin to get the photography of the evolution of deformation of the clad using X-ray source. It can be further visualized, modeled and experiments can be conducted to get the scenario with multiple pins. Out of pile tests are being conducted because the clad is ductile in the beginning of life and the concern is ballooning. Whereas at the end of the life, the material becomes brittle due to irradiation and the concern becomes rupture. High sensitivity X-ray radiography method is used to measure the deformation of the specimen. The details of the test facilities are discussed in the subsequent sections.

6.2.1. HTCTTF Facility

HTCTTF constitutes a stainless steel pressure vessel, clad tube specimen and electric furnace held together by the stand. The experimental setup is shown in Figure 6.1.

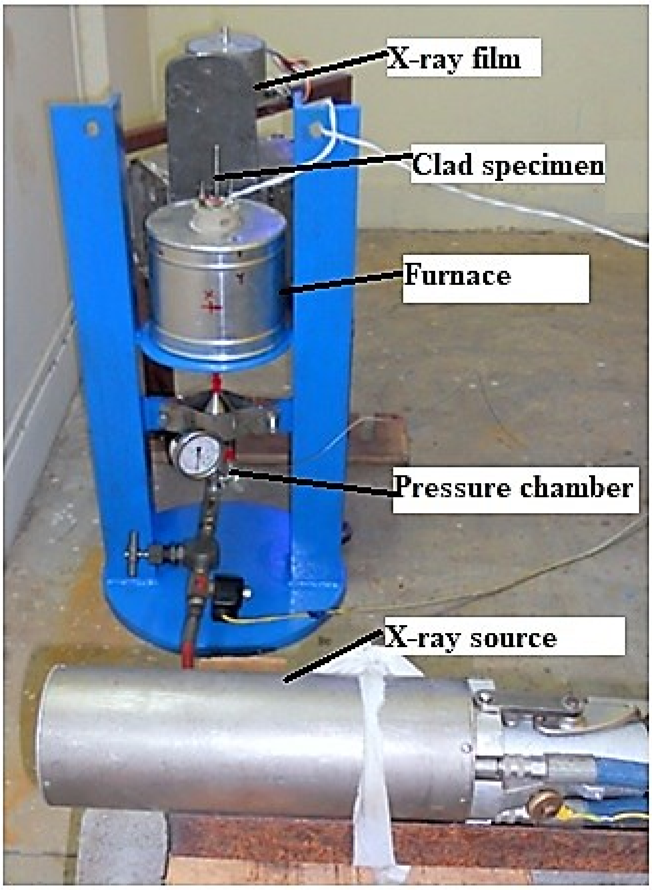

Figure 6.1 High Temperature Clad Tube Testing Facility

The test specimen for testing is a hollow clad tube welded to the fuel pin end plug on one side, and is welded to the pressure chamber at the bottom end. The clad tube is 32 cms long and 6.6 mm diameter, with a thickness of 0.45 mm. The details of the test specimen are given in section 6.4 below.

The pressure chamber has three adapters fitted for pressure gauge, safety valve, and relief valve. It is filled with argon gas at high pressure, to simulate the fission gas pressure. The closed tube under internal pressure facilitates biaxial state of stress in the clad tube.

The furnace is positioned such that the middle portion of the fuel pin is heated to the maximum temperature and the clad weld is far away such that the heat transfer to the weld is negligible. This arrangement ensures that the critical location is not the weld location. The furnace is 150 mm long and has 200 mm outer diameter and 10 mm inner diameter. The length of the heating zone is 50 mm. It is designed to withstand high temperature (up to 1473 K) for the desired period uninterruptedly with a heating rate (up to 200 K /minute). It has a high quality nichrome heating element of 0.5 mm diameter wounded to a ceramic. This set up is insulated by ceramic wool. It is coupled with a PID controller along with a silicon controlled resistor, to achieve the exact temperature required.

High intensity X-ray system (Baltograph 160) is deployed to measure the deformation of the clad tube inside the furnace at desired time intervals. Conventional radiography films were used to capture the images. The details of the X-ray imaging are discussed in section 6.3 below. The temperature profile and the change in diameter with time are recorded using thermocouples and X-rays respectively.

6.2.2. RABITS facility

The design of the HTCTTF is improved and the RABITS facility, which can test multiple pins simultaneously has been developed with a higher capacity furnace. X-rays were used to capture the variation in the fuel clad tube diameter occurring within the furnace.

Conventional radiography films were used to capture the images in the initial tests. It is subsequently replaced by DFPD. The photograph of the RABITS facility is shown in Figure 6.2.

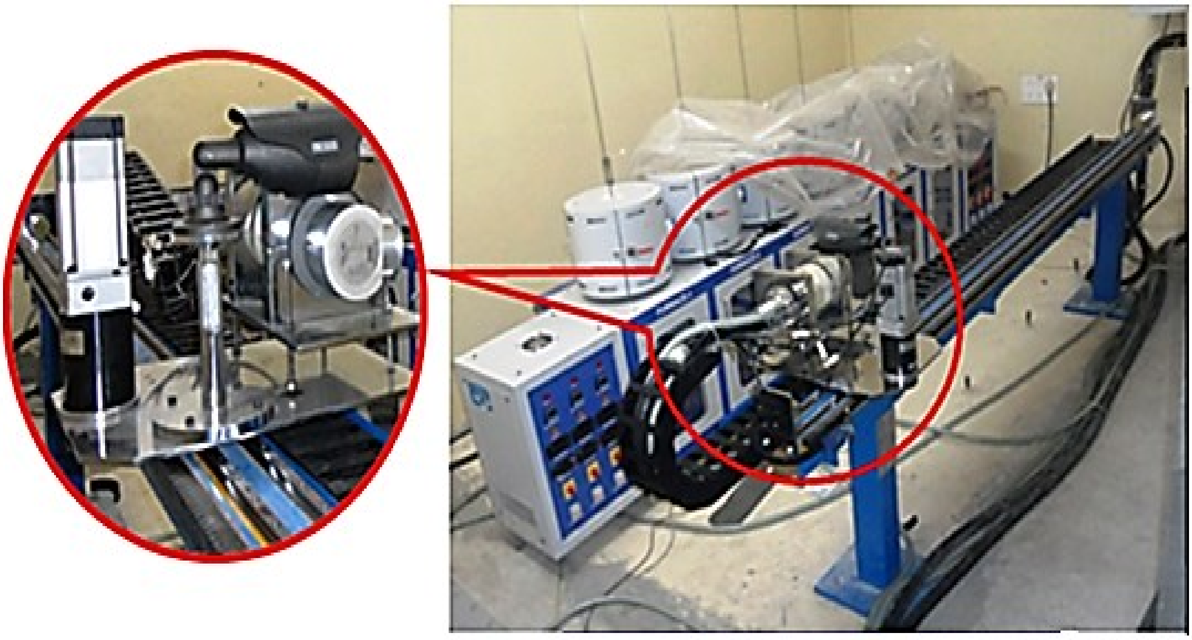

Figure 6.2 Photograph of the RABITS facility

The salient features of this integrated high temperature experimental facility are

- Simultaneous testing of multiple fuel clad tubes, yet having independent control
- Online monitoring of the specimens
- Radiological protective shielded room

6.2.2.1. Simultaneous testing of multiple fuel clad specimens

The RABITS facility is designed such that six specimens can be tested simultaneously. Towards this, an elegantly fabricated cabinet enclosure has been constructed. The cabinet front has separate shutters for each section under each furnace. Each section consists of a pressure chamber (provided with pressure gauge) hung from the top of the cabinet. The shutters have perspex windows for observation of the pressure gauge while under test. The schematic of the outer view of RABITS facility is shown in Figure 6.3.

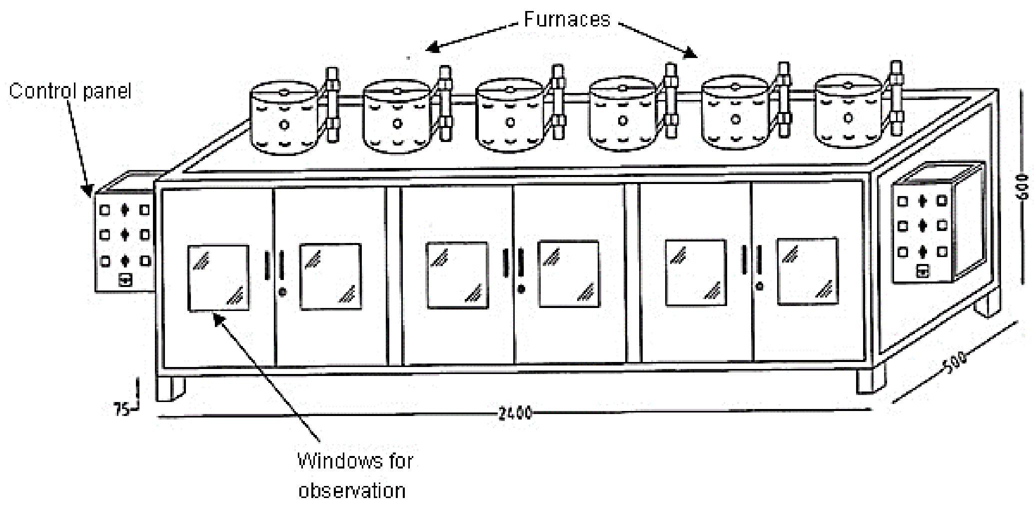

Figure 6.3 Schematic of the outer view of RABITS facility

The specimens are welded to the pressure chambers. The clad specimen passes through the centre of the furnace. Each chamber can be controlled independently to set different temperature and pressure, so that parallel experiments can be carried out using the same facility. The schematic of the section view of the RABITS facility is given in Figure 6.4.

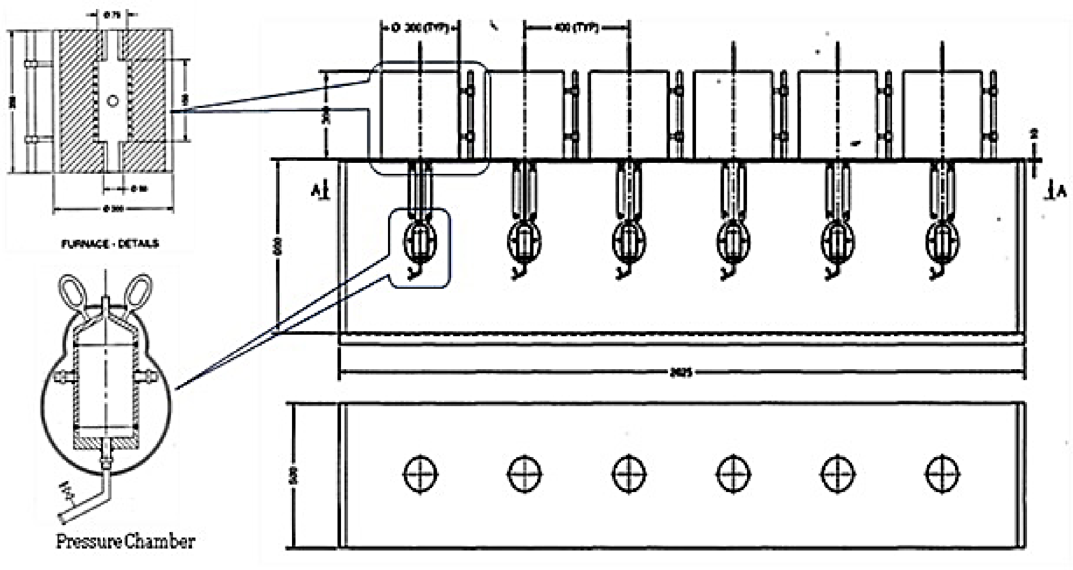

Figure 6.4 Section view of the RABITS facility

Each section consists of a pressure chamber (provided with pressure gauge) hung from the top of the cabinet, designed such that it can withstand a high pressure of the order 100 bar. Also, it helps in accommodating the pressure surges in the specimen upon heating. There is a provision to hang the pressure chambers from the top as shown in Figure 6.4, thus eliminating the stands and clamps to hold it. This design facilitates the free expansion of the pressure chambers downwards relieving it from any constraints.

Each furnace is a cylindrical and vertical model, split type single zone furnace with a maximum operating temperature of 1373 K and accuracy +/- 1 K. The inner chamber is formed to withstand a temperature up to 1423 K. The inner chamber has 75 mm diameter and 150 mm height with 75 mm hot zone length. There is a heating element evenly distributed around the inner chamber. High-quality ceramic fiber insulation is provided all round the sides of the inner chamber to have a skin temperature, not exceeding 50 K at maximum operating temperature. Six sets of furnaces are mounted on the top of the cabinet. The cabinet has two control panels mounted one on each side. Each control panel houses three sets of furnace control and indicating instruments which independently controls the furnaces.

6.2.2.2. Online monitoring of the specimens

High sensitivity X-ray machine is used for online monitoring of the specimens enclosed inside the furnaces. Also, to enable simultaneous testing of the specimens, a trolley is designed to hold the X-ray source and travel to the desired location which is controlled remotely from the control room. The details are given below.

A) X-ray machine

A constant potential 225 kV X-ray machine with metal ceramic X-ray tube and 40° x 30° beam angle has been procured. The voltage range is 10 kV - 225 kV and current range is 0-15 mA. The picture of the X-ray tube is shown in Figure 6.5. It consists of 4 variable focal spots 0.25 mm/ 0.3 mm/ 0.5 mm and 0.8 mm and maximum power outputs of 290 W/ 540 W/ 1020 W and 1600 W respectively. The variofocus X-ray system with focal spot technology offers extraordinarily small in-performance variable focal spot. Compared to conventional X-ray tubes, variofocus focal spot is less than half the size and considerably more symmetrical, providing the power of high-power X-ray tubes.

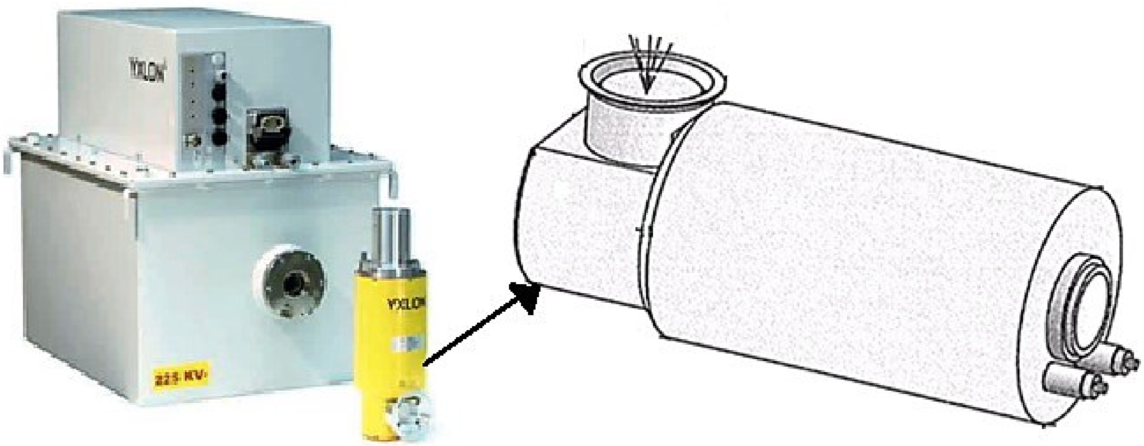

Figure 6.5 Constant potential 225kV X-ray machine

The control unit has provision to record exposure parameters, a facility for recalling the exposures; automatic warm-up and provision for auto trips due to high target loading or when the temperature of the target/oil exceeds prescribed limits.

(i) Benefits in comparison to conventional X-ray:

- Better detail visibility due to a minimum effective focal spot of 250 microns.
- Reduced inspection time, because the user can use an optimized focal spot with more power.
- Circular shape focal spot for the same image quality in and perpendicular to the tube axis.

(ii) Unique benefits:

- Magnification up to 10 times
- Focal spot size can be optimized for the application and provide maximum detail visibility
- Minimum effective focal spot of 250 Microns and 292 W power
- Circular focal spot for best image quality
- Closed design in a standard 225kV housing with standard high voltage cable

B) Remote controlled mobile support for X-ray source

X-ray source has been supported on a mobile platform. This mobile platform can be controlled precisely from the remote control room. The conceptual sketch of this mechanism is shown in Figure 6.6.

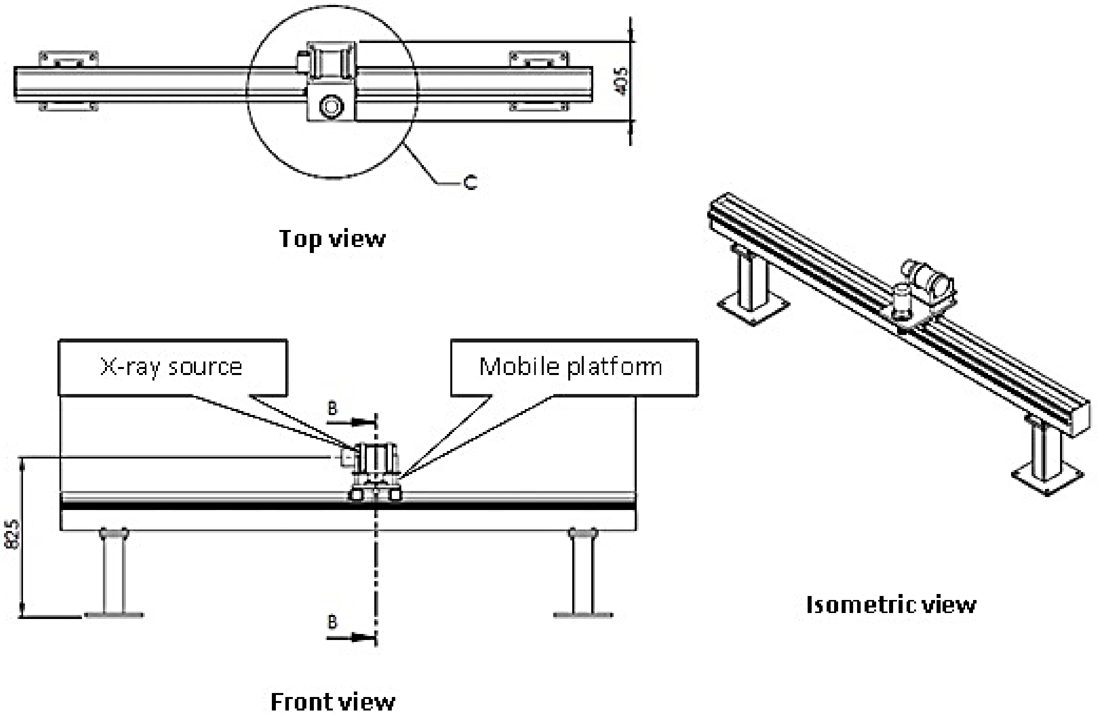

Figure 6.6 Conceptual sketch of the mobile platform

Towards ensuring the precise control, appropriate drive motor mechanism is attached with the mobile platform. With this, the X-ray source can be comfortably placed on the mobile platform and it can be used for capturing the images of multiple specimens without having any physical intervention. There is a provision for height adjustment of the X-ray source up to 75 mm. The remote controlled panel connected with this mechanism will have the provision to move the X-ray source in forward and reverse direction. The camera and the laser pointer mounted along with the mobile platform help in online monitoring of the X-ray source with reference to the specimen.

6.2.2.3. Radiological protective shielded room

A dedicated X-ray unit operating facility is constructed at the Structural Mechanics Lab for the RABITS facility. The design of the room is made such that proper shielding is provided. Shield design calculation for the X-rays has been done using three-dimensional code MCNP4C3 [138] for the gamma rays dose rate using normal concrete of mass density 2.4 g/cc. The shield design dose rate criterion has been taken as 1 μSv/h. A safety factor two has been included for shield calculation.

The room has been constructed with normal concrete (2.4 g/cc) of thickness 65 cm in the beam facing side, 35 cm along the other three sides and 25 cm concrete equivalent shield on the roof of the installation hall to satisfy the dose criterion of 1 μSv/h as per the given dimensions of the set up.

6.3. X-ray imaging: theory and methods

6.3.1. Imaging principle

Radiographic examination is usually done by using either electromagnetic radiation, which are in the form of X-rays or gamma rays, or by using neutrons. In the present study, radiography was done using X-rays. The X-rays are attenuated depending upon the density, thickness and composition of the material and the length of travel of the X-rays [139]. Radiography usually refers to a radiographic process, which generates a perpetual image on a film. When the inspection is done by perceiving the real-time image on a fluorescent screen (instead of a film), it is called as real-time inspection.

6.3.2. Real-time inspection

The three essential elements of radiography are X-ray source, the object and the sensing material. The X-ray source used for the experiment had a constant potential of 225 kV. The object is the fuel clad specimen enclosed in the furnace. The sensing material is conventional radiography films. DFPD has been used as the sensing material in some of the tests where the point of onset of ballooning had to be captured precisely. The X-ray source used when DFPD is used as sensing material had a constant potential of 450 kV, for better online monitoring. The DFPD used for the experiment has a 16 inches screen, and it has the capability to acquire images at 30 fps, with a resolution of 400 μm [140]. Figure 6.7 shows the elements of radiography used in the experiments.

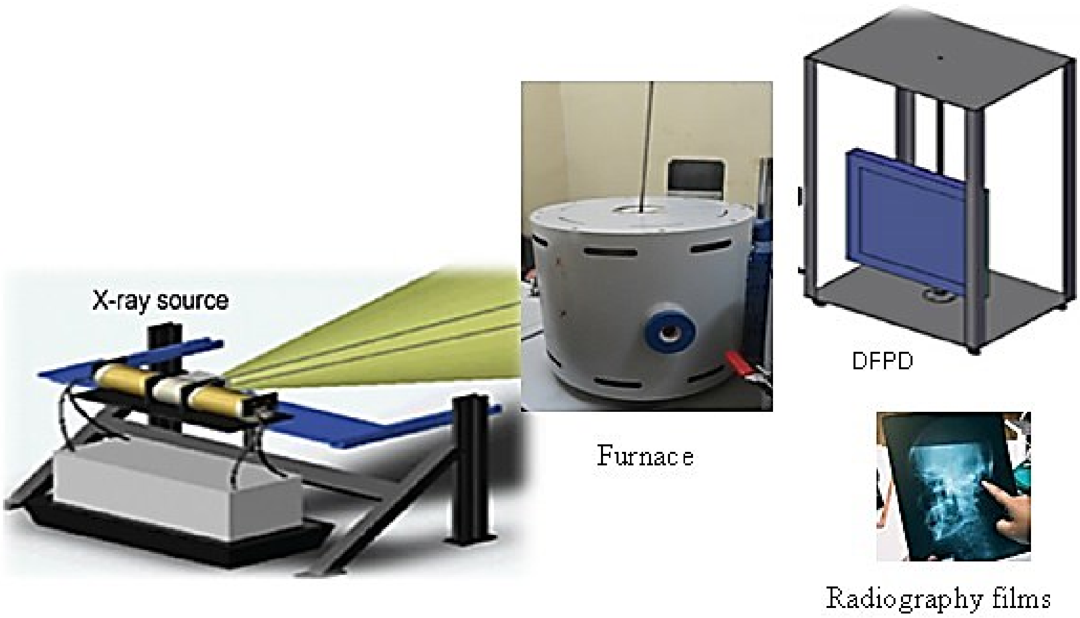

Figure 6.7 Basic elements of radiography used in the experiment

6.4. Fuel clad tube material

The clad material used to carry out the tests in the RABITS facility is 20 % cold worked alloy D9 (15Cr-15Ni-Mo-Ti-Si), which is the fuel clad material of the PFBR. The chemical composition of this material was tailored for enhancing its void swelling resistance which is a prime requirement for the fuel clad tubes deployed in fast breeder reactors. Cold work further improves the void swelling resistance of this material as it results in precipitation of fine MX precipitates of the type Ti (C, N) during elevated temperature exposure [141]. The MX formed because of cold working and subsequent high temperature exposure also enhances the creep and tensile strength of this material [142], [143]. The optimized grain size for alloy D9 clad is

15-30 μm [144]. Though the mechanical strength can be enhanced by reducing the grain size further, the higher grain boundary area fraction formed consequently could result in extensive precipitation of $M_{23}C_6$. The formation of $M_{23}C_6$ precipitates would deplete the matrix of carbon thereby reducing the propensity for formation of the more beneficial MX [141]. The MX not only enhance the mechanical strength but also improve the void swelling resistance of this material, therefore retaining carbon in the matrix for subsequent precipitation of MX during elevated temperature exposure is crucial.

The specimens used for the testing are hollow fuel clad tubes made of 20 % cold worked Alloy D9 material, which are 6.6±0.02 mm in diameter and 0.45 mm in thickness. The clad tubes were fabricated from forged round bars, which were initially hot extruded and subsequently cold worked by fixed plug drawing operation. The chemical composition of Alloy D9 is given in Table 6.1. In the current investigation, the testing was done in the cold worked condition without being aged. The microstructure consisted of only austenite without any significant precipitation.

Table 6.1 Chemical composition (in wt.%)

	C	Cr	Ni	Mo	Mn	Si	Ti	N	S	Si	P	Al	B	Fe
Alloy D9	0.04	14.04	15.15	2.25	1.78	0.61	0.26	0.0037	<0.002	0.61	0.007	0.006	0.0015	Bal.

6.5. Experiments conducted and results

Ballooning tests have been carried out in both HTCTTF and RABITS facility. The specimens are designated as H1, R1 and so on, where ‘H’ refers to the HTCTTF facility, ‘R’ refers to the RABITS facility, and the number refers to the specimen number.

A considerable number of tests have been carried out in the present investigation. The trend in the behavior of the material matches in all the tests. Hence the repeatability of the experiments has been taken care. The results of each test have been used for understanding specific aspects of ballooning and are reported accordingly.

It may be noted that there is an expansion of argon gas in the hot zone of the furnace, which is compensated due to the surging action of the pressure chamber, which is at room temperature. Hence the pressure in the specimens is maintained constant.

6.5.1. Understanding ballooning in Alloy D9 material (specimen H1)

Ballooning in fast reactors has not been reported in the literature. The key question is thus whether ballooning is likely to occur in fast reactors. The associated question is what are the operating conditions at which it can occur and how coolability is affected. As a first step, it was planned to test a fast reactor clad and hold at various temperatures and to get a preliminary knowledge about the temperature range at which ballooning is likely to take place.

Towards this, an experiment has been conducted at the HTCTTF with specimen H1. The D9 clad tube is pressurized to 100 bars and the temperature is raised in steps from room temperature. It is held for some time at each temperature. X-ray radiographs have been captured periodically throughout the experiment. Based on proper image processing, the change in dimensions of the tube has been measured and is plotted against time as shown in Figure 6.8. It is observed that the fuel clad deforms slowly with increase in temperature and time till it reached 1273 K. On maintaining the temperature for 40 minutes, ballooning of the pin has been observed with 25 % hoop strain (OD 8.28 mm), and is followed by rupture.

The inference from this preliminary test was that ballooning in D9 material can take place at the temperature range of ~ 1273 K. With this preliminary information, the next set of experiments have been planned to reach a set temperature in the range of 1223 K to 1273 K.

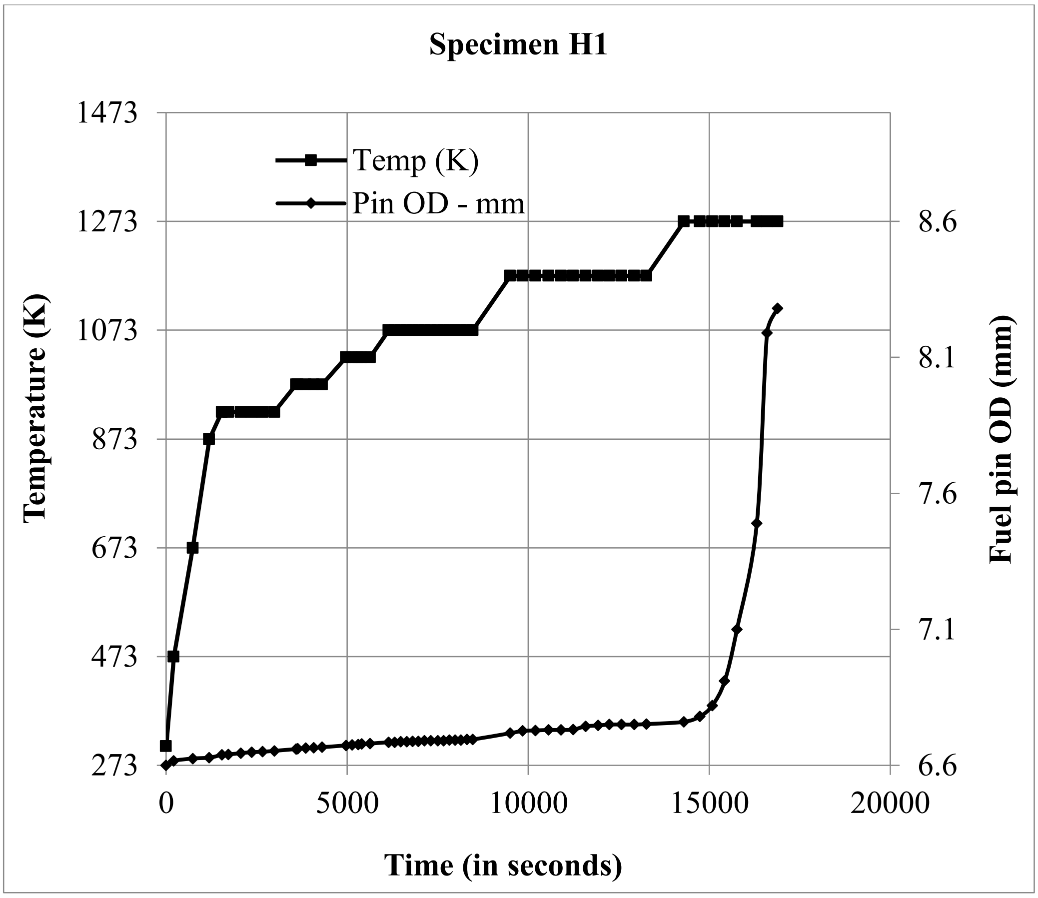

Figure 6.8 Preliminary ballooning test on Alloy D9 clad material

6.5.2. Assessment of design safety limits

The second stage of the investigation is to verify the DSLs defined at various DBEs. DBEs are classified into four categories of events based on the frequency of occurrences, namely, category-1, which is the normal operation; category-2, which are the upset events with frequency > 10^{-2}/ry; category-3, which are the emergency events with frequency < 10^{-2}/ry and > 10^{-4}/ry; and category-4, faulted category with frequency < 10^{-4}/ry and > 10^{-6}/ry. Events with frequency < 10^{-6}/ry are the beyond design basis events.

DSLs have been defined in order to assess that the design provisions of the system/components are adequate to ensure safety. The temperature limits for all category and time durations are as follows:

Category 1: 973 K and CDF < 0.25

Category 2: 974 K – 1023 K for 75 min and 1023 K – 1073 K for 15 min and CDF < 0.25

Category 3: 974 K – 1023 K for 15 min and 1023 K – 1073 K for 6 min and 1123 K – 1173 K for 2 min and CDF < 0.25

Category 4: 1473 K (rupture is allowed but coolable geometry has to be maintained).

The details of the specimens H2, H3 and H4 are given in [145]. The test conditions and the salient results are summarized below.

6.5.2.1. Test details of specimen H2 and results

Specimen H2 is held at 60 bars pressure and reached 1243 K temperature at a heating rate of 27 K/min. It is observed that there is only 2.1 % dilation at the end of 3.5 hours. Ballooning to 32% (diameter increase) is observed after 3.5 hours. The failure of the specimen is observed after 2 cycles. The temperature profile and the change in diameter with time are depicted in Figure 6.9.

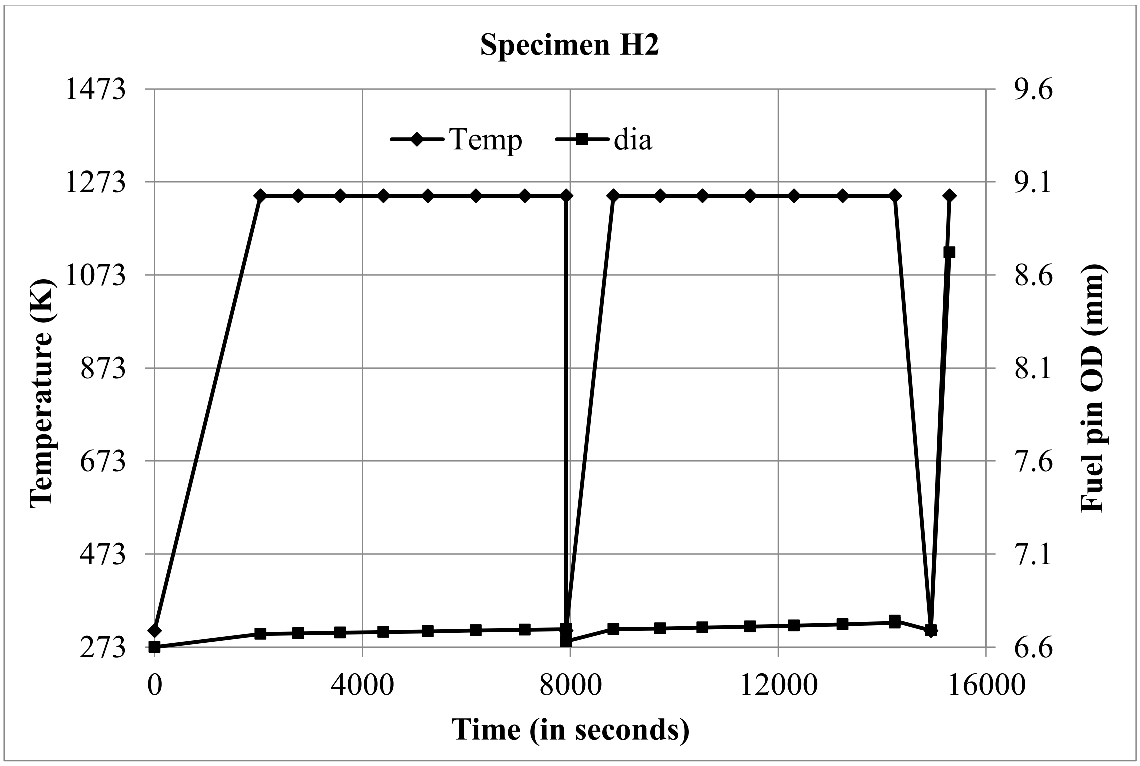

Figure 6.9 Temperature profile and diameter change with time for specimen H2

The DSLs have been checked with the experimental data and it is found that ballooning will not take place upto category-3 events as there is enough margin [145].

6.5.2.2. Category-4 event: effect of heating rate (specimens-H3, H4)

Under category-4 event, fuel failure is permitted but radioactivity limits will be adhered. Safety objective in this case is to maintain coolability of the subassemblies. Two specimens, H3 and H4 have been tested at 60 bar pressure, which is the maximum operating pressure of the PFBR clad tube, to simulate the category 4 event criteria. The maximum temperature limit of category-4 event is 1473 K. The experiment has been conducted for two specimens for different heating rates.

- Specimen H3 has been heated to 1473 K at a heating rate of 100 K/min.
- Specimen H4 has been heated to 1473 K at a heating rate of 40 K/min.

During relatively faster heating of specimen H3, a small leak is observed before attaining the set temperature of 1473 K. The maximum deformation observed is 7.8 mm (18 % strain). During slower heating rate of 40 K/min, the specimen ruptured two minutes after attaining 1200 K. The leak in specimen H3 and the crack opening in specimen H4 are shown in Figure 6.10. The maximum deformation observed is 8.51 mm (29 % strain).

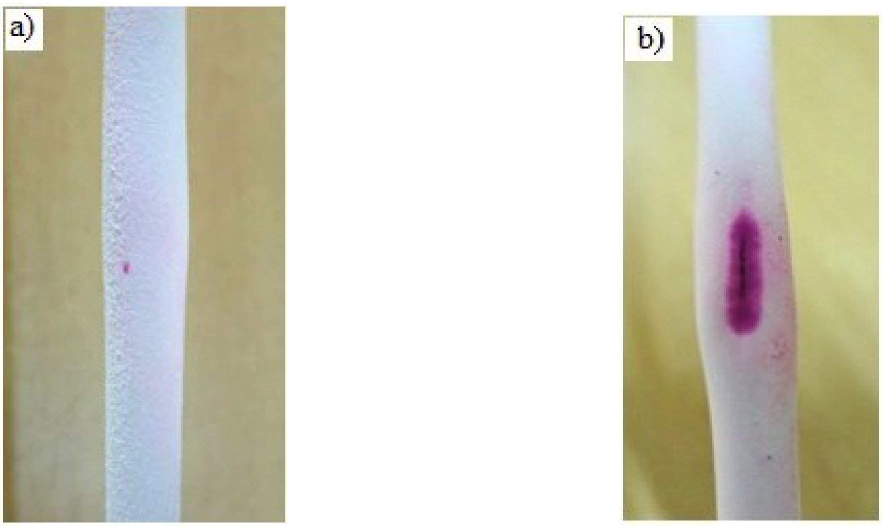

Figure 6.10 a) Leak at faster heating rate b) Ballooning and crack opening at slower heating rate

The actual heating rate during an enveloping event of category-4 event, i.e, primary pipe rupture is 100 K/s. It can be inferred from the results that the clad ruptures before ballooning during fast heating and ballooning is not expected during the design basis events of PFBR. Nevertheless, a large number of experiments need to be carried out to arrive at this conclusion. Many more tests have been carried out to confirm the same.

6.5.3. Specimen R1

Specimen R1 is tested at the RABITS facility. It is pressurized to 65 bars and is passed through the split type furnace as shown in Figure 6.11. The temperature of the furnace is set to 1223 K. The specimen at high temperature is observed through high-temperature quartz window provided in the furnace.

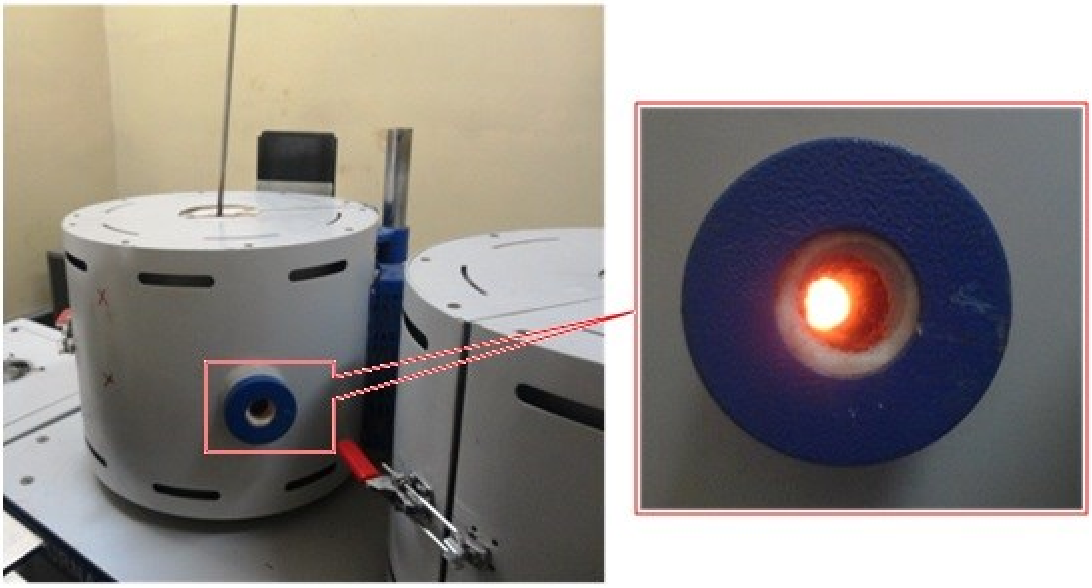

Figure 6.11 Clad tube in furnace in RABITS facility

6.5.3.1. Online monitoring

The position of the trolley is adjusted accurately with the help of the laser pointer to focus on the center of the furnace. Proper safety measures have been taken and the X-ray radiographs of the specimen have been taken during heating from room temperature to 1223 K at every 5 minutes interval. The X-ray films are placed on the furnace body such that the X-rays fall on it (Figure 6.12a). A sample radiograph is shown in Figure 6.12b. The distance between the vertical lines in the radiograph is the diameter of the clad. The diameter is measured (Figure 6.12c) at every shot to estimate the strain. It may be noted that the diameter of the bulge is measured in pixels using the I-See software. The pixels of the letters in the same image are known, and it is compared with the pixels at the maximum bulge location to get the bulged diameter. This procedure minimized the error due to the distance of the object from the X-ray film.

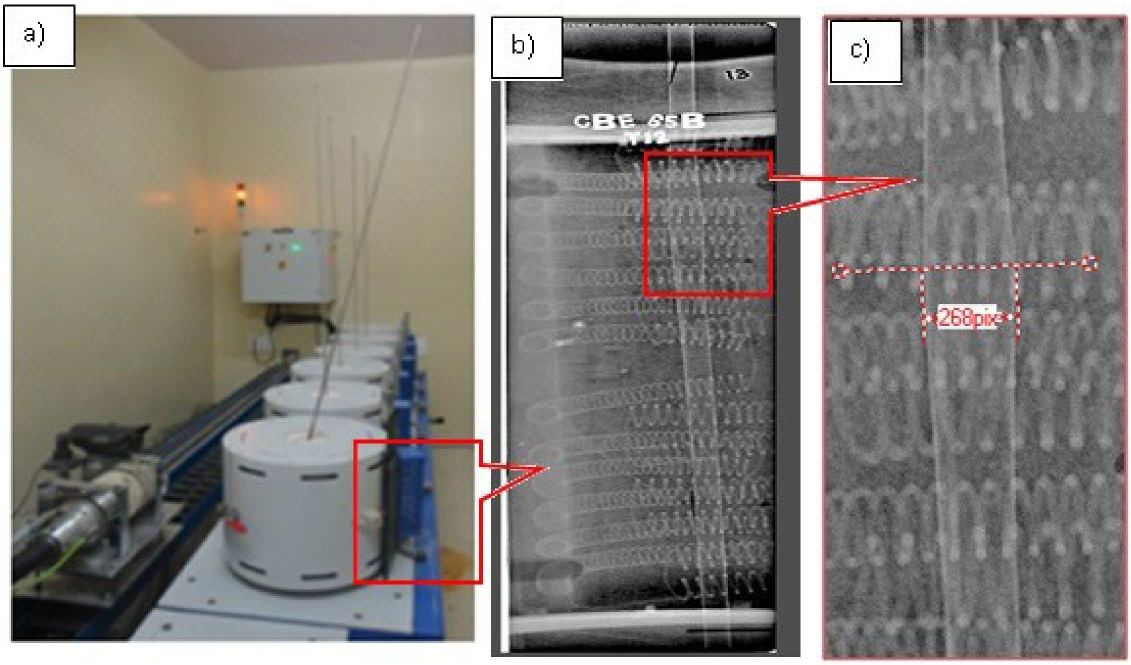

Figure 6.12 a) position of X-ray film b) Radiograph c) clad diameter

6.5.3.2. Experimental results

The temperature and diameter at each shot are recorded and the variation of strain with time and the temperature history are plotted in Figure 6.13. The time taken for attaining the set temperature of 1223 K is 70 minutes. The time taken for rupture after reaching the set temperature is 16 minutes. Ballooning with 28 % strain has been observed before rupture.

It may be noted in Figure 6.12a, that there is a bending in the specimen due to the long specimen of 1.2 m (unsupported at the top). This can aggravate the damage caused to the specimen, which is not considered in the present results. Nevertheless, the effect of length can be a topic to be studied in future. The measured temperatures are at the surface of the furnace, with an accuracy of +/- 1 K. There can be losses in the heat transferred to the specimen, which is neglected. The clad specimen of which 150 mm is in the furnace, is heated to 1223 K.

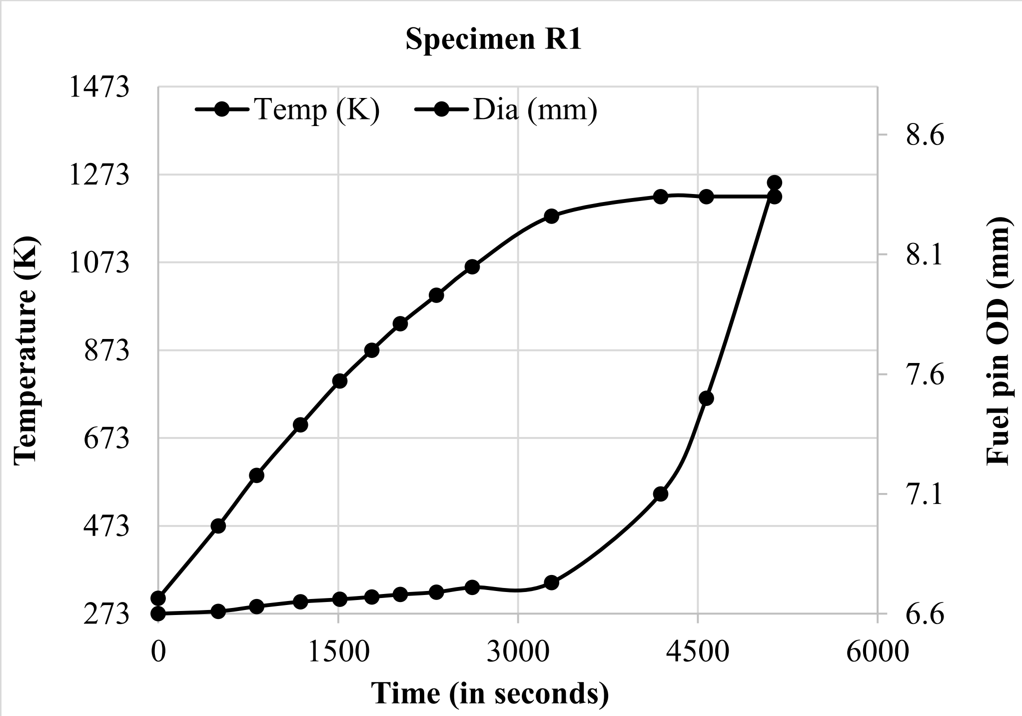

Figure 6.13 Specimen R1: Temperature and strain with time

6.5.3.3. Ballooning during category-3 event

The results are used to study the possibility of ballooning during a category-3 event. Table 6.2 compares the experimental results with the defined limits (section 6.5.2). The results show that during a category-3 event, there will be no rupture and no ballooning taking place in the fuel clad till the defined time. The time spent in creep regime in the experiment is pessimistic when compared to that defined at 1173 K. The total strain recorded at the maximum temperature of a category-3 event (1173 K) is 1.97 %. It is evident that ballooning does not initiate up to this temperature. Ballooning takes place only after 16 minutes after reaching 1223 K. Thus we can conclude with high confidence that the coolable geometry will be maintained during a category-3 event of the reactor.

Table 6.2 Design check for category-3 event

Category-3 Design Safety Limits		**Experimental Results**		
Temperature	**Time**	**Temperature**	**Time held**	**Cumulative Strain**
974 K – 1023 K	15 min	974 K – 1023 K	6 min	1.36 %
1023 K – 1073 K	6 min	1023 K – 1073 K	6 min	1.67 %
1123 K – 1173 K	2 min	1123 K – 1173 K	5 min	1.97 %

6.5.3.4. Effect of heating rate on ballooning

It is evident from Figure 6.13 that there is a ballooning of 28 % before rupture at 86 minutes. This high dilation is because of the slow heating rate of 20 K/min. The results match with the observations in Section 6.5.2.2. From this, it can be concluded that, slower the heating rate, higher is the dilation and higher the heating rate, sooner is the rupture. This can be attributed to the generation of more number of defects in the pre-stressed material subjected to higher heating rates, which is observed in SEM by Peng et al. [146]. Thus ballooning, and therefore the coolant flow blockage can occur when the heating rate is low.

The actual heating rate during an enveloping event of category-4 event is of the order of 100 K/s. It can be inferred from the experiments that the clad will rupture (not balloon) during transients in PFBR due to the higher heating rate of the clad tube thus ensuring the coolable geometry. But, there may be situations in the reactor, like local blockage at the spacer wire, due to which there can be a gradual increase in temperature which can go undetected due to the mixing of the coolant at the top of the location. This can eventually lead to local ballooning and hence coolant flow blockage locally. As there are provisions for detecting the failure of clad tubes and flow blockage if the damage location enlarges, this may not result in a catastrophe in PFBR. Nonetheless, extensive research on ballooning in fast reactors needs to be emphasized to preclude the phenomenon.

6.5.4. Specimen R2

Specimen R2, that is tested at the RABITS facility is pressurized to 80 bars and heated at an average rate of 19 K /min. The specimen burst ruptured at a temperature of 1143 K, after attaining a circumferential strain of 30 %. The temperature profile and the change in diameter are shown in Figure 6.14. The burst specimen is used for carrying out fractography tests (Section 6.6.2).

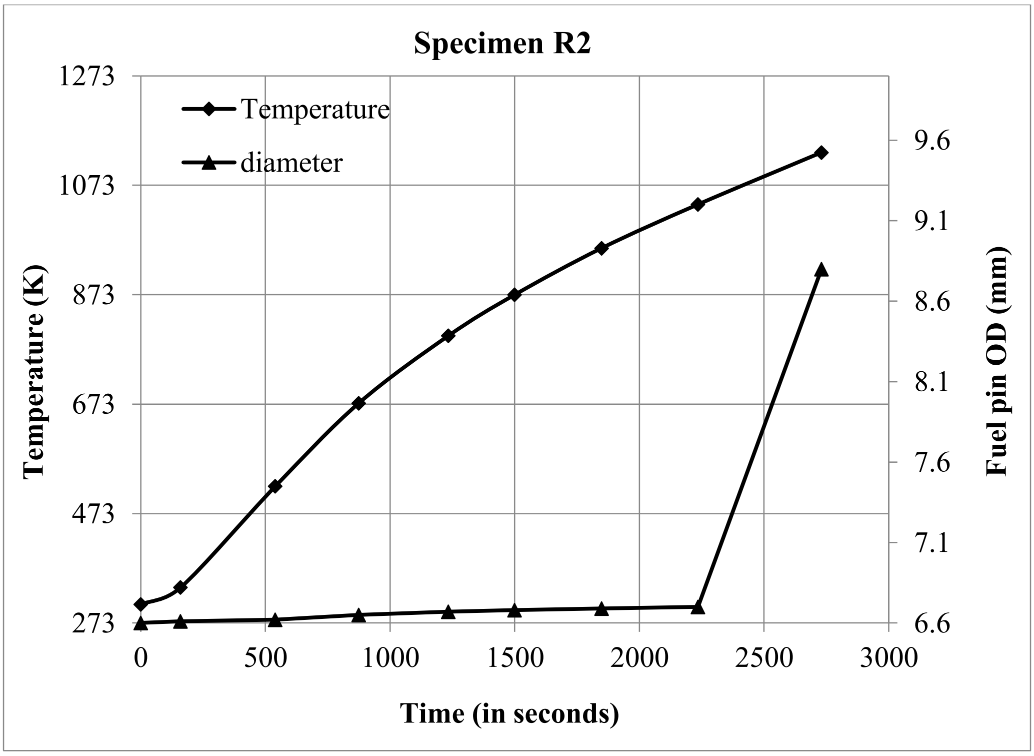

Figure 6.14 Specimen R2: Temperature and diameter change with time

6.5.5. Specimen R3: Hypothetical power raising case

A hypothetical power raising case is considered with a heating rate of 3 K /min (180 K/h), where the power raising operation is not ceased even after reaching the maximum envisaged temperature. Specimen-R3 is pressurized to 55 bars and is heated at the rate of 3 K/min. X-ray images have been captured at required intervals and the diameter of the clad tube at each instance, along with the temperature profile has been plotted in Figure 6.15.

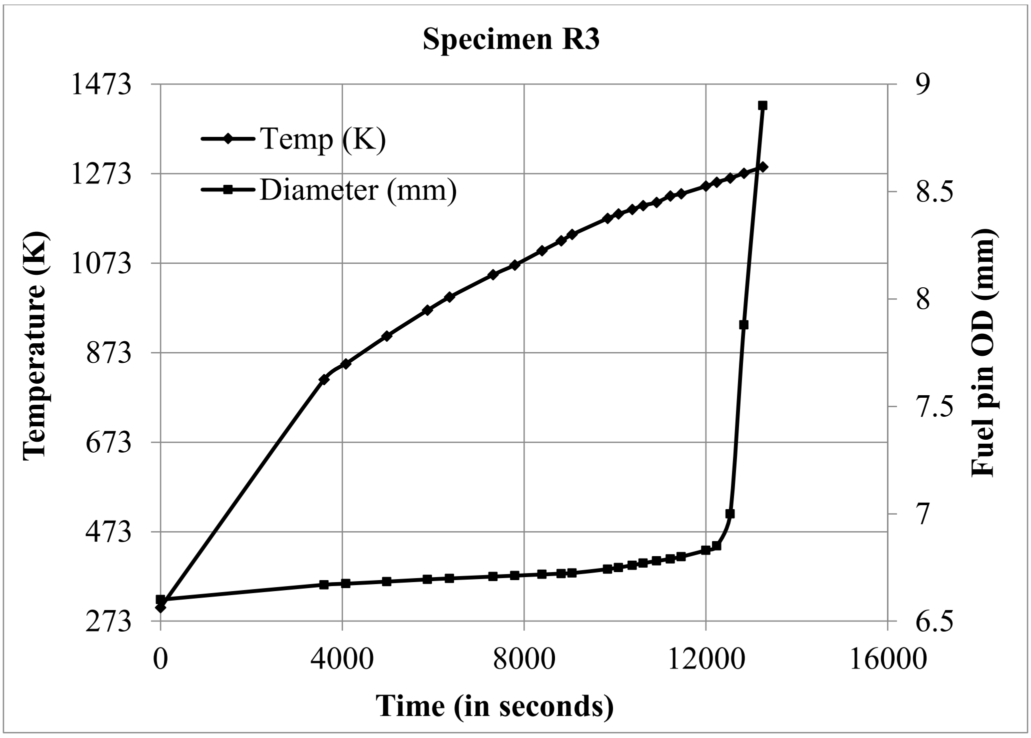

Figure 6.15 Specimen R3: Temperature and diameter change with time

It is observed that the change in diameter is insignificant initially and there is a sudden onset of ballooning at 12540 s (3.5 h), when the temperature reaches ~1273 K. Ballooning of 33 %, followed by rupture takes place at a temperature of 1288 K. The specimen burst opened, with a 'tap' sound.

Thus, it can be inferred that ballooning can take place at slow heating rates if it is allowed to reach higher temperatures, resulting in coolant flow blockage and severe damage. The heating rate during power raising operation in pool-type fast reactors is very slow (~60 K/h, i.e., 1 K/min). Care should be taken to ensure the termination of the withdrawal of control rods at the envisaged temperature. Nevertheless, there are provisions like stroke limiting device, which prevents continual withdrawal of a control rod beyond a certain level by a passive mechanism [147].

6.5.6. Specimen R4: Onset of plastic instability

The R4 specimen tested at the RABITS facility is pressurized to 80 bars at an initial temperature of 555 K. The temperature was then increased at an average heating rate of 24 K /min. The temperature profile and evolution of ballooning are shown in Figure 6.16.

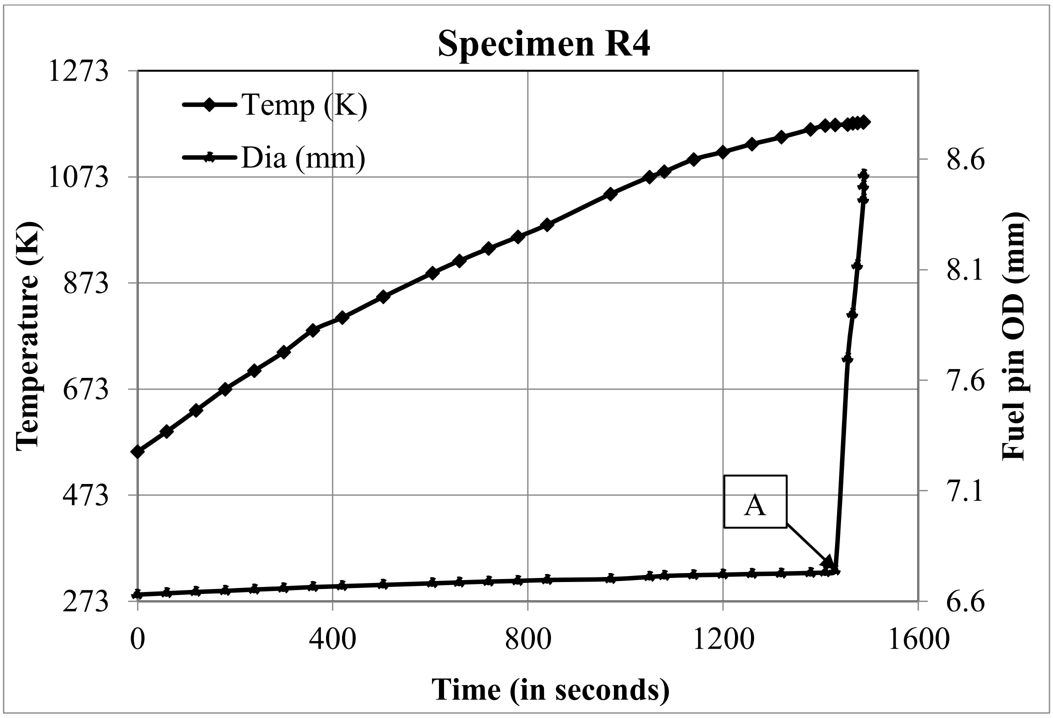

Figure 6.16 Specimen R4: Temperature and diameter change with time

The X-ray images were acquired using the DFPD at 25 fps. As the objective of the test is to capture the evolution of ballooning, i.e., the increase in diameter of the clad tube before rupture, 25 fps was sufficient to record the phenomenon. Higher number of frames would have been needed if the clad burst was the objective. The specimen burst ruptured after ballooning at a temperature of 1177 K.

The schematic explaining the ballooning phenomenon is depicted in Figure 6.17. The initial diameter of the clad tube was 6.6 mm and the deformation accumulation was very negligible during the initial phase of testing. A noticeable bulge of 7.7 mm is observed at 1456 s, which corresponds to a temperature of 1172 K. Ballooning progresses into burst between 1456 s to 1488 s, and the X-ray images are shown in Figure 6.18. The maximum diameter of the clad before rupture is 8.53 mm, and the hoop strain is 29.2 %. Thus the deployment of DFPD continuously captures the evolution of ballooning, which occurred in a few seconds.

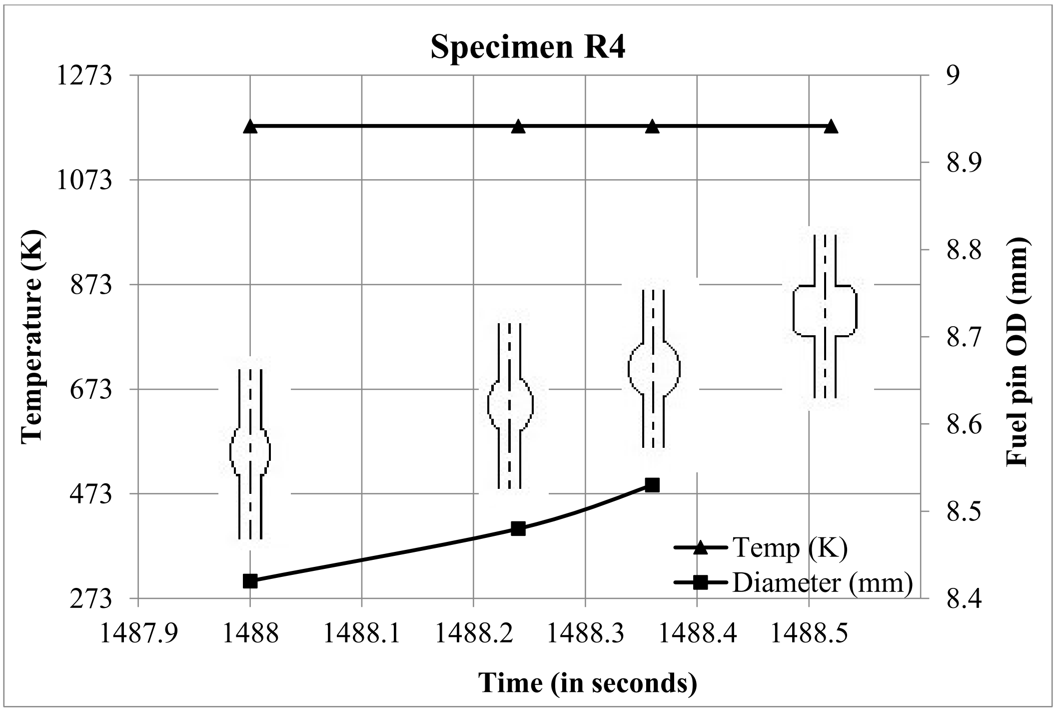

Figure 6.17 Schematic of ballooning phenomenon in specimen R4

Figure 6.16 shows the point of onset of ballooning (point A). It is observed that there was material instability till the point-A. Beyond this point, the deformation was rapid, and this was the mechanical instability (plastic instability) that resulted in large bulge and then rupture. The results match with the investigations done by [148]. The ballooning curve, established using DFPD (Figure 6.16), matches with that predicted for D9 alloy (shown in Figure 6.19), using the instability criteria, as given in equation 6.1 [148].

$$\varepsilon_{eq} > \frac{2n}{(2\sqrt{3} - m\sqrt{3})} \tag{6.1}$$

where, ε_{eq} is the equivalent strain, m is the strain rate sensitivity parameter and n is the strain hardening parameter. The material properties are taken from [149].

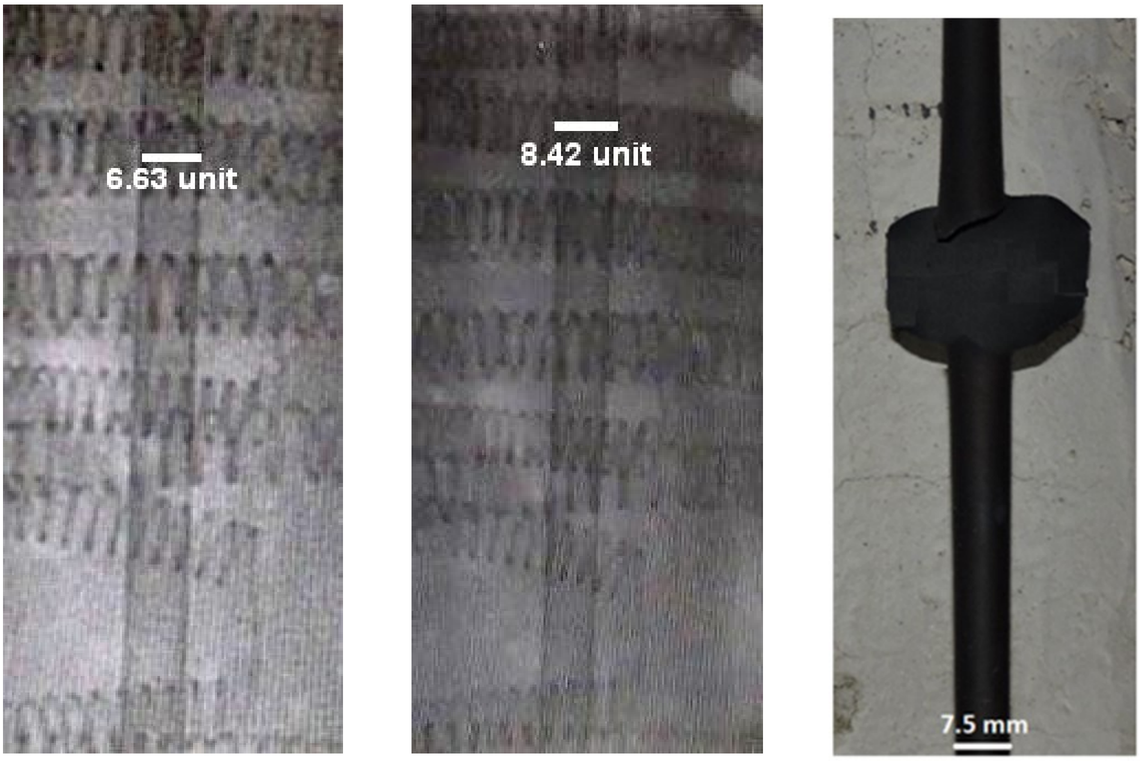

a) time = 0 s, temp=555 K outer diameter=6.63 mm

b) time =1488 s,temp=1176 K outer diameter = 8.42 mm

c) time =1488.52s, temp=1176 K, burst open

Figure 6.18 Evolution of ballooning with time in specimen R4

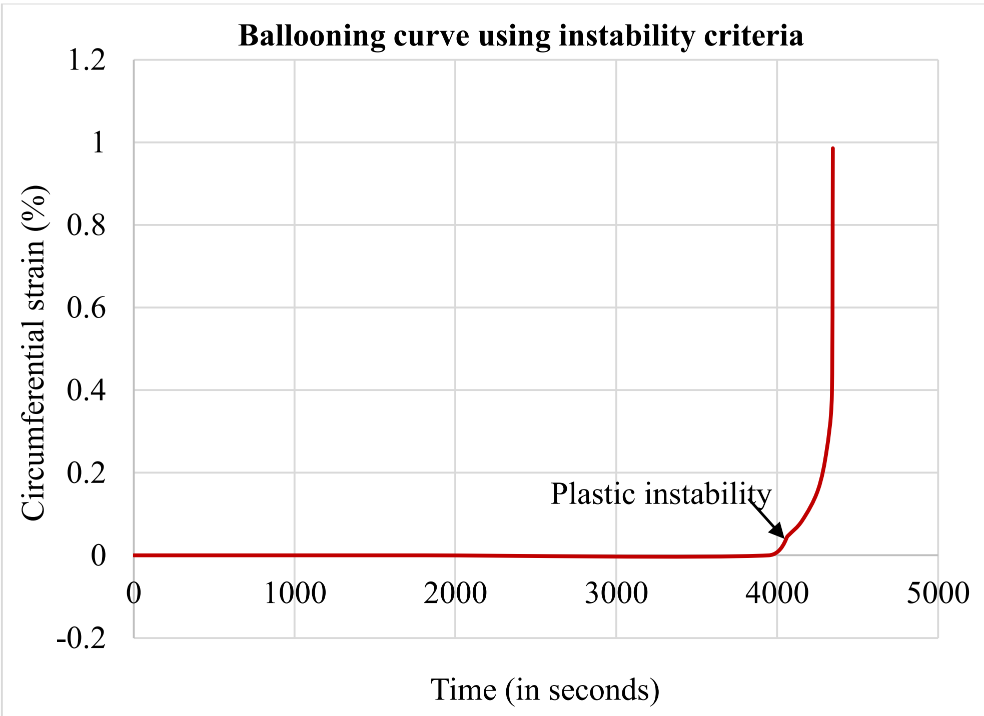

Figure 6.19 Ballooning curve established using instability criteria [148]

6.6. Microstructural studies

6.6.1. Optical metallographic findings for test specimen (R1)

The details of the experiment are discussed in section 6.5.3. Microstructural investigations were carried on the longitudinal sections along various regions of the R1 specimen and are shown in Figure 6.20.

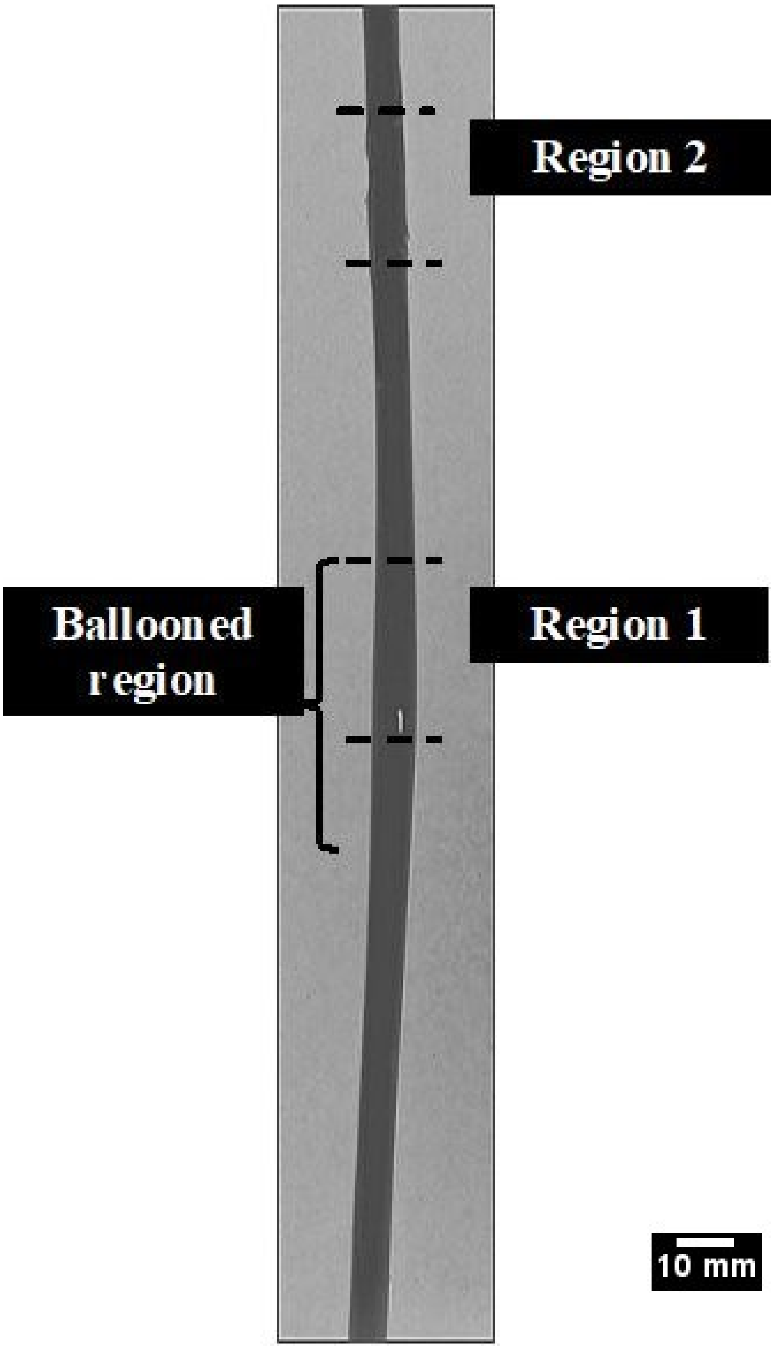

Figure 6.20 Optical imaging for specimen (R1)

The following three regions (in Figure 6.20) were investigated for microstructural changes

1) Ballooned region –marked as region 1 (outer diameter =7.6 mm)

2) Adjacent to ballooned region-marked as region 2 (outer diameter =6.7 mm)

3) The unaffected region (not indicated in the figure)

6.6.1.1. Region-3- unaffected region

The microstructure in the unaffected region comprised of fine grains with deformation bands which where induced by cold working. The thickness of the clad tube in as received condition is around 450 µm (Figure 6.21a). Grains size in this condition is around 20±7µm (Figure 6.21b).

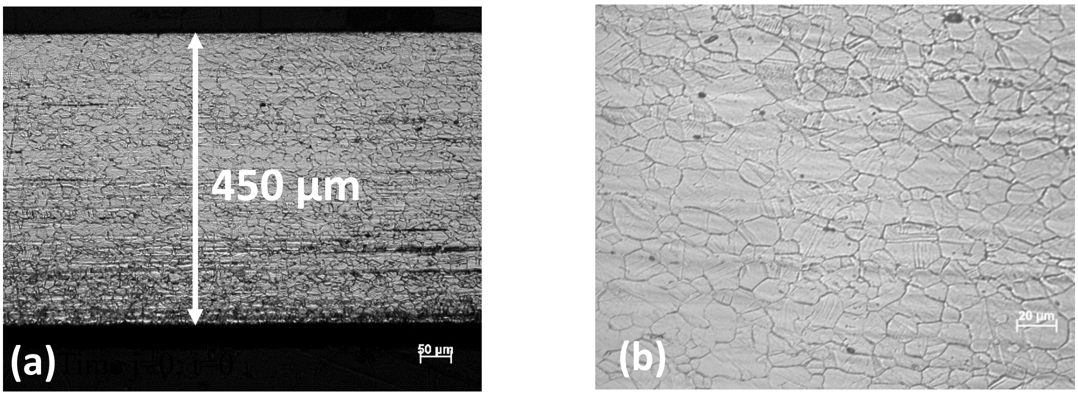

Figure 6.21 a) Thickness in region-3 b) Grain size in region-3 in specimen R1

6.6.1.2. Region-2- Adjacent to ballooned region

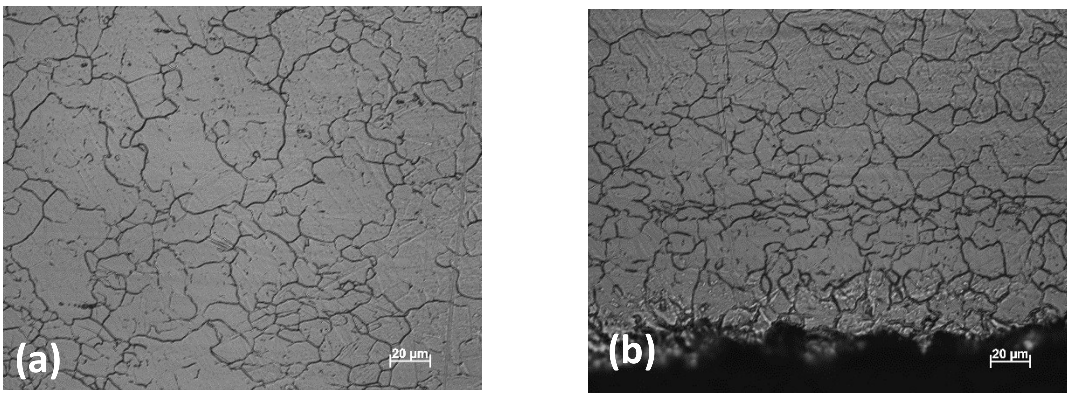

Figure 6.22 Grain coarsening in region-2 in specimen R1

The grain size in the region adjacent to the ballooned region (region-2) enhanced marginally (to 50±10 µm), as shown in Figure 6.22. There was hardly any change in the outer diameter in this region.

6.6.1.3. Region-1- Ballooned region

In the ballooned region, there is a thickness reduction from 450 µm to 400 µm (Figure 6.23a). Grains had coarsened significantly in this region (Figure 6.23b). There were some intergranular cracks which originated from the surface (Figure 6.23c and Figure 6.23d). The outer diameter of the clad in this region had enhanced to 7.6 mm.

A) Loss in strength/reduction in thickness

The loss in strength resulted in localized plastic deformation, as a consequence there was considerable reduction in thickness (Fig.9a) and high dilation (Fig.6) in the ballooned region.

B) Grain coarsening

It could be seen that in the ballooned region there was considerable grain coarsening (Figure 6.23b) when compared to the region of the clad tube which was not subjected to any thermal change (Figure 6.21b). The grain size was in the range of 50±10 µm in the ballooned region when compared to 20±7 µm in the region unaffected by the thermal variation. The grain size progressively increased from the un-dilated region towards the ballooned region. Though the kinetics for grain growth in un-stabilized stainless steels (stainless steels which do not contain titanium and niobium) is more favorable above 1323 K, in the current investigation unstable grain growth was observed after exposure at 1223 K for D9 (which is a stabilized stainless steel) [143]. The possible cause for grain growth to occur at relatively lower temperature range is the prior cold work which is imparted to this steel for enhancing void swelling resistance and creep strength [144].

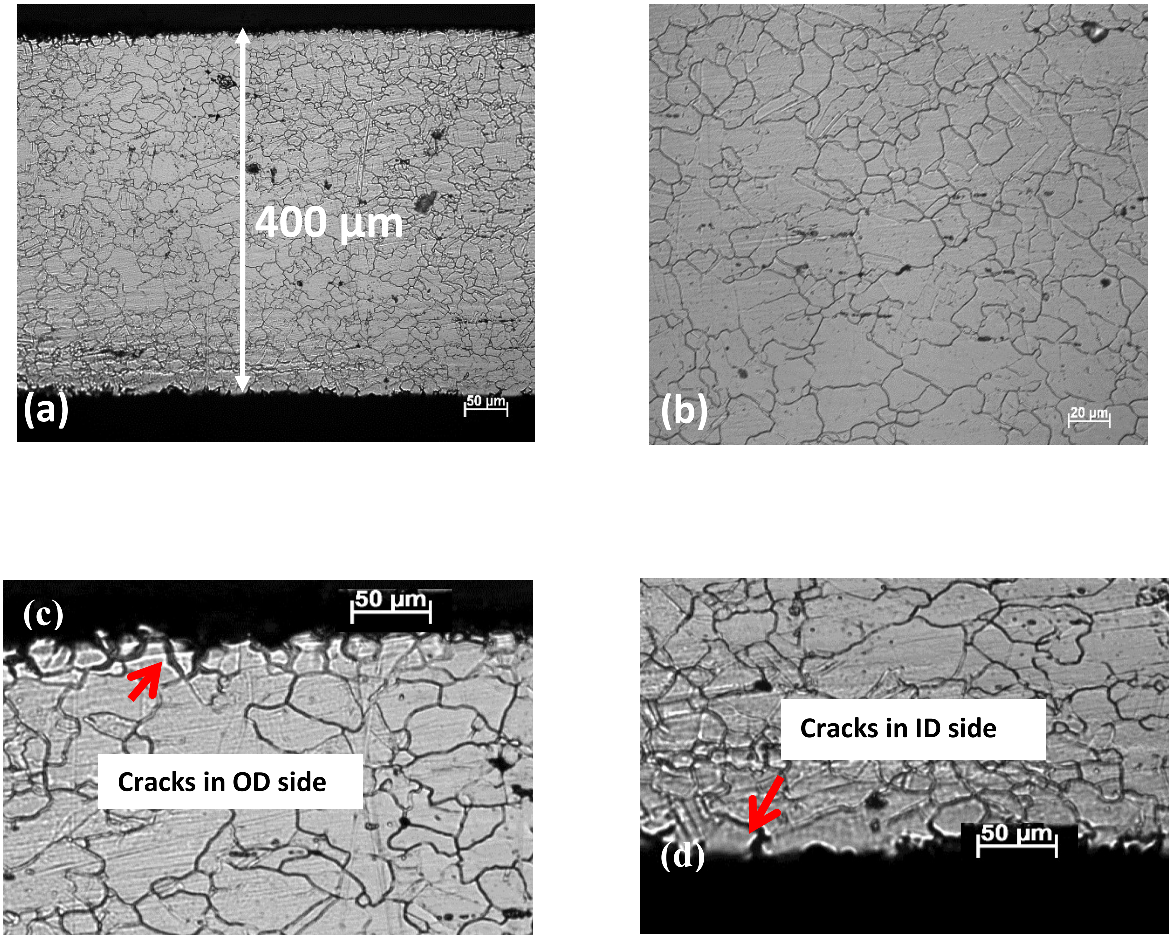

Figure 6.23 Microstructural changes in ballooned region-1 in specimen R1

Hardness reduction

Grain growth softens the microstructure, thereby decreasing the strength which was initially achieved due to cold work. This is evidenced by the progressive decrease in hardness from the region unaffected by the thermal cycling (266 HVN) towards the ballooned region (155 HVN). It should also be noted that the residual stress evolved during the drawing operation could also enhance the hardness in the unaffected region. The observed hardness is the resultant of the microstructural state and the induced residual stress in the clad tube. The residual stress however relaxes during exposed to elevated temperature. Therefore, the hardness in the ballooned region is the resultant of the microstructural state only. The factors contributing to the strength of the D9 alloy are the cold work and the finer grain size. However, exposing the specimen to high temperature and internal pressure led to progressive loss of strength derived from both cold working and finer grain size. The ultimate failure of the clad occurred after thinning of the specimen that led to a significant loss in the load bearing cross-sectional area. Thus, it can be stated that the microstructural instability caused by significant grain coarsening resulted in localized strength reduction which subsequently led to plastic instability causing ballooning.

Precipitates of the form $M_{23}C_6$ and MX usually form when D9 Alloy is exposed to elevated temperature which can influence the hardness and strength of this alloy. The temperature range at which precipitation of $M_{23}C_6$ occurs is 773 - 1173 K in stabilized austenitic stainless steels [143]. However, as the temperature in the current investigation was around 1223 K precipitation of $M_{23}C_6$ is unlikely to occur. Precipitation of MX occurs in defect structures like dislocations and stacking faults. As the test temperature in the current investigation is high enough to anneal all defect structures, this precludes the precipitation of MX carbides. Thus it can be concluded that there was no significant role of precipitates on the strength variation in the ballooned and the un-dilated regions.

6.6.2. Fractography investigation of ballooned specimen R2

Fractography of the failed specimen (R2) has been done to determine the cause of its failure. The test details of specimen (R2) is given in section 6.5.4. The burst specimen (R2) was ultrasonically cleaned with ethanol prior to fractographic investigation in the Scanning Electron Microscope (SEM).

The fractographs of the ballooned specimen are shown in Figure 6.24. Fractographic examination on the failed clad tube specimen indicated the presence of fine dimples across the entire cross section which is a signature of ductile failure. The region adjoining the ballooned portion had undergone excessively localized yielding (tube thickness in this region was in the range of 190-225 μm, when compared to the thickness of around 140 μm in the top portion). The failure resulted due to the plastic instability associated with ballooning.

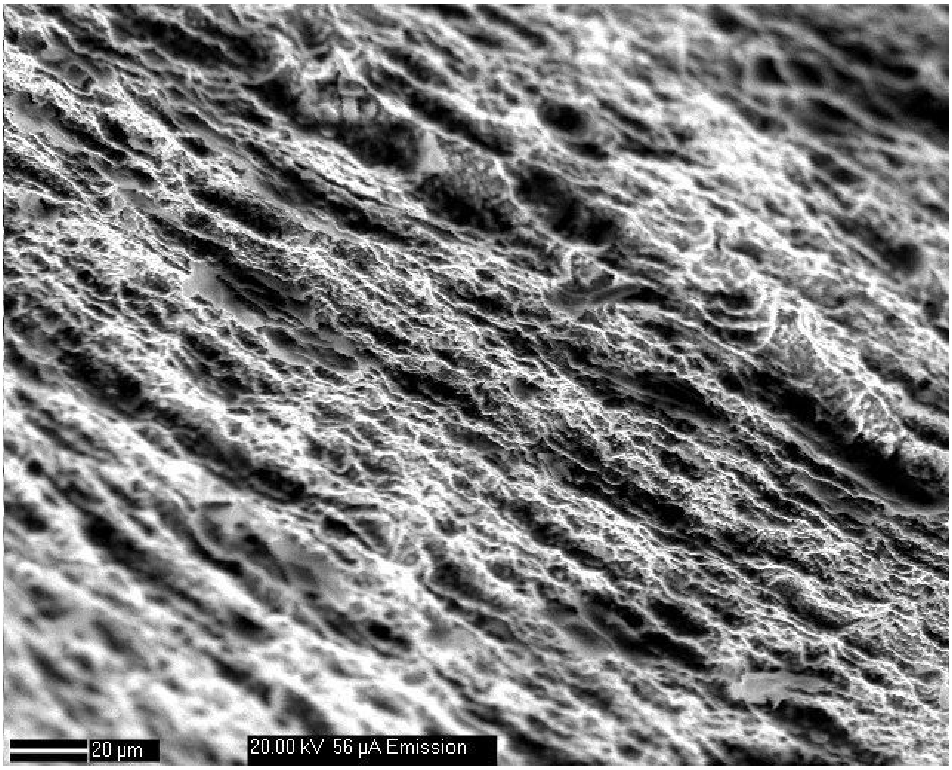

Figure 6.24 Fractograph of the ballooned specimen R2

6.6.3. Comparison between ballooned and ruptured specimens

Creep test has been carried out on clad tubes at 973 K and at a uniaxial stress level of 250 MPa stress. The clad tube was tested in a standard dead weight creep machine [150]. The clad specimen geometry is shown in Figure 6.25. The rupture life is 473 hours. The fractograph of the ruptured clad tube is given in Figure 6.26. The clad tube under creep testing conditions exhibited brittle failure in contrast to the ballooned specimen (Figure 6.24). The rupture ductility in this case was around 8%.

The failure mode is intergranular brittle fracture as grain facets are visible in the fractograph of ruptured tube. On the other hand, dimples were only visible in case of the ballooned tube. Though signatures of intergranular cracking are also seen in the ballooned sample, they are much more prominent in the creep tested tubes.

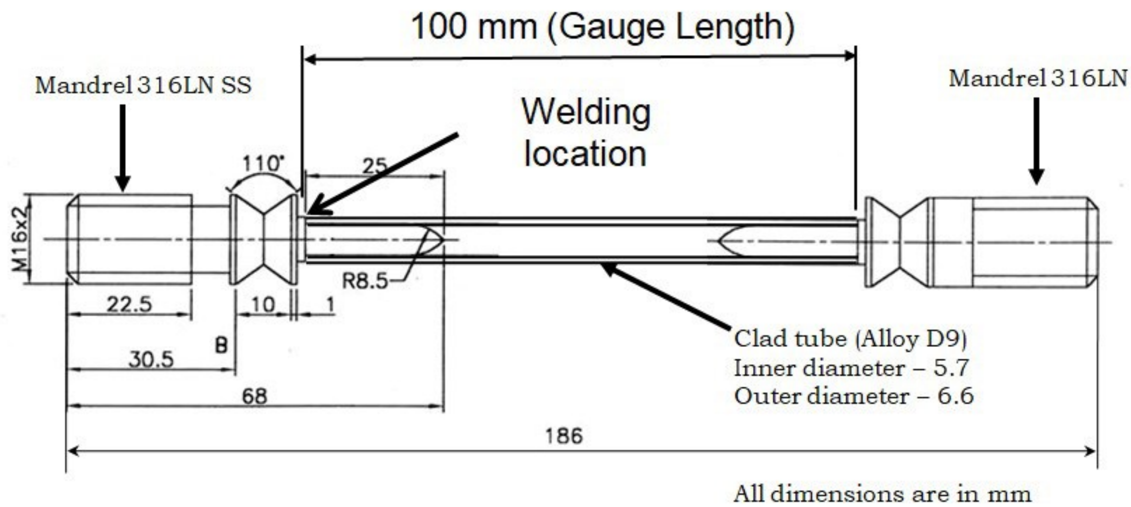

Figure 6.25 Clad tube specimen drawing for uniaxial creep test

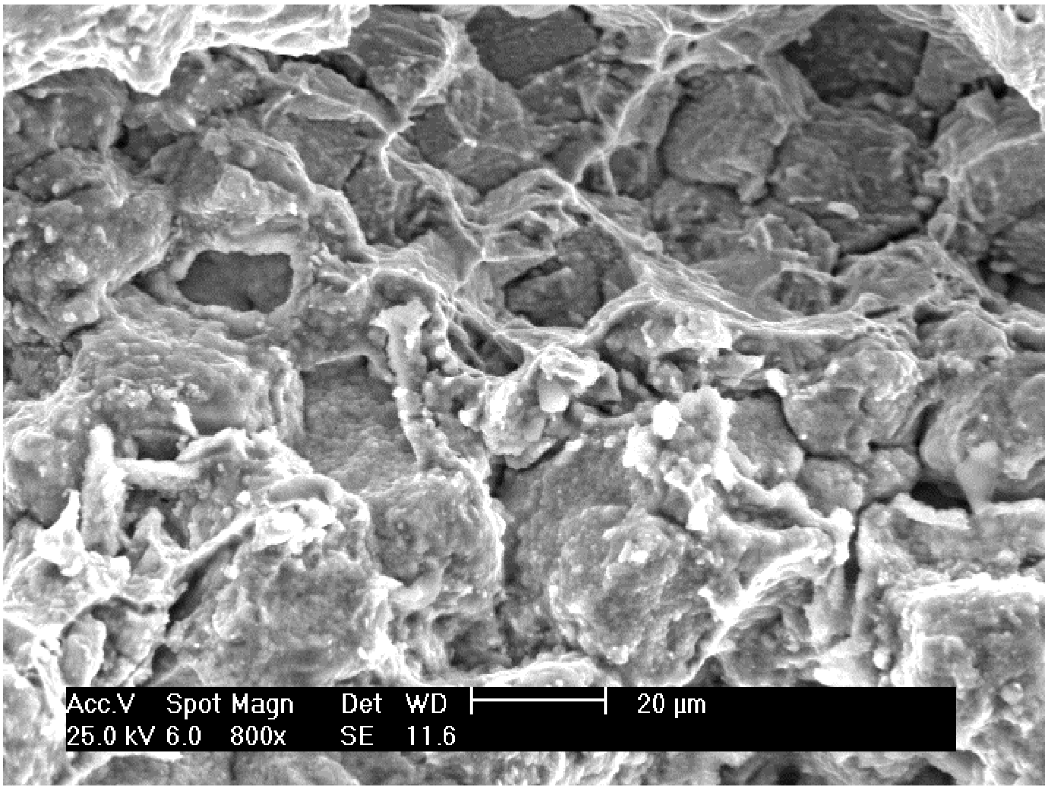

Figure 6.26 Fractograph of ruptured clad tube

6.7. Discussion and inferences

Ballooning tests have been carried out in both HTCTTF and RABITS facility. The specimens are designated as R1, H1 and so on, where 'R' refers to the RABITS facility, 'H' refers to the HTCTTF facility, and the number refers to the specimen number. The test matrix is depicted in Table 6.3.

Table 6.3 Summary of the ballooning test details

Specimen name	Pressure (bars)	Initial tempe rature (K)	Heating rate (K/min)	Rupture temperat ure (K)	Result/ bulging (%)	Remarks
H1	100	303	varying heating rates	1273	25	Specimen held at various temperature to find the temperature at which ballooning can take place
H2	60	303	27	1243	32	Optical imaging done, ballooning took place after 2 cycles
H3	60	303	100	1023	18	Rupture without significant ballooning due to faster heating rate
H4	60	303	40	1473	29	Ballooned before rupture due to slower heating rate
R1	65	303	15	1223	28	Optical imaging
R2	80	303	19	1143	30	Fractography
R3	55	303	3	1288	33	Hypothetical power raising
R4	80	555	24	1177	29.2	Onset of ballooning is captured using DFPD

Two pressure values, i.e., 60 bars and 80 bars have been selected for comparison. 65 bars (R1) and 55 bars (R3) was a slight deviation from the targeted 60 bars, due to technical difficulty in exactly setting the pressure value. Specimen H1 was tested at 100 bars for preliminary understanding of the phenomenon. Optical imaging was also done for specimen H2. As the observations from optical imaging for specimen H2 are similar to that of R1, the results for R1 alone are reported in the thesis.

The following are the inferences from the ballooning tests carried out so far.

1. At faster heating rates, the clad ruptures at lower temperatures, while at slower heating rates it reaches high temperatures. The time spent to reach the high temperature is more at slower heating rates and hence, the percentage of bulging is higher.
2. Slower the heating rate, higher is the dilation and higher the heating rate, sooner is the rupture with less bulging. This can be attributed to the generation of more number of defects in the pre-stressed material subjected to higher heating rates.
3. From specimens H2 and R1, we can conclude with high confidence that the coolable geometry will be maintained during a category-3 event of the reactor.
4. The rupture temperature decreases with increase in pressure (R2, R4).
5. The fuel clad tubes reached higher rupture temperatures when tested in HTCTTF, when compared to the RABITS facility, due to the differences in the furnaces. However, the trend in the behavior of the clad tubes remains the same in both the test facilities.
6. It is inferred from a hypothetical power raising case (R3), that ballooning can take place at slow heating rates if it is allowed to reach higher temperatures, resulting in coolant flow blockage and severe damage. The heating rate during power raising operation in pool-type fast reactors is very slow (~60 K/h, i.e., 1 K/min). Care should be taken to ensure the termination of the withdrawal of control rods at the maximum envisaged temperature.
7. The onset of ballooning has been captured using DFPD. There was material instability till the point of onset of ballooning. Beyond this point, the deformation was rapid, and there was the mechanical instability (plastic instability) that resulted in large bulge and then rupture. The results match with the investigations done by [148]. The material instability in the clad specimens has been observed by optical imaging and fractography, while the geometric instability has been captured using DFPD.

8. Fractography tests confirm that ballooning is a ductile failure. It is compared with ruptured clad specimen that failed by brittle failure, and the difference in the fractographs were observed.
9. It is observed from optical imaging that the extent of grain coarsening decreased with increase in distance from the dilated region. The regions which were far from the dilated portion had retained the strength which was imparted due to the cold work and relatively finer grain size. This is evident from the hardness values and presence of deformation bands in the microstructure. Therefore it can be concluded that the region which was under internal pressure dilated considerably due to the elevated temperature condition.
10. Though the onset of the ballooning can be attributed to the microstructural instability, the subsequent growth of the ballooned region is due to the result of the mechanical instability resulting from loss in cross section as described below.

    The hoop stress (σ_h) generated due to internal pressurization of the clad tube can be related to clad tube thickness (t), diameter (d) and internal pressure (P_i) by equation 6.2.

$$\sigma_h = \frac{P_i d}{2t} \tag{6.2}$$

    Consequent to the onset of localized deformation in the pressurized clad tube, its diameter dilates and its thickness reduces. Thus for the same applied internal pressure, the resultant hoop stress acting on the radial surface increases considerably, further enhancing the propensity to dilate. The dilation progresses readily until the reduction in thickness is considerable enough to cause final failure which is manifested as breakage.
11. The failed specimens R1, R2, R3, R4 are shown in Figure 6.27. A longitudinal crack is observed in specimen R1 at 65 bars pressure, whereas the specimens R2 and R4 burst opened fully at 80 bars pressure. Specimen R3 also opened up, but the shape of the opening

is smoother when compared to R2 and R4 specimens. It could be due to lower pressure and lower heating rate in R3.

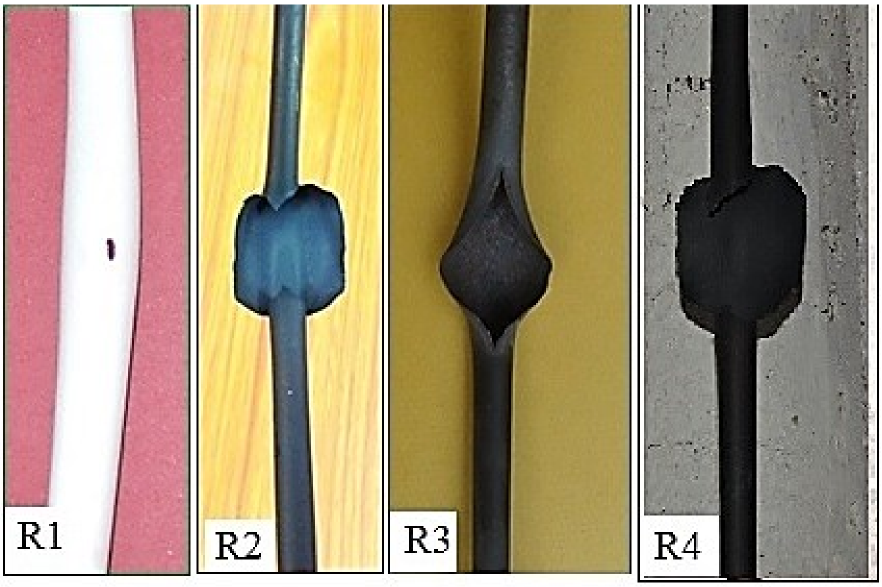

Rupture temp (K)	1223	1143	1288	1177
Heating rate (K/min)	15	19	3	24
Pr (bars)	65	80	55	80

Figure 6.27 Typical failure modes at various combinations of test conditions

6.8. Closure

The effect of heating rate on fuel clad tubes has been studied intensively. It is found that ballooning is a plastic instability that can occur at slow heating rates and can block the coolant flow in the reactor core. It is inferred from the tests that the clad balloons before rupture during slow heating, while it ruptures without significant dilation during faster heating. Thus, slow heating poses a greater risk to the reactor when compared to fast transients. As the heating rate during power raising operation is slow, the clad tubes may balloon if allowed to reach high temperatures. Hence, care should be taken to ensure that the fuel pins do not reach to high temperatures during slow heating. The summary of the thesis, and the future works are discussed in the next chapter.

References

[138] R. Prasad Rajeev and Sen Sujoy. Calculations and Design of Shield for 225 keV, 10 mA X-Rays RABITS Facility. Internal Report, No. RSSD/RSS/310 (2013).

[139] F.C. Campbell. Inspection of Metals – Understanding the basics, copyright (2013), ASM International, p.233-261.

[140] Avinash Kumar Acharya, Anil Kumar Sharma, Ch.S.S.S. Avinash, Sanjay Kumar Das, Lydia Gnanadhas, B.K. Nashine, P.Selvaraj. Investigation of molten fuel coolant interaction phenomenon using real time X-ray imaging of simulated woods metal-water system. Nuclear Engineering and Technology, 49, (2017) 1442-1450.

[141] M. Fujiwara, H. Uchida, S. Ohta, S. Yuhara, S. Tani, Y. Sato. Development of modified type 316 stainless steel for fast breeder reactor fuel cladding tubes. In: Garner FA, Packan NH, Kumar AS, editors. Radiation induced changes in microstructure: 13th international symposium (part I). ASTM STP: 955. p. 127–145.

[142] V.D. Vijayanand, P. Parameswaran, M. Nandagopal, S. Panneer Selvi, K. Laha, M.D. Mathew. Effect of prior cold work on creep properties of a titanium modified austenitic stainless steel. Journal of Nuclear Materials, Volume 438, Issues 1–3, July (2013), Pages 51-57.

[143] V.D. Vijayanand, K. Laha, P. Parameswaran, M. Nandagopal, S. Panneer Selvi, M.D. Mathew. Influence of thermo-mechanical treatment on the tensile properties of a modified 14Cr–15Ni stainless steel. Journal of Nuclear Materials, Volume 453, Issues 1–3, October (2014), Pages 188-195.

[144] S.L. Mannan, S.C. Chetal, Baldev Raj and S.B. Bhoje. Selection of materials for Prototype Fast Breeder Reactor. Transactions- Indian Institute of Metals, April (2003).

[145] Rosy Sarkar, R. Suresh Kumar, N. Raghu, P. Chellapandi, S.C. Chetal. Assessment of design safety limits for fuel cladding based on benchmark tests. Procedia Engineering, volume 55, (2013), pages 355-360.

[146] X. Peng, X. Zhang, J. Fan, B. Chen. Effect of heating rate on the thermomechanical behavior of aluminum alloy LY12 and a phenomenological description. International Journal of Solids and Structures 43 (2006), 3527-3541.

[147] K. Natesan, K. Velusamy, P. Selvaraj, P. Chellapandi. Estimation of maximum stroke length for the stroke limiting device of CSRDM. CFBR/01151/DN/1001/Rev-A (2009).

[148] Anurag Gupta. Ballooning in fuel clads: A study in the constitutive theory and stability of thermoplastic response. IGCAR–IIT Kanpur Collaborative Project, (2018).

[149] Dipti Samantaray, Sumantra Mandal, A. K. Bhaduri & P. V. Sivaprasad. An overview on constitutive modelling to predict elevated temperature flow behavior of fast structural materials. Transactions of the Indian Institute of Metals, 63:823-831, (2010).

[150] V. David Vijayanand. Aspects of integrity assessment of 316LN Austenitic stainless steel weld joint under creep. A thesis submitted to the Board of Studies in Engineering Sciences in partial fulfillment of requirements for the Degree of Doctor of philosophy of Homi Bhabha National Institute, August, (2016).

Chapter 7

Summary and Conclusions

7.1. Conclusions

Thermal transients in pool-type fast reactors namely, power raising and crash cooling have been investigated towards optimization and simplification of the existing schemes. The reactor components and fuel clad tubes have been identified to be the critical components. The reactor components have been analyzed using conventional code for the locations submerged in sodium, whereas a numerical model has been developed for the free level interface of sodium and cover gas locations. The developed numerical model, which is analytically validated, can be used to study the physics of partially immersed components in any fluid. Structural damage assessment of the reactor components during crash cooling recommends eliminating controlled cooling during shutdown, thus simplifying the shutdown scheme. Parametric studies on primary sodium heating rates suggest that 56 K/h is the optimum heating rate with minimal structural damage and minimum time for power raising operation. The study forms a benchmark for other fast reactors for deciding upon the heating rate during start-up of the reactor.

Fuel clad experiments show that clad ballooning is a plastic instability. Though the onset of the ballooning can be attributed to the microstructural instability, the subsequent growth of the ballooned region is due to the result of the mechanical instability resulting from loss in cross section. Ballooning can take place at slow heating rates if it is allowed to reach high temperatures. Hence care should be taken during power raising to limit the heating to the envisaged temperature. Fractography tests confirm that ballooning is a ductile failure, and clad specimen rupture is a brittle failure. It is observed from optical imaging that the extent of grain coarsening increased with decrease in distance from the dilated region. The summary and highlights of the thesis are pictorially represented in Figure 7.1.

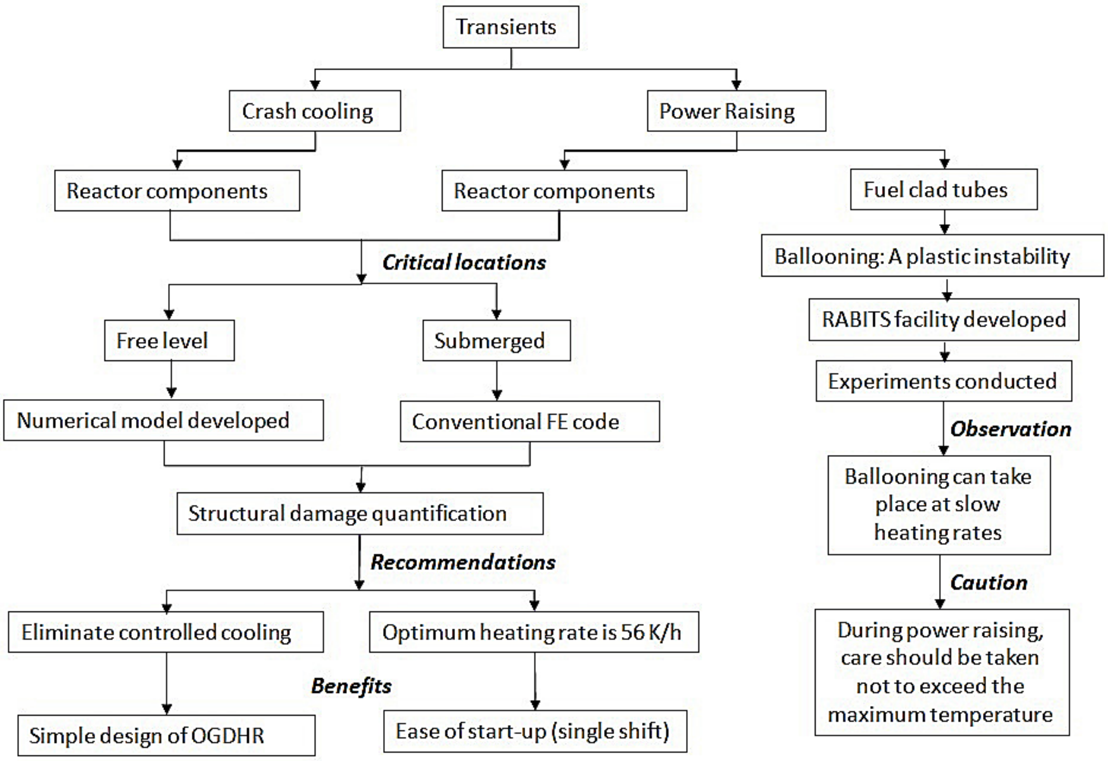

Figure 7.1 Summary and highlights of the thesis

7.2. Future directions

Some of the possible directions for future work are suggested below:

- Thermo-mechanical analysis for power raising and crash cooling can be carried out for future fast reactors with the methodology developed in the present thesis.
- 3D FE analysis for the tubesheet of IHX shall be performed to compare with the results.
- Clad ballooning experiments can be carried out at 56 K/h (~1 K/min) to check the possibility of ballooning at the recommended power raising rate.
- Evaluation on creep damage of fuel cladding tube associated with various heating rates can be carried out analytically.
- A set of experiments with varying parameters can be carried out to establish a regime where dilation will be prominent during actual service conditions.
- The effect of irradiation on the onset of ballooning can be studied experimentally and analytically.